Co-funded by the Erasmus+ Programme of the European Union

PowerLaPs

Innovative Education & Training in High Power Laser Plasmas

Laser plasma diagnostics

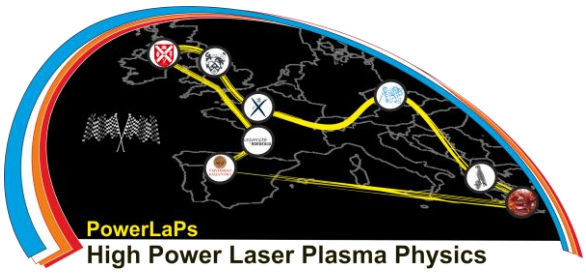

Output Identification: O4
Output Title: Laser plasma diagnostics

O4 Laser Plasma Diagnostics - Theory and Experiments

O4 - Theory

O4 – Theory

PowerLaPs

Innovative Education & Training in High Power Laser Plasmas

Laser plasma diagnostics - Theory and Experiments

Chapter 1: An Introduction to Laser-plasma process diagnostics

L. Volpe

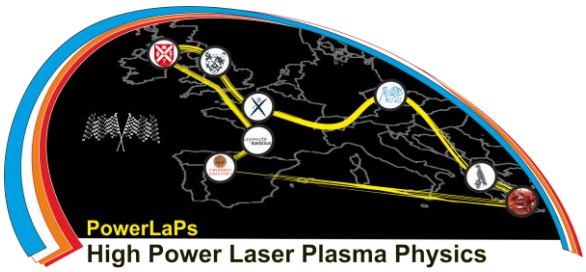

1 Laser-driven proton sources and applications

1.1 Laser-driven Proton sources

For several years laser-driven proton acceleration –or ion acceleration- has been studied and mostly at the level of proof-of-principle experiments[1] and many theoretical models have been proposed for its interpretation[2]. Most of the experimental results have been obtained by using ps long pulse lasers (Nd-YaG). The advent of the Ti-Sa laser have reduced the laser pulse duration of three order of magnitude thus allowing to reach the same intensities with lower energy. Now with the relative high repetition rate of VEGA is time to start considering users close to their final applications. Probably one of the most relevant technological applications of modern laser systems is the acceleration of protons (or other ions[3]) in the two limits of ultra-low emittance high energy[4] or high emittance at moderate energy. The physics of the proton/ion acceleration has been studied over more than one decade[5]. It has a number of potential applications, and so a number of potential users. Among those applications, probably the most relevant group are the medical applications, such as ion beam[6] therapy[7]. The medical community is giving a high degree of recognition to proton and ion beams as a new tool in tumour therapy[8] named proton

[1] H Daido, *et al., Review of laser-driven ion sources and their applications*, Reports on Progress in Physics **75** (2012) 056401
[2] A. Macchi, M. Borghesi, M. Passoni, *Ion acceleration by superintense laser-plasma interaction"* Reviews of Modern Physics, volume 85, (2013)
[3] A V Korzhimanov, *et al., Production of multiply charged ion beams with an energy of tens of MeV/nucleon by ultrahigh-power laser radiation for nuclear physics problems,* Quantum Electronics 43 (2013) 217-225. Although in this paper they are proposing the use of circularly polarized 8 fs pulses.
[4] T E Cowan, *et al.,* Ultra-low emittance, high current proton beams produced a laser virtual cathode sheath accelerator, Nuclear Instruments and Methods in Physics Research A, 544 (2005) 277-284.
[5] V T Tikhonchuk, Physics of laser-assisted ion acceleration, Nuclear Instruments and Methods in Physics Research A, **620** (2010) 1-13.
[6] Sh Kawata, *et al.,* Laser ion acceleration toward future ion beam cancer therapy –Numerical simulation study- Laser Theraphy 22 (2013) 103-114.
[7] U Masood at al, A compact solution for ion beam therapy with laser accelerated electrons, Applied Physics B, Lasers and Optics, 2014.
[8] U Linz and J Alonso, Physical Review Special Topics – Accelerators and Beams, 10 (2007) 094801.

therapy[9], and the feasibility of laser accelerators[10,11] for this purpose is considered[12,13].

Regarding laser-driven ion acceleration, we can make estimates of the maximum proton/ion energy, conversion efficiency, shape of the energy spectrum, etc. based either on actual data or extrapolations (scaling laws), obtained in analytical models, PIC simulations, or experimental measurements. There are a few fs lasers around the world preparing or doing such experiments[14], and there is a lot of different configurations for that. Experimental results obtained by Ogura[15] and collaborators in 2012 can be used as "reference case". By using 7 Joule energy, 40 fs laser pulse duration 1021 W /cm2 and irradiating targets of 800 nm thickness, they reported proton energies up to 40 MeV. The physics of proton acceleration depends on many parameters but the laser intensity seems to be the most important indeed all the scaling laws confirm such behaviour[16],

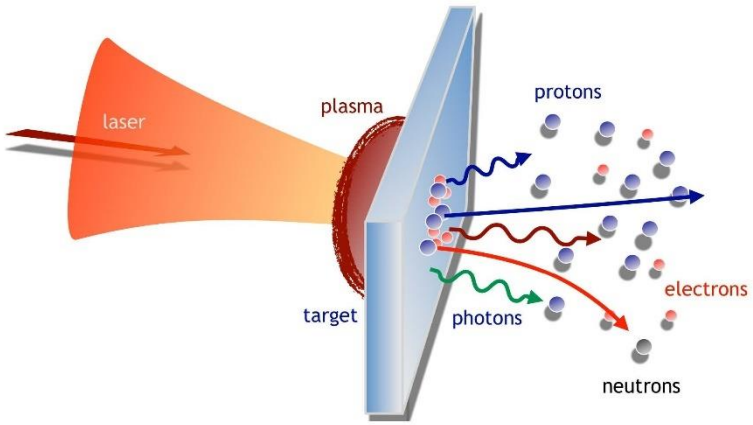

Cartoon of the solid target experiment giving accelerated particles.

We must bear in mind that the estimation of achievable parameters in laser-driven ion acceleration is complicated by the inherent complexity of the process and the variety of mechanisms that operate at each stage of the interaction, starting from the initial ionisation, plasma formation, absorption of the main pulse energy, plasma evolution, and

[9] A R Smith, Proton therapy, Physics in Medicine and Biology, 51 (2006) R941
[10] A Maksimchuk, et al., *High-energy ion generation by ultrashort laser pulses*, Plasma Physics Reports, 30 (2006) 473
[11] K W D Ledingham, *A visión for laser induced particle acceleration and applications,* Hyperfine Interactions 171 (2006) 69
[12] S V Bulanov and V S Khoroshkov, Plasma Physics Reports 5 (2002) 453
[13] D Habs, T Tajima, and U Köster, *Laser-Driven Radiation Therapy,* in *Current Cancer Treatment: Novel Beyond Conventional Approaches*, O. Ozdemir (Ed.), (Intech, Rijeka). 2011.
[14] S Agosteo, The LILA (laser induced light ions acceleration) experiment al LNF, Nuclear Instruments and Methods in Physics Research B, 331 (2014) 15-19. These authors are using the laser FLAME at Frascati, very similar to VEGA-2, but a bit more powerful.
[15] K Ogura, *et al., Proton acceleration to 40 MeV using a high intensity, high contrast optical parametric chirped-pulse amplification/Ti:sapphire hybrid laser system,* Optics Letters 37, (2012) 2868.
[16] M Carrié, *et al.,* Effect of femtosecond laser pulse duration on thin foil accelerated protons, Nuclear Instruments and Methods in Physics Research A, 620 (2010) 36-40.

finally ion propagation.

Usually it is difficult to identify a dominant regime, and often several regimes are present at different stages of the interaction. A possible classification of the different schemes can be done by considering separately laser-solid and laser-plasma interaction.

Laser-solid interaction

Target normal sheet acceleration (TNSA)
This is the most common methods which has been tested experimentally during the last two decades. In this scheme the laser beam interact with an opaque target in the so called skin layer region. Protons (which are present, as impurities on both sides of the target) are accelerated by the quasi-static electric field generated by the hot electrons escaping the rear surface of the target. For that maximum proton energy depends linearly on the hot electron temperature which scale linearly with the square root of the laser intensity. TNSA protons are characterized by a broad exponential decreasing spectrum with a (experimentally proved) high energy cut-off of about 60-70 MeV. TNSA scheme have been tested over a wide range of target thickness (1-100 microns) and laser pulse duration (40 fs - 1 ps) and with respect to this, recently, it has been shown that the best TNSA performance can be obtained by using 100 fs long pulses17. However, as explained before, the results obtained by Ogura et al in the reference of the previous page are encouraging for testing some TNSA-related models like the strong charge separation and the coulomb explosion at the CLPU centre.

Radiation Pressure Acceleration (RPA, laser piston)
This scheme has been extensively studied both theoretically and experimentally. When a high-intensity (~PW) laser pulse with sufficiently large focal spot interacts with a thin foil ("light sail" regime), the radiation pressure can push forward the electrons of the foil. The consequent charge separation field (the ions respond slowly) efficiently accelerates the ions. The same mechanism can be achieved even for thicker foils ("Hole boring" regime) on condition to use circular laser polarization which can inhibit electron heating due to the JxB force. Providing at least one PW RPA mechanism could provides proton up to 100 MeV and ions up to 350 MeV with a few per cent of energy spread. The extreme requirements of this mechanism (high intensity > 10^{22} W/cm^2, high laser contrast > 10^{10} and very thin targets ~ few tens of nm) place him among the challenges for the system PW VEGA-3

→ Transparency regime: Break-out afterburner (BOA)
This mechanism represents the transition between TNSA and RPA. because it has the same requirements as RPA at lower laser intensities (> 5 1019 W/cm2) with linear polarization. when ultra-thin foils are used as targets, the expansion of the foil may lead to the onset of transparency during the short-pulse interaction, when the electron density fall down till to the limit value which is given by the relativistic critical density. At the moment

[17] Tochitsky et al., "*Summary report of Working Group 6: Laser-plasma acceleration of ions*" AIP Conf. Proc. 1507 (2012) 231

the higher proton kinetic energy has been obtained experimentally in this regime at the Trident (Nd-Yag 150 TW contrast > 1010 over 100 nm CH2 target).

Laser-plasma interaction at near-critical density

Gas target is an alternative to solid foil. Indeed it can operate at high rep. Rate, it is easily adjustable for target density and material, and it also less susceptible to the laser pre-pulse (i.e you do not need high contrast).
→ Shock Wave acceleration and hole boring
Recently 20 MeV mono energetic (energy spread of few per cent) proton beam has been obtained by the interaction of a linearly polarized 5 TW CO_2 laser with H_2 gas jet (the so called SWA)[18] [19]. In this scheme the combined effect of the laser heated electrons and the plasma density gradient (near the critical density) create a local temperature and density discontinuity which induce the formation of an electrostatic shock. This shock during travelling in the target overtakes and reflect the protons accelerating them to twice the shock velocity. In a similar configuration few MeV protons have been generated via "hole boring[20]" acceleration. In this mechanism the laser-plasma interaction occurs due to the piston action of the radiation pressure of the laser pulse which directly accelerate ions at the interaction surface[21]. These accelerating schemes were started to be investigated using 1 mm lasers (which requires plasma with a maximum density of the order of 10^{21}/cc i.e. the critical density) at LULI and on the Titan laser facility at Livermore.

It is important to point out that the optimal conditions for hole boring would be achieved by using circular polarization to quench undesired electron heating and for linear polarization HB may become the dominant mechanism at intensities exceeding 5 10^{20} W/cm^2, as suggested by a theoretical argument. Different mechanisms tend to produce different proton spectra, in some cases this can be very relevant[22].

1.2 Proton Stopping Power in plasmas

The measurement of the energy loss of light ions in a warm dense plasma, where significant theoretical uncertainties on the stopping power are reported due to electron degeneracy and coupling and experimental data are missing. The understanding of ion stopping in this regime is of great interest both from a fundamental scientific point of view and for the modeling of inertial confinement fusion plasmas. The considered projectiles are

[18] D. Haberberger et al, "*Collisionless shocks in laser-produced plasma generate monoenergetic high-energy proton beams* " Nature Physics, 8 (2012)
[19] M.Gauthier, et al. Investigation of longitudinal proton acceleration in exploded targets irradiated by intense short-pulse laser Physics of Plasmas (1994-present) 21 , 013102 (2014);
[20] E. D'Humieres et al., "*Investigation of laser ion acceleration in low-density targets using exploded foils*" Plasma Physics and Controlled Fusion 55, 124025 (2013)
[21] A. Macchi, "Theory of Light Sail Acceleration by Intense Lasers: an Overview", High Power Laser Science and Engineering 2, e10 (2014)
[22] Tung-Chang Liu, et al., Generation of quasi-monoenergetic protons from thin multi-ion foils by a combination of laser radiation presure acceleration and shielded Coulomb repulsion, New Journal of Physics, **15** (2013) 025026/16

quasi-monoenergetic light ions created from a D3He “exploding pusher” capsule imploded by 6 LMJ quads. The probed warm dense plasma is created by the isochoric heating of a thin low Z material located inside a metal-coated plastic cavity by X-rays driven by 6 other LMJ quads. Temperatures close to 30 eV at solid density are reached, corresponding to a target electron coupling of $\Gamma \sim 0.3$ and an electron degeneracy $q \sim 2$. The energy spectra of the ions that passed through the target are recorded with the SEPAGE charged-particle spectrometer. The target conditions are probed with Thomson scattering technique by using K-alpha radiation induced by heating of a back-lighter foil with the PETAL beam. The scattered spectra are measured with the HRXS spectrometer. Proton imaging of the target with radiochromic films also enables to diagnose the electron density as well as the electric and magnetic fields in the target.

WDM

The study of plasmas at extreme densities is a fundamental branch of modern plasma science that can be relevant for astrophysics, for nuclear fusion technology and to get new conceptual states of matter.

Ultra-high-intensity proton and ion beams can be used as sources for fast ignition in laser-induced fusion. Although the beam parameters needed for this application are very far from being achieved, and even further from the scope of CLPU, experiments with the VEGA system may contribute to tackle some of the requirements of this application, i.e. heavy ion acceleration, limited bandwidth, ion energies of the order of 25–40 MeV/nucleon, and high conversion efficiencies.

The collimation or focusing of ions can be applied to the fast isochoric heating of dense plasmas for the equation-of-state measurement and characterization of matter in extreme conditions (e.g. Warm Dense Matter, for planetary science and astrophysics). In this experiment, the sample thickness should be less than the distance of the Bragg peak from the surface. Thus uniform heating of a dense plasma with thickness of a few um can be achieved, which is advantageous compared with optical laser heating. In experiments performed so far, a second ultra-short laser pulse was used to produce X-rays for spectroscopic measurements or scattering in Warm Dense Matter.
VEGA-3 can also be used (at lower intensity and on a larger focal spot) for conventional optical laser “large volume” heating experiments which could also provide uniform plasma heating thus avoiding 2D effects

Degenerated Plasmas

Ion stopping in dense plasmas is an important topic in various fields of modern physics that is still far from being completely understood. It plays a central role in Inertial Confinement Fusion (ICF) for the target self-heating by alpha-particles that triggers ignition and thermonuclear gain [Hurricane2016], and it is even more crucial for target heating schemes using ion beams as main drivers like heavy-ion fusion or ion-driven fast ignition. Ion stopping in plasmas is also essential in high-energy-density physics for the generation and the characterization of Warm Dense Matter (WDM) [White2012], in astrophysics as

well as for plasma diagnostics using ion beams [Golubev1998, Mackinnon2006, Volpe2011, Rygg2008]. Moreover, a detailed understanding of the ion-stopping processes is relevant for other related transport properties based on Coulomb collisions in plasma, like electrical and thermal conductivity or temperature equilibration [Gericke2002a, Haun2002]. Except in very hot burning ICF plasmas, the ion stopping power is only due to the target electrons. The electronic stopping power reaches a maximum when the projectile velocity is nearly equal to the thermal velocity of the plasma electrons (vp ~ vth). This peak in stopping power leads to the Bragg peak where a large proportion of the ion energy is deposited into a small target volume. Depending on the dominant Coulomb collisions involved in the beam-plasma interaction, different theoretical models can be used for the stopping power [Cayzac2015]. For high velocities vp >> vth, standard perturbative models usually apply and are supported by experimental data [Hoffmann1990, Dietrich1990, Frank2013]. For velocities approaching the stopping-power peak vp ~ vth the beam-plasma coupling becomes important and the theoretical description of the stopping power is difficult since it requires to account for the effects of both close binary collisions and collective plasma excitations. Consequently, large discrepancies appear between the predictions of different stopping-power models [Cayzac2015, Gericke2003, Edie2013]. Experimentally, investigating the regime vp~vth is challenging, especially due to a strong stopping power dependence with temperature and density, requiring a precise characterization of the target conditions.

The theoretical modelling of the stopping power is even more challenging when the plasma target features electron coupling (non-ideality) and electron degeneracy. Electron coupling and degeneracy are quantified by the dimensionless parameters Γ and q respectively, a being the average distance between the electrons and EF the Fermi energy of the free electron gas.

$$\Gamma = \frac{e^2}{a\left(k_b T_e + E_F\right)}, \theta = \frac{k_b T_e}{E_F}$$

Electron coupling (for Γ > 0.1) and degeneracy (under q < 10) are expected to significantly influence the ion collisions with the plasma electrons, and thus the stopping power in coupled and degenerate plasmas concern WDM targets in general and especially in ICF in the cold and dense deuterium-tritium fuel surrounding the hot spot. The knowledge of particle transport properties in such targets is required for guiding and interpreting experiments involving WDM targets generated by ion beams, for example for equation-of-state investigations, and especially for better understanding the mechanisms leading to ignition in ICF targets More generally, it has fundamental implications for non-equilibrium statistical mechanics and the underlying atomic processes. However, until today, ion stopping in WDM conditions remains largely unknown and very large discrepancies, of up to 50% or even more are reported between the theoretical predictions [Zwicknagel1999, Gericke2002b, Deutsch2014, Hayes2015, Edie2013] and experimental data are highly needed to benchmark the models. As shown in the previous references, differences between various stopping power models are largest around the stopping power peak vp ~ vth. Precise ion-stopping measurements typically require “pump–and-probe” experiments with well-characterized ion beam and plasma target conditions. The ion “probe” should be as mono-energetic as possible and can be provided by an accelerator source or by laser-induced nuclear reactions. A WDM sample can be produced via different heating

mechanisms (the "pump"): i) direct laser irradiation (mostly used with femtosecond pulses, leading to strong density and temperature gradients), ii) ion beam irradiation (uniform heating in most of the target volume as the majority of the energy is deposited at the Bragg peak), iii) X-ray irradiation (uniform volumetric heating but low conversion efficiency). The latter method provides uniform plasma samples but requires more laser energy due to the conversion of laser beams into X-rays. Kilojoule and Megajoule facilities are best suited for this type of target heating method.
In the context of WDM studies, a recent experiment [Zylstra2015] was performed at the OMEGA laser facility using monoenergetic protons created from DHe3 exploding pusher targets as projectiles, probing a warm dense beryllium sample isochorically heated by X-rays and featuring $\Gamma = 0.3$ and $q = 2$. In that work, the high-velocity stopping regime was probed using 14.63 MeV protons, with a corresponding velocity ratio $v_p/v_{th} > 10$ for which differences between theoretical stopping power predictions are small. The results were in agreement with well-established high-velocity stopping formalisms and did not allow to discriminate between classical and quantum stopping power models. Moreover, the plasma parameters could not be directly measured and were instead deduced from previous similar experiments.

1.3 Proton Radiography in PLASMA

(I) INTRODUCTION:
Transverse point projection Proton Radiography (PR) [1] has been used to measure the target density during the compression in many ICF experiments. Proton beam source can be generated by fusion products in exploding-pusher implosions of D3He-filled glass-shell, providing monoenergetic beam with energy ~15 MeV [2,3] or by Laser-target interaction providing multi energetic beam with a Peak energy ~ 50 Mev [4,5]. Laser based protons are characterized by small source, high degree of collimation and short duration. The multi energetic proton spectrum also allows probing the implosion at different times in a single shot, thanks to the difference in time of flights for protons at different energies. This is a clear advantage over other diagnostics (e.g. hard X-ray), which require several shots in order to follow the complete implosion history. PR using laser-generated protons, and radiochromic films (RCF) as detectors, has already been used in experiments at Rutherford Appleton Laboratory (RAL) [6] to probe the implosion of a spherical shell; experimental results were analyzed and compared with MC simulations. However, the analysis done in [6] is based on the usual approach to proton imaging, in which, the proton energy loss during the target penetration is neglected assuming a direct correspondence between time of flight and stopping range of proton inside the detector. This approach has proven to be very successful in the detection of electric and magnetic fields in plasmas [7,8] but, as we will show in the following, it fall if applied to a the typical ICF conditions in which protons penetrating thick and dense targets suffer severe multiple scattering (MS) and energy losses. These effects have previously been considered in

static PR by Roth et al. [9], but acquire a new and deeper meaning in our dynamic situation, bringing to mixing of the images formed by protons with different energies. This implies a more careful analysis of RCF images, dropping the simple layer-to-time correspondence, and requiring detailed comparison with computer simulations. Whenever such analysis is done, we get a good agreement between experimental results and hydro simulations. Starting from conventional point of view, in ref [6] the authors associated on RCF layer to a given probing time, and actually restricted most of their analysis to one layer only. In this way they oversimplify the physical interpretation. The low density and hot temperature plasma corona play a fundamental rules in formation of image on detector due to the relative low proton energy because of SP in plasma is higher than that in solid target. PR technique has also been used in next experiment at RAL in 2008 to study fast electron propagation in cylindrical compressed target [10,11]. Starting with the new point of view reported in this paper we performed a more accurate analysis of the proton radiography experimental results. The results are under publications [11]. Here a basic review of the classical scheme of PR is presented, discussing on the principal phenomena, such as the SP and the MS, which could affect PR performance changing the physical state of the medium. These phenomena are connected to the variation of parameters (density, temperature and ionization degree) during target implosion. Target implosion can be divided in three spatial regions: (I) the plasma corona (large size) low density, high ionization and high temperature (II) the shocked region (small size) high density medium ionization and low temperature (III) the unperturbed target (medium size) solid density. Hydrodynamical code CHIC [12] has been used to produce density, temperature and ionization degree profiles which have been used as initial condition for PR MC simulations. MC code MCNPX [13] has been adapted to describe MS, plasma effects on SP and 3D simulations is performed in order to reproduced the complete hydrodynamical history of the imploding target. We also show that MS effects are dominant in (I) and (II) regions and we develop a simple analytic formula to study the performance of PR as a function of initial experimental parameters in that regions.

(II) PROTON RADIOGRAPHY

Proton radiography set up, for a typical ICF [6,10] experiments, is shown in fig. 1 in which a point-like multi energetic proton source is used to probe a cylindrical target. Protons with different energy probe the target at different time and deposit their energy at different position inside the detector. The detector is made by a series of active layers (RCF) positioned in a stack one after each other; the measured optical density on each RCF active layer is proportional to deposited energy [14]. Thanks to the Bragg peak proprieties protons deposit most of their energy at the end of its travel inside the detector then we can arrange the position of the radiochromic films inside of the stack so that each film collect

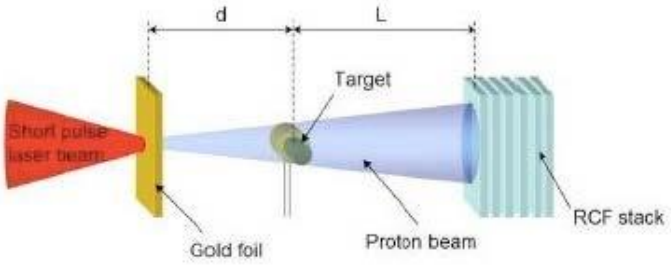

the energy range carried on by protons corresponding to defined stage in the target hydrodynamic evolution. Considering all the RCF it is possible to obtain a series of images to the imploding target relative to different implosion times. The covered time range is related to the energy range and to the distance between proton source and probed target. As example let us assume the following experiment condition distance between source and target~1 cm energy range from 1 to 10 MeV the covered time range is about 500 ps. The theoretical magnification of the system is M=(d + L)/d~4.5.

Fig. 1 : Schematic of the proton radiography setup

(III) NUMERICAL SIMULATION

Numerical simulations are necessary in order to reproduce and to give a correct interpretation of the PR experimental results and to study experimental set up for next experiments.

The simulation processes consist in two different steps in which we use consequently Hydrodynamic CHIC [12] and Monte Carlo MCNPX [13] codes.

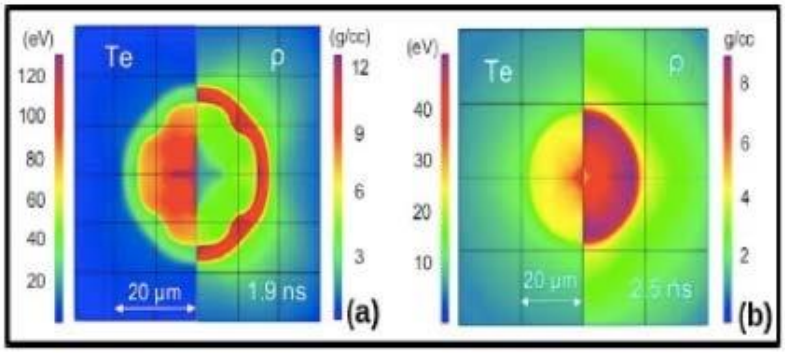

Fig. 2 : Density and temperature 2D maps obtained running chic code to reproduce the cylindrical compression performed at RAL laboratory in 2008 [10,11] (a) target fill with 1 g/cc plastic foam (b) target fill with 0.1 g/cc plastic foam.

a) CHIC hydro simulations: Starting from laser proprieties (pulse duration, intensity and frequency), target composition and target geometry (planar cylindrical, spherical) we simulate the hydrodynamical evolution of the compressed target obtaining 2D or 3D density, temperature and ionization degree maps (see fig. 2). As example we show in

Fig. 2 simulations performed for the RAL-08 experiment set up [6].
The CHIC code includes bi-dimensional axisymetrical hydrodynamics based on a cell-centered Lagrangian scheme, electron and ion conduction, thermal coupling and detailed radiation transport. In our case, the ionization and opacity data are tabulated assuming a local thermodynamic equilibrium (LTE), depending on the plasma parameters. The equations of state implemented in the code are based on a QEOS model [15] or SESAME tables [16].
b) MC simulations: we extract the profiles from density, temperature and ionization degree 2D (or 3D) maps in order to implement target design in to MC input file. MC code input file require also the geometrical configuration of the experiment (chamber and detector design) and the spatial and energy distribution of the proton beam used to probe the target (see section proton energy spectrum).

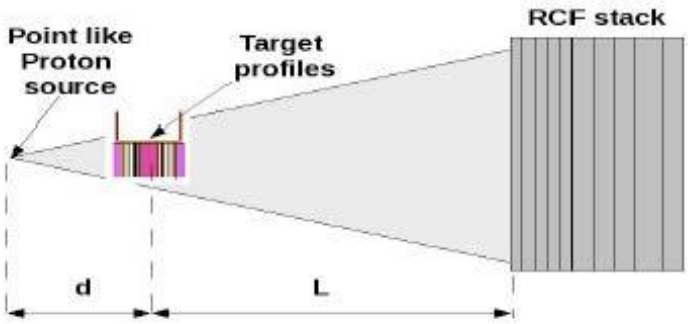

Fig. 3 : representation of the MCNPX input file
MCNPX is a general-purpose Monte Carlo N–Particle code that can be used for neutron, photon, electron, protons and other particles transport. The MC code is able to reproduce the experimental set-up in all its relevant parts: the proton source (energy spectrum and spatial distribution of the proton source obtained from RCF analysis), the target and detector characteristic (material composition, density profile and geometry). SP of protons in the target is described by using Bethe's theory [17] while MS effects are described by Rossi's theory [18]. Simulations of image formations were finally done as follows: i) We assume a time sampling of hydro profiles (density, temperature and ionization degree (Fig. 3)). ii) For each hydro time, we run a MC simulation using the relative proton energy and protons number (see section III), calculating the energy deposition in each RCF layer. Each hydro-time corresponds to a different time-of-flight of incoming protons, i.e., to a different proton energy (The total number of particle (normalized to 1) used in all simulations must be equal to 1). However, here we consider the energy deposited by such protons in all RCF layers and not only in the one corresponding to the Bragg peak of the emitted protons, as it is usually done (of course, images will be formed only in RCF layers before that corresponding to the initial Bragg peak and in this one). iii) The full proton spectrum is covered running different simulations changing hydro times (i.e. The hydro profiles). In this way, for each RCF layer we get a series of mono-energetic, fixed-time, 2D images. iv) Finally for each RCF layer, we sum all images at different times. In this way the

resulting images on each layer will contain the contribution of all the protons of the beam, which probed the target at different times (depending on their energy). As just explained before SP and MS effects must be considered in order to obtain a good agreement with experimental results.

plasma effects: Here we introduced some modifications in order to account for the differences between Bethe's theory and the actual SP in plasmas. Such "plasma effects", connected to the variation of parameters (density, temperature and ionization degree) during target implosion, must be taken into account comparing MC simulations with experimental data and hydrodynamic simulations . Indeed, there is a significant region in the imploding target (plasma corona) in which the temperature becomes very high (T ~ 1 keV) which implies a large number of free electrons (ionization degree) with respect to the bound electrons and a correspondent enhancement of SP. Conventional MC codes as MCNPX, FLUKA, SRIM, do not take into account such effects because were built to describe particle transport in cold matter (i.e temperature and ionization effects are not taken into account). A number of theoretical studies on ion beam interaction with plasmas are found in literature [19] and an experimental proof of the increase of the ion SP in ionized target material has been obtained in ref [20]. A self-consistent theory of energy loss of ions in plasmas is given by means of the Vlasov-Poisson equations [19]. Our analysis is developed within this framework (it is important to point out that there exist many other approach which lead to the same results, see for example [21].) and leads to the following formula for SP in partially ionized plasma (all the details are shown in Appendix).

$$(1)\quad \left[\frac{dE}{dx}\right] = 1.23\cdot 10^{-9}\frac{\rho}{AE_p}\left[q_i L_f + (Z-q_i)L_b\right]$$

where Lf and Lb are respectively the free and bound electrons terms (eqs. A2 and A5). Eq. 1 represent the energy loss by protons with energy Ep(MeV) passing through partially ionized plasma with atomic and mass number Z A, density r(g/cc) and ionization degree qi. The temperature effects are taken into account by the term Lf which is a function of T(eV). The general equation in (1) lead to the Bethe SP formula [17] when qi becomes 0

$$(2)\quad \left[\frac{dE}{dx}\right]_c = 1.23\cdot 10^{-9}\frac{Z\rho}{AE_p}\ln\left[2149\frac{E_p}{\bar{I}}\right]$$

and lead to the Bohr SP formula [22] when qi becomes equal to Z

$$(3)\quad \left[\frac{dE}{dx}\right]_p = 1.23\cdot 10^{-9}\frac{q_i\rho}{AE_p}\ln\left[235.8\sqrt{\frac{AE_p^3}{q_i\rho}}\right]$$

Comparison between Bethe and Bohr formula is shows in Fig.5(a) as a function of proton energy for the same material (Mylar), temperature T=1 keV and density r = 0.1 g/cc. This difference showed in Fig.5(a) is principally due to the fact that free electrons are excited more easily than bound ones and it seems that it occurs predominantly for low density regions (e.g. r<1 g/cc). It is important to note that eqs. 1,2,3 are valid only in the classical free gas approximation (eqs. A11 in the Appendix), i.e for low density and high temperature as showed in Fig. A1. One simple way to include plasma effects without changing the code in MCNPX is to replace the "real" density profile (Fig.6) rh given by hydro simulation with an "effective" profile re calculated by imposing g the SP used by MC code (eq. 2) to be the same as the one which takes place in plasma

(eq. 3) in the region where the classical free gas approximations are satisfied.

$$(4)\ \left[\frac{dE}{dx}\right]_c(\rho_e)=\left[\frac{dE}{dx}\right]_p(\rho_h)$$

The effective density depends on the hydro density through a factor h which depend on the density, temperature and ionization degree of the plasma and on proton energy Ep.

$$(5)\ \rho_e=\eta\rho_h;\ \eta=\frac{q_i}{Z}\left[\frac{L_f}{L_b}+\frac{Z-q_i}{q_i}\right]$$

Note that in the low density plasma corona region (fully ionized plasma qi=Z) eq. 5b becomes h~Lf/Lb which imply that if Lf>Lb then h>1 and re>rh according with Fig.5(a) and with experimental results obtained in ref[20]. On the other hand , in the solid target region (qi=0) eq. 5b becomes h=1 which imply re=rh.

The above mentioned method affect also the estimation of the MS by the MC code introducing a magnification factor in the Rossi formula implemented in the code (the Rossi formula was obtained in plasma configuration). We calculated the error due to the magnification factor which is almost everywhere less than 10% of the SP coefficient. In

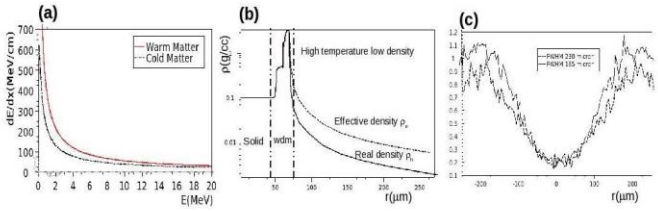

Fig.5 are shown two different profiles obtained running MC simulation once with original density profile (rh). and the other with the modified one (re).

Fig 4: (a) Proton stopping power in cold matter (eq.2 line below) vs Proton stopping power in plasma (eq.1 line above) as a function of proton energy at the same material (Mylar), temperature T=1 keV and density r = 0.1 g/cc. (b) real density profile rh compared to effective density profile re. (c) MC simulation of proton energy deposition in layer corresponding to a Bragg peak for Ep=3.2 MeV using real density profile rh (line above) and using effective density profile re (line below).

Proton energy spectrum: One of the most important ingredient for the MC simulations input file is the spatial and energy distribution of the initial proton beam. This essential information can be obtained by measuring the energy deposited in each RCF layer for a shot in which the cylindrical targets is removed (i.e., protons traveling undisturbed). We had uncertainties deriving from shot-to-shot variations in energy and angular distribution of emitted protons. In particular, following [23] and assuming z as the propagation direction, the energy deposited in the kth RCF layers (eq. 6) is given by the convolution of the energy deposition curve B(zk,x,y,E) (characterized by the presence of the Bragg peak) and the proton energy distribution P(E,x,y) (where x,y are placed in the plane normal to z).

$$(6)\ S_k(x,y)=\int_0^{E_{max}}B_{\Delta z_k}(x,y,E_p)P(x,y,E_p)dE;\quad B_{\Delta z_k}=\int_{\Delta z_k}B(z,x,y,E_p)dz$$

Assuming a discrete energy spectrum according to energy discretization emerging from RCF configuration (the finite number of RCFs layers gives us informations about finite value of energy only) we can approximate the integral in eq. 6 obtaining a matrix system

which can be inverted in order to determine the spatial and energy spectrum of the initial proton beam. Fig. 5 shows the spatial integrated initial spectrum function P(Ei) as was obtained solving eq. 6 for different energies which are related to different RCF layers compared with the corresponding images for a shot without target "free shot". The "almost"' exponential form (trapezoidal) of the spectral function agree with typical spectral function form obtained in proton acceleration experiments (see for examples ref[5,22]). The spectral analysis of proton beam give us two fundamental informations: i) the integrated (over a RCFs surface) energy spectrum (Fig.5) ii) the divergence as a function of energy (the angular divergence can be calculated starting from the diameter of the spatial profiles functions for each discrete energies and the proton source-detector distance). These results are implemented as initial condition for the MC simulations together with the density profiles obtained by CHIC code modified following the scheme showed in the previous section (plasma effects)

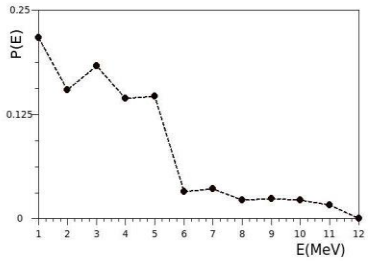

.

Fig.5: Spatial integrated initial spectrum P(E) calculated inverting the matrix system obtained by the approximation of eq.6 for the case of shot without cylinder.

A quantitative analysis of the energy and spatial distributions of protons after they are passed through the cylinder has been done starting from RCFs images obtained by shots with cylindrical target. The integrated energy spectrum of the proton beam after passing through the cylinder show a consistent reductions of number of particle in the low energy region (Ep < 4 MeV). This is due to the fact that proton with energy below that value of energy overcome a maximum areal density of the order of 13 mg/cc which is the typical mean value of the dense plasma core in our conditions. Multiple scattering effects: It is important to perform an analytical evaluation of MS because it is really the main responsible of the observed larger size of the proton images. This allows to evaluate the right object size and also to evaluate the necessary conditions for getting good proton radiographies. We can estimate the effect of MS on the detected size of the cylinder, by defining the blurring factor as

$$(7)\quad \xi = L\vartheta,\ \vartheta = \frac{E_s}{2}\sqrt{\frac{1}{L_R}}\frac{\sqrt{A\left[g/cm^2\right]}}{E[MeV]};\ A = \int_{-\infty}^{\infty}\rho(x)dx$$

where A is a generalization of the areal density for cylindrical geometry (usually A is defined as the product of the density times the longitudinal extension of the probed material), L is the distance between the cylinder and detector and q is the mean angular deflection of a proton with energy Ep traversing a material with density r, Es is a constant =15 MeV and Lr is the radiation length:

$$(8)\quad \frac{1}{L_R\left[g/cm^2\right]} = 1.4\cdot 10^{-3}\frac{Z^2}{A}\ln\left[\frac{181}{\sqrt{Z}}\right]$$

Eq 7 was obtained by Rossi in [18] using a definition for the Radiation length which is different from the one used today [24] so when using this formula, one must be careful to take this difference into account. At each hydro time (i) the approximate size Di of the image formed on the kth layer will be convolution of the real size fi of the cylinder image with the blurring coefficient xi

$$(9)\quad D_i = \frac{1}{M}\sqrt{(\phi_i M)^2 + \xi_i^2}$$

Finally, the image formed on the layer k will have a size Dk given by the FWHM of the image Ik=Sili,k obtained by the convolution of all the images Ik,i.In principle eqs. 9 can be inverted deducing the real size of the cylinder for each layer. In order to estimate MS effect using the Rossi formula in eq. 7 we should calculated the areal density A (eq.7(c)). The areal density is usually defined in planar target geometry as the product between the density of the material (which is assumed constant) and the thickness of the target (along the direction perpendicular to the target surface). If the density profile along the longitudinal direction is not constant this agree with the so called Gaussian approximation (the product of the peak density with the FWHM). In this experiment (and generally in all ICF experiments) the cylinder density profile cannot be represented by a gaussian function (see Fig.7) it is instead characterized by three regions: (I) the plasma corona, (low density but large size) (II) the shocked region (high density short distance) (III) the unperturbed target (original target density). Hence the proton traveling inside the target will see the value of the peak density only for short distance (~ 20 mm).

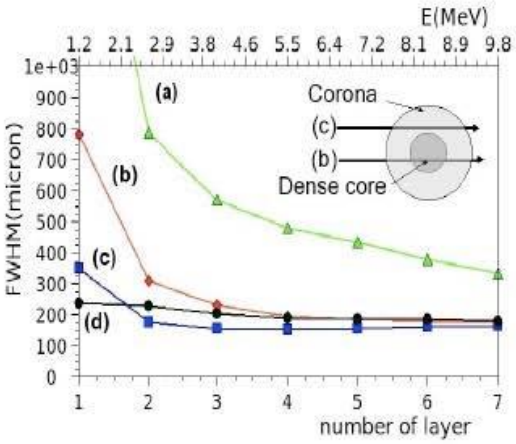

Fig. 6 estimation of cylinder size as a function of different layers (mono energetic images for shot n° 9) using Rossi's formula (eq.7) and assuming different definition of the areal density: (a) Gaussian approximation A=rL, (b) numerical integration of density profile for protons traveling into the center of the compressed cylinder $A[-r_c, r_c]$ (where rc is the core radius) , (c) numerical integration of density profile over all space $A[-\infty, \infty]$, (d) numerical integration of density profile in plasma corona region only $A[-\infty, r_c \cup r_c, \infty]$.

In these conditions the Gaussian approximation leads to an overestimation of the blurring

coefficient and the areal density must be calculated by detailed integration of the density profiles (eq. 7(c)). Moreover in this experiment the produced protons had a relatively low energy, the energy loss when they cross the target, and the multiple scattering effects are therefore quite large. In particular the protons passing through the dense core of the imploded target are scattered more than the protons passing through the external plasma corona so the images on layers are mainly formed in negative by external protons. In this case the areal density in Rossi's formula must be calculated by integrating the density profile only in the plasma corona region (i.e. Considering external protons only). Fig 6 shows estimations of the cylinder size (FWHM) for a typical shot in RAL-08 experiment [6,7] using Rossi's formula to calculate blurring coefficient and assuming different definition of the areal density A. The estimation based on the Gaussian approximation is far from simulation predictions while the estimations based on numerical integration of the hydro density profile are more precise. It is important to note that, as we have mentioned before, for low energy (first layers) A must be calculated only in plasma corona region.

(IV) PROTON RADIOGRAPHY RESOLUTION:

Strong condition: In this paper we have shown that the mechanism of PR in warm dense matter (ICF experiment) is quite different from that in cold matter due to the presence of a large number of collisions. Many MC simulations were made [6] but was never introduced any criterion for measuring the resolution of proton radiography in ICF. Here we want to define a criterion to estimate the resolution degree of the system starting from the parameters and the experimental set-up. To do this let us consider the experimental set-up shown in Fig.7(a) in which a point-like proton source irradiates a finite size object projecting its image on the detector. In principle, if the MS is negligible, the object will appear transparent (i.e r=0) and the projected image size will appear enlarged by a factor M (eq. 9b) which correspond to the geometrical magnification.

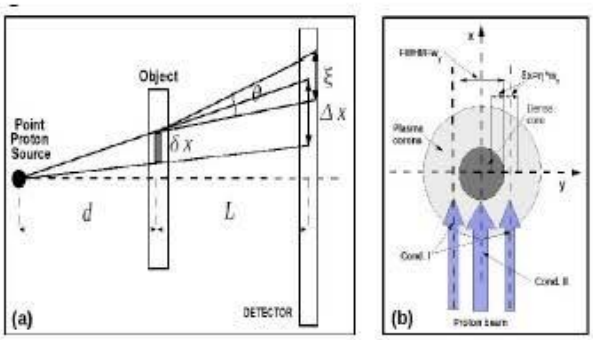

Fig.7: (a) scheme of proton radiography resolution for "strong condition". (b) scheme for "weak condition"

In particular, defining a generic distance between two points in the object dx, the projected size on the detector becomes Dx=M dx. Nevertheless the effect of the coulomb MS is never negligible and the protons passing through the object are deflect by a mean angle q giving a mean displacement x=Lq which can be estimate using the Rossi's formula in eq.7. Therefore the projected image on the detector will appear enlarged by a factor m

with respect to that would appear if there were no scattering (Dx) i.e by a factor mM with respect to the initial distance (dx) (we start from eq.9 using Dx instead of f).

$$(10)\ \mu = \sqrt{1+\left(\frac{\bar{\xi}}{\delta x}\right)^2};\ \bar{\xi} = \xi f M$$

Starting from the above considerations we can infer that the blurring coefficient must remain less or of the same order than resolution that we would like to obtain dx in order to avoid the crossover between different single proton trajectory and to prevent a consequent loss of the initial spatial target information's carry on by protons. The above mentioned condition can be written in terms of blurring coefficient (i.e x/M is the resolution of our system in analogy with Rayleigh's criterion in optics.):

$$(11)\ 0 \le \bar{\xi} \le \delta x$$

or in terms of the a dimensional parameter m:

$$(12)\ 1 \le \mu \le \sqrt{2}$$

We refer to the above condition (eq.11 and 12) as the "strong condition". If the strong condition is satisfied we can use proton radiography in conventional way and the gray scale obtained by the RCF analysis will be proportional to the density gradient of the probed target. A simple estimation of the m parameter can be done considering the protons passing through the dense core in RAL-08 case: the size of the core is ~60 mm then we look for a resolution dx~20 mm; the blurring coefficient x/M can be estimated assuming the maximum energy for protons (10 MeV), which are passing through an area density A~0.05 g/cm2 and a magnification factor M=4.5. The result is m~7 which is larger than the maximum value in eq. 12 confirming that for low energy protons the strong condition cannot be applied because of they are not able to probe the dense core. On the other hand, considering protons passing through the plasma corona, the areal density is A~0.002 g/cm2 and at the same conditions we obtain m~2 which is a more reasonable value. Fig.9 shows the mean scattering angle q vs. areal density for different proton energy. Typical value for our experiment are shown. The maximum resolution obtained in the region of the plasma corona at the RAL-08 experiment is about 20 mm due to the low energy of the probed protons (< 10 MeV), while If we would like to probe a typical core density target in omega [25] we need to use a very high energy proton energy (~ 250 MeV). The Grey region corresponds to the SP limit obtained by fitting simulations based on the ions SP formula in eq.1. In particular we calculated the minimum energy required for a proton to overcome certain areal density of carbon (Z=6 A=12) $E_m[MeV] \approx 30\sqrt{A[g/cm^2]}$. Inserting the minimum energy into the Rossi formula for the mean scattering angle (eq.7(a)) we obtain the maximum scattering angle for proton to overcome certain areal density $\vartheta_m \approx \sqrt{A[g/cm^2]}/E_m[MeV] \approx 1.9^\circ$ (i.e protons with scattering angles lower than the maximum will overcome the areal density).

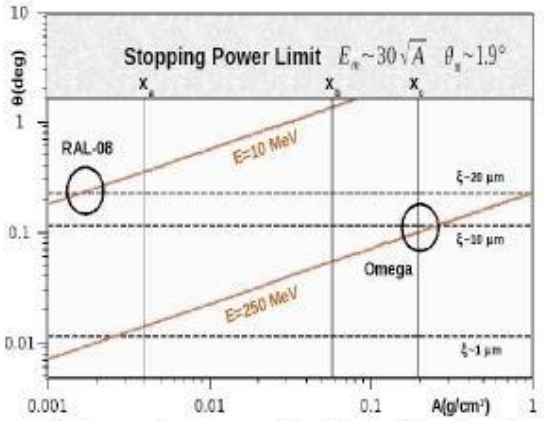

Fig.8: Mean scattering angle q vs. areal density for different proton energies. xa) A~0.004 g/cm2 proton trajectory calculated through plasma corona and, xb) A~0.05 g/cm2 trajectory through core for the present experiment, xc) A~0.2 g/cm2 trajectory (theory) for a typical Omega target. If we assume d=L=1cm (M=2) we get the corresponding spatial resolution limits: ~20 mm, ~10 mm or ~1 mm. The grey region corresponds to the SP limit qmax~1.9°.

weak condition: The above considerations suggest that proton radiography technique can be used for ICF only under specific conditions which depends also by the geometrical features of the experiment. As example let assume a very sharp target density profiles; as just explained before protons which pass through the dense core are stopped or diffuse while those which pass through the corona are deviated by a mean scattering angle which could be acceptable. Thanks to the sharp profiles the differences in areal density between the external and the internal protons becomes be very huge giving a high contrast an then an acceptable resolution. Here we developed a criterion to estimate the resolution of the system in the above mentioned condition as a function of the sharpness of the target profile and we refer to this criterion as "weak condition". Let start assuming a 2D supergaussian density profile (where g is related to slope of the distribution):

$$(13)\quad A_{x,y}(r) = \rho_g \exp\left[-\ln 2\left(\frac{x^\gamma + y^\gamma}{w^\gamma}\right)\right]$$

(where we have defined w=FWHM/2). protons arriving by the x-direction will probe certain density profiles Ay(g) as a function of their y position:

$$(14)\quad A_y(y) = \int_a A_{x,y}(y)dx = A_1(y)\exp\left[-\ln 2\left(\frac{x}{w}\right)^\gamma\right];\quad A_1(y) = \rho_g \int_a \exp\left[-\ln 2\left(\frac{x}{w}\right)^\gamma\right]dx$$

the resulting Blurring coefficient will be

$$(15)\quad \zeta_y(y) = \frac{\Gamma c\sqrt{A_y(y)}}{E_g} = \frac{\Gamma c\sqrt{A_1(y)}}{E_g}\exp\left[-\frac{\ln 2}{2}\left(\frac{x}{w}\right)^\gamma\right];\quad \Gamma = \frac{L}{M} = \frac{Ld}{L+d};\quad c = \frac{E_s}{2\sqrt{L_s}}$$

Following the scheme in fig.16(b) The "weak condition" can be written as follows: (I) The blurring occurring by protons passing through the plasma corona (region of the density distribution outside the FWHM Fig.8(b)) must be of the same order of the resolution (dx=2hw) which we would like to obtain (the resolution must be a fraction of the FWHM). (II) The blurring occurring by protons passing through the plasma core (region of the density distribution inside the FWHM) must be larger than the 2 FWHM of the target

density profiles.

$(I)\ \xi_{(w+2\eta w)}(\gamma) < 2\eta w;\ (I)\ \xi_{(w-2\eta w)}(\gamma) > 4w$

The above conditions can be rewritten as follws:

$$(I)\ 2^{\frac{1}{2}[1+2\eta]^{\gamma}} - \frac{\Gamma c\sqrt{A_x \rho_p}}{2\eta w E_p} > 0;\quad (II)\ \frac{\ln 2}{2}\left[(1+2\eta)^{\gamma} - (1-2\eta)^{\gamma}\right] + \ln\left(\frac{\eta}{2}\right) > 0$$

The I condition depend on the experimental parameters (r, Ep, w, G) and on the geometry of the target density profiles (g,h) it gives us the resolution of proton radiography for all the protons passing outside of the core which is limited by the FWHM. The II conditions depend on the geometry of the target density profiles (g, h) and it guarantees that the protons passing through the core does not participate to form the image on layer. Of course in the "weak condition" regime we accept to loss all the information about the internal core of the target and we look at its size only. From experimental point of view the supergaussian degree g is not convenience anyway we can use the relation between the gaussian degree g and the slope of the density profiles calculated in w (A'(w))

$$(16)\ A'(w) = \frac{\ln 2}{2}\left(\frac{\rho_p}{w}\right)\gamma$$

Let us check the weak condition for the two interesting cases RAL-08 [10,11] and Omega typical experiments [25]. The II condition is independent on the experimental parameters and it leads to the conditions: dx>20 mm for g=2 and dx>10 mm for g=4. The I condition gives dx>85 mm for g=2, dx>30 mm for g=4 and dx>15 mm for g=6 for the RAL-08 experiment (r~5 g/cc, E~10 MeV, w~60 mm) and gives dx>90 mm for g=2, dx>30 mm for g=4 and dx>18 mm for g=6 for a typical Omega target (A~0.2 , E~15 MeV, w~60 mm).

(IV) CONCLUSIONS:

PR has been used to diagnose the implosion of cylindrical targets, but a detailed analysis is required in order to allow comparison with hydro simulations. The simple RCF-layer-to-time relation, does not hold here because of image mixing. The information carried on by protons passing through the dense core is lost because they are scattered more than the protons passing through plasma corona. The last ones then form the images on detectors "in negative". Moreover, we have shown that in these condition (RAL-08), SP is higher in low density plasma than in cold matter and how we can take into account this effect in MC simulation, SP and the Multiple Scattering (MS) could affect PR performance changing the physical state of the medium. MS is reduced for high-energy protons and, with respect to this problem, we have deduced two different criterion (strong and weak) to predict the minimum energy needed in order to reach a good resolution in ICF experiments.

(V) APPENDIX:

Proton Stopping Power in plasma:

For our intent we prefer to write all the formula in unit of MeV for proton beam energy Ep, g/cc for density r of the probed material and eV for the temperature kbT of the plasma. We start writing the Classical non relativistic Bethe SP formula for cold matter [17].

$$(A1)\ \left[\frac{dE}{dx}\right]_c = 1.23\cdot 10^{23}\frac{\rho Z}{AE_p}L_b$$

where

$$(A2)\ \ln\left[2149\frac{E_p}{\bar{I}}\right];\quad \bar{I}=8Z\left(1+\frac{1.8}{\sqrt{Z}}\right)$$

eq A1 represent the energy loss by proton with energy Ep passing through a material with atomic and mass numbers Z and A and solid density rc=(A/Z)(nb/Na) where nb is the bound electrons density, Na the Avogadro number and is the mean ionization potential. When the proton beam pass through a plasma instead of cold matter eq. A1 is not able to describe all the physical phenomena occurring during the interaction as for example the temperature effects. The right SP formula can be obtained starting from a self-contained representation of the theory of energy loss of ions penetrating classical plasma given by non relativistic Vlasov-Poisson equations [19].

$$(A3)\ \left(\partial_t+\vec{v}\cdot\partial_{\vec{r}}+\frac{e}{m}(\partial_{\vec{r}}\phi)\cdot\partial_{\vec{v}}\right)f(\vec{r},\vec{v},t)=0;\ \nabla^2\phi=-4\pi Ze\delta(\vec{r}-\vec{v}t)+4\pi e\int f(\vec{r},\vec{v},t)\,d^3v-4\pi n_0 e$$

which leads to the following solution:

$$(A4)\ \left[\frac{dE}{dx}\right]_p=1.23\cdot10^{-9}\frac{\rho}{AE_p}\left[q_iL_f+(Z-q_i)L_b\right]$$

where:

$$(A5)\ L_f=G(x)\ln(\lambda_d k)+H(x)\ln(x);$$

$$(A6)\ G(x)=erf\left(\frac{x}{\sqrt{2}}\right)-\sqrt{\frac{2}{\pi}}x\exp\left(-x^2/2\right);$$

$$(A7)\ H(x)=-\frac{x^3}{3\sqrt{2\pi}\ln(x)}\exp\left(-x^2/2\right)+\frac{x^4}{x^4+12};$$

$$(A8)\ x=33\sqrt{\frac{E_p}{K_bT}};\ (A8);\ \lambda_d=7.6\cdot10^{-12}\sqrt{\frac{AK_bTE_p}{q_i\rho_p}};$$

$$(A9)\ k=Min\left[7.46\cdot10^{11}\left(E_p+1.8\cdot10^{-3}K_bT\right),2.4\cdot10^{11}\sqrt{E_p}\right]$$

Here ld is the debye length in unit of m, k in m-1 is the inverse of the impact parameter and rp=(A/qi)(nf/Na) is the plasma density with nf defined as the free electron density. The above equations can be derived assuming two condition which must be always satisfied [19]:

(c1) Free gass Maxwell-Boltzmann statistic approximation and (c2) Collisionless approximation.

With our notation the above conditions can be written:

$$(A11)\ K_bT(eV)>66.7\left(\frac{q_i}{A}\right)^{2/3}\rho^{2/3}(g/cc)\approx K_bT>42\rho^{2/3}\quad (A12)\ K_bT(eV)>58.8\left(\frac{q_i}{A}\right)^{1/3}\rho^{1/3}(g/cc)\approx K_bT>46.7\rho^{1/3}$$

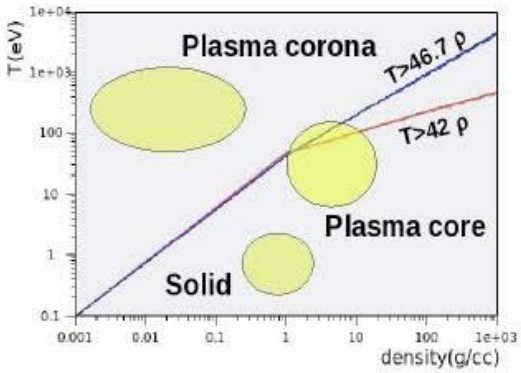

Fig.A1: Temperature (eV) vs. density (g/cc) plane. The filled circle regions represented by the in the graph represent the three different state of matter occurring in RAL-09 experiment. The region above the blu-line (T>42rp) is that in which the conditions in eq. A11 is satisfied while the region above the red-line (T>46.7rp) is that in which the conditions in eq. A11 is satisfied

Fig. 1 shows the region of temperature-density plane (completely ionized (qi=6) carbon target (A=12)) in which conditions 1 and 2 are satisfied. The filled circles represent the three different state of the target in RAL-09 experiment. Note that SP formula in eq. A5 is able to describe the energy loss by protons in the plasma corona region only and partially in the plasma core region (high density and temperature). The cold region can be described also by eq. A5 in the limit of non ionized plasma (qi=0 i.e solid state) in which it become equal to eq. A4. For ICF Physics the Temperature of the proton beam which probed the target (~10 MeV) is always greater than the temperature of the probed plasma (~1 KeV), then the free term in eq. A5 becomes:

$$(AS_{bis})\quad L_f \approx \ln\left[60\sqrt{\frac{AE_p^2}{q_i\rho_p}}\right];$$

which lead to the following simplified formula (starting from eq. A4):

$$(AS_{bis})\quad \left[\frac{dE}{dx}\right]_p = 1.23\cdot 10^{-9}\,\frac{q_i\rho}{AE_p}\cdot\left[\ln\left[60\sqrt{\frac{AE_p^2}{q_i\rho_p}}\right]+\frac{(Z-q_i)}{q_i}\ln\left[2149\frac{E_p}{I}\right]\right];$$

References:

[Cayzac2015] W.Cayzac et al., Phys. Rev. E 92, 053109 (2015)
[Cayzac2017]: Cayzac, W. et al. Experimental discrimination of ion stopping models near the Bragg peak in highly ionized matter. Nat. Commun. 8, 15693 doi: 10.1038/ncomms15693 (2017).
[Deutsch2010] C.Deutsch et al. The Open Plasma Physics Journal, 2010, 3, 88-115
[Deutsch2014] C. Deutsch, et al, NIMPA 733, 39-44 (2014)
[Dued1986] S. Atzeni et al., Computer Phys. Commun. 169,153 (2005); S. Atzeni, Computer Phys. Commun. 43, 107 (1986)
[Dietrich1990] K-G. Dietrich et al., Zeitschrift fur Physik D Atoms Molecules Clusters 16, 229-230(1990)
[Edie2013] D.J. Edie et al., EPJ Web of Conferences 59, 5018 (2013)
[Frank2013] A.Frank et al., Physical Review Letters 110, 115001 (2013)
[Frenje2015] J.A. Frenje et al., PRL 115, 205001 (2015)
[Gericke2002a] D.O. Gericke et al., Physical Review E 65, 036418 (2002)
[Gericke2002b] D.O. Gericke et al., Physical Review E 65, 036406 (2002)
[Gericke2003] D.O. Gericke et al., PRE 67, 037401 (2003)
[Glenzer2003] S.H. Glenzer et al, PRL 90, 175002 (2003)
[Glenzer2007] S.H. Glenzer et al, PRL 98, 065002 (2007)
[Glenzer2009] S. H. Glenzer and R. Redmer, Rev. Mod. Phys. 81, 1625 (2009)
[Golubev1998] A.Golubev et al., Phys. Rev. E 57, 3363 (1998)
[Gregory2006] G. Gregori et al., J. Quant. Spectr. Rad. Transf. 99, 225 (2006)
[Hayes2015] A. Hayes et al., PoP 22, 082703 (2015)
[Haun2002] J. Haun, Physical Review E 65, 046407 (2002)
[Hoffmann1990] D.H.H. Hoffmann et al., Physical Review A 42, 2313-2321 (1990)
[Hurricane2016]
[Li2006] C.K. Li et al., Rscl 77, 10E725 (2006)
[Li1993] C.-K. Li and R. D. Petrasso, Phys. Rev. Lett. 70, 3059 (1993).
[Mackinnon2006] A. J. Mackinnon et al., Phys. Rev. Lett. 97, 045001 (2006)
[More1985] R. M. More, Adv. At. Mol. Phys. 21, 305 (1985)
[Park2008] H.-S. Park et al., Phys. Plasmas 15, 072705 (2008)
[Peter91] T. Peter and J. Meyer-ter-Vehn, Phys. Rev. A 43, 1998 (1991)
[Rygg2008] J. R. Rygg, Science 319, 1223 (2008)
[Rygg2015] J.R. Rygg et al., Rscl 86, 116104 (2015)
[Ramis2014] R. Ramis et al., Phys. Plasmas, 21, 082710 (2014)
[Temporal2013] M. Temporal et al., Eur. Phys. J. D, 59, 205 (2013)
[Temporal2015] M. Temporal et al., Eur. Phys. J. D, 69, 12 (2015)
[Volpe2011] L. Volpe et al., PoP 18, 012704 (2011)
[White2012] T.G. White et al., Sci. Rep. 2, 889 (2012)
[Zylstra2015] A. Zylstra et al., PRL 114, 215002 (2015)
[Zwicknagel1999] G. Zwicknagel, Phys. Rep. 309, 117 (1999)
[1] M. Borghesi, et al., Plasma Physics. Control. Fusion, 43, A267 (2001) radiografia
[2] J. R. Rygg, et al., Science, 319, 1223 (2008)
[3] C. K. Li, et al., Phys. Rev. Lett., 100, 225001 (2008)
[4] E.L. Klark, et al, Phys. Rev. Lett. 84(4), 670-673, (2000) tnsa

[5] K. Zeil, et al, New Journal of Physics 12 (2010) 045015 (16pp)
[6] A. J.Mckinonn, et al., Phys. Rev. Lett., 97, 045001 (2006)
[7] M. Borghesi, et al., Phys. Rev. Lett. 82 1529 (2003)
[8] D. Batani, et al., Phys. Plasmas 16 1 (2009)
[9] M.Roth, et.al., PRST Acc. Beams 5, 061301 (2002)
[10] F. Perez, et al., Plasma. Physics. Control. Fusion, 51, 124035 (2009); B. Vazour, et. al., to be published (2010)
[11] L.Volpe, et al, submitted to Phys. Rev. E; L. Volpe, et al, submitted to Phys. of. Plasma
[12] P.H. Maire, J. Breil, R. Abgral, and J. Ovadia, SIAM SISC, 29, 1781 (2007)
[13] https://mcnpx.lanl.gov.
[14] http://www.gafchromic.com/
[15] A.J. Kemp, J. Meyer-ter-Vehn, Nuclear Instruments and Methods in Physics Research, Section A (1988): Accelerators, Spectrometers, Detectors and Associated Equipment, 415 (3), pp. 674-676.
[16] *SESAME Report on the Los Alamos Equation of State Library*. Report No. LALP-83-4, T4 Group, LANL, Los Alamos
[17] H. Bethe, Ann. Phys. (N.Y.) 5, 325 (1930)
[18] B. Rossi and K. Greisen, Rev. Mod. Phys., 13 (1941); V. L. Highland, Nucl. Instrum. Methods 129, 497 (1975).
[19] T.A. Mehlhorn, J. Appl. Phys., 52, 6522 (1981); T. Peter, J. Meyer-ter-Vehn, Phys. Rev. A, 43, 4, 1998 (1991) and Phys. Rev. A, 43, 4, 2015 (1991); C. Deutsch, et al, Nuclear Instruments and Methods in Physics Research, Section A 278 (1989) 38-43
[20] F.C. Young, et al., Phys. Rev. Lett., 49, 549 (1982)
[21] C.K.Li and R. D. Petrasso, Phys. Rev. Lett. 70 3059-3052 (1992)
[22] N. Bohr, Phylos. Mag. 30, 581 (1915)
[23] E. Breschi, NIMA, 522, 190 (2004)
[24] http://pdg.lbl.gov/2008/AtomicNuclearProperties
[25] www.omegalaser.co.uk
[26] www.Hiper-laser.org

PowerLaPs

Innovative Education & Training in High Power Laser Plasmas

Laser plasma diagnostics - Theory and Experiments

Chapter 2: Optical diagnostics for laser plasma characterization

C. Salgado, M. Tatarakis, W. Hill

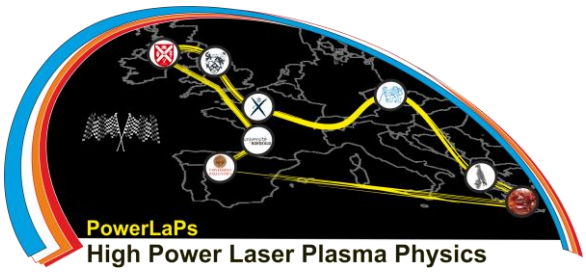

2.1 Under critical and near critical dense plasmas: laser-driven particle acceleration and diagnostics

2.1.1 Introduction

This report is a summary of a lecture given at the school PowerLaPs 04/LTT-C4 on Laser Plasma Diagnostics – Theory and Experiments, held and organized at the University of Salamanca, in the context of the Erasmus + KA2 project titled "Innovate Eduation and Training in High Power Laser Plasmas", at Salamanca, March 25th to 29th, 2019.

The versatility of high power lasers has resulted in their use in a broad range of scientific fields, including novel particle accelerators, fusion research, laboratory astrophysics, condensed matter under high pressure, novel X-ray sources and strong-field quantum electrodynamics, among others. Present-day short pulse, high power laser systems have reached the petawatt (10^{15} W) level. When such power is tightly focused in a spot with a diameter of few wavelengths λ ($\simeq$ 1 μm for sub-picosecond systems), intensities exceeding 10^{21} W cm^{-2} may be achieved. The corresponding strength of the EM fields is such that any sample of matter exposed to such fields becomes instantaneously highly ionized, i.e. turned into a plasma, and the freed electrons oscillate with momenta largely exceeding $m_e c$ (where m_e is the electron mass and c is the speed of light). The nonlinear dynamics of such relativistic plasma in a superstrong EM field is the basis of advanced schemes of laser-plasma sources of high energy electrons, ions and photons which are characterized by high brilliance and ultrashort duration.

The capability of intense lasers to create efficient accelerating plasma structures paves the way to compact, versatile platforms for research and medical applications. Such particle sources are based upon the ability of plasmas to support electric fields orders of magnitude larger than the breakdown threshold fields of conventional accelerators. Energetic electron and ion beams can be produced by focusing a relativistic-intensity (I_L > 10^{18} W cm^{-2}) laser pulse onto a gas or a solid target. Two main regimes of laser-driven particle acceleration/heating can be identified, depending on the transparency properties of the ionized medium. For electron densities much lower than the so-called critical density (i.e., $n_e \ll n_c = m_e \epsilon_0 \omega / e^2$, where ω is the laser frequency, e the electron charge, m_e the electron mass and ϵ_0 the permittivity of vacuum), the laser pulse can propagate large distances ($L \gg \lambda = 2\pi c/\omega$) through the plasma and generate a strong wakefield. This high-velocity (v ~ c) plasma wave can trap part of the background electrons and, for optimized laser-plasma parameters, accelerate them to ultrarelativistic energies with possibly narrow energy spectra. The resulting electron beam, with charge in the nC range, can also act as an efficient x-ray generator. In the opposite limit of a highly overcritical plasma ($n_e \gg n_c$), the laser is mainly reflected and/ or absorbed at the plasma surface, where electrons are stochastically heated in the MeV range, with a broad energy distribution. The high electron current (~0.1 – 50 MA) that ensues can then serve as a source of ultrafast (isochoric) target heating, ion acceleration at the target rear or x-ray radiation. Although the mean energy (ϵ_h) of the hot electron distribution is a complex function of the laser-plasma parameters, it is commonly assumed to obey the ponderomotive scaling, $\epsilon_h \cong m_e c^2(\sqrt{1 + a_0^2/2} - 1)$, where $a_0 = eE_0/m_e c\omega$ is the normalized laser amplitude.

2.1.2 Under dense targets: electron acceleration

The pioneer theoretical work performed in 1979 by Tajima and Dawson has shown how an intense laser pulse can excite a wake of plasma oscillation through the nonlinear ponderomotive force associated to the laser pulse. In their proposed scheme, relativistic electrons were injected externally and were accelerated through the very high electric field sustained by relativistic plasma waves driven by lasers.

In their former article, the authors have proposed two schemes: the laser beat wave and the laser wakefield. Several experiments have been performed in the beginning of the nineties following their idea, and injected electrons at the few MeV level have indeed been accelerated by electric fields in the GV/m range in a plasma medium using either the beat wave or the laser wakefield scheme.

Controlled injection in laser plasma acceleration that lead to high electron beam quality is particularly challenging due to the very small value of the length of the injected bunch that has to be a fraction of plasma wave wavelength, with typical values in the [10-100µm] range. Doing so, electrons witness the same accelerating field, leading to the acceleration of a monoenergetic and high quality bunch. Electrons can be injected if they are located at the appropriate phase of the wake and/or if they have sufficient initial kinetic energy. Different schemes have been demonstrated today and allow to control the phase of injected electrons.

In the 2000's, the first scheme for electron controlled injection was theoretically predicted and experimentally proved. The so-called bubble regime was proposed by Pukhov and Meyer-Ter-Vehn in 2002. It leads to the production of a quasi-monoenergetic electron beam. At lower laser intensity, the blow-out regime, also allows to obtain such an electron distribution. In those two regimes, the focused laser energy is concentrated in a very small sphere, of radius shorter than the plasma wavelength. The associated ponderomotive force expels radially electrons from the plasma, forming a positively charged cavity behind the laser, and surrounded by a dense region of electrons. As the radially expelled electrons flow along the cavity boundary and collide at the bubble base, transverse breaking occurs providing a well localized region of injection in the cavity. Since the injection is well localized, at the back of the cavity, it gives similar initial properties in the phase space to injected electrons. The trapping stops automatically when the charge contained in the cavity compensates the ionic charge, leading to the generation of a quasimonoenergetic electron beam that was experimentally demonstrated in 2004. Finally, the rotation in the phase-space also leads to a decrease of the spectral width of the electron beam. Electron beam quality is also improved because electrons that are trapped behind the laser do not interacted anymore with the electric field of the laser. The scheme of principle of the bubble/blow-out regime is illustrated on figure 1.

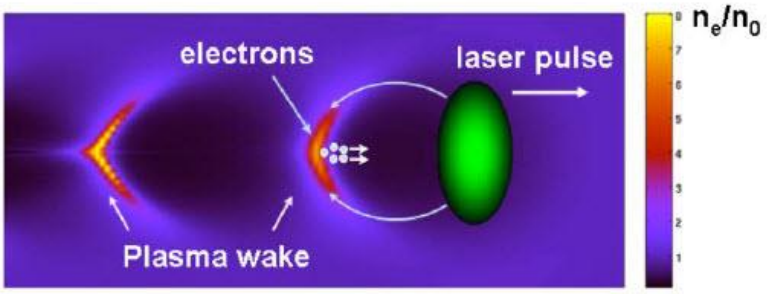

FIG. 1. The laser pulse that propagates from left to right, expels electrons on his path, forming a positively charged cavity. As the radially expelled electrons flow along the cavity boundary and collide at the bubble base, before being accelerated behind the laser pulse. From V. Malka, "Laser Plasma Accelerators" arXiv:1112.5054 [physics.plasm-ph].

Other injection mechanism that were developed later were based on shaping the target (injection in a density gradient), modifying the composition of the gas (injection triggered by ionization) or using multiple laser beams (injection with colliding laser pulses), just to name a few.

On the other hand, the trapped electrons on the laser wakefield incur Betatron oscillations across the propagation axis and emit x-ray photons. The Betatron x-ray beam is broadband, collimated within tens of milliradians with femtosecond duration.

Applications of these electron and x-ray photon beam sources range from medical, fundamental particle physics, inertial confinement fusion, warm-dense matter, medical therapy, etc.

2.1.3 Near-critical targets: ion acceleration

Laser-based ion acceleration has received considerable attention over the last two decades for the potential applications to diverse research areas: fundamental particle physics, inertial confinement fusion, warm-dense matter, medical therapy, etc. It is expected that with the fast development of multi-PW laser facilities laser ion acceleration will be able to generate ion beams with energies in excess of 100 MeV, required by many applications. Up to now laser systems were only able to achieve the acceleration of ions with energies approaching 100 MeV. While most of the experimental results were obtained in the Target Normal Sheath Acceleration (TNSA) regime, higher ion energies are expected to be generated by employing advanced regimes of laser ion acceleration. These regimes include, Radiation Pressure Acceleration (RPA), Shock Acceleration (SA), Relativistic Transparency (RIT), and Magnetic Vortex Acceleration (MVA). Analytical and computer simulation estimates show that a PW or several PW laser system may be able to generate ions with energies ranging from several hundred MeV to GeV per nucleon. We note that near-critical dense targets as well as composite targets with near-critical dense parts attracted a lot of attention recently not only to be used for ion acceleration, but also for brilliant gamma-ray and electron-positron pair production. All these results rely on the physics of intense laser pulse interaction with near-critical plasma.

Few studies have addressed the case of intense short-pulse lasers interacting with near-critical ($n_e \sim n_c$) plasmas. This relative lack of interest is probably due to the experimental difficulty of achieving, in a controlled way, the required high gas densities ($n_e \sim 10^{20-21}\mathrm{cm}^{-3}$) and, also, to the fact that such systems are *a priori* ill-suited to efficient wakefield electron acceleration. In recent years, however, high-density gases have attracted increasing attention as promising high-energy ion sources, based on a variety of mechanisms. First, as in solid foils, the so-called target normal sheath acceleration (TNSA) can arise from the spacecharge field set up at the plasma boundaries by the laser-driven hot electrons. Second, in a dense enough plasma, the front-side ions are pushed by the 'laser piston', i.e., the space-charge field resulting from the laser ponderomotive force on the electrons. Third, under specific conditions, the laser piston or the electron pressure gradients created in an inhomogeneous plasma can launch a collisionless electrostatic shock, accelerating a fraction of the background ions to energies possibly larger than through TNSA. Further, for tightly focused lasers, ion acceleration can proceed via the electric field induced by magnetic vortices moving down density gradients.

Other possibilities for achieving near-critical targets under study nowadays are foam targets and exploding foils. Nevertheless, they are not so well-suited for the high repetition rate operation of the new Ti:Sa systems as the high-density gaseous targets. Using a different laser wavelength could be also a possibility. However, most of the ultra-intense lasers in the world are operating in the near infrared.

2.1.4 Optical probing diagnostics for under dense/near-critical plasmas experiments

Wake-induced alteration of an ultrashort transverse probe pulse can yield a snapshot related to the wake's internal plasma density or magnetic field profile, or both, with high spatial resolution at a desired time after or before the interaction. When shot-to shot-fluctuations are small, a sequence of such images from successive shots forms a movie of the evolving wake.

Shadowgraphy

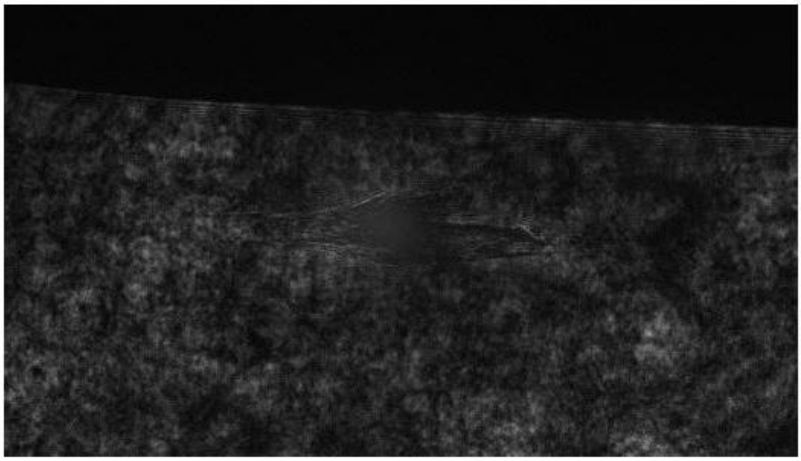

FIG. 2. Shadowgram of a near-critical plasma.

Imaging of a plasma transverse backlighted with an ultrashort optical probe (normally frequency-doubled with respect to the driver laser beam and mutually synchronized) is the common technique to perform a shadowgram. Information about the plasma structure and density in translated to the probe rays by refraction or, for high enough densities, even absorption. With the proper spatial resolution and using few-fs long probes is possible to resolve the fine structure of the wakefield accelerators (plasma waves).

Interferometry

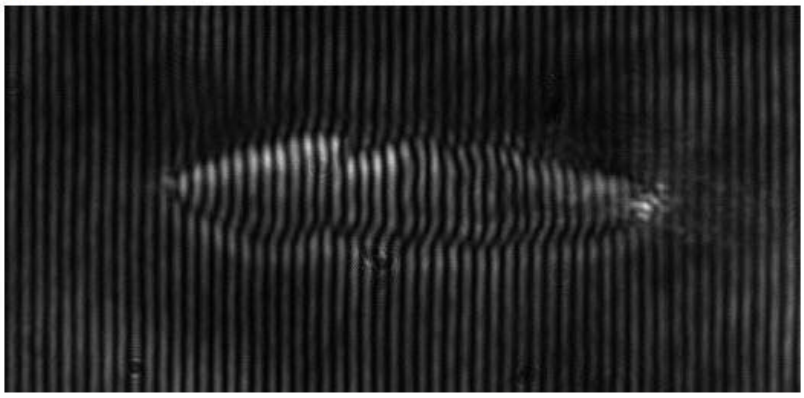

FIG. 3. Interferometer of a near-critical plasma.

Transversal interferometry gives a direct measurement of the plasma density. An ultrashort optical probe is made to interfere with itself, being one of the interferometer arms free, meanwhile the other travels through the plasma. The resulting interferometer contains the information about the phase shift acquired by the second arm, which, after imposing cylindrical symmetry, yields the electronic plasma density profile.

Faraday Rotation

Inside plasma electron accelerators, the current density of accelerating electrons and the displacement current density of time-varying plasma-wave electric fields produce an azimuthal magnetic fields that reach kilo-Tesla strength in plasma surrounding a bubble. A transverse linearly polarized probe impinging on the wake thus "sees" magnetic field components that are both parallel and perpendicular to the wavevector of the probe that alter its polarization by the Faraday effect. The Faraday effect locally rotates probe polarization, which remains linear. Probe rays propagating above or below the central axis of the plasma-wave experience components that retain their direction along each ray's entire path. Consequently, Faraday polarization rotation accumulates up to an angle, on the order of 1º.

References:

A. Macchi, "Basics of Laser-Plasma Interaction: a Selection of Topics", arXiv:1806.06014 [physics.plasm-ph]

L. Volpe *et al.*, "Generation of high energy laser-driven electron and proton sources with the 200 TW system VEGA 2 at the Centro de Laseres Pulsados", High Power laser Science and Engineering, (2019), Vol. 7, e25, 6 pages.

J. Park *et al.*, "Ion Acceleration in Laser Generated Mega Tesla Magnetic Vortex",

A. Debayle *et al.*, "Electron heating by intense short-pulse lasers propagating through near-critical plasmas", New J. Phys **19** (2017) 123013.

V. Malka, "Laser Plasma Accelerators" arXiv:1112.5054 [physics.plasm-ph]

M. C. Downer *et al.*, "Diagnostics for plasma-based electron accelerators", Review of Modern Physics 90(2018), 035002. Open access: https://www.hzdr.de/publications/PublDoc-12484.pdf

2.2 A cylindrical plasma model for Faraday rotation measurements

Consider a plasma with cylindrical symmetry as shown in figure 1.

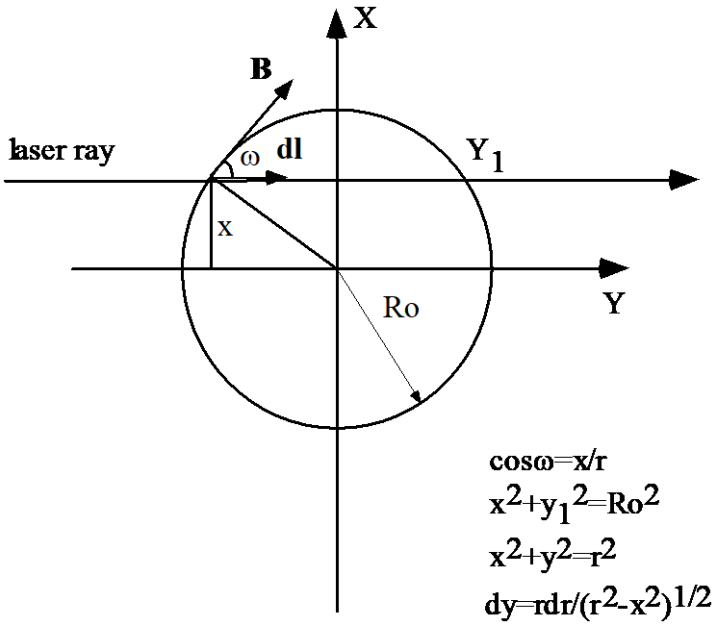

Figure 1. The cylindrical plasma model

A linear polarised laser ray propagates at a distance x from the axis of the cylindrical plasma. A paraxial approximation is used, thus it is assumed that refraction is very small, so the wave path is a line along the plasma. As discussed in Appendix 1 when a linear polarised electromagnetic wave propagates in a magnetised plasma, it remains linear polarised, but the plane of polarisation is rotated by an angle given by the equation,

$$\theta = 2.6312 \times 10^{-13} \lambda^2 \int_l n_e \mathbf{B} \cdot \mathbf{dl} \qquad (1)$$

where **B** is the magnetic field strength vector, **dl** is the element vector of the optical path which in our case $\mathbf{dl} = \mathbf{dy}$, λ is the wavelength of the probing beam and n_e is the electron

number density of the plasma. All the quantities are in S.I units. If the above formula is normalised at 100 Tesla for the magnetic field, 10^{26} m^{-3} for the electron density, 100 μm for the propagation distance and 1 μm for the wavelength, then the rotation angle can be written as,

$$\theta_{degrees} = 15\left(\frac{\lambda}{1\mu m}\right)^2\left(\frac{n_o}{10^{26}m^{-3}}\right)\left(\frac{B_o}{100T}\right)\int_y \xi_n\xi_B\mathbf{i}\cdot\frac{\mathbf{dy}}{100\mu m} \qquad (2)$$

where n_o and B_o are the peak values of the electron density and magnetic field strength respectively, ξ_n, ξ_B are the distribution functions of the electron density and the magnetic field respectively and **i** is the unit vector for the magnetic field direction. In terms of the current within radius r, $I(r)=\frac{2\pi rB(r)}{\mu_o}$ flowing in the plasma cylinder and considering the line density $N = 2\pi\int_0^{R_o} n_o\xi_n(r)rdr$, equation 2 becomes,

$$\theta_{degrees} = 96\left(\frac{\lambda}{1\mu m}\right)^2\left(\frac{N_o}{10^{19}m^{-1}}\right)\left(\frac{I}{100kA}\right)\left(\frac{100\mu m}{R_o}\right)^3\int_y \xi_n\xi_B\mathbf{i}\cdot\frac{\mathbf{dy}}{100\mu m} \qquad (3)$$

For a parabolic density profile $\xi_n = 1-\frac{r^2}{R_o^2}$, and for a uniform current $\xi_B = \frac{r}{R_o}$ the above integral can be solved analytically to give,

$$g(x) = \int_0^{R_o} \xi_n\xi_B\mathbf{i}\cdot\frac{\mathbf{dy}}{100} = \frac{2R_o}{100}\left[\frac{x}{R_o}\sqrt{1-\frac{x^2}{R_o^2}}\right] \qquad (4)$$

Therefore, the rotation angle can be written as,

$$\phi = f(\lambda, N_o, R_o, I) \cdot g(x), \tag{5}$$

where g(x) is the distribution function for the rotation angle for a parabolic density profile,

$$g(x) = \frac{2}{3}\frac{x}{R_o}\left(1 - \frac{x^2}{R_o^2}\right)^{3/2} \tag{6}$$

and $f(\lambda, N_o, R_o, I)$ is a function which includes the plasma parameters namely the line density, radius and current as well as the wavelength of the probe beam,

$$f(\lambda, N_o, R_o, I) = 96\left(\frac{\lambda}{1\mu m}\right)^2\left(\frac{N_o}{10^{19}\,m^{-1}}\right)\left(\frac{I}{100\,kA}\right)\left(\frac{100\mu m}{R_o}\right)^3\left(\frac{2R_o}{100\mu m}\right) \tag{7}$$

The rotation angle θ can now be calculated for various pinch parameters. For a plasma with this geometry the distribution function will be always the same. Only the function $f(\lambda, N_o, R_o, I)$ will vary with the variation of one or more of the pinch parameters. The function g(x) is shown in figure 2.

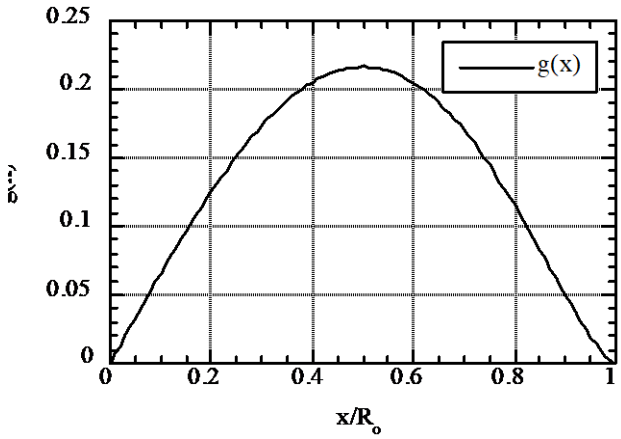

Figure 2. The distribution function g(x) for a parabolic density profile

It can be seen from figure 2 that the maximum rotation takes place at $x = \frac{R_0}{2}$.

The $f(\lambda,N_O,R_O,I)$ is a linear function of the current for fixed values of wavelength, line density and radius. The electron line density for a fully ionised 33 μm carbon fibre pinch is $N_O=6.7x10^{20}$ m^{-1}. Figure 3 shows a representative graph for the $f(\lambda,N_O,R_O,I)$ for a fully ionised 33 μm carbon fibre as a function of current I, for different radius R_O and for fixed λ=0.532 μm.

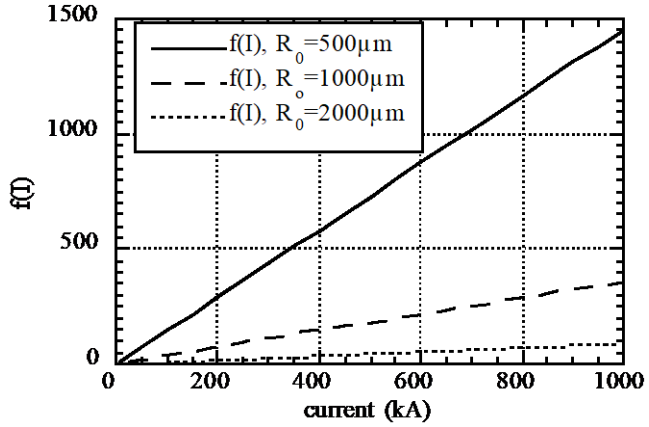

Figure 3 The f function for a 33 μm carbon fibre for different radius

From the above figures the rotation angle can be calculated for any pinch parameters, by multiplying the distribution function g from figure 2 with the corresponding figures to the wanted pinch parameters from figure 3. For example, the rotation angle for a linear polarised laser beam of 0.532 μm wavelength propagating into such a plasma with 2 mm radius when 100 kA current is flowing through it is shown in figure 4.

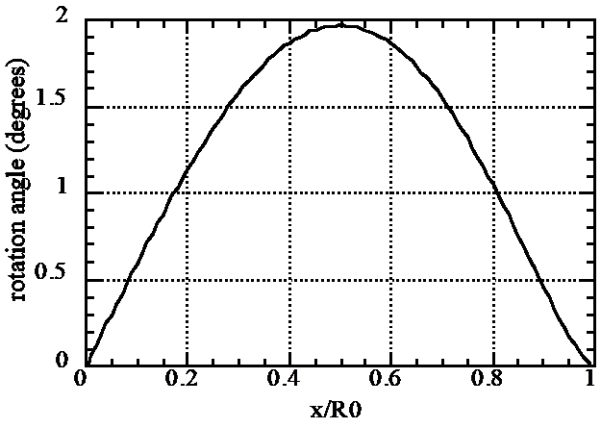

Figure 4. The rotation angle for λ=0.532 μm for a 2mm diameter pinch, with 100 kA uniform current for N_O=6.7x10^{20} m^{-1}

In a real plasma the density distribution function is not parabolic and the degree of ionisation varies. Nevertheless, the above analysis offers a quantitative estimate for the expected faraday rotation for a given set of plasma parameters and wavelength of the brobe beam.

2.3 Time-History Diagnostic Tool for Laser-Accelerated Protons

Compact platforms for laser-driven ion acceleration hold promise for technological advances in science and society; medical applications for cancer therapy [1-4], equation of state studies [5-6] and novel fast neutron sources [7] are just three examples. Laser-based approaches are promising for a number of reasons including the fact that they (1) occupy small footprints and are less expensive than conventional accelerators, (2) can provide high average ion flux, due to relatively high repetition rate of the drive laser system and (3) are inherently pulsed with durations are several orders of magnitude shorter than what conventional accelerators offer and, in in principle, can be tailored. Typically, laser-generated proton bunches, for example, are nonrelativistic and composed of different energy components, each having its own generation time history. Proton clusters with a significant energy spread have advantages when *long* flight times to their intended targets are employed – bunches invariably become negatively chirped, making them useful for energy-dependent measurements. The energy distribution verses time (i.e., during and immediately following generation), however, is not well understood and is likely to be mechanism specific. Knowledge of this early time history could avail new knobs for controlling, and tailoring the energy content and spread of laser-generated proton bunches, making their application to contemporary problems even more valuable.

To characterize laser-based proton acceleration fully, there is a crucial need for diagnostic tools with differential energy and time capabilities; in particular, these need to have sub-picosecond temporal resolution. In this lecture we will discuss a novel approach based on following the early proton time history with K-alpha (K_α) radiation and an X-ray streak camera. The technique we will discuss exploits **p**roton **i**nduced **X**-ray **e**mission (PIXE) (see Fig. 1) [8,9] as the source of K_α radiation while utilizing (1) a **s**ynchronous **p**roton **e**nergy **s**elector (SPES), (2) an X-ray spectrometer and (3) a sub-picosecond X-ray streak camera.

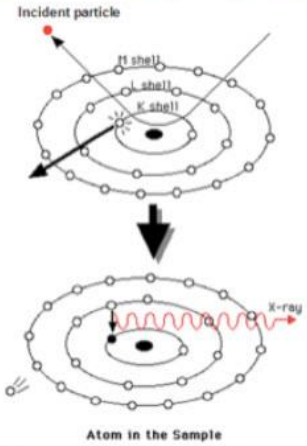

Fig. 1: PIXE process: (upper) a K-shell electron is ejected (thick trajectory) by a proton (thin trajectory); (lower) an M-shell electron falls (arrow) to fill the hole, while generating a K_α X-ray (wavy arrow).

Our discussion will focus the **T**arget **N**ormal **S**heath **A**cceleration (TNSA) mechanism, where it is believed that protons are accelerated by a refluxing, accelerated electron cloud [10-12]. The cloud not only takes time to develop, it is known to be composed of different energy components with time histories of their own [13]. It is not unreasonable to expect that the protons accelerated early in the process will have a different energy than those accelerated later in the electron cloud's development. It should be clear from the discussion thus far that protons must be measured before the chirp sets in. When SPES is applied immediately after acceleration, the time histories are essentially frozen in, which extends the period of time over which the time history can be measured.

Figure 2 shows how this can be done. The energy selector is placed near to the proton

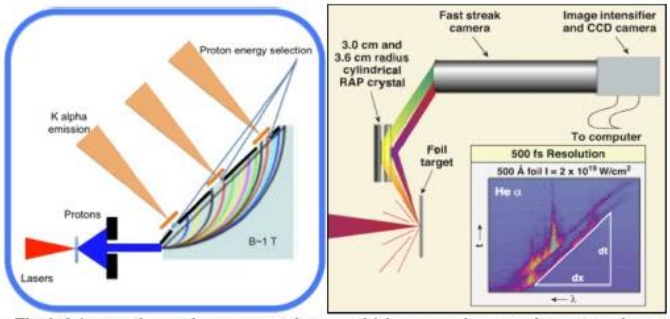

Fig 2: The left image shows the magnet selector, which can work as synchronous selector along all diagonal straight surfaces starting form the injection point. Because K_α radiation is insensitive to magnetic fields, the tracer layer can be placed directly into the magnet. The right image shows a prototype arrangement with an LLNL T-REX streak camera fielded with two von Hámos crystals. The inset shows the $1s^2$-$1s2p$ (upper trace), $1s^2$-$1s3p$, and $1s^2$-$1s4p$ (lower trace) of Al. ([14,15]

generation target. The energy components are sent through spatially separated K_α X-ray generators. The X-rays are then analysed with von Hámos crystals and a streak camera to determine the time history of each component. Figure 3 shows many of the principle components needed to run such a diagnostic.

References

[1] "Radiotherapy for the future," B. Jones, BMJ **330**, 979 (2005).

[2] "Laser-driven proton oncology – a unique new cancer therapy?," K. W. D. Ledingham, W. Galster and R. Sauerbrey, Br. J. Radiol. **80**, 855 (2007).

[3] "Energetic ions generated by laser pulses: A detailed study on target properties," M. Roth, A. Blazevic, M. Geissel, T. Schlegel, T. E. Cowan, M. Allen, J.-C. Gauthier, P. Audebert, J. Fuchs, J. Meyer-ter-Vehn, M. Hegelich, S. Karsch, and A. Pukhov, Phys. Rev. ST Accel. Beams **5**, 061301 – Published 4 June 2002; "Proton Radiobiology," F. Tommasino and M. Durante, Cancers **7**, 353 (2015)

[4] "Numerical simulation of isotope production for positron emission tomography with laser-accelerated ions," E. Lefebvre, J. Appl. Phys. **100**, 113308 (2006).

[5] "Equation of State Measurement of Dense Plasmas Heated with Fast Protons," G. M. Dyer, A. C. Bernstein, B. I. Cho, J. Osterholz, W. Grigsby, A. Dalton, R. Shepherd, Y. Ping, H. Chen, K. Widmann, and T. Ditmire, Phys. Rev. Lett. **101**, 015002 (2008).

[6] "Measurement of the equation of state of solid-density copper heated with laser-accelerated protons," S. Feldman, G. Dyer, D. Kuk, and T. Ditmire, Phys Rev E **95** 031201(R) (2017).

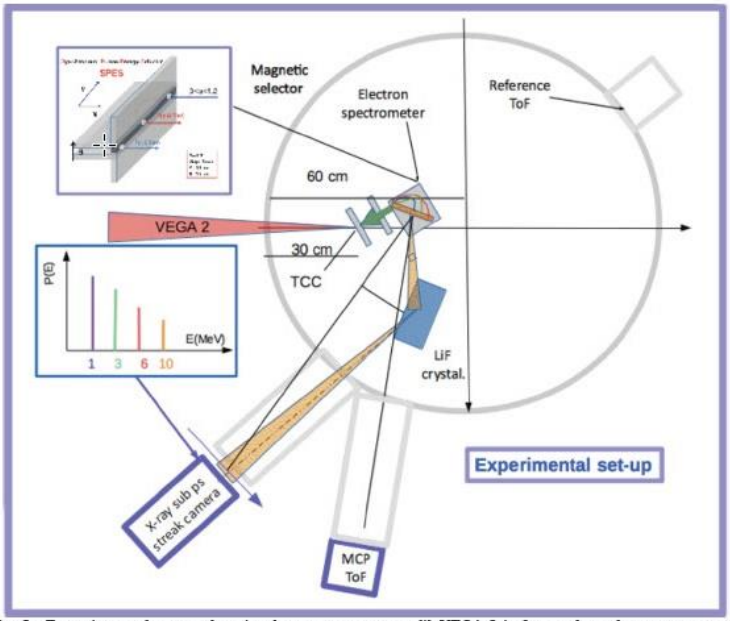

Fig. 3: Experimental setup showing key components: (i) VEGA 2 is focused on the proton target with an $f/13$ off-axis parabola and running at 0.1 Hz; (ii) TNSA generation of protons from 2 μm Mylar + 100 μm Al, mounted on a 3-axis motorized target holder containing several hundreds targets; (iii) Protons are magnetically selected (SPES) and guided into a copper layer designed to optimize PIXE (Proton Induce X ray Emission) for different energy bands; (iv) K_α components of PIXE are collected and focused by an X-ray Spectrometer (two von Hámos crystals) into the sub-picosecond X ray streak camera; (v) A Lanex screen placed on the left side of the SPES is used to control the energy spectrum of electron population.

[7] "Bright Laser-Driven Neutron Source Based on the Relativistic Transparency of Solids," M. Roth, D. Jung, K. Falk, N. Guler, O. Deppert, M. Devlin, A. Favalli, J. Fernandez, D. Gautier, M. Geissel, R. Haight, C. E. Hamilton, B. M. Hegelich, R. P. Johnson, F. Merrill, G. Schaumann, K. Schoenberg, M. Schollmeier, T. Shimada, T. Taddeucci, J. L. Tybo, F. Wagner, S. A. Wender, C. H. Wilde, and G. A. Wurden, Phys. Rev. Lett. **110**, 044802 (2013).

[8] "Inner-Shell Vacancy Production in Ion-Atom Collisions," J. D. Garcia, R. J. Fortner, and T. M. Kavahagh, Rev. Mod. Phys. **45**, 111 (1973).

[9] "Proton Induced X-ray Emission – A tool for non-destructive trace element analysis," I. M. Govil, Current Science, **80**, 1542 (2001).

[10] "Energetic proton generation in ultra-intense laser-solid interactions," S. C. Wilks, A. B. Langdon, T. E. Cowan, M. Roth, M. Singh, S. Hatchett, M. H. Key, D. Pennington, A. MacKinnon, and R. A. Snavely, Phys. Plasmas **8**, 542 (2001).

[11] S. P. Hatchett, C. G. Brown, T. E. Cowan, E. A. Henry, J. S. Johnson, M. H. Key, J. A. Koch, A. B. Langdon, B. F. Lasinski, R. W. Lee, A. J. Mackinnon, D. M. Pennington, M. D. Perry, T. W. Phillips, M. Roth, T. C. Sangster, M. S. Singh, R. A. Snavely, M. A. Stoyer, S. C. Wilks, and K. Yasuike, "Electron, photon, and ion beams from the relativistic interaction of Petawatt laser pulses with solid targets," Phys. Plasmas **7**, 2076 (2000).

[12] "MeV Ion Jets from Short-Pulse-Laser Interaction with Thin Foils," B. M. Hegelich, S. Karsch, G. Pretzler, D. Habs, K.Witte, W. Guenther, M. Allen, A. Blazevic, J. Fuchs, J. C. Gauthier, M. Geissel, P. Audebert, T. Cowan, and M. Roth, Phys. Rev. Lett. **89**, 085 002 (2002).

[13] "A picosecond time-resolved electron energy spectrometer based on Čerenkov radiation," L. N. Elberson, Y. Ping, R. L. Shepherd, P. K. Patel, A. J. Mackinnon, and W. T. Hill, III, Rev. Sci. Instrum. **80**, 023302 (2009).

[14] "Evaluation of bent-crystal X-ray backlighting and microscopy techniques for the Sandia Z machine," D. B. Sinars, G. R. Bennett, D. F. Wenger, M. E. Cuneo, and J. L. Porter, Applied Optics **42** 19 (2003).

[15] "Development of x-ray radiography for high energy density physics," A. Morace, L. Fedeli, D. Batani, S. Baton, F. N. Beg, S. Hulin, L. C. Jarrott, A. Margarit, M. Nakai, M. Nakatsutsumi, P. Nicolai, N. Piovella, M. S. Wei, X. Vaisseau, L. Volpe, and J. J. Santos, Phys. Plasmas **21**, 102712 (2014).

2.4 Focal-Volume Photonic Vacuum Gauge

Ultra-short, ultra-intense laser pulses with powers ranging from a few hundred terawatts to multiple petawatts now allow a host of investigations that heretofore have never been possible. For example, in the absence of all matter, i.e., a perfect vacuum, petawatt lasers will enable the realization of an 86-year old dream – probing the essence of the quantum vacuum via photon-photon scattering, vacuum polarization [1]. Vacuum polarization will provide critical tests of nonlinear aspects of quantum electrodynamics (QED), which makes a precise prediction about how extreme intensities will polarize the virtual electron-positron pairs replete in the quantum *plasma* vacuum [2,3]. The roadmap to these measurements requires a number of technological advances to be made including novel ways (1) to create a vacuum beyond what can be established with commercially available vacuum technology and (2) to measure a local pressure well below 10^{-12} mbar, which is also not feasible with commercially available technology. Consequently, custom approaches are required. This lecture focus on some of the details of (2) and how one might go about creating a *photonic vacuum gauge* to measure the local particle density in the focus of an ultra-intense laser.

The principle behind the proposed tool is outlined theoretically in Refs. [4,5], which relies on the fact that focused, intense laser pulses will liberate electrons from a neutral gas and accelerate them to relativistic energies ($E_e \sim m_e c^2$) within one optical cycle. Electrons are ubiquitous in the presence of strong lasers so an ability to determine their density will provide a handle on the local particle density in the focus. The demarcation of intense that we will use is a peak intensity, I, $\sim 10^{18}$ W/cm^2, which is related to a *normalized vector potential*, $a_0 \approx 0.85 \times \lambda_0[\mu\text{m}]\sqrt{I[10^{18}\,\text{W/cm}^2]} \sim 1$ (for $\lambda_0 = 0.8\ \mu$m). At this intensity, and above, most (if not all) the valence electrons of an atom or a molecule are removed, turning a neutral gas into a plasma, locally. As intensities approach and exceed 10^{19} W/cm^2, inner shell electrons are removed. Subsequent to removal, the free electrons are accelerated by the laser field and thus radiate, which is known as Thomson scattering. Thomson scattering is often thought of as the low-energy analog of Compton scattering. Gao [1] points out, however, this is technically true when limiting the interaction between the field and the electron to its wave response, which is appropriate at relatively low intensities or for $a_0 \ll 1$ ($I \ll 10^{18}$ W/cm^2). At high intensities, however, collective behavior of the photons must be included to predict the electron's response correctly in the focus. The *ponderomotive energy*,

$$U_P = \frac{e^2 E_0^2}{4 m_e \omega_0^2} = \frac{r_e \lambda_0^2}{2\pi c} I, \tag{1}$$

provides an idea of how many photons are interacting collectively with the electron; e, m_e, r_e, c, ω_0, and E_0 are the charge and mass of the electron, the classical electron radius, the speed of light in vacuum, the carrier frequency of the field and the field amplitude of the field respectively in Eq. 1. The number is given by $U_P/\hbar\omega_0$, which can exceed 10^4, and can be viewed as the number of photons in a small volume given by $r_e\lambda_0^2/2\pi$. In this case, electrons can be accelerated to relativistic energies leading to relativistic Thomson scattering (RTS). Not all the electrons liberated by the field participate in RTS. Many are scattered out of the field due to a *ponderomotive force*. When $a_0 \ll 1$ the force is just the gradient of the expression in Eq. 1 and aligned with the electric field. Thus, many of the

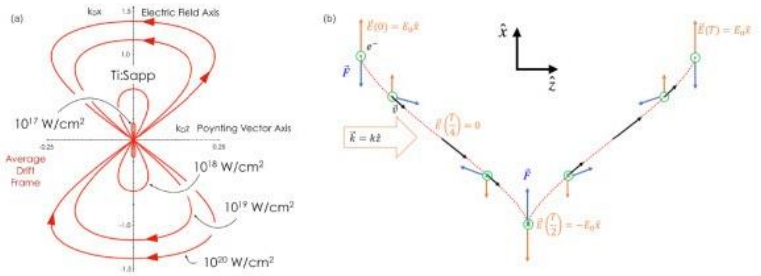

Fig. 1: The trajectory of an electron during one period of an intense field with the electric field along the x-axis axis and it k-vector pointing along the z-axis; (a) the average drift frame and (b) the lab frame.

electron liberated at lower intensities are scattered out of the focal volume. At higher intensities, things get more complicated because of the magnetic field and relativistic speeds. Under these conditions electrons can be accelerated along the propagation direction of the field leading to interesting trajectories. In general, only electrons freed on axis near the peak of the field will participate and experience the full strength of the field. For these electrons the trajectory depends on the frame of reference. Figure 1 (a) shows that in a frame associated with the average drift velocity of the electron, the trajectory is a relatively simple figure 8, which is oriented along the polarization axis. In the lab frame, the trajectory shows the electron moving along the propagation direction of the field with transverse motion punctuated by cusps. Acceleration is large at these cusps because of the sudden change in direction leading to the electrons radiating strongly (RTS) with a spectrum very different from the low intensity case.

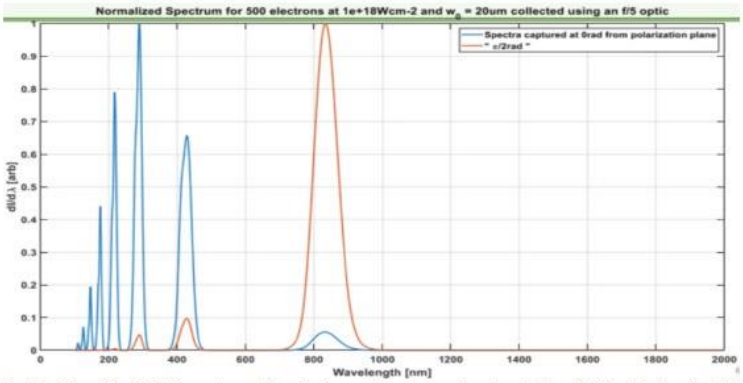

Fig. 2: Simulated RTS spectrum for electrons born on axis at rest in a field of intensity 10^{18} W/cm², observed perpendicular to the k-vector parallel (blue) and perpendicular (red) to the electric field of the laser.

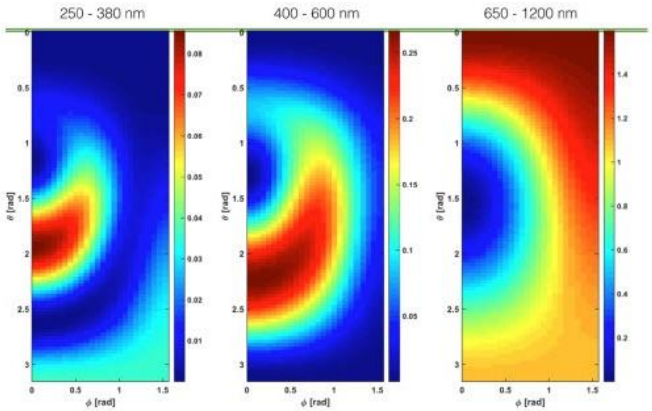

Fig. 3: Angular and wavelength-dispersed RTS radiation for a single electron initially on axis at rest in a field with $I = 10^{18}$ W/cm^2.

There are two cusps/cycle leading to RTS spectrum having a prominent 2nd-harmonic component relative to the laser wavelength. It is clear from Fig. 1 that the electron's motion is not simple harmonic motion in either frame. Thus, the spectrum contains multiple harmonics as shown in Fig. 2. The forward motion of the electron in the lab frame causes the observed RTS to be Doppler shifted to the red of the laser wavelength to an observer in the lab frame. At the same time, because the motion is relativistic the angular dependence of the RTS is directional and wavelength dependent. Figure 3 shows one example of the dispersed radiation for a single electron on axis born with $I \sim 10^{18}$ W/cm^2. The spectral and angular distributions depend on the field intensity while the signal strength depends on the electron density. Consequently, RTS can be used as a photonic-based *in situ* diagnostic tool.

References

[1] "Scattering Processes Produced by Electrons in Negative Energy States," O Halpern, Phys. Rev. **44**, 855 (1933).
[2] Folgerungen aus der Diracschen Theorie des Positrons," W. Heisenberg and H. Euler, Z. Phys. **98**, 714 (1936).
[3] Nonlinear Phase Shift from Photon-Photon Scattering in Vacuum," A. Ferrando, H. Michinel, M. Seco, and D. Tommasini, Phys. Rev. Lett. **99**, 150404 (2007)
[4] "Measuring Extreme Vacuum Pressure with Ultraintense Lasers," A. Paredes, D. Novoa and D. Tommasini, Phys. Rev. Lett. **109**, 253903 (2012).
[5] "Optimized photonic gauge of extreme high vacuum with Petawatt lasers," A. Paredes, D. Novoa, D. Tommasini and H. Mas, J. Phys. B: At. Mol. Opt. Phys. **47**, 065601 (2014).
[6] "Thomson Scattering from Ultrashort and Ultraintense LaserPulses," J. Gao, Phys. Rev. Lett. **93**, 243001 (2004).

PowerLaPs

Innovative Education & Training in High Power Laser Plasmas

Laser plasma diagnostics - Theory and Experiments

Chapter 3: Longitudinal diagnostics of particle beams through coherent radiation emission

G. Gatti

3.1 Introduction to temporal coherence

Pre: ***introduction to (temporal) coherence***. Let's see what happens when different fields interact (linear behavior, vacuum or low intensity) N fields or fields of N emitter. The total field is simply:

$\boldsymbol{E}_{TOT}=\boldsymbol{E}_1+\boldsymbol{E}_2+\ldots+\boldsymbol{E}_N$ the superposition of the fields. Now let's see how the resultant intensity looks like:

$$I_{TOT}=|\boldsymbol{E}_{TOT}|^2=I_1+I_2+\ldots+I_N+\sum_{i=1}^{N}\sum_{j\neq i}\boldsymbol{E}_i\tilde{\boldsymbol{E}}_j$$

The first part, the sum of intensities is made by N terms while the cross terms express the interference terms between different fields. The second ensemble is composed by N(N-1) elements. In case the fields are monochromatic or of relatively sharp line-width, then the intensity terms are constant in time, or at least slowly variable respect to some characteristic time (e.g. response of the detector).
On the other hand, the other terms will have a different carrier frequency. Let's look more inside them:
$I_{ij}=2A_iA_j\cos(\Delta\omega t+\Delta\varphi)$ These cross terms are in general "fast" oscillating terms in time. These are the interference terms. We can now set a time of coherence, that is: given the highest frequency difference $\Delta\omega$ We'll have an oscillating period of $T_{coherent}=2\pi/\Delta\omega$. For intervals much shorter than this time duration, than the $N(N-1)\propto N^2$ terms will give a net contribution to the intensity, otherwise, their oscillation will on average cancel

with no net contribution. In order to resume: we can state that when the contributions are coherent, they scale as the square of the number of emitters (i.e. of fields) when there's no coherence, the scaling is proportional to the number of emitters.

So, going to the ***field generated by N emitters*** (particles) in a linear regime (in principle we'll account to be in vacuum), we know that being $\boldsymbol{E}_i(t)$ the field emitted by the i-th particle, the total field is simply $\boldsymbol{E}_T(t)=\sum_{i=1}^{N}\boldsymbol{E}_i(t)$.

3.2 Spectrum Emitted from a particle bunch

The basic ansatz for all the following steps is that the particles (e.g. electrons) are *uncorrelated*, though they undergo the same emission process (e.g. Transition, Cherenkov, Synchrotron etc.).
The method we are going to develop is absolutely independent on the type of radiation emitted as long as the assumptions are satisfied. Let's now switch to the frequency domain through the following Fourier pair of transformations that we adopt throughout the lecture (in agreement with the paper):

$$\boldsymbol{E}_T(\nu)=\int_{-\infty}^{\infty}\boldsymbol{E}_T(t)e^{-2\pi i\nu t}dt \quad ; \quad \boldsymbol{E}_T(t)=\int_{-\infty}^{\infty}\boldsymbol{E}_T(\nu)e^{2\pi i\nu t}d\nu \ .$$

Let's transform the field superposition.

$$\boldsymbol{E}_T(\nu)=\sum_{i=1}^{N}\int_{-\infty}^{\infty}\boldsymbol{E}_i(t)e^{-2\pi i\nu t}dt=\sum_{i=1}^{N}\int_{-\infty}^{\infty}\boldsymbol{E}_1(t+\Delta t_i)e^{-2\pi i\nu t}dt$$

$$\boldsymbol{E}_T(\nu)=\sum_{i=1}^{N}e^{2\pi i\nu\Delta t_i}\int_{-\infty}^{\infty}\boldsymbol{E}_1(t)e^{-2\pi i\nu t}dt=\boldsymbol{E}_1(\nu)\sum_{i=1}^{N}e^{2\pi i\nu\Delta t_i}$$

The Freq. domain field appears as the one of a single particle weighted by a sum of exponential terms accounting for the superposition of different delay contributions.

Let's now look at the energy (/power) spectrum. $\frac{dU}{d\nu}=\langle 2\epsilon_0 c|\boldsymbol{E}(\nu)|^2\rangle$ Where the angle brackets are here an

ensemble average over different particles configurations (the micro position in the bunch is different for each bunch).
For a deterministic signal (field) it would be the same expression without the ensemble that takes into account the statistical distribution of particles. This expression connects microscopic configurations with a macroscopic quantity. Let's now look in detail at the particle ensemble configuration and consequences, relating to the following figure (Fig.1).

Let's take into account a bunch of particles, that is an ensemble of particles with similar parameters. In the center of our reference system there will be our reference particle, and somewhere far away, a detector in the point P sensing the emitted field. So, let's express as zero the arrival time of the reference particle field on the detector and the others' particle delay respect to the reference

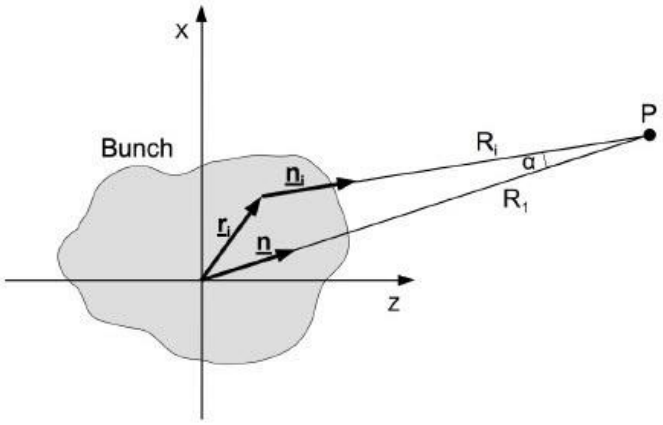

Fig. 1: The reference system used throughout the calculations

particle as $\Delta t_i = \frac{(R_i - R_1)}{c}$. In the far field condition the two unit vectors pointing from the ref. electron and the i-th one to the detector are almost parallel $\underline{n} \| \underline{n}_i$. From the vector relation

$R_1\underline{\boldsymbol{n}}=\underline{\boldsymbol{r_i}}+R_i\underline{\boldsymbol{n_i}}$ with the far-field condition from the previous scalar multiplying by he i-th unit vector we get: $R_i=R_1\underline{\boldsymbol{n}}.\underline{\boldsymbol{n_i}}-\underline{\boldsymbol{n_i}}.\underline{\boldsymbol{r_i}}\approx R_1-.\underline{\boldsymbol{n}}.\underline{\boldsymbol{r_i}}$. We can now rewrite the delay simply as $\Delta t_i=\frac{-\underline{\boldsymbol{n}}.\underline{\boldsymbol{r_i}}}{c}=-\underline{\boldsymbol{k}}.\underline{\boldsymbol{r_i}}/(ck)$ with $\underline{\boldsymbol{k}}=\frac{2\pi}{\lambda}\underline{\boldsymbol{n}}$. Thanks to such result we can now write the energy spectrum, this time we write in terms of the wavelength (more handy in the measurements) by the conversion differential relation $\frac{dU}{d\lambda}=\frac{c}{\lambda^2}\frac{dU}{d\nu}$, to get:

$\frac{dU}{d\lambda}=\frac{2\epsilon_0 c^2}{\lambda^2}\left\langle\left|\underline{\boldsymbol{E_1}}(\underline{\boldsymbol{k}})\sum_{i=1}^{N}e^{-i\underline{\boldsymbol{k}}.\underline{\boldsymbol{r_i}}}\right|^2\right\rangle=\left[\frac{dU}{d\lambda}\right]_1\left\langle\left|\sum_{i=1}^{N}e^{-i\underline{\boldsymbol{k}}.\underline{\boldsymbol{r_i}}}\right|^2\right\rangle$. Here we put the index 1 to the power spectrum of the first (reference) particle. This is a deterministic factor not entering the ensemble average (all the particles emit the same, the random factor is about mutual position in the bunch).

Let's now focus on the ensemble average which is the factor accounting for the bunch contribution (i.e. the interesting one).

$$\left\langle\left|\sum_{i=1}^{N}e^{-i\underline{\boldsymbol{k}}.\underline{\boldsymbol{r_i}}}\right|^2\right\rangle=\left\langle\left(\sum_{i=1}^{N}e^{-i\underline{\boldsymbol{k}}.\underline{\boldsymbol{r_i}}}\right)\left(\sum_{j=1}^{N}e^{i\underline{\boldsymbol{k}}.\underline{\boldsymbol{r_j}}}\right)\right\rangle=\sum_{i=1}^{N}1+\left\langle\sum_{i=1}^{N}\sum_{j\neq i}e^{-i\underline{\boldsymbol{k}}.\underline{\boldsymbol{r_i}}}\;.e^{i\underline{\boldsymbol{k}}.\underline{\boldsymbol{r_j}}}\right\rangle$$

Now, thanks to the first ansatz of uncorrelation between electrons we can split the product in the following way (average of product equal to the product of the average). We remind that it is always an N(N-1) number of terms:

$\left\langle\left|\sum_{i=1}^{N}e^{-i\underline{\boldsymbol{k}}.\underline{\boldsymbol{r_i}}}\right|^2\right\rangle=N+\left\langle\sum_{i=1}^{N}e^{-i\underline{\boldsymbol{k}}.\underline{\boldsymbol{r_i}}}\right\rangle.\left\langle\sum_{j\neq i}e^{i\underline{\boldsymbol{k}}.\underline{\boldsymbol{r_j}}}\right\rangle$. We introduce now the normalized 3D particle density distribution.

$S_{3D}(\underline{\boldsymbol{r}})=\frac{1}{N}\left\langle\sum_{i=1}^{N}\delta(\underline{\boldsymbol{r}}-\underline{\boldsymbol{r_i}})\right\rangle=\frac{1}{N-1}\left\langle\sum_{j\neq i}\delta(\underline{\boldsymbol{r}}-\underline{\boldsymbol{r_j}})\right\rangle$. Here the two expected values are equal because the statistics (probability density of the distribution) are the same (same ensemble of particles obey to the same statistics). It can be estimated as ambiguous to state that the two statistics are independent when they obey to the same probability density function, but every particle is independent, that is: they obey the same statistics but each

particle is like an independent trial, or tossing of the same "dice".

$$\left\langle \left| \sum_{i=1}^{N} e^{-i\underline{\mathbf{k}}\cdot\underline{\mathbf{r}}_i} \right|^2 \right\rangle = N + N(N-1)\int_{\sigma} S_{3D}(\underline{\mathbf{r}}) e^{i\underline{\mathbf{k}}\cdot\underline{\mathbf{r}}} d\underline{\mathbf{r}} \int_{\sigma} S_{3D}(\underline{\mathbf{s}}) e^{i\underline{\mathbf{k}}\cdot\underline{\mathbf{s}}} d\underline{\mathbf{s}}$$

This is simply proved recalling that the delta is "bringing" its argument to the exponential factor. The domain of integration sigma is the space occupied by the particles (space region of the bunch).

3.3 Form factor

From the previously introduced particle density distribution, we define the very important function, the *Form Factor* as: $F_{3D}(\underline{\mathbf{k}}) = \int_{\sigma} S_{3D}(\underline{\mathbf{r}}) e^{-i\underline{\mathbf{k}}\cdot\underline{\mathbf{r}}} d\underline{\mathbf{r}}$. We recognize simply the 3D Fourier Transform of the particle distribution. Here we are mainly concerned with the longitudinal part. So, assuming a longitudinal wave vector we can introduce the longitudinal Form Factor as: $F(\lambda) = \int_{-\infty}^{\infty} S(z) e^{-2\pi i z/\lambda} dz$, where the longitudinal charge distribution is obtained simply integrating through the transverse variables in this way: $S(z) = \int_{\sigma} S_{3D}(\underline{\mathbf{r}}) dx\, dy$. We can now write with the new tools the energy (/power) spectrum of the bunch in the following way: $\frac{dU}{d\lambda} = \left(\frac{dU}{d\lambda}\right)_1 \left[N + N(N-1)|F(\lambda)|^2\right]$. This expression is the corner-stone and the beginning of our reconstruction procedure. Let's now comment extensively the meaning of the formula. The Energy spectrum results as the sum of two contributions, one, proportional to the number of particles will be called the incoherent part and depends uniquely on the single particle spectrum, so it doesn't bring any information on the bunch distribution itself. The second part is proportional to the square of the particle number and will be called the *coherent part* of the emitted radiation. Moreover it is weighted by the form factor, the Fourier transform of the particle distribution, hence it carries a crucial information on the bunch that we'll use to measure the time distribution in this case. What does all this mean on a direct physical interpretation point of view? We'll make the example of a rect distribution, but start from a simple drawing. For wavelengths longer than the pulse duration, the superposition of the particles'

contribution will be in phase (i.e. coherent), that means: the randomness in the particle distribution (the delays) is not weighting enough to slip the contributions out of phase. On the other hand, for waves smaller than the bunch length, the contributions won't superimpose coherently, but on the average will cancel each other. Since the coherent superposition is boosting the intensity (square of the number), we'll observe an abrupt increase of signal sweeping the wavelength above the cut-off frequency (for example by means of a spectrometer).

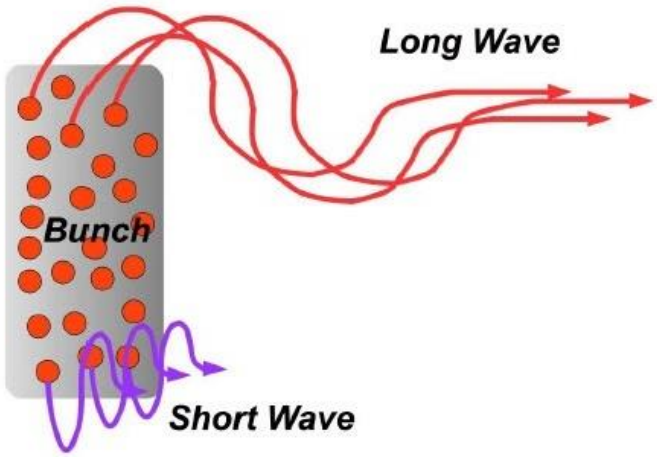

3.4 Reconstruction of Bunch charge distribution

Let's now figure-out how to reconstruct the bunch charge distribution from the measured energy spectrum a not so easy task. First of all let's do a comment. The coherent radiation is linked to the bunch distribution, but only through the square modulus of the form factor, that is: the phase information is lost. So it is not possible to just anti-transform (Fourier). There's an essential part missing. We'll introduce what is known as the Kramers-Kronig formulas (K-K) to retrieve the phase, within some boundaries. K-K relations directly connect Real and Imaginary part of a complex

analytical function. A causal linear system can be defined through an impulse response function h(t) equal to zero for t<0 (causality). In that case the transfer function of the system (Fourier Transform of the impulse response function) is proved to be analytical in part of the complex plane, so K-K relations will hold there, and real and imaginary parts will be dependent one from the other. The condition to be a causal linear system is satisfied by a great majority of physical systems. Same for the process of emission by a bunch.

Let's start requesting that the bunch distribution is zero for negative z (causality before mentioned). It is simply an overall time shift which transforming is a phase factor, unimportant on the physical point of view.

Extension to complex domain

We will now extend the Real frequency domain (i.e. Fourier Domain) to a complex frequency domain (i.e. Laplace Domain). We will see that complex analysis will be fundamental in unfolding our problem. So we introduce the new complex frequency $\nu=\nu_r+i\,\nu_i$. The exponential factors in the transforms which are now complex take the form $e^{i\alpha\nu}=u(\nu_r,\nu_i)+i\,v(\nu_r,\nu_i)$ with α real. It is possible to show through the Cauchy-Riemann relations that this is an analytic function of the complex frequency. We recall the Cauchy-Riemann (C-R)equations: $\frac{\partial u}{\partial \nu_r}=\frac{\partial v}{\partial \nu_i}$; $\frac{\partial u}{\partial \nu_i}=-\frac{\partial v}{\partial \nu_r}$. We can easily verify that applying to the exponential, given $u(\nu_r,\nu_i)=\cos(\alpha\nu_r)e^{-\alpha\nu_i}$ that $v(\nu_r,\nu_i)=\sin(\alpha\nu_r)e^{-\alpha\nu_i}$

$\frac{\partial u}{\partial \nu_r}=-\alpha\sin(\alpha\nu_r)e^{-\alpha\nu_i}=\frac{\partial v}{\partial \nu_i}$ so, C-R eq. Are satisfied and $\frac{\partial u}{\partial \nu_i}=-\alpha\cos(\alpha\nu_r)e^{-\alpha\nu_i}=-\frac{\partial v}{\partial \nu_r}$

the complex exponential is an analytic function. Within the integral defining the form-factor $F(\nu)=\int_0^\infty S(z)e^{-2\pi i\nu z/c}dz$ the exponential function multiplies a Real function not depending on the complex frequency, hence analytic on the same complex plane.

Kramers-Kronig relations

In several important cases of application K-K relations are useful because they connect the Real and Imaginary part of a function. As we explained K-K relations are valid in the extremely important case of the response function (transfer function) of a linear, causal system. A valuable example is given by the Real and Imaginary part of the refractive index, and it is possible to show that also a particle bunch is behaving as a linear, causal system in response to the radiation emission of particles. Nevertheless, in our case the problem is not so straightforward, since we have the modulus of the function and we miss the phase. Let's see how we can overcome such issue. Let's write again the form factor in a different way:

$F(\nu)=\rho(\nu)e^{i\Theta(\nu)}$ and take the logarithm of this same quantity:

$[\rho,\Theta]\in\mathbb{R}$

$\ln F(\nu)=\ln\rho(\nu)+i\Theta(\nu)$. It is probably clear why we apply the logarithm: we have split the modulus and phase into Real and Imaginary part. Let's show that the logarithm is analytic. Again, if this is true, C-R equations for the logarithm: $\frac{\partial\rho}{\partial\nu_r}=\rho\frac{\partial\theta}{\partial\nu_i}$ must $\frac{\partial\rho}{\partial\nu_i}=-\rho\frac{\partial\theta}{\partial\nu_r}$ be satisfied. We proved that the Form-factor is an analytic function, so the C-R equations $(\frac{\partial\rho}{\partial\nu_r}-\rho\frac{\partial\theta}{\partial\nu_i})\cos\theta=(\frac{\partial\rho}{\partial\nu_i}+\rho\frac{\partial\theta}{\partial\nu_r})\sin\theta$ $(\frac{\partial\rho}{\partial\nu_i}+\rho\frac{\partial\theta}{\partial\nu_r})\cos\theta=(-\frac{\partial\rho}{\partial\nu_r}+\rho\frac{\partial\theta}{\partial\nu_i})\sin\theta$ are satisfied. Simply multiplying the first equation by the cosine term and the second by the sine and subtracting, we obtaining the first C-R equation for the logarithm. Multiplying the first by sine and second by cosine and summing we simply obtain the second C-R equation. We proved that the logarithm is analytic. More in detail: we can assume that the logarithm of the form factor is analytic over the complex frequency plane, except in the places where it vanishes (zeros of the modulus). For the moment we don't take the zeros into account but move forward on the proof. Though ignoring the presence of finite zeros in the magnitude of the form factor, we cannot neglect that the response function (form-factor) vanishes at

extremely high frequencies. To overcome this problem we introduce an auxiliary function: $f(\nu)=\frac{(\nu_0\nu-i^2)\ln F(\nu)}{(\nu^2-i^2)(\nu_0-\nu)}$. Such $|f(\nu)|=\frac{|\nu_0\nu-i^2|\sqrt{\ln^2\rho(\nu)+\Theta^2(\nu)}}{|\nu^2-i^2||\nu_0-\nu|}$ function is analytic everywhere (product of analytic functions) except in the isolated singularities $\nu=\nu_0$; $\nu=\pm i$. We can now apply the residue theorem applied to the auxiliary function in the contour C shown in the picture.

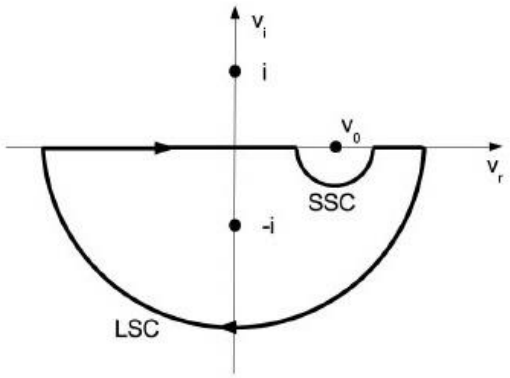

$\oint_C f(\nu)d\nu=\sum_k I_k(C)Res\,[f(\nu_k)]$. This is the theorem of residue. The folding index accounts for multiple turns and negative numbers for clock-wise direction. More in particular, we recall here that for a singularity of order 1, the Residue value is easy calculated according to the following formula:

$Res\,[f(z_o)]=2\pi i\lim_{z\to z_o}(z-z_0)f(z)$. Now returning to our contour integral, we observe that the only singularity inside the contour is at $\nu=-i$. So, $\oint_C f(\nu)d\nu=-2\pi i\lim_{\nu\to\nu_0}(\nu-\nu_0)f(\nu)=-i\pi\ln F(-i)$.

With such important result it's time to split the integral in three parts. The two semicircles (large and small) named SSC and LSC and the path on the real axis R that we wish to extend to the infinite value through a principal value integral (according to Cauchy's definition).

$\oint_C f(\nu)d\nu=\oint_{LSC} f(\nu)d\nu+\oint_{SSC} f(\nu)d\nu+\int_R f(\nu)d\nu=-i\pi\ln F(-i)$

Let's recall the expression of the Form-Factor:

$$F(\nu)=\int_0^{\infty} S(z)e^{-2\pi i\nu z/c}dz$$

The condition that the distribution vanishes for negative z, ensures that only positive values are in the integrand in the lower half plane of our contour $\nu_i<0$ and bounded (i.e. the reader should notice that in other textbooks this condition is in the upper plane, due to simply adopting another convention sign for the Fourier/Laplace pair of transforms). It also vanishes at $\nu_r\to+\infty$ because the charge distribution cannot have details of infinite frequency (as stated before). With such prerequisite we can make the ansatz that the magnitude of the Form-Factor goes to zero faster that some negative power $\rho(\nu)<|\nu|^{-\alpha}$ $|\nu|\to\infty$. This assumption implies that the integral over LSC is zero as we are going to show:

$$0\le\lim_{|\nu|\to\infty}\left|\int_{LSC} f(\nu)d\nu\right|\le\lim_{|\nu|\to\infty}\int_0^{\pi}|f(\nu)|_{\nu=|\nu|e^{i\varphi}}|\nu|d\varphi\le\lim_{|\nu|\to\infty}\frac{\pi\alpha\nu_0\ln|\nu|}{|\nu|}=0$$

The expression of the frequency is just sweeping in angle because is on a circle, but remember that the integrand depend on both angle and magnitude, then we exchange the integral and limit sign.

$$\lim_{|\nu|\to\infty}|f(\nu)|=\lim_{|\nu|\to\infty}\frac{\left|\nu_0\nu-i^2\right|\left|\ln\rho(\nu)+i\Theta(\nu)\right|}{\left|\nu^2-i^2\right|\left|\nu_0-\nu\right|}=\lim_{|\nu|\to\infty}\frac{\nu_0|\nu|}{|\nu|^3}\left|\ln\rho(\nu)\right|$$

This has been found comparing the infinite orders and dropping out the additive constants, included the phase one, that is not constant but a bounded quantity in 0-2π. Then we substitute the inequality and integrate in the angle since now the integrand depends only on modulus.

From here we use the fact that

$\rho(\nu)<|\nu|^{-\alpha}$ $|\nu|\to\infty$ So that we can write the above limit as:

$$\lim_{|\nu|\to\infty}\frac{\nu_0}{|\nu|^2}|\ln\rho(\nu)|\le\lim_{|\nu|\to\infty}\frac{\nu_0}{|\nu|^2}|-\alpha\ln|\nu||$$

Substituting this into the integral we find.

$$\lim_{|\nu|\to\infty}\int_0^{\pi}|f(\nu)||\nu|d\varphi\le\lim_{|\nu|\to\infty}\alpha\frac{\nu_0}{|\nu|}|\ln|\nu||\int_0^{\pi}d\varphi$$

that explains why the integral LSC goes to zero.

Let's now see the SSC one. The path is a semicircle centered on ν_0 , real freq. >0. We want in this case in order for the other integral to get the principal value over the real axis that the radius of the circle goes to zero. We can evaluate such integral writing the auxiliary function as: $f(\nu)=g(\nu)/(\nu_0-\nu)$, where we explicitly extrapolate the singularity keeping another function *g*, continuous in the surroundings of ν_0 . Being the path centered around the singularity we can write $\nu_0-\nu=\epsilon e^{i\varphi}$ and see how the integral looks like: $\lim_{\epsilon\to0}\oint_{SSC}f(\nu)d\nu=\lim_{\epsilon\to0}g(\nu_0)\oint_{SSC}\frac{1}{\nu_0-\nu}d\nu$ again expressing the differential in polar form

$$\lim_{\epsilon\to0}\oint_{SSC}f(\nu)d\nu=\lim_{\epsilon\to0}g(\nu_0)\int_{\pi}^{0}\frac{1}{\epsilon e^{i\varphi}}(-i\epsilon e^{i\varphi})d\varphi=i\pi g(\nu_0)=i\pi\ln F(\nu_0)$$

Thanks to the previous results we can now express the principal value of the integral over the real frequencies (from here we assume all real frequencies):

$$\lim_{\hat{\nu}\to\infty}\int_{-\hat{\nu}}^{\hat{\nu}}f(\nu_r)d\nu_r=-i\pi\ln F(\nu_0)-i\pi\ln F(-i)$$

We take the Real part of both members. Recalling that $F(-i)$ is real (charge distribution is real and from the transform), such term goes to zero. Then $\Re[-i\pi\ln F(\nu_0)]=\pi\Theta(\nu_0)$, this is quite easily seen by looking at the function F .

For the integral we can easily show that the Real operator (being additive) can go under integral. So, further developing:

$\Theta(\nu_0)=\frac{1}{\pi}\lim_{\hat{\nu}\to\infty}\int_{-\hat{\nu}}^{\hat{\nu}}\Re[f(\nu_r)]d\nu_r$ being the auxiliary function product of real numbers by *F*, we get the Real part simply by taking

the one of *F* as follows:

$$\Theta(\nu_0)=\frac{1}{\pi}P\int_{-\infty}^{\infty}\frac{(\nu\nu_0-i^2)\ln\rho(\nu)}{(\nu^2-i^2)(\nu_0-\nu)}d\nu \ .$$

Thanks to the properties of Fourier Transform,

$\tilde{F}(\nu)=F(-\nu)\Rightarrow\rho(-\nu)=\rho(\nu)$, for such reason we can limit the integration to positive frequencies.

This is done transforming the negative frequency domain simply by variable replacement $\nu=-\nu'$ to get:

$$\int_{-\infty}^{0}\frac{(\nu\nu_0-i^2)\ln\rho(\nu)}{(\nu^2-i^2)(\nu_0-\nu)}d\nu=\int_{0}^{\infty}\frac{(-\nu\nu_0-i^2)\ln\rho(\nu)}{(\nu^2-i^2)(\nu_0+\nu)}d\nu \ .$$ We sum the two integrals in the positive domain:

$$\Theta(\nu_0)=\frac{1}{\pi}\int_{0}^{\infty}\frac{(\nu\nu_0-i^2)\ln\rho(\nu)}{(\nu^2-i^2)(\nu_0-\nu)}+\frac{(-\nu\nu_0-i^2)\ln\rho(\nu)}{(\nu^2-i^2)(\nu_0+\nu)}d\nu$$ which with a little bit of algebra gets simply:

$$\Theta(\nu_0)=\frac{1}{\pi}\int_{0}^{\infty}\frac{\ln\rho(\nu)}{(\nu^2-i^2)}[2\nu_0\frac{(\nu^2-i^2)}{(\nu_0^2-\nu^2)}]d\nu$$ to get the final form of the paper which gets quite more compact and simpler.

$$\Theta(\nu_0)=\frac{2\nu_0}{\pi}\int_{0}^{\infty}\frac{\ln\rho(\nu)}{\nu_0^2-\nu^2}d\nu$$ There is only a problem, now we have a singularity (a pole at ν_0 since we are in positive domain) .

The trick is to subtract a vanishing quantity, that is:

$$\frac{2\nu_0}{\pi}\int_{0}^{\infty}\frac{\ln\rho(\nu_0)}{\nu_0^2-\nu^2}d\nu$$, we have just to show that it is going to zero.

$$\frac{\ln\rho(\nu_0)}{\pi}\int_{0}^{\infty}\frac{2\nu_0}{\nu_0^2-\nu^2}d\nu=\lim_{\epsilon\to0}[\int_{0}^{\nu_0-\epsilon}\frac{2\nu_0}{\nu_0^2-\nu^2}d\nu+\int_{\nu_0+\epsilon}^{\infty}\frac{2\nu_0}{\nu_0^2-\nu^2}d\nu]$$

He uses two primitive functions which deriving we can show giving the integrand.

They are the following

$$\frac{\ln\rho(\nu)}{\pi}\lim_{\epsilon\to 0}\left[\left|\ln\frac{\nu_0+\nu}{\nu_0-\nu}\right|_0^{\nu_0-\epsilon}+\left|\ln\frac{\nu_0+\nu}{\nu-\nu_0}\right|_0^{\nu_0-\epsilon}\right]=0$$

Let's derive one and the other to prove that is true

$$\frac{d}{d\nu}\left[\ln\frac{\nu_0+\nu}{\nu_0-\nu}\right]=\frac{\nu_0-\nu}{\nu_0+\nu}\left[\frac{1}{\nu_0-\nu}+\frac{\nu_0+\nu}{(\nu_0-\nu)^2}\right]=\frac{1}{\nu_0+\nu}+\frac{1}{\nu_0-\nu}=\frac{2\nu_0}{\nu_0^2-\nu^2}$$

$$\frac{d}{d\nu}\left[\ln\frac{\nu_0+\nu}{\nu-\nu_0}\right]=\frac{\nu-\nu_0}{\nu_0+\nu}\left[\frac{1}{\nu-\nu_0}-\frac{\nu_0+\nu}{(\nu-\nu_0)^2}\right]=\frac{1}{\nu_0+\nu}-\frac{1}{\nu-\nu_0}=\frac{2\nu_0}{\nu_0^2-\nu^2}$$

They differ for a constant, so the derivative is the same.
Now let's show that the quantity actually vanishes. The first member of the sum is:

$$\lim_{\epsilon\to 0}\left|\ln\frac{\nu_0+\nu}{\nu_0-\nu}\right|_0^{\nu_0-\epsilon}=\lim_{\epsilon\to 0}\left[\ln\frac{\nu_0+\nu_0-\epsilon}{\nu_0-\nu_0+\epsilon}-\ln\frac{\nu_0}{\nu_0}\right]=\lim_{\epsilon\to 0}\left[\ln\frac{2\nu_0-\epsilon}{\epsilon}\right]$$

Here's the second

$$\lim_{\epsilon\to 0}\left|\ln\frac{\nu_0+\nu}{\nu-\nu_0}\right|_{\nu_0+\epsilon}^{\infty}=\lim_{\nu\to\infty}\left[\ln\frac{\nu_0+\nu}{\nu-\nu_0}\right]-\lim_{\epsilon\to 0}\left[\ln\frac{2\nu_0+\epsilon}{\epsilon}\right]=-\lim_{\epsilon\to 0}\left[\ln\frac{2\nu_0+\epsilon}{\epsilon}\right]$$

Now we just sum under the limit sign the two non-vanishing terms remaining

$$\lim_{\epsilon\to 0}\left[\ln\frac{2\nu_0-\epsilon}{\epsilon}-\ln\frac{2\nu_0+\epsilon}{\epsilon}\right]=\lim_{\epsilon\to 0}\ln\left[\frac{2\nu_0-\epsilon}{\epsilon}\ \frac{\epsilon}{2\nu_0+\epsilon}\right]=\ln(1)=0$$

So, it is proven. Thanks to this last result we can finally write the phase retrieval expression as the sum of the previous phase plus the vanishing quantity, the final K-K relation:

$$\Theta(\nu_0)=\frac{2\nu_0}{\pi}\int_0^{\infty}\frac{\ln(\rho(\nu)/\rho(\nu_0))}{\nu_0^2-\nu^2}d\nu$$

Since the modulus is even, we see that automatically the phase is an odd function (property of Fourier Transform).
The singularity is removed, the proof is given by a Taylor expansion. It is probably more effective to observe that the logarithm goes to zero faster. We get our result! Now we can write the distribution function as the anti-transform of the Form-Factor having the amplitude and phase of this.

$$S(z)=\int_{-\infty}^{\infty} F(\nu)e^{2\pi i\nu z/c}d\nu=\int_{0}^{\infty}[F(\nu)e^{2\pi i\nu z/c}+\tilde{F}(\nu)e^{-2\pi i\nu z/c}]d\nu$$

Summing we can find our distribution in the space-domain

$S(z)=2\int_{-\infty}^{\infty}\rho(\nu)\cos(\frac{2\pi\nu}{c}z+\Theta(\nu))d\nu$ or simply in the time-domain by the substitution (for relat. Particles z=ct)

$$S(t)=2\int_{-\infty}^{\infty}\rho(\nu)\cos(2\pi\nu t+\Theta(\nu))d\nu$$

Zeros in the Form Factor (Blaschke products)

In order to deal with functions having zeros, which are a singularity for the logarithm it is possible to artificially "remove" the zero by multiplying with a function that we call the Blaschke product.

So, given the function $F(\nu)$ with a zero that for simplicity we'll assume to be simple in $\mu_n=\mu_r+i\mu_i$, we remove the zero by multiplying with the function $B_n(\nu)=\frac{\nu-\tilde{\mu_n}}{\nu-\mu_n}$. So, in general we'll have a new function $\hat{F}(\nu)=F(\nu)\prod_n B_n(\nu)$. We cannot erase the zeros, so the trick is to remove a zero from the lower half plane (where we integrate and the function is bounded) and put it in the upper half plane.

It is quite easy to see that on the real axis the Blaschke product has modulus equal to 1, so that the contribution remaining on the real axis is a phase factor. Another detail, on the real axis the product is the ratio between complex conjugate quantities, so, the overall phase can be written also as twice the one in the numerator. We can write explicitly the expression for the modulus of the Blaschke product as:

$|B_n(\nu)|=\sqrt{\frac{|\nu|^2+|\mu_n|^2-2(\nu_r\mu_{nr}-\nu_i\mu_{ni})}{|\nu|^2+|\mu_n|^2-2(\nu_r\mu_{nr}+\nu_i\mu_{ni})}}$ analyzing this quantity is more evident that on the real axis it is equal to 1. Furthermore in the lower half plane (where our discussion has been developed), the

modulus results <1 ($\nu_i<0$), so the function multiplied remains bounded by the product with the Blaschke factor. After such explanation is clear that we can express the Blaschke product on the real axis as a phase factor. The phase would appear as:

$$\Theta_B(\nu)=atan\frac{\Im(B(\nu))}{\Re(B(\nu))}=atan\frac{2\mu_i(\nu-\mu_r)}{(\nu-\mu_r)^2-\mu_i^2}$$

Simply showing the intermediate steps: multiplying by the denominator complex conjugate to have Real and Im part, than doing the ratio and getting the expression above.

$B(\nu)=\frac{\nu-\mu_r+i\mu_i}{\nu-\mu_r-i\mu_i}=\frac{(\nu-\mu_r)^2-\mu_i^2-i\mu_i(\nu-\mu_r)}{(\nu-\mu_r)^2+\mu_i^2}$. It is also possible to show that the phase is a monotonic function of frequency, but it seems that such result is not used. Even though, being the inverse tangent a monotonic function, we just see the argument function:

$\frac{d}{d\nu}[\frac{2\mu_i(\nu-\mu_r)}{(\nu-\mu_r)^2-\nu_i^2}]=-2\mu_i\frac{(\nu-\mu_r)^2+\mu_i^2}{((\nu-\mu_r)^2-\nu_i^2)^2}>0$ f o r $\mu_i<0$ which was proven before.

The intermediate steps to get to the final expression of the derivative are:

$$\frac{d}{d\nu}[\frac{2\mu_i(\nu-\mu_r)}{(\nu-\mu_r)^2-\nu_i^2}]=2\mu_i[\frac{1}{(\nu-\mu_r)^2-\mu_i^2}-\frac{2(\nu-\mu_r)^2}{((\nu-\mu_r)^2-\mu_i^2)^2}]=2\mu_i\frac{(\nu-\mu_r)^2-\mu_i^2-2(\nu-\mu_r)^2}{((\nu-\mu_r)^2-\mu_i^2)^2}$$

So, after showing that the phase is monotonic, we can prove a more important result on the influence of the Blaschke phase on the function for the reconstruction. From the symmetry property of the Fourier transform, we know that $F(\nu)=\tilde{F}(-\tilde{\nu})$, so, in practice, for each zero located at $\mu=\mu_r+i\mu_i$, we'll also have another one at $-\tilde{\mu}=-\mu_r+i\mu_i$. In the end we'll also have to take into account a Blaschke product for this zeros pair and the consequent phase introduced by these pairs. Let's see the product first:

$$B_{pair}(\nu)=\frac{\nu-\mu_r+i\mu_i}{\nu-\mu_r-i\mu_i}\ \frac{\nu+\mu_r+i\mu_i}{\nu+\mu_r-i\mu_i}=\frac{(\nu+i\mu_i)^2-\mu_r^2}{(\nu-i\mu_i)^2-\mu_r^2}=\frac{\nu^2+2\nu\mu_i-\mu_r^2-\mu_i^2}{\nu^2-2\nu\mu_i-\mu_r^2-\mu_i^2}$$

Following more

$B_{pair}(\nu)=\frac{\nu^2+2i\nu\mu_i-|\mu|^2}{\nu^2-2i\nu\mu_i-|\mu|^2}$ from this point we can easily get the phase contribution of the Blaschke pair product. Still the phase contribution is the same, inverse tangent of the ratio Im to Re part. So, one option is to multiply the last expression by the complex conj of the denominator to get Re and Im and get the expression as in the paper. It goes like this:

$B_{pair}(\nu)=\frac{(\nu^2-|\mu|^2+2i\nu\mu_i)(\nu^2-|\mu|^2+2i\nu\mu_i)}{(\nu^2-|\mu|^2)^2+4\nu^2\mu_i^2}$ here it is sufficient to develop the numerator to get Re and Im. Then the Denominator being real in the ratio for the phase calculation is cancelled. With such step we get just the expression in the paper. Though as we mentioned we prefer to get the phase in the following way. Recalling the previous expression:

$B_{pair}(\nu)=\frac{\nu^2+2i\nu\mu_i-|\mu|^2}{\nu^2-2i\nu\mu_i-|\mu|^2}=\frac{A}{\tilde{A}}\quad \Theta_{pair}(\gamma)=2\,atan\frac{2\nu\mu_i}{\nu^2-|\mu|^2}$

From this expression much simpler, still for $|\nu|\ll|\mu|$ we get $\Theta_{pair}(\nu)\approx-4\mu_i\frac{\nu}{|\mu|^2}$. A phase contribution proportional to the frequency in the time domain represents simply a shift of $2c\frac{\mu_i}{\pi|\mu|^2}$ (in fact from the definition used, a shift of t_0 that is a – in the argument gives a factor $e^{-2\pi i\nu t_0}$). This shows that the zeros far away from the frequencies of interest (e.g. emission process) do not contribute to the key point of the reconstruction. Still from the same expression we can get the approximation for the $|\nu|\gg|\mu|$, where simply the phase contribution from the B-pair product is zero. The Blaschke products show what is evident in general in these kind of methods: the reconstruction is ambiguous. A pure phase factor will not affect the amplitude form factor, nevertheless this could change significantly the time behavior of the radiation. Given in principle the ambiguity for the form factor of a number of additional Blaschke products, sometimes the phase retrieval found by the formula (K-K) is also called *the minimum or canonical phase*, having in mind that adding-up further terms, the form factor still

would be the same (but not the phase).

Example

Let's build a bunch shape (analytic). Possibly a function easily converted to Fourier domain so to have the analytic expression in freq. Domain with the given frequencies, cut-off and so on. Then we should interpolate this to simulate an instrument measurement with a number of sampling frequencies and possibly an extrapolation at high and/or low frequency. We'll make the ansatz that the single particle spectrum is broadband and probably constant at those frequencies (or known so to extrapolate). If we make the hyp. Of a number of particles we can estimate the difference of one and another signal. Then we'll compare the reconstruction with the original spectrum and bunch shape.
Then we have to see applying the FFT what are the starting point and the end point frequencies.

We know that the frequency step is given by the time window and the frequency window by the time step. In this case things will be reversed. There will be a frequency sampling and this will affect the time window. The frequency window will affect the time sampling.

Let's take into account a charge of bunch of 100pC. With the electron charge of 1.602E-19 C=1.602E-7pC. It's 3.74E7 electrons. In this way we get simply that if we want to compare the intensity of the spectrum between coherent and incoherent emission, the ratio would be $N-1\approx N$. So, we have 7 orders of magnitude factor, quite a good reason to neglect the incoherent part (when performing a measurement).

Removed Singularity

We found problems of noise in the surrounding of the ν_0 point trying to find a numerical solution where the function should be continuous. Let's develop in Taylor the numerator: $f(\nu)=\ln(\rho(\nu)/\rho(\nu_0))$. The first three derivatives are.

$$\frac{\ln(\rho(\nu)/\rho(\nu_0))}{\nu_0^2-\nu^2}=\frac{\ln(\rho(\nu_0+\Delta\nu)/\rho(\nu_0))}{(\nu_0+\nu)(-\Delta\nu)}$$

$$\frac{\ln(\rho(\nu)/\rho(\nu_0))}{\nu_0^2-\nu^2}=\frac{([\frac{\rho'(\nu_0)}{\rho(\nu_0)}]\Delta\nu+\frac{1}{2}[\frac{\rho''(\nu_0)}{\rho(\nu_0)}-\frac{(\rho'(\nu_0))^2}{(\rho(\nu_0))^2}]\Delta\nu^2+o(\Delta\nu^3))}{(\nu_0+\nu)(-\Delta\nu)}$$

This gives a simplified expression when $\Delta\nu>(\Delta\nu)^2$ (i.e. in the old singularity where the lowest term dominates) in this case

in the old singularity holds now $\lim_{\nu\to\nu_0}\frac{\ln(\rho(\nu)/\rho(\nu_0))}{\nu_0^2-\nu^2}=-\frac{\rho'(\nu_0)}{2\nu_0\rho(\nu_0)}$, and let's put also the constants in front to have the full integrand:

$$-(2\frac{\nu_0}{\pi})\lim_{\nu\to\nu_0}\frac{\ln(\rho(\nu)/\rho(\nu_0))}{\nu_0^2-\nu^2}=-\frac{\rho'(\nu_0)}{2\nu_0\rho(\nu_0)}=-(2\frac{\nu_0}{\pi})\frac{\rho'(\nu_0)}{2\nu_0\rho(\nu_0)}$$

$$-(2\frac{\nu_0}{\pi})\lim_{\nu\to\nu_0}\frac{\ln(\rho(\nu)/\rho(\nu_0))}{\nu_0^2-\nu^2}=-\frac{\rho'(\nu_0)}{\pi\rho(\nu_0)}$$

for the closer points we can use the first two terms of the Taylor expansion. For the points close to this critical point is better to use the same Taylor expansion, that is when the condition $(\Delta\nu)^3<(\Delta\nu)^2$ holds. This is the requested approximation.

$$\frac{\ln(\rho(\nu)/\rho(\nu_0))}{\nu_0^2-\nu^2}\approx-\frac{([\frac{\rho'(\nu_0)}{\rho(\nu_0)}]+\frac{1}{2}[\frac{\rho''(\nu_0)}{\rho(\nu_0)}-\frac{(\rho'(\nu_0))^2}{(\rho(\nu_0))^2}]\Delta\nu)}{(\nu_0+\nu)}$$

This could seem not an evident proof that the function is now well behaved, but it can be shown that a Taylor expansion is the proof. For those interested, see the difference between a Laurent expansion and a Taylor one.

Hints on alternative methods (Iterative algorithm)

The introduction on coherent longitudinal diagnostics by means of the K-K relations is due as a formal introduction and gives a direct

$$f(\nu_0)=0, f'(\nu)=\frac{1}{\rho(\nu)}\frac{d\rho}{d\nu}, f''(\nu)=\frac{-1}{\rho^2(\nu)}\frac{d\rho(\nu)}{d\nu}+\frac{1}{\rho(\nu)}\frac{d^2\rho(\nu)}{d^2\nu},$$
$$f'''(\nu)=\frac{2}{\rho^3(\nu)}\frac{d\rho(\nu)}{d\nu}-\frac{2}{\rho^2(\nu)}\frac{d^2\rho(\nu)}{d^2\nu}+\frac{1}{\rho(\nu)}\frac{d^3\rho(\nu)}{d^3\nu}$$

Let's now take profit of the form of the formula inverting a normalized Gaussian pulse.

$S(t)=\frac{1}{\sqrt{2\pi\sigma_t^2}}e^{-t^2/2\sigma_t^2}\Rightarrow F(\nu)=\rho(\nu)=e^{-2(\pi\nu\sigma_t)^2}$ Inserting into the phase retrieval, we get an easy expression because of the logarithm:

$$\Theta(\nu_0)=\frac{2\nu_0}{\pi}\int_0^\infty -2(\pi\sigma_z)^2\frac{(\nu^2-\nu_0^2)}{\nu_0^2-\nu^2}d\nu=\frac{2\nu_0}{\pi}\int_{\rho\neq 0} -2(\pi\sigma_z)^2\frac{(\nu^2-\nu_0^2)}{\nu_0^2-\nu^2}d\nu$$

$\Theta(\nu_0)=4\pi\sigma_z^2\nu_0\alpha$ where we express alpha as the integration constant. So, in this case we can see that we have a linear phase contribution. This is simply (according to Fourier transform) a shift: the phase is ambiguous respect to shifts as expected.

Numerical Integration for minimal phase

Analytically there's no singularity in ν_0, but let's show this numerically. Let's develop in Taylor $\ln(\rho(\nu))=\ln(\rho(\nu_0+\Delta\nu))$ to simplify the integrand. Being the series approx. Useful only in proximity of the point ν_0 we could impose a limit in the $\Delta\nu$ in order to use one or the other function.

So: $\frac{\partial\ln(\rho(\nu))}{\partial\nu}=\frac{\rho'(\nu)}{\rho(\nu)}$, $\frac{\partial^2\ln(\rho(\nu))}{\partial^2\nu}=\frac{\rho''(\nu)}{\rho(\nu)}-\frac{(\rho'(\nu))^2}{(\rho(\nu))^2}$

Now we can write the first Taylor terms:

$$\ln(\rho(\nu_0+\Delta\nu))=\ln(\rho(\nu_0))+[\frac{\rho'(\nu_0)}{\rho(\nu_0)}]\Delta\nu+\frac{1}{2}[\frac{\rho''(\nu_0)}{\rho(\nu_0)}-\frac{(\rho'(\nu_0))^2}{(\rho(\nu_0))^2}]\Delta\nu^2+o(\Delta\nu^3)$$

With such development we try to write again the integrand hereafter:

formula ready to put hands on data and analyze possible results. Nevertheless the reader during the explanation has probably understood that this method presents some critical aspects. We are going to enlighten these and present a possible alternative method more robust respect to these problems.

The problem found in the bunch longitudinal profile reconstruction is a general mathematical problem found in many different fields and applications.

The idea is to fully reconstruct a signal (that we'll suppose being divided in N samples) that needs 2N values to be defined by using only N values (i.e. the amplitude, missing the phase value). The phase retrieval problem is found also in two dimensions (e.g. propagation of a 2D light field), nevertheless the 1D problem presents more issues and fundamental ambiguities. The difference is the additional information given by the boundary conditions between one cell and the closer ones. Anyway, it is clear that in order to find additional unknown values we need to set additional properties to the waveform, as we did (e.g. causality).

We will see that the K-K algorithm is not robust respect to some ambiguities, so that different waveforms can be supported by the same amplitude spectrum and still fulfill the K-K.

The main limitation of the KK method are:

- The modulus of the spectrum should be known for "all frequencies".
- The minimal phase must be a good approximation of the total phase.

The core of this aspect is included in the Blaschke products that we have described. The zeros close to the real axis have an impact on the final phase, while the ones far away only bring a shift factor (i.e. linear phase), so that these are additional solutions but not relevant in term of bunch profile.

The origin of the iterative algorithm we present comes from 2D optics, where an unknown wavefront is propagated from the object to the detector plane. The algorithm has to fulfill the constraints measured for example in the Fourier space and possible information on the "support" in real space. Normally is typical to make a guess about finite size of the field by additional information. In 2D the algorithm tends to be robust respect to noise and

unknown ambiguities. In 1D there are fundamental ambiguities harder to remove.

$$FT[s(t); s(t+t_0); e^{i\alpha} s(t); \tilde{s}(-t)] \Rightarrow \rho(\omega)$$

The ambiguities with shift, constant phase factor are not important. The reverse in time is more difficult to handle and the iterative algorithms (also in 2D) can have stagnation effects in which the algorithm bounces between one and the other solution. In 1D the reconstruction problems are even more serious with difficulties when the profile is composed by scaled replica of the same pulse (or when the algorithm bounces between combination of such solutions). The additional conditions can greatly improve the convergence of such algorithms.

Additional improvements have been added recently to the algorithm in the iterative process, and then a further phase of selection of different solutions coming from different initial guess for the phase. Such step has shown to bring additional stability respect to noise and ambiguities.

Such new method is divided in two steps:

- Iterative phase retrieval algorithms for different independent guess of the phase
- post-selection of the results.

Iterative phase retrieval algorithm

We start from the measured quantity in frequency domain:

$\rho_{Meas.}(\omega)$, while the signal that we want to reconstruct is $s(t)$

Since we deal with data in form of array (for example through DFT or FFT), we will use this notation $s_j \; ; \; s^{(n)}$

Where the subscript refer to the array element and the superscript to the iteration number.

Initialization step of the algorithm is to define a random phase $\varphi^{(0)}$

This initial phase will be assigned to the measured spectrum to form

$$S^{(0)} = \rho_{Meas.} \exp[i\varphi^{(0)}]$$

the iteration no. 0 of the complex spectrum.

Now we can define the iteration loop through the following algorithm:

- Inverse FT the zero-th complex spectrum to get the zero-th longitudinal distribution: $FT^{-1}[S^{(0)}]=s^{(0)}$
- Impose time domain constraints coming from any possible *a priori* knowledge on the support of the function. Update the time domain function to $\tilde{s}^{(0)}$
- Calculate the FT to get the following iteration in frequency domain:

$$FT[\tilde{s}^{(0)}]=S^{(1)}\Rightarrow\varphi^{(1)}=arg[S^{(1)}]$$

- Update the frequency domain by applying the measured spectrum constraint

$$S^{(1)}=\rho_{Meas}\varphi^{(1)}$$

The iteration procedure can be repeated up to convergence, when the solution gets to a steady state and doesn't change in apreciable way.
In order to have some indicator to be used to state when to stop the iteration we may use two figures of merit:

$$\Delta_k=\sum_j\frac{\left|s_j^{(k+1)}\right|-\left|s_j^{(k)}\right|}{\left|s_j^{(k)}\right|}$$

And a second one:

$$\epsilon_k=\sum_j\frac{\left|S_j^{(k)}\right|-\rho_{Meas\,j}}{\rho_{Meas\,j}}$$

The second FOM refers to the adherence of the spectrum amplitude to the measured data before applying the constraint of the measured data. When both FOM will be below some thresholds fixed by the user the algorithm is completed.

As we mentioned the constraint in time domain are very important for the convergence of the algorithm. Typical condition is that the

duration of the bunch (i.e. also reported as support of the function) is limited to a certain quantity.
With a too small support the algorithm will find problems to converge, while for bigger support some ambiguities will arise and the algorithm will find problems bouncing between ambiguous solution. An approximation to be taken with care is the use of the autocorrelation to estimate the bunch support.
A very easy condition comes from the fact that the bunch distribution is a positive and real function, so the Hermitian ambiguity doesn't occur and we only have the time reversal.

Several "tricks" can be used during the iterations when applying the time domain constraints. The so-called Hybrid input-output methods, imposing a mix of condition in the input and output results have shown more rapid convergence. Another class of methods known as the Error Reduction ones have shown less tendency to stagnation. Recent results have shown excellent performances of the so-called "shrink-wrap" algorithms that continuously update the support of the function. All these methods can be beneficial in case of specific waveforms.

Post-selection of results

After the iteration process has given N different independent results (i.e. N arrays of size J). Let's now call s_j^A

the solution A (in the j sample). The aim of this step is to select the best solutions and average them considering the Merit Functions defined in the previous section. The selection is made considering the best value for the ε, that means the algorithm resembling closer connection with the measured data. We make a general check that Δ is also low, denoting convergence of the algorithm and in principle the smallest ε is used as reference solution s_j^R

Once the reference solution has been selected, the other solutions are going to be compared to this in terms of ambiguities of the algorithm, that is, the time shift and time reversal. We'll run some normalized, discrete cross correlations between these solutions and the reference one as follows:

$$c_h^n = \frac{\sum_j s_j^R s_{j+h}^M}{\sqrt{\sum_j \left|s_j^R\right|^2}\sqrt{\sum_j \left|s_{j+h}^M\right|^2}}$$

$$\bar{c}_l^M = \frac{\sum_j s_j^R s_{J-j+l}^M}{\sqrt{\sum_j \left|s_j^R\right|^2}\sqrt{\sum_j \left|s_{J-j+l}^M\right|^2}}$$

Taking into account that we are dealing with arrays of size J, these cross correlations are to be considered as cyclic. For each solution we find the values of shift that maximize the cross correlations calling them

$$\bar{h} \;;\; \bar{l} \;\Rightarrow\; c_{\bar{h}}^M ; \bar{c}_{\bar{l}}^M$$

We will sort all the solutions according to the criterion of closer proximity to the reference solution by the ambiguous factor of the cross correlations:

$$p_n = max\left(c_{\bar{h}}^M, \bar{c}_{\bar{l}}^M\right)$$

All the solutions above a certain threshold of this figure of merit will be selected and averaged to get the final solution.

Many customization could be made in the fine steps of the algorithm and in general these kind of methods have shown to work much better in the phase retrieval.

PowerLaPs

Innovative Education & Training in High Power Laser Plasmas

Laser plasma diagnostics - Theory and Experiments

Chapter 4: Incoherent longitudinal diagnostics

G. Gatti

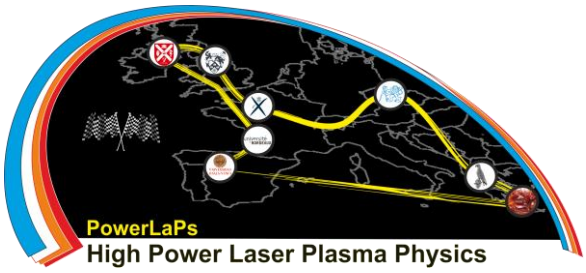

4.1 Explanation on Incoherent longitudinal diagnostics

We start recalling some essential concepts of temporal coherence, necessary to explain intuitively and then formally the idea behind the time duration measurement of a bunch by fluctuation of the emitted radiation.
As a starting point, the coherence concept has been introduced in order to explain the presence of interference between two fields. The time coherence refer to the presence of interference between two fields in the same spatial point, but at different time delays. The more contrast will have the fringes of a Michelson interferometer (contrast means that the fringes will be able to completely cancel the contribution of the fixed intensity by their negative interference), the more will be considered the coherence degree between the two beams. Let's write the intensity read by a detector at the exit of a Michelson, depicted hereafter.

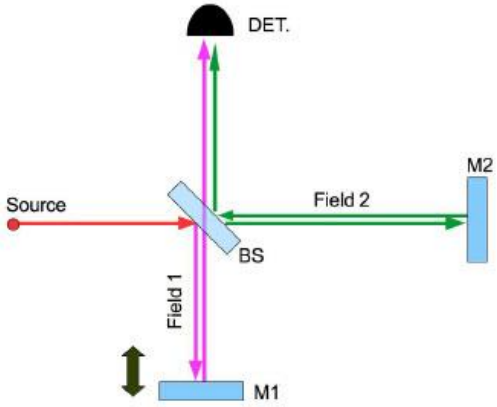

Let's write the intensity:

$$I_d(\tau)=\left\langle \left| K_1 u(t)+K_2 u(t+\tau) \right|^2 \right\rangle = (K_1^2+K_2^2) I_0 + 2K_1K_2 \Re[\Gamma(\tau)]$$

$$\Gamma(\tau)=\langle u(t+\tau)\tilde{u}(t)\rangle$$

The intensity as usual is given by a baseline of intensity due to the single arms and then a term of interference, totally represented by the autocorrelation function, also named self-coherence function.

We can simply re-write the expression normalizing the autocorrelation function to get what is known to be complex degree of coherence.

$$I_d(\tau)=(K_1^2+K_2^2)I_0[1+\frac{2K_1K_2}{K_1^2+K_2^2}\Re(\gamma(\tau))]$$

Where the complex degree of freedom is:

$$\gamma(\tau)=\frac{\Gamma(\tau)}{\Gamma(0)},\ \ |\gamma(\tau)|\leq 1$$

Let's briefly recall here that the autocorrelation is a symmetric expression and that the maximum is in zero (through properties of Fourier transform).
We can now simplify the intensity expression in order to resemble the familiar behavior of an interferogram with its fringes as usual. For such reason we make the ansatz of a quasi monochromatic field. The ansatz is for the autocorrelation, but being the spectrum of the autocorrelation the energy spectrum of the signal, we can say that one resembles more or less the other. Let's take into account a general polychromatic field, this can be written as:

$$V(t)=A(t)e^{-j\Phi(t)}e^{-j\omega_0 t}=2\int_0^\infty \bar{V}(\omega)e^{-j\omega t}d\omega$$

Where we just extract the mean frequency contribution.

$$A(t)e^{-j\Phi(t)}\approx A(0)e^{-j\Phi(0)}=2\int_0^\infty \bar{V}(\omega)d\omega$$
$$t\ll 1/\Delta\omega$$

We can now see that for a quasi monochromatic field, for times below the inverse of the bandwidth we can approximate the amplitude and phase of the signal as a constant. Please, notice that such approximation has been made for an arbitrary time, so this means that it is valid for whatever point in time domain. We can now approximate by such an expression the complex degree of freedom:

$$\gamma(\tau)\approx|\gamma(0)|\exp[-j(\bar{\omega}\tau-\alpha(0))]$$
$$\tau\ll 1/\Delta\omega$$

We can now re-write the intensity in a simplified way, resembling familiar

expressions found in many textbooks. For sake of simplicity we account the amplitude of the two arms as equal:

$$I_D(\tau)=2K^2 I_0[1+|\gamma(0)|\cos(\bar{\omega}\tau+\alpha(0))]$$

This now resembles the well known waveform encountered in case of a monochromatic signal. Let's see what happens in case of different values for the complex degree of coherence (and different time delay).

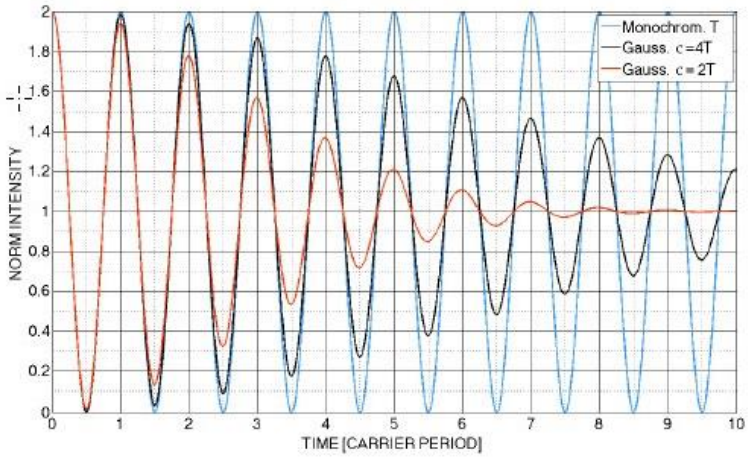

As a comment to the graph we introduce here the well known quantity that is defined as the fringe visibility:

$$V=\frac{I_{max}-I_{min}}{I_{max}+I_{min}}$$

When we have maximum visibility equal to 1 we have perfect coherence, and also complex degree of coherence equal to 1. When the complex degree is 0 we have total incoherence that is visibility also 0, in this case, interference is never detected. Normally we are in the middle of these two limiting positions, where monochromatic beams represent perfect coherence and obviously not existing in the real world. What we have shown is that for signals of a certain bandwidth, and delays below a certain characteristic time, that we'll call the coherence time, we can approximate the signal as monochromatic, hence perfectly coherent:

$$\Delta t_c \approx 1/\Delta\omega$$

This is the general behavior of a light beam.
(Here if there's time a more intuitive explanation about coherence time taking

into account the frequency content).

4.2 Heuristic explanation of time domain behavior

Let's try to analyze what happens on a general point of view in time domain to a partially coherent light field. In our discussion we are interested in pulsed light signals and we'll stick our treatment to that.

The previous equations have shown that a light signal is not able to produce interferometric patterns after slipping over its coherence time (i.e. or length if multiplying by c).

Let's try to understand which time domain waveform reflects such behavior.

In time domain, we can think the light beam as composed by different intervals approximately of the order of the coherence time. Every such slice is internally coherent, but every slice is completely incoherent respect to the other slices (for example in a Michelson interferometer). This means that every of these intervals is completely uncorrelated from the others. Let's now postulate about a possible intensity measurement of such pulse. We can readily state that the full intensity will be given by the sum of the contribution of such coherent slices. Let's state that given the pulse duration, there will be a number N of slices included in it:

$$N = \tau_P \Delta\omega = \tau_P / \tau_C$$

Let's now take into account the shot to shot fluctuation of the full pulse. From the previous considerations we'll state that the intensity is composed by N independent contributions (i.e. the slices) given by N random variables. These variables can be considered obeying the same statistics, but being independent variables (i.e. no correlation). With such a few and general assumptions we can get an insight in the pulse fluctuation statistics respect to the slice statistics:

$$\sigma_I^2 = N\sigma_W^2 \quad ; \quad \mu_I = N\mu_W$$

$$\frac{\sigma_I}{\mu_I} = \frac{1}{\sqrt{N}} \frac{\sigma_W}{\mu_W}$$

The intensity fluctuation can give us an insight on the number of coherent slices present in the pulse, together with the knowledge of the spectral width. This shows us the potential of such a technique. Now let's try to formalize more such method. As for the coherent reconstruction, we are building a method that is able to work with many radiation sources (e.g. Cherenkov, TR etc.). The important part is that the emission has to be broadband enough to satisfy the different requests of the method.

So, let's start from a general electron bunch distribution radiating through a generic physical process. The electric field radiated by an electron at the time

t and towards an angle **θ** is written as follows:

$$e(t,\boldsymbol{\theta})$$

Where the angles are defined in this way and are taken respect to the beam direction of propagation, z, according to the following picture:

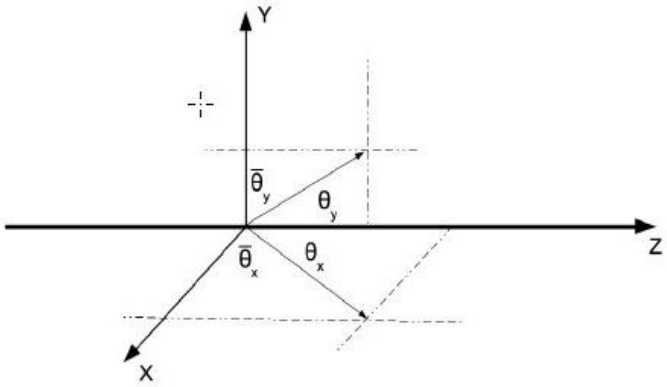

The ansatz on the angles is that they are small.

$$\boldsymbol{\theta}=(\theta_x,\theta_y) \quad , \quad |\theta_x|,|\theta_y| \ll 1$$

From the picture we can see that the vector **θ** having as component the two angles respect to the direction of motion corresponds to the unit vector pointing at a detector at the angle **θ**. Using the same notation as for the coherent case:

$$\hat{n}=(\cos\bar{\theta}_x,\cos\bar{\theta}_y)=(\sin\theta_x,\sin\theta_y)\approx(\theta_x,\theta_y)$$

The other ansatz is that the divergence of the electron beam is small so that the divergence of the radiation is the only one to be accounted for and we don't have to convolute this with the divergence distribution of the beam.
With this background we can now write the general far-field in the same way it was done for the coherent approach summing all the electrons' contributions:

$$E(t,\boldsymbol{\theta})=\sum_{k=1}^{N} e\left(t-t_k-\frac{1}{c}\boldsymbol{r_k}.\boldsymbol{\theta},\boldsymbol{\theta}\right)$$

Here, as seen in the coherent approach, the time is: $t_k = \frac{\Delta z_k}{c}$

while the vector r_k is the vector pointing at the k electron position in 2D transverse space x,y. Recalling that the **θ** vector is the unit vector pointing at the detector, we see that:

$$\frac{1}{c}\boldsymbol{r}_k \cdot \boldsymbol{\theta} = \frac{1}{c}\hat{n} \cdot \boldsymbol{r}_k$$

exactly the same delta time given by the transverse position of the electron as found in the previous lecture. Let's now give additional details on the formalism presented. The position of the electrons are considered to be random within a certain distribution. Such position will fluctuate from shot to shot, but in the long term the whole ensemble will give a certain bunch distribution. Let's introduce some normalized distributions:

$$f(t)\,dt \quad , \quad \int f(t)\,dt = 1$$
$$F(\boldsymbol{r})\,d\boldsymbol{r} \quad , \quad \int F(\boldsymbol{r})\,d\boldsymbol{r} = 1$$

We split the distribution in transverse and longitudinal, where the quantities on the left represent the probability to find an electron in that position. As for the previous lecture, the ansatz for the particle position is that they belong to the same distribution but different particles are independent, so that:

$$\langle t_k t_i \rangle = \langle t_k \rangle \langle t_i \rangle$$
$$\langle x_k x_i \rangle = \langle x_k \rangle \langle x_i \rangle$$
$$\langle y_k y_i \rangle = \langle y_k \rangle \langle y_i \rangle$$

We are finally going to look at the spectral properties of the radiation emitted by the bunch, by Fourier transforming the time domain quantities:

$$\hat{E}(\omega,\theta) = \int_{-\infty}^{\infty} E(t,\theta) e^{j\omega t}\,dt = \hat{e}(\omega,\theta) \sum_{k=1}^{N} e^{j\omega t_k + j\frac{\omega}{c}\boldsymbol{r}_k \cdot \theta}$$

The interested quantity is in general the energy spectrum being proportional to the modulus square of the electric field spectrum. The overall power measured by the detector is also supplied by additional correction factors accounting for spectral and angular filtering proper of a transport beamline. So, we'll focus on the overall power spectrum:

$$P(\omega,\theta) = S(\theta) R(\omega) \left|\hat{E}(\omega,\theta)\right|^2$$

Now we introduce a new function in order to distinguish the single particle spectrum and the ensemble contribution of the full bunch:

$$T(\omega,\theta)=S(\theta)R(\omega)\left|\hat{e}(\omega,\theta)\right|^2$$

And re-write again the full bunch power spectrum as:

$$P(\omega,\theta)=T(\omega,\theta)\sum_{k,l=1}^{N}e^{j\omega[t_k-t_l+(\boldsymbol{r}_k-\boldsymbol{r}_l).\theta/c]}$$

This is the power spectrum of the full bunch. Just, it is the power spectrum for a particular distribution of the bunch, so let's try to get the average power spectrum of the bunch recalling the same procedure used in the coherent case, introducing the bunch normalized particle distribution functions in time and transverse space. We give here the procedure for time domain, the same is repeated. Dropping out the single particle contribution for the moment being, let's look at the exponential sum:

$$\frac{1}{N}\sum_{k=1}^{N}e^{j\omega t_k}=\frac{1}{N}\sum_{k=1}^{N}\int\delta(t-t_k)e^{j\omega t}dt$$

Where we used the delta train in order to put the exponential in a continuous variable. The 1/N factor is a normalizing factor of the distribution. As we expect, going to average over the different bunches trials, we should average to the bunch distribution. So, let's average with the distribution function introduced before:

$$\left\langle\frac{1}{N}\sum_{k=1}^{N}e^{j\omega t_k}\right\rangle=\frac{1}{N}\sum_{k=1}^{N}\int\int\delta(t-t_k)f(t_k)e^{j\omega t}dt_k\,dt=\int f(t)e^{j\omega t\,dt}$$

I'm not well convinced of using the delta in terms of normalization.
So, again we see that averaging over the different realizations of the bunch we get the Fourier transform of the bunch distribution, that we introduced and defined as the Form Factor (i.e. the abs square of it). With this identity we can write the average power spectrum:

$$\langle P(\omega,\theta)\rangle=T(\omega)(N+N^2\left|\hat{f}_t(\omega)\right|^2\left|\hat{F}(k\theta)\right|^2)$$

Where we divided the bunch distribution to give two form factor, a longitudinal one and a transverse one according to the following formulas:

$$\hat{f}_t(\omega)=\int_{-\infty}^{\infty}f_t(t)e^{j\omega t}dt$$
$$\hat{F}(k\theta)=\int_{-\infty}^{\infty}F(\boldsymbol{r})e^{jk\theta.r}dx\,dy$$

Let's recall the extensive comments made on this formula during the previous lecture. We can observe a coherent part of radiation proportional to N^2 and an incoherent part proportional to N. The coherent part is weighted by the bunch form factor, so that we can distinguish two limiting cases, let' say low and high frequencies. Guessing for example the time distribution as a normalized gaussian of variance σ_t^2

We can easily see the two different regimes as coherent and incoherent dominated regime:

$$\omega<\sigma_t^{-1} \Rightarrow N^2\left|\hat{f}_t(\omega)\right|^2 \gg 1$$

$$\omega>\sigma_t^{-1} \Rightarrow N^2\left|\hat{f}_t(\omega)\right|^2 \ll 1$$

This time we'll focus on high frequencies and incoherent emission. According to the features of the two emissions, one could ask why we want to use incoherent radiation, since that doesn't contain any form factor, that is what carries the bunch distribution information. This objection is indeed true, but only in the averaged distribution. In the power spectrum, the contribution of the bunch is still present. Let's try to reconnect this point to the initial introduction aimed to give a direct insight into this phenomenon.

4.3 Deeper explanation on the fluctuation source

Each realization of the bunch (and the related radiation emitted) reflects the intrinsic stochastic distribution of the particles. Such random process creates a random fluctuation of the overall intensity emitted for every process realization. The fluctuations come out from the interference between different particle contributions. On the high frequency scale (wavelengths comparable with the position fluctuation inside the bunch) such random changes have a role, while in the low frequency scale (coherent radiation), such fluctuations are negligible respect to the wavelength and to the interference pattern. Averaging over many pulses will smear out such fluctuations, since in the long term, all the stochastic process realization will converge towards the average bunch distribution. As it is probably evident from the previous analysis, the average power spectrum in the incoherent case (i.e. high frequency) is simply reduced to:

$$\langle P(\omega,\theta)\rangle = N\,T(\omega,\theta)$$

As we said, there's no more bunch information out of this, but let's see what happens if we go for high order statistics (i.e. for people who are familiar with the topic, this resembles the intensity correlations of Hunbury-Brown theory):

$$\langle P(\omega,\theta)P(\omega',\theta')\rangle = T(\omega,\theta)T(\omega',\theta') \sum_{k,l,m,n=1}^{N} \langle e^{j\omega(t_k-t_l)+j\omega'(t_m-t_n)}\rangle \sum_{k,l,m,n=1}^{N} \langle e^{jk\theta.(r_k-r_l)+jk'\theta'(r_m-r_n)}\rangle$$

Here we can see the two sums relative to the time and space parts, respectively as from the publication. Here the uncorrelation is between time and space. Let's look more closely at the sums reported here:

$$\left\langle \sum_{k,l,m,n=1}^{N} e^{j\omega(t_k-t_l)+j\omega'(t_m-t_n)} \sum_{k,l,m,n=1}^{N} e^{jk\theta.(r_k-r_l)+jk'\theta'(r_m-r_n)} \right\rangle$$

Let's now reorganize the sums in order to extract the constant terms and simplify the expression:

$$\langle (\sum_{k=l} e^{j\omega(t_k-t_l)+jk\theta(r_k-r_l)} + \sum_{k\neq l} ..)(\sum_{m=n} e^{j\omega(t_m-t_n)+jk\theta(r_m-r_n)} + \sum_{m\neq n} ..)\rangle = \langle (N+\sum_{k\neq l} ..)(N+\sum_{m\neq n} ..)\rangle$$

This turns into:

$$\langle (N+\sum_{k\neq l} ..)(N+\sum_{m\neq n} ..)\rangle = \langle N^2 + N\sum_{k\neq l} .. + N\sum_{m\neq n} .. + \sum_{k\neq l} .. \sum_{m\neq n} ..\rangle$$

Using the substitution of the sum by the integral introduced before we can write:

$$N^2\left(1+N\left|\hat{f}_t(\omega)\right|^2\left|\hat{F}_t(k\theta)\right|^2 + N\left|\hat{f}_t(\omega')\right|^2\left|\hat{F}_t(k'\theta')\right|^2\right) + \langle \sum_{k\neq l} .. \sum_{m\neq n} ..\rangle$$

It is time now to point out some detail on the form factors given by the incoherent regime we are working with, so that:

$$N\left|f(\omega)\right|^2 \ll 1 \quad , \quad \omega > \omega_{cutoff}$$

Same condition is expressed for the transverse form factor.
So, translating such conditions to the average sums above we only have the following terms remaining:

$$N^2 + \langle \sum_{k\neq l} e^{j\omega(t_k-t_l)+jk\theta.(r_k-r_l)} \sum_{m\neq n} e^{j\omega'(t_m-t_n)+jk'\theta'.(r_m-r_n)} \rangle$$

Let's reorganize the elements under the average brackets in order to further extend our comments:

$$\left\langle \sum_{k,l,m,n=1}^{N} e^{j\omega(t_k-t_l)+j\omega'(t_m-t_n)} \sum_{k,l,m,n=1}^{N} e^{jk\theta.(r_k-r_l)+jk'\theta'.(r_m-r_n)} \right\rangle$$

If we proceed with the average with the same procedures used above, we'll have different terms corresponding to the form factors seen already and approximated to zero. Looking more carefully the two sums we'll realize that the only indexes originating non negligible terms are the ones for which the time and space frequencies are subtracted one from each other. Such indexes are k=n, l=m, in such a way to get:

$$\left\langle \sum_{k,l=1}^{N} e^{j(\omega-\omega')(t_k-t_l)} \right\rangle \left\langle \sum_{k,l=1}^{N} e^{j(k\theta-k'\theta').(r_k-r_l)} \right\rangle \;;$$

$$k=n, l=m, k\neq l$$

And then, in terms of form factors:

$$\left\langle \sum_{k,l=1}^{N} e^{j(\omega-\omega')(t_k-t_l)} \right\rangle \left\langle \sum_{k,l=1}^{N} e^{j(k\theta-k'\theta').(r_k-r_l)} \right\rangle = N^2 \left|\hat{f}_t(\omega-\omega')\right|^2 \left|\hat{F}(k\theta-k'\theta')\right|^2$$

It is easy to realize that for relatively reduced spectrum (temporal and spatial) the frequency difference is going to be limited and so the form factors will be not negligible as much as it happened for the coherent case, in a more subtle way here. Let's write the complete expression of the power spectrum autocorrelation:

$$\langle P(\omega,\theta)P(\omega',\theta')\rangle \approx N^2 T(\omega,\theta)T(\omega',\theta')[1+\left|\hat{f}_t(\omega-\omega')\right|^2 \left|\hat{F}(k\theta-k'\theta')\right|^2]$$

We'll use the autocorrelation a few steps ahead. Let's now focus on the full radiated energy that we'll also use to get to our fluctuations' analysis.

$$\epsilon = \int P(\omega,\theta)\, d\omega\, d\theta_x\, d\theta_y \;;\; \langle\epsilon\rangle = \int \langle P(\omega,\theta)\rangle\, d\omega\, d\theta_x\, d\theta_y$$

As we are interested to the incoherent fluctuations, the core quantity under analysis will be:

$$\delta^2 = \frac{\langle \Delta\epsilon^2\rangle}{\langle\epsilon\rangle^2}$$

Let's use a well known result from basic statistics:

$$\langle \Delta\epsilon^2\rangle = \langle (\epsilon - \langle\epsilon\rangle)^2\rangle = \langle\epsilon^2\rangle - \langle\epsilon\rangle^2$$

Let's look at the members of such equations:

$$\langle\epsilon^2\rangle = \langle [\int P(\omega,\theta)\, d\omega\, d\theta]^2\rangle = \langle \int P(\omega,\theta)\, d\omega\, d\theta \int P(\omega',\theta')\, d\omega'\, d\theta'\rangle$$

$$\langle\epsilon\rangle^2 = [\int \langle P(\omega,\theta)\rangle\, d\omega\, d\theta]^2 = \int \langle P(\omega,\theta)\rangle\, d\omega\, d\theta \int \langle P(\omega',\theta')\rangle\, d\omega'\, d\theta'$$

Now thanks to this result we can use the autocorrelation expression found before. In order to have more compact formulas we'll use such notation:

$$P=P(\omega,\theta)\ ,\ P'=P(\omega',\theta')$$

So, let's write the delta expression with the new results:

$$\delta^2=\langle\epsilon\rangle^{-2}\int[\langle PP'\rangle-\langle P\rangle\langle P'\rangle]d\omega d\omega' d\theta d\theta'$$

using the previous quantities found for autocorrelation and average power:

$$\langle\Delta\epsilon^2\rangle=N^2\int TT'[1+|\hat{f}_t(\omega-\omega')|^2|\hat{F}(k\theta-k'\theta')|^2]d\omega d\omega' d\theta d\theta'-N^2\int TT' d\omega d\omega' d\theta d\theta'$$

And now we can write the final expression for the average fluctuation of the intensity measured:

$$\delta^2=\frac{\langle\Delta\epsilon^2\rangle}{\langle\epsilon\rangle^2}=\frac{N^2\int TT'[|\hat{f}_t(\omega-\omega')|^2|\hat{F}(k\theta-k'\theta')|^2]d\omega d\omega' d\theta d\theta'}{N^2[\int T d\omega dd\theta]^2}$$

This is the formula we were looking for, even though it doesn't give us insight into the process. For this purpose, we choose an easy spatial, temporal distribution of the bunch in order to get some significative result that can support all the introduction we gave on a heuristic base.

Let's analyze a particular and easy case in order to illustrate what we have been introducing much before. Choosing a gaussian normalized distribution function in time, so that, according to the convention had here for Fourier Transform we have the following pair and the consequent form factor:

$$f_t(t)=\frac{1}{\sigma_t\sqrt{2\pi}}e^{\frac{-t^2}{2\sigma_t^2}}\ \Rightarrow\ \hat{f}_t(\omega)=e^{-\frac{\sigma_t^2\omega^2}{2}}$$

$$|\hat{f}_t(\omega)|^2=e^{-\sigma_t^2\omega^2}$$

For sake of simplicity let's assume perfect transmission and the filter functions being:

$$T(\omega,\theta)=1$$

Let's operate the integral for the time frequency domain given that the integrand is here separated in products and so the different integrals are

carried out independently:

$$\delta^2=\int_{-\infty}^{\infty}\int_{-\infty}^{\infty}\left|\hat{f}_t(\omega-\omega')\right|^2 d\omega\, d\omega'=\int_{-\infty}^{\infty}\int_{-\infty}^{\infty}e^{-\sigma_t^2(\omega-\omega')^2}d\omega\, d\omega'$$

neglecting for the moment the spatial part. Let's develop this:

$$\delta^2=\int_{-\infty}^{\infty}\int_{-\infty}^{\infty}e^{-\sigma_t^2(\omega^2+\omega'^2-2\omega\omega')}d\omega\, d\omega'=\sqrt{\frac{\pi}{\sigma_t^2}}$$

$$\int_{-\infty}^{\infty}e^{-(ax^2+bx+c)}dx=\sqrt{\frac{\pi}{a}}e^{\left[\frac{b^2-4ac}{4a}\right]}$$

$$a>0$$

Here we get a first result for the simple gaussian case that is the core of the information we were looking for: the time distribution. Nevertheless let's also calculate the integral for the spatial parts, still with a simple gaussian distribution:

$$k'\theta'\approx k_0\theta' \;;\; \left|\hat{F}(k_0(\theta-\theta'))\right|^2=e^{-k_0^2[\sigma_x^2(\theta_x-\theta_x')^2+\sigma_y^2(\theta_y-\theta_y')^2]}$$

$$\int_{-\infty}^{\infty}\int_{-\infty}^{\infty}\left|\hat{F}(k_0(\theta-\theta'))\right|^2 d\theta_x d\theta_{x'} d\theta_y d\theta_{y'}=\sqrt{\frac{\pi}{k_0^2\sigma_x^2}}\sqrt{\frac{\pi}{k_0^2\sigma_y^2}}$$

Putting all together we finally find the complete expression for the intensity variation:

$$\delta^2=\sqrt{\frac{\pi}{\sigma_t^2}}\sqrt{\frac{\pi}{k_0^2\sigma_x^2}}\sqrt{\frac{\pi}{k_0^2\sigma_y^2}}$$

This is directly showing us the result we were looking for. The fluctuation analysis of the intensity is directly related to the standard deviation of the time duration. The spatial distribution also has a role and contributes to the fluctuations, so that this should be taken into account. Let's analyze a more realistic case with the spectral and angular transfer function different from a unit constant.

$$T(\omega,\theta)=T_0 e^{-\frac{(\omega-\omega_0)^2}{2\sigma_\omega^2}-\frac{\theta_x^2}{2\sigma_{\theta_x}^2}-\frac{\theta_y^2}{2\sigma_{\theta_y}^2}}$$

We'll keep using the same gaussian form-factors previously employed.It is possible to prove that in this case, the energy fluctuation is:

$$\delta^2 = \frac{1}{\sqrt{1+4\sigma_\omega^2\sigma_t^2}} \frac{1}{\sqrt{1+4k_0^2\sigma_{\theta_x}^2\sigma_x^2}} \frac{1}{\sqrt{1+4k_0^2\sigma_{\theta_y}^2\sigma_y^2}}$$

For small transverse beam size, the expression reduces to:

$$\delta^2 \approx \frac{1}{\sqrt{1+4\sigma_\omega^2\sigma_t^2}}$$

From the knowledge of the spectral variance, for example by a filter, the expression can be further simplified if the following stands:

$$\sigma_t \gg \frac{1}{2\sigma_\omega} \approx \sigma_{tc}$$

This means that there are many coherence length in the duration of the pulse, that is another way to say that the pulse is incoherent. If so, the energy fluctuation reduces simply to:

$$\delta^2 \approx \frac{1}{2\sigma_\omega\sigma_t} = \frac{\sigma_{tc}}{\sigma_t} = \frac{1}{M}$$

With M being the number of coherence lengths included in the pulse duration, or the number of independent slices inside the pulse. We recall exactly the same result that we found by mean of a general and more heuristic approach. In the textbooks talking about coherence we can find that each slice radiation can be modeled with a Poisson stochastic process whose intensity has 100% fluctuation. This simply brings us to find the result that we have seen here for a bunch radiation and in the heuristic case. Fixed the spectral range, we can see that the measurement is more effective for short bunches. For too long bunches, the smearing effect brings a low fluctuation.
Of course, the real world is not that easy and we saw that for example, the transverse finite size brings an additional contribution to the fluctuation that is not related to the time information. Getting more deeply into the experimental conditions, we also need to evaluate the number of photons implied in the measurement. If the photon number is too low, we'll need to take into account an additional fluctuation due to the photon shot noise contribution. Another added stochastic phenomenon is given by the photon to electron conversion in the detector used. All such fluctuation terms should be added in quadrature

(in the denominator of the delta square).

4.4 Possible improvements

It would be possible to decouple the detector shot noise contribution by applying different neutral density filters. In this way it is possible to change only one contribution to the variation and after evaluation decouple that from the measurement. The transverse size contribution can be also decoupled by using different bandpass filters with the same central frequency but different bandwidth. The longitudinal term only depends on the bandwidth while the transverse only on the central frequency. By different filters it would be possible to estimate and decouple one of the two variations. The charge variation can also play a role. This is due to the fact that in theory the N (charges) cancel each other, but this happens when the average on the bunch has the same charge. If the charge also fluctuates, this factor should be taken into account and used to re-normalize. This can be done by measuring the charge shot to shot.

PowerLaPs

Innovative Education & Training in High Power Laser Plasmas

Laser plasma diagnostics - Theory and Experiments

Chapter 5: Streak cameras and related measurements

G. Gatti

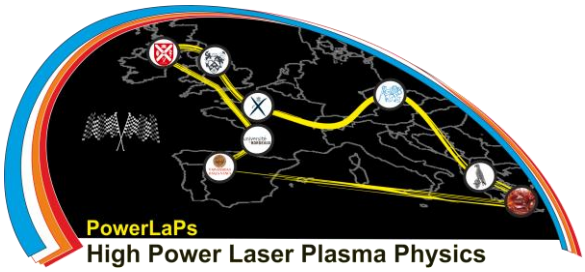

5. Introduction to streak cameras and related measurements

The Streak-Camera is a device aimed to perform high-speed time resolved measurement of light pulses. The high flexibility that this device can offer, ranging from the ns time scale up to the hundreds of fs one, the wide range of photon energies (IR to X-rays), makes it an essential tool in laser-matter interactions. The concept of the Streak-Camera has been fruitfully extended with laboratory prototypes to surrounding fields (attosecond science, particle accelerators etc.). We are going to introduce the basic inner components of these devices with some hints on possible applications.

5.1 Motivation

Time-domain characterization of light, especially for fast phenomena is a very important topic in many branches of physics (e.g. biology, chemistry, accelerator physics, plasma physics etc.). The time variable is the more subtle to unveil, especially on short scales, where the conventional electronics start to have limitations. Very wide application on laser related phenomena.

BW ≈ GHz → Time Response ≈ ns

Many techniques adopted in different frameworks and time-scales to circumvent this problem. With Streak-Cameras we pass from conventional electronics to "unwired" electronics, where electrons travel into the vacuum of a streak-tube.

It is very well suited to cover (with different devices) the range below 1 ns up to a few hundreds of fs. In the ultrafast time-domain, some limitations of the device make harder to work, and side problems arise (e.g. time jitter, synchronization etc...).

5.2 Concept

As in many other instruments, in slight different way, the idea is to convert the time variable into a space variable and measure space where we suppose to have a higher resolution and less limitations compared to time.

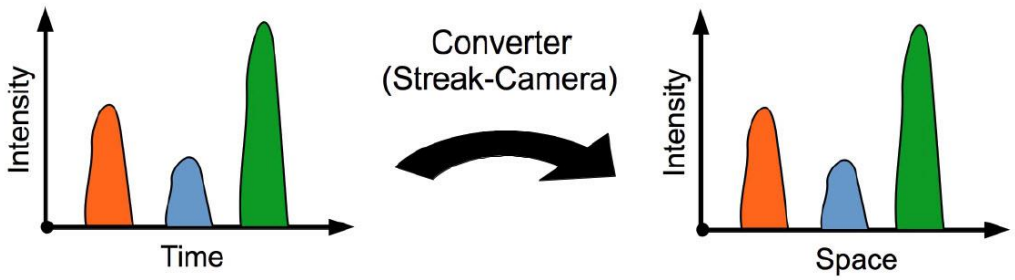

If we succeed, we map Intensity vs. Time into Intensity vs. Space. This is the definition of an Image. We will use the space (i.e. pixel position for the time variable and the intensity of the pixel, or count for the Intensity variable).

Normally we don't map 2D (Time and Intensity) into 2D ,but 3D (Time, Space, intensity into 3D, where we employ one dimension for Time, one for Space, and one for Intensit

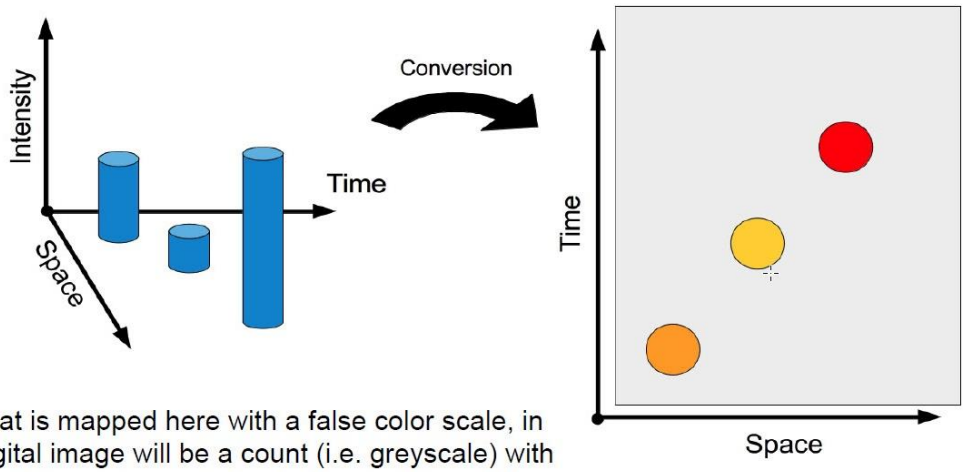

What is mapped here with a false color scale, in a digital image will be a count (i.e. greyscale) with a certain range according to the number of bits. For example 0-255 for 8 Bits Images.

False colors replace the Intensity scale

5.3 Implementation

Photons are converted into electrons, deflected by time varying electric field into an imaging screen, where the electron distribution in space is again converted into photor and read by a conventional digital camera.

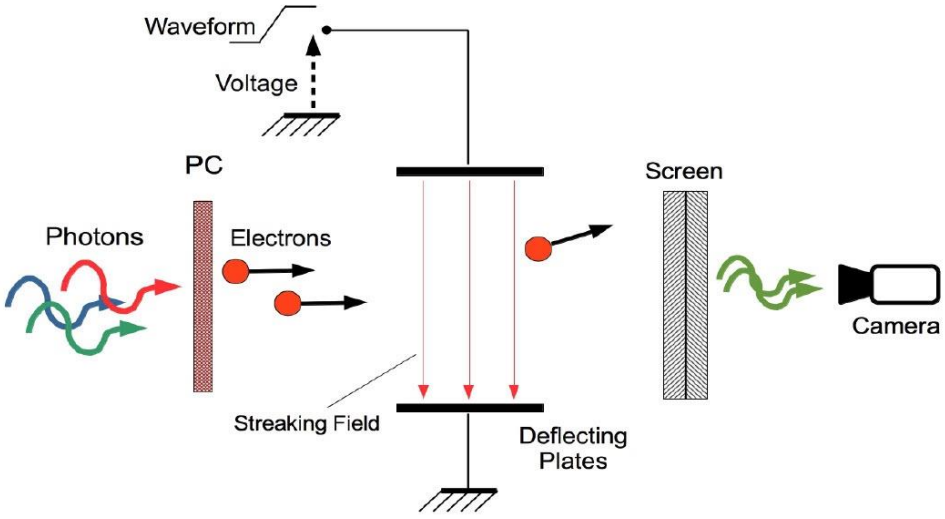

Apart from the rough description, things are not so easy. And such scheme doesn't work.
Guess why?
The Spatial "footprint" of electrons plays a big role in resolution

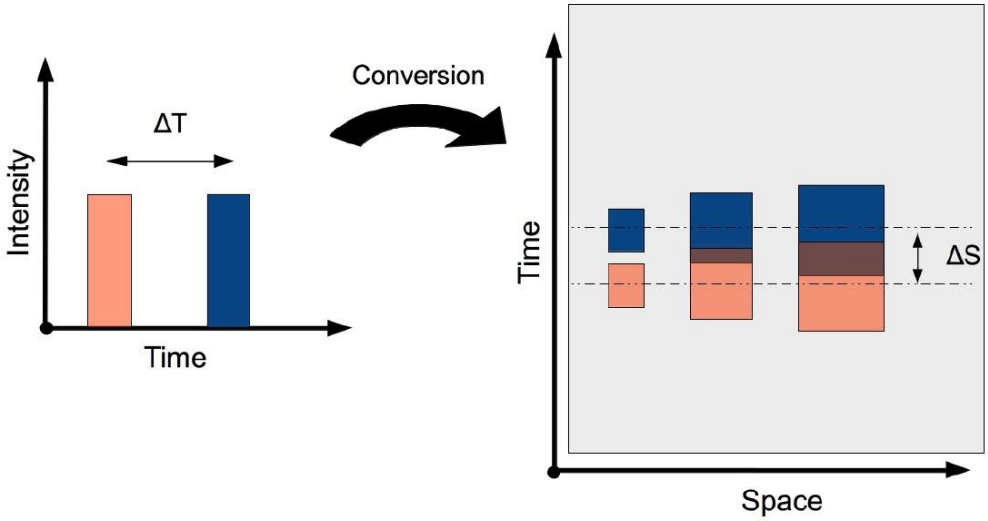

The footprint would be the Point Spread Function of the system, that is, the size of the electron beam for a delta function in space with no streaking field.

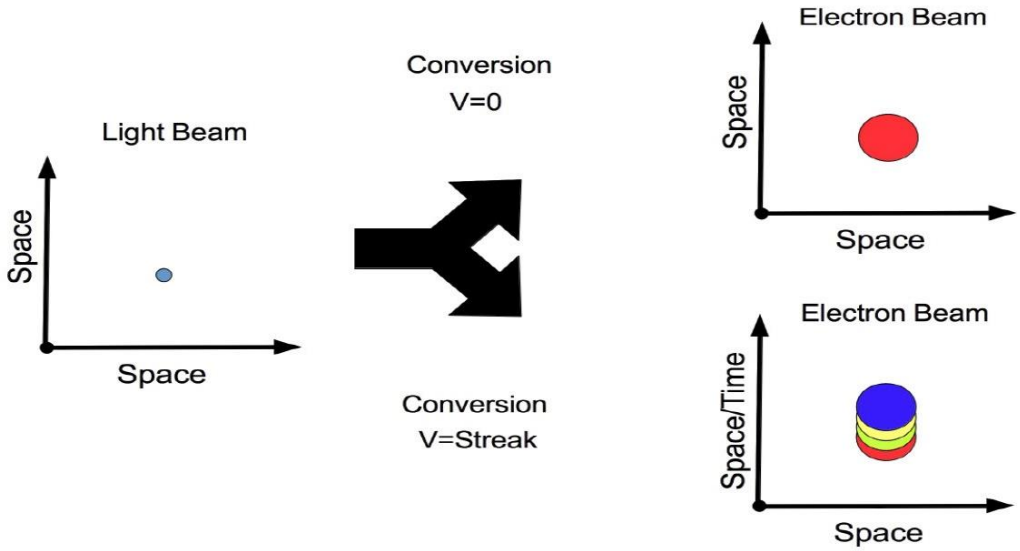

Solution: minimize the PSF, this is done in two steps

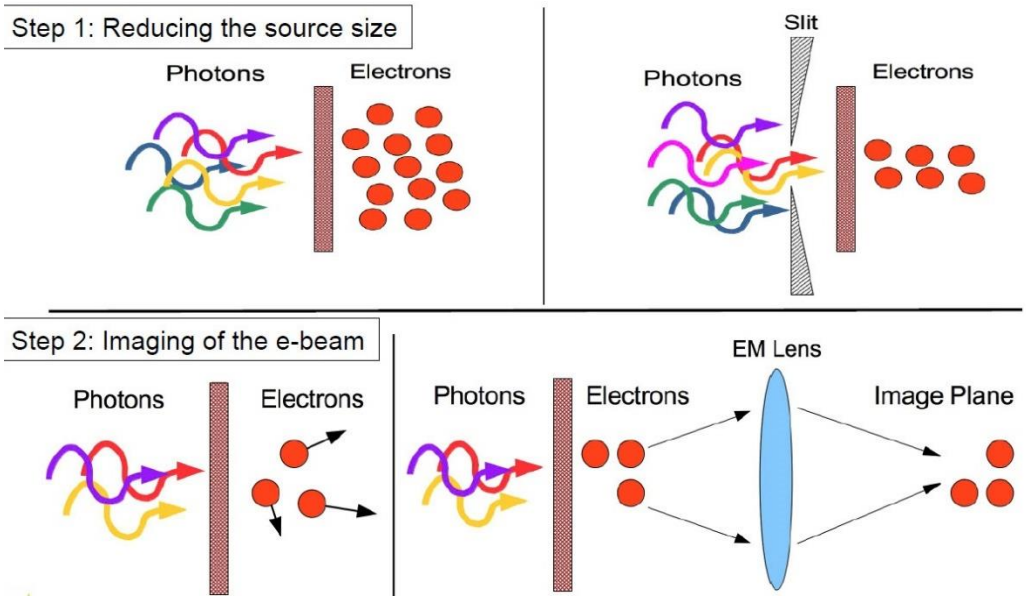

Summary: we can now outline the building blocks of a typical Streak-Camera with a short description aimed at displaying the task carried-out by each.

BUILDING BLOCKS

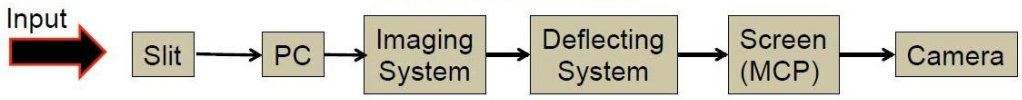

- **Slit:** Normally movable, allows for minimizing the electron source size improving resolution
- **PhotoCathode:** Converts the incoming photons into (photo)electrons via the photo-electric effect. We'll see in the limitations that a polarized anode is also necessary.
- **Imaging System:** It is an ensemble of magnetic or electrical elements performing an image of the e-source plane on the screen plane (keeping a small el. size though the angular spread).
- **Deflecting System:** It is the device aimed to impart the deflection to the electrons and hence the time to space conversion.
- **Screen:** It is a device in charge of reconverting the electrons into photons, preserving the spatial information and most of the times intensifying the image.
- **Camera:** It is a digital camera with the proper dynamic range and the coupling optics to make the image of the Screen distribution and give as output the final image.

5.4 Building blocks

Slit

It is apparently a simple element, though there are some details to be mentioned

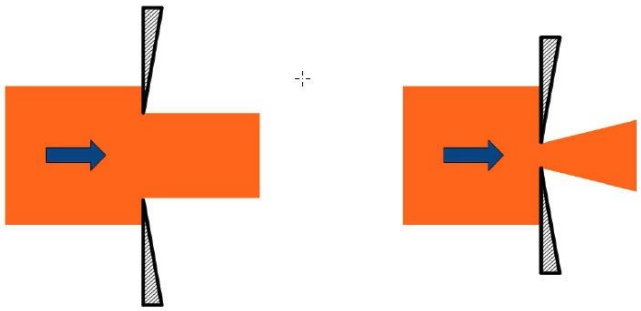

Diffraction gives an out divergence

$$\theta \propto \lambda / D_{slit}$$

Focus mode: There's a "preparation" mode of alignment of the Streak-Camera where the Streaking Field is not applied. Here we can optimize the coupling of the light and set the optimal width of the slit in order to optimize the PSF.

Optimal Size

In order to minimize the PSF normally the slit is closed up to sampled by at least 2/3 pixels (magnification here taken into account). In general opening ranges less than 20 μm bring deep diffraction patterns and are to be excluded.

Photocathode

The Photo-Cathode is the element converting the incoming photons into electrons by the photo-electric effect. The intrinsic assumption is that the time shape of the light is well preserved (prompt response) and the spatial resolution as well.

Assumption: linear photoemission, *1 photon interacts exciting 1 electron*

Lot of complex phenomena happen around the photo-cathode, we try to give an insight and a baseline for those interested to go deeper into the topic (bibliography)

The most direct and used method of modelling photoemission is due to Berglund/Spicer and known as the 3-steps model. The process is divided into 3 main phases:

1. ***Absorption of a photon by an electron (i.e. photoelectron)***
2. ***Electron escape towards the surface***
3. ***Overcome of the surface barrier***

Each step includes an impressive number of details, given that the specific type of material and the specific experimental scenario can change abruptly the outcome of the process

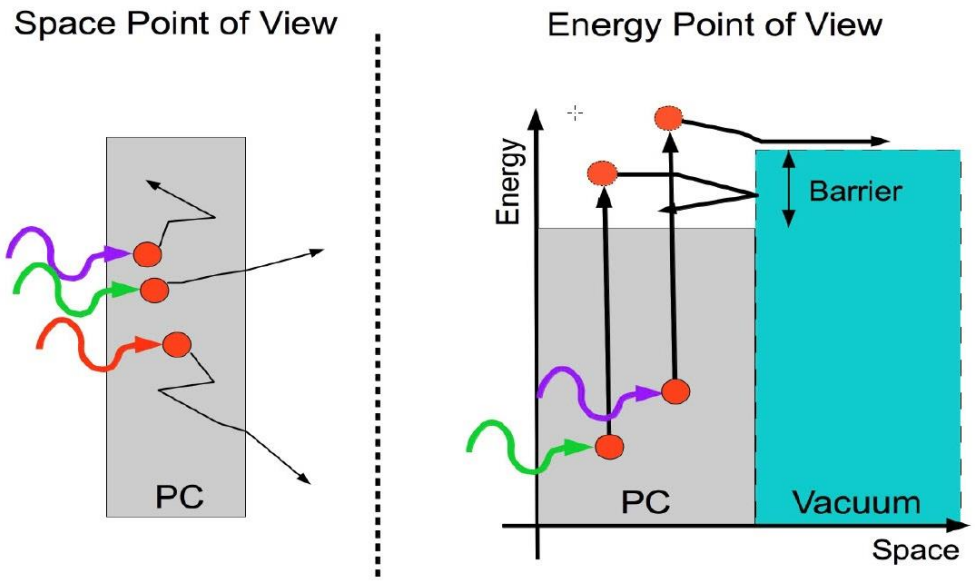

1. Absorption of a photon by an electron (i.e. photoelectron)
2. Electron escape towards the surface
3. Overcome of the surface barrier

1. We want full absorption of photons (poor reflection), to lead to high QE and proper absorption inside the material. We want possibly the photoelectrons not being generated to far away from the exit surface. We also would like the PC to be broadband at least for the Streak-Camera.

2. The excited electron can drift with a random direction. It usually has collisions according to the specimen, changing direction and decreasing energy. Normally in a metal e-e scattering is dominating where e-p is in a semiconductor.

3. Once in proximity of the barrier, the electron needs to have a kinetic energy perpendicular to the barrier at least as big as the energy gap. The barrier obviously is not constant and is affected deeply by a vast class of surface phenomena. Though electrons can escape it is necessary to apply a polarization: an accelerating voltage to favor the electron extraction (more clear later).

Focusing system

The aim is performing a high quality imaging, so it is good to have a perfect (el/magnetic lens), though respect to light optics, the problems increase, but we'll see these aspects in the non-idealities.

Typical type of Lenses

Tube Lenses

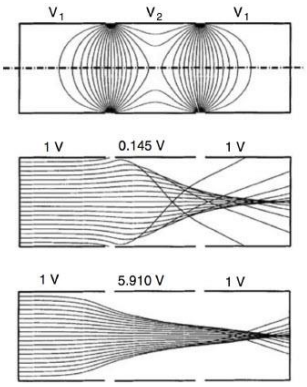

Aperture Lenses

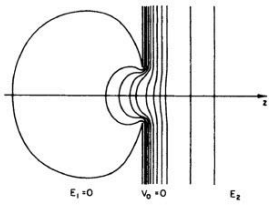

Quadrupole Lenses

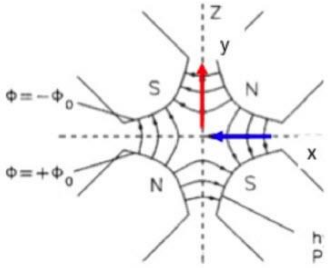

Electric and magnetic lenses suffer aberrations as much as the optical ones, more complex configurations of multiple elements to correct aberrations are possible

Typical: Spherical, Chromatic, Astigmatism etc...

Deflecting system

The requirements of the deflecting system is the fastest possible ramping field, which is the "brute force" factor for increasing the Streak-Camera Resolution.

Warning: the two simple deflecting plates for high speed operations (KV/ps) start having bandwidth problems. More complex structure with embedded Transmission lines are employed in the highest resolution devices

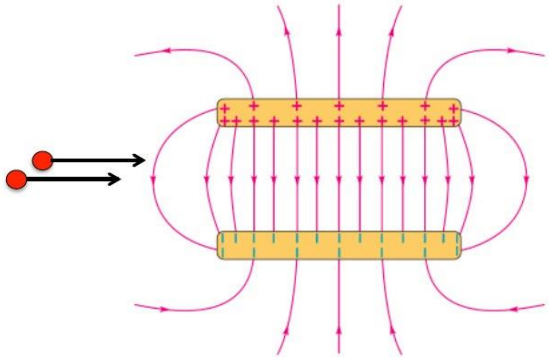

Fringing field introduces a different deflection and transit time for electrons on different positions.

Mitigation limiting the access window in the deflection plates and grounding part of the fringing fields.

Screen (MCP)

The Micro Channel Plate is a flexible and valuable device and it is basically an electron multiplier. Can work with photons, charged particles and with different configurations. Can be used in time domain (e.g. ToF, Gating) or in imaging mode, with a phosphor.

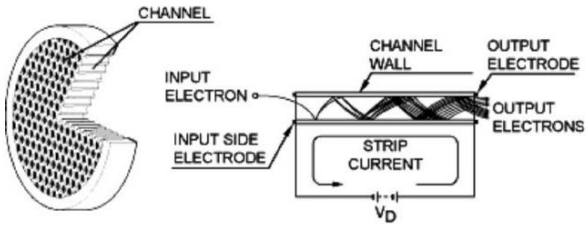

It is a device that can be configured for different purposes. It is a multichannel electron multiplier.

Several stages can give more gain. The gain is around 1E2-1E4 per stage. The maximum resolution (channel) is around 20μm. More gain decreases the resolution.

The ones for streak cameras have a phosphor screen on the back to make an image. It usually emit in the green.

Through the voltage we can change the gain.

Camera

Quite easy to be explained. The analog image of the phosphor, in the back of the MCP has to be acquired (digitally). We need an imaging device (i.e. camera) and an optical imagine system from the object plane (the phosphor) to the sensor plane.

The camera needs to have the right sensitivity and dynamic range to fully capture the features of the image. The assembly imaging system plus camera need to fulfill a resolution on the order of the MCP one. Main choices of imaging systems are optical but optically bonded fiber arrays are employed.

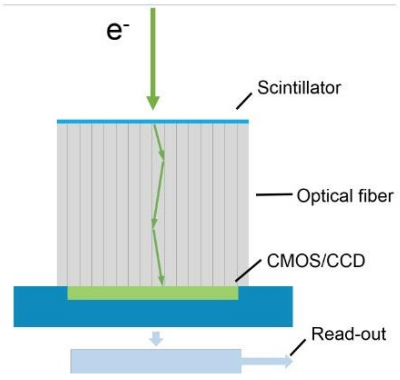

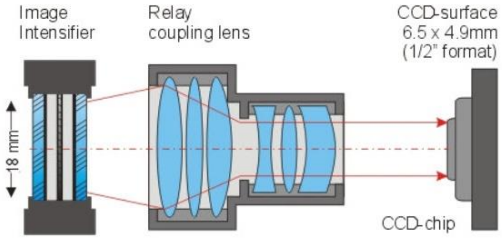

Fiber is very efficient and preserves the camera from ionizing radiation. Needs specialized manufacturing

5.5 Limitations

All the different parameters representing a limiting factor can be translated in an additional ΔT to be added to the minimum response function.

Main aspects

1. Time spread photocathode
2. Energy Spread
3. Time Spread in the Imaging (Ideal+Chromatic)
4. Fringing Fields in deflectors
5. Space Charge

1. The different absorption depth of the photons, the different random paths with collisions spread the response time. The choice of material and geometry can mitigate this effect. Usually this factor counteracts Quantum Efficiency

2. Let's take into account that the transport is not going to increase the energy spread. The intrinsic spread of photoemission (photon bandwidth, collisions, random paths) translates in different velocities, and delay between faster and slower el. Mitigation through very high anode voltage (Mv/m). The energy gained by the electrons makes the spread negligible, and if el. relativistic flattens velocity and turns-off the space charge (another point).

3. We have analyzed the lenses in terms of imaging performances, but we have a further intrinsic problem:
different trajectories bring a different path and time spread. Mitigation is made through limiting aperture of the optic (reduce charge). At least this benefits the aberrations. Chromatic effects also bring further time spread apart from the increase in the PSF.

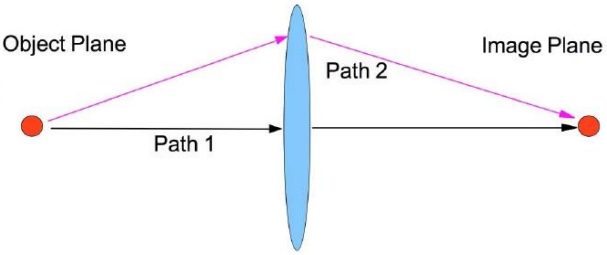

4. The fringing affects the final spot in the image plane, but also the transit time of the el. Again, limiting the aperture can help and also short and shielding of the dispersed field can mitigate the problem.

Space-charge (i.e. Coulomb repulsion/attraction) has a complex and multi-fold effect in the Streak-Camera output. Let's try to analyze the main aspects.

- SC makes harder to extract charge by the PC. It can be seen as an image-charge. This is the first reason to have an extraction field through a high voltage anode.
- SC limits the maximum current through the Child-Langmuir law. Still high voltage anode helps counteracting this effect.
- SC induces a time spread of the pulse. At the same time induces an energy spread which affects (see energy spread) and increase the transit-time spread. Still the anode voltage helps because SC decreases abruptly with the energy.

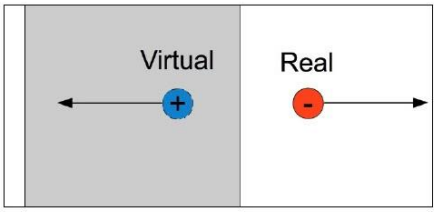

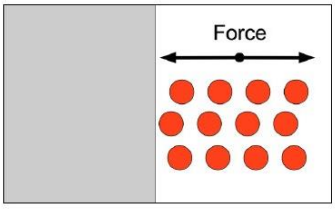

Bibliography

Streak-Cameras

- P.A. Jannimagi,
- Bin Li et al.,*Design of a sub 100-fs X-ray streak camera,* CLF Ann. Report 2007/08, pg. 85-89
- C.B. Johnson et al., *Circular-scan streak tube with solid-state readout*, Applied Optics, Vol.19 No. 20 (1980)

Charged Particle Optics

- D. Heddle, *Electrostatic Lens Systems*, IOP Publishing
- A.B. El-Kareh, *Electron Beam, Lenses, and Optics*, Academic Press
- J.W. Mayer, E. Rimini, *Ion Beam Handbook for Material Analysis*, Academic Press

Photoemission

- W. Spicer, A. Herrera-Gomez, *Modern Theory and Applications of Photocathodes*, SLAC-PUB-6306
- A.H. Sommer, *Photoemissive Materials*, Wiley

Particle Beam Dynamics

- M. Reiser, *Theory and Design of Charged Particle Beams*, Wiley

PowerLaPs

Innovative Education & Training in High Power Laser Plasmas

Laser plasma diagnostics - Theory and Experiments

Chapter 6: Ultrafast laser pulses characterization for applications

Í. J. Sola

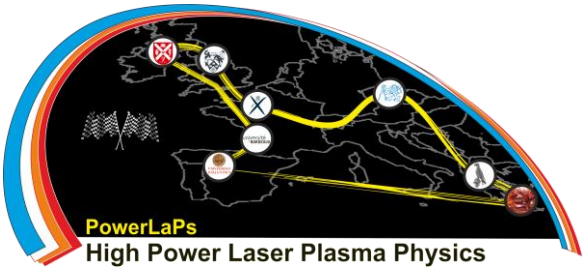

6 Ultrafast laser pulses characterization for applications

6.1 Introduction

The recent advances obtained in the development of ultrafast pulsed lasers have contributed decisively in a large number of fields (atomic and molecular physics, plasmas and particle acceleration, chemistry, telecommunication, biophotonics, etc.) Now-a-days, it is possible to generate pulses of light with a few femtoseconds (10^{-15} s) [1–3] of duration or even shorter, in the attosecond domain (10^{-18} s) [4], being the shortest events ever generated and measured by humans. These ultrafast pulses are, on one hand, an exceptional tool for exploring the fastest processes of nature [5,6], e.g., electronic dynamics in atoms, how chemical reactions and bonds are produced or knowing how materials react to disturbances. On the other hand, the ability to accumulate significant amounts of energy in extremely short time periods allows the interaction with matter at multiple levels: from changing the properties of light (non-linear processes) to accelerate particles and induce nuclear reactions, including micro- and nano- processing of materials (industrial, medical, biological applications, etc.), control and induction of processes, telecommunications, etc.

Thus, the knowledge of the ultrafast pulses and their characteristics (time duration and structure) has become essential in all the experiments and applications involving those light bursts. Accordingly, during the last decades, the development of a broad range of systems for the reconstruction of ultrafast pulses has evolved in parallel to the generation and applications of these pulses. In the present lecture we will firstly introduce the fundamentals of ultrashort pulse characterisation and, secondly, we will review some of the main pulse characterisation techniques, highlighting their concepts, capabilities and their range of application in experiments.

The present document shows a schematic overview of the two sessions, not intending to be a comprehensive review of the lecture content but an index of some of the main ideas.

6.2 Ultrafast pulses

Ultrafast pulses can be represented on both, time and spectral domain [7–9]. Eq. (1) represents a pulse in the time domain:

$$E(t) = \sqrt{I(t)}\exp\left[i(\omega_0 t - \varphi(t))\right] \tag{1}$$

where I(t) is the time evolution of the intensity, ω_0 is the carrier frequency and φ(t) the time phase. Thus, the pulse evolution is defined not only by I(t), but also by the time phase. In fact, the instantaneous frequency of the pulse depending on time can be defined as

$$\omega_{INST}(t) = \frac{d\left[\omega_0 t - \varphi(t)\right]}{dt} = \omega_0 - \frac{d\varphi(t)}{dt} \tag{2}$$

Therefore, if a pulse presents a time phase constant on time, the instantaneous frequency stays constant along the pulse duration.

On the other hand, the pulses can be described in the spectral domain:

$$E(\omega) = \sqrt{S(\omega)}\exp\left[-i\varphi(\omega)\right] \tag{3}$$

where S(ω) is the spectral intensity and φ(ω) the spectral phase.

Both representations (Eq. (1) and (2)) are linked by the Fourier Transform and its inverse

$$E(\omega) = \int_{-\infty}^{\infty} E(t)\, e^{-i\omega t} dt \tag{4}$$

$$E(t) = \frac{1}{2\pi}\int_{-\infty}^{\infty} E(\omega)\, e^{i\omega t} d\omega \tag{5}$$

Thus, for a complete description of the pulse it is needed the amplitude and the phase in one domain. By means of the Fourier Transform or its inverse, the description in the other can be obtained straightforward.

In the spectral domain, the spectral phase can be written as a Taylor expansion around the central wavelength ω_0:

$$\varphi(\omega) = \varphi(\omega_0) + \tau_g(\omega_0)(\omega - \omega_0) + \frac{GDD(\omega_0)}{2!}(\omega - \omega_0)^2 + \frac{TOD(\omega_0)}{3!}(\omega - \omega_0)^3 + \ldots \tag{6}$$

where $\tau_g(\omega_0)$ stands for the first derivative of the spectral phase, the Group Delay Dispersion (GDD) is the second derivative and the Third Order Dispersion (TOD) is the third derivative. The quadratic component (GDD) and superior (TOD, fourth order dispersion FOD, etc.) are the responsible of the pulse distortion from the Fourier limit. For example, the GDD affects to the time pulse mainly as a time broadening, while the TOD creates post- or pre-pulses (it depends on the TOD sign) around the main one. Due to the material dispersion, the laser pulses propagating through it acquires spectral phase, distorting the time pulse form.

6.3 Autocorrelation

Due to the limitations on time response of the electronic devices, the best alternative to perform pulse measurements on a femtosecond range is to use optical techniques, where the light pulses are compared to a reference one, typically itself. One of the first approaches to fs pulse measurements was the autocorrelation [10]. Generally, in a first stage, two replica of the test pulses are obtained by means of an interferometer set-up, where time delay among both can be controlled by introducing or extracting optical path at one interferometer arm. Secondly, both pulses are specially overlapped into a nonlinear medium so, only if also there is some time overlapping among the replica, a nonlinear signal appears. Therefore, the nonlinear signal shows the time delays where both pulses "feel" each other. Mathematically, this can be written as the autocorrelation of the pulse. Finally, the nonlinear signal is detected (e.g., by a photodiode).

Depending on the optical set-up and the nonlinear type of interaction (e.g., second harmonic generation –SHG-, third harmonic generation –THG-, etc.), several types of autocorrelators can be found, e.g.,:

- Intensity autocorrelator (SHG). Typically, but not exclusively, the two replica cross into the nonlinear medium following non-collinear paths. Because of the momentum conservation, the nonlinear signal (SHG) appears at the angle bisector. In this geometry, the nonlinear signal depending on the arm delay time presents the form of the autocorrelation of the pulse intensity.
- Interferometric autocorrelator (SHG). Both replica follow a collinear path, so the nonlinear signal shows an interference pattern.
- THG autocorrelator. The nonlinear medium generates a third order signal or, alternatively, a first nonlinear medium is used for generating second harmonic, which is overlapped with fundamental radiation within a second nonlinear medium where a sum of frequency happens, appearing the third harmonic. This kind of autocorrelators presents less ambiguities and typically are used to study the ns and ps range pedestal of the pulse, an important issue for high intensity experiments.

In general, the autocorrelation techniques give limited information concerning the time pulses:

- Since different pulse forms present the same autocorrelation, no exact information concerning the pulse structure can be extracted. In the same sense, no accurate information concerning the phase (spectral or time) can be obtained, but an estimation.
- They give a rough idea of the pulse duration. Since the autocorrelation width depends on the pulse actual form, and that remains unknown, the exact value of the pulse duration depends on the pulse form guess. Therefore, the technique provides an estimation of the pulse duration.
- Some aspect of the pulse structure, as the presence of satellite pulses or pedestal can be glimpsed in an autocorrelation figure.

6.4 FROG

The Frequency-resolved Optical Gating (FROG) technique [8,11] can be considered as an evolution of the autocorrelators. In general, it conserves the geometry of an autocorrelator but replacing the nonlinear signal intensity detector (e.g., a photodiode) by a spectrometer. Therefore, the autocorrelation signal is wavelength resolved. This additional information has been proven to be sufficient to give more information concerning the pulse and its phase. In fact, optical gating is performed over the test pulse, since the spectrum of a part of the pulse, selected by the optical gate, can be observed. Therefore, information concerning the spectral phase can be obtained. However, in order to extract it from the raw data, iterative procedure is needed [8,11–13].

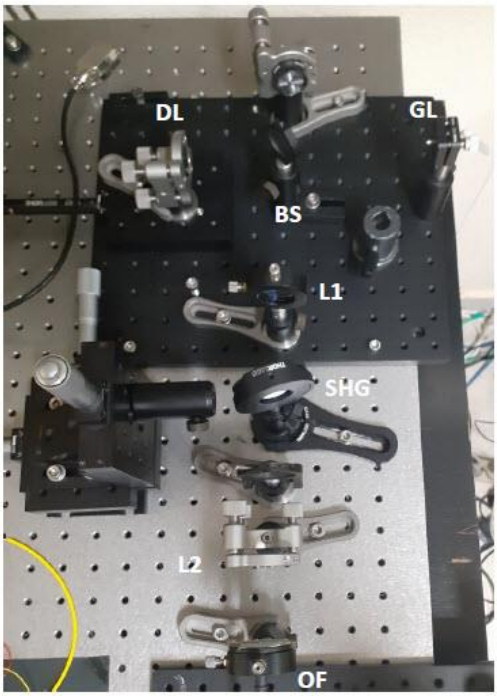

Figure 1. A FROG set-up implementation [14] *for characterisation of pulses delivered by an erbium doped fibre laser in mode locking regime, emitting in the 1550 nm – 1650 nm spectral region. The light goes out the optical fibre by a GRIN lens (GL), which collimates the beam. A beam splitter (BS) divides the beam into two arms. In one of them, a motorised delay line (DL) introduces the delay among the two interferometer arm. By means of a convergent lens (L1), they overlap no collinearly inside a SHG crystal (SHG). The nonlinear signal generated by both replicas is focused by a second lens (L2) onto an optical fibre (OF) and analysed by a spectrometer (not in the figure).*

Some FROG technique characteristics and capabilities are:

- Spectral amplitude and phase can be obtained, obtained an almost complete pulse reconstruction.
- Few cycle pulses can be characterised.
- Some ambiguities in the phase reconstruction appear:
    - The zero order component of the dispersion, also known as the Carrier-Envelope Phase (CEP), which shows the relation between the carrier oscillations and the pulse envelope, remains unknown. This issue is common to most of the reconstruction techniques.
    - In the systems based on the SHG nonlinear process there is an ambiguity concerning the sign of the spectral phase what means, in the time domain, to ignore the time arrow direction. However, additional FROG measurements can be used to solve this ambiguity. Some THG based FROGs do not present such ambiguity.
- Because of the need of an iterative algorithm to reconstruct the pulses, the pulse measurement requires some computation time apart from the raw data acquisition. However, fast algorithms have been developed in order to give very quick reconstructions [13].

6.5 SPIDER

The Spectral Phase Interferometry for Direct Electric-field Reconstruction (SPIDER) [15] is a reconstruction technique based on the Fourier Transform Spectral Interferometry. The later uses a known pulse (reference) at a certain time delay of the pulse to measure (test). The resulting spectrum exhibits an interferential pattern, as it can be theoretically understood from the resulting spectral intensity of the superposition of the two delayed fields:

$$S(\omega) = \left|E(\omega) + E_{Ref}(\omega)\, e^{-i\omega\tau}\right|^2 = \left|E(\omega)\right|^2 + \left|E_{Ref}(\omega)\right|^2 + 2\left|E(\omega)\, E_{Ref}(\omega)\right| \cos\left[i(\phi_\omega(\omega) - \phi_\omega^{Ref}(\omega) + i\tau\omega)\right] \quad (7)$$

where $E(\omega)$ is the test pulse field with spectral phase $\phi_\omega(\omega)$, $E_{Ref}(\omega)$ is the reference pulse field with spectral phase $\phi_\omega^{Ref}(\omega)$ and τ is the delay among both pulses. Just by a Fourier Transform based algorithm, e.g. the commented in [16], it is possible to extract the test pulse spectral phase. This is a well-known technique, used at different research fields and applications in order to study a certain physical system by comparing a reference pulse with the changes induces into the spectral phase of a probe pulse passing through the system under study. However, in order to characterise a certain pulse, a reference is needed. Please note that if the reference pulse is taken to be the test pulse itself, in Eq. 7 the information concerning the spectral phase disappears from the cosine argument.

In order to overcome this limitation, the SPIDER technique interferes a certain test pulse with a replica of itself delayed τ on time and showing a spectral shearing of $\delta\omega$. Thus, the new interference expression becomes

$$S(\omega) = \left|E(\omega) + E(\omega+\delta\omega)\, e^{-i\omega\tau}\right|^2 = \left|E(\omega)\right|^2 + \left|E\ (\omega+\delta\omega)\right|^2 + 2\left|E(\omega)\, E\ (\omega+\delta\omega)\right| \cos\left[i(\phi_\omega(\omega) - \phi_\omega(\omega+\delta\omega) + i\tau\omega)\right] \quad (8)$$

Now, the information about the pulse spectral phase remains in the cosine argument. By applying the above commented reconstruction algorithm, it is possible to extract the spectral phase. Then, by combining it to the spectral amplitude, it is possible to obtain the time domain pulse description via Fourier Transform.

SPIDER presents the following characteristics:

- It allows to recover the phase without iterative retrievals so, in principle, is faster than FROG
- The set-ups are typically quite complex because of the need of introducing both, τ and $\delta\omega$.
- The technique is well suited for reconstructing pulses no very far from the Fourier limit conditions. Few cycle pulses can be characterised.
- No ambiguity concerning the sign of the spectral phase nor the time sense but, on the other hand, the CEP cannot be extracted.

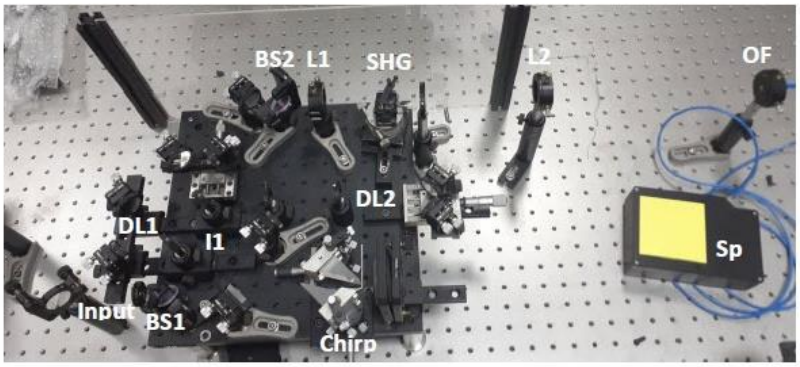

Figure 2. A SPIDER set-up implementation [17] for characterisation of pulses delivered by an Ti:Sa laser in mode locking regime, emitting in the 800 nm spectral region. The pulses are divided into two arms by means of a beam splitter (BS1). A first one passes through a first interferometer, creating two pulse replicas with a time delay controlled by a delay line (DL1). The second arm stretches the pulse by means of a grism set-up (Chirp). Both arms are recombined in a parallel geometry by a beam splitter (BS2). The delay among the arms is controlled by a second delay line (DL2). The two beams are focused no collinearly by a lens (L1) onto a SHG crystal (SHG). The cross nonlinear signal is coupled into an optical fibre (OF) by a lens (L2) and spectrally analysed by means of a spectrometer (Sp).

6.6 Last remarks

The lecture sessions are aimed to present the fundamentals of ultrafast pulses and some of the techniques used to their characterisations. Nowadays, the catalogue of techniques has become very broad, including other strategies [1,18–20]. In addition, since there is an increasing use of pulsed beams with growing complexity, new techniques have been introduced in order to characterize not only the time evolution of the pulsed beams, but also their time evolving polarization [21] or spatio-temporal distributions [22], for example.

References

1. A. Wirth, M. T. Hassan, I. Grguras, J. Gagnon, A. Moulet, T. T. Luu, S. Pabst, R. Santra, Z. A. Alahmed, A. M. Azzeer, V. S. Yakovlev, V. Pervak, F. Krausz, and E. Goulielmakis, "Synthesized Light Transients," Science (80-.). **334**, 195–200 (2011).
2. M. Nisoli, S. De Silvestri, O. Svelto, R. Szipöcs, K. Ferencz, C. Spielmann, S. Sartania, and F. Krausz, "Compression of high-energy laser pulses below 5 fs.," Opt. Lett. **22**, 522–524 (1997).
3. F. Silva, B. Alonso, W. Holgado, R. Romero, J. S. Román, E. C. Jarque, H. Koop, V. Pervak, H. Crespo, and Í. J. Sola, "Strategies for achieving intense single-cycle pulses with in-line post-compression setups," Opt. Lett. **43**, 337 (2018).
4. G. Sansone, E. Benedetti, F. Calegari, C. Vozzi, L. Avaldi, R. Flammini, L. Poletto, P. Villoresi, C. Altucci, R. Velotta, S. Stagira, S. De Silvestri, and M. Nisoli, "Isolated single-cycle attosecond pulses," Science (80-.). **314**, 443–446 (2006).
5. M. Hentschel, R. Kienberger, C. Spielmann, G. A. Reider, N. Milosevic, T. Brabec, P. Corkum, U. Heinzmann, M. Drescher, and F. Krausz, "Attosecond metrology," Nature **414**, 509–513 (2001).
6. P. B. Corkum and F. Krausz, "Attosecond science," Nat. Phys. **3**, 381–387 (2007).
7. C. Rullière, *Femtosecond Laser Pulses: Principles and Experiments* (2003).
8. R. Trebino, *Frequency-Resolved Optical Gating : The Measurement of Ultrashort Laser Pulses* (Kluwer Academic, 2000).
9. B. E. A. Saleh and M. C. Teich, *Fundamentals of Photonics* (Wiley-Interscience, 2007).
10. J. A. Armstrong, "Measurement of picosecond laser pulse widths," Appl. Phys. Lett. **10**, 16–18 (1967).
11. D. J. Kane and R. Trebino, "Characterisation of arbitrary femtosecond pulses using frequency-resolved optical gating," IEEE J. Quantum Electron. **29**, 571–579 (1993).
12. K. W. DeLong, B. Kohler, K. Wilson, D. N. Fittinghoff, and R. Trebino, "Pulse retrieval in frequency-resolved optical gating based on the method of generalized projections," Opt. Lett. **19**, 2152 (1994).
13. D. J. J. Kane, "Recent progress toward real-time measurement of ultrashort laser pulses," IEEE J. Quantum Electron. **35**, 421–431 (1999).
14. M. López-Ripa, "Optical fibre pulsed lasers," MsC Thesis. University of Salamanca (2019).
15. C. Iaconis and I. A. Walmsley, "Spectral phase interferometry for direct electric-field reconstruction of ultrashort optical pulses," Opt. Lett. **23**, 792–794 (1998).
16. L. Lepetit, G. Chériaux, and M. Joffre, "Linear techniques of phase measurement by femtosecond spectral interferometry for applications in spectroscopy," J. Opt. Soc. Am. B **12**, 2467 (1995).
17. A. Sánchez González, "Implementation of a SPIDER system of reconstruction of ultrafast pulses," Msc Thesis. University of Salamanca (2013).
18. V. V. Lozovoy, I. Pastirk, and M. Dantus, "Multiphoton intrapulse interference IV Ultrashort laser pulse spectral phase characterization and compensation," Opt. Lett. **29**, 775 (2004).
19. M. Miranda, T. Fordell, C. Arnold, A. L'Huillier, and H. Crespo, "Simultaneous compression and characterization of ultrashort laser pulses using chirped mirrors and glass wedges," Opt. Express **20**, 688–697 (2012).
20. V. Loriot, G. Gitzinger, and N. Forget, "Self-referenced characterization of femtosecond laser pulses by chirp scan," Opt. Express **21**, 24879 (2013).
21. W. J. Walecki, D. N. Fittinghoff, A. L. Smirl, and R. Trebino, "Characterization of the polarization state of weak ultrashort coherent signals by dual-channel spectral interferometry," Opt. Lett. **22**, 81–83 (1997).
22. C. Dorrer, "Spatiotemporal Metrology of Broadband Optical Pulses," IEEE J. Sel. Top. Quantum Electron. **25**, 1–16 (2019).

PowerLaPs

Innovative Education & Training in High Power Laser Plasmas

Laser plasma diagnostics - Theory and Experiments

Chapter 7: High harmonic generation as a diagnostic for laser contrast using simulations and experiments

M. Yeung

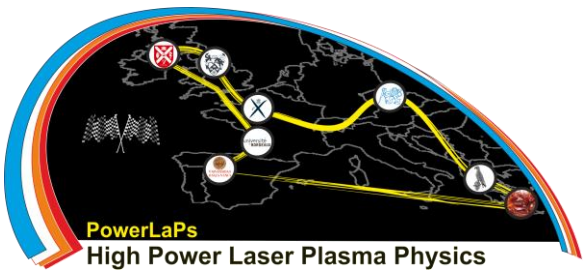

7. High harmonic generation as a diagnostic for laser contrast using simulations and experiments

Overview:

Laser contrast is a key parameter for any high-power laser system as it defines the actual plasma conditions during the main interaction. Extreme ultraviolet radiation produced via high harmonic generation during such interactions are a good benchmark for the preplasma conditions and, hence, the contrast of the driving laser pulse. Signatures are present in the overall efficiency of the various mechanisms and in the fine structure of the spectrum. These give access to details about the plasma in the regime of steep density gradients below λ.

1. Laser contrast

A critical parameter for any high-power laser system, particularly for intense laser-solid interactions, is the contrast of the laser pulse. This is simply the ratio between the peak pulse intensity and the intensity of any light that travels ahead of the main pulse. This can be short prepulses, amplified spontaneous emission or a "shoulder" on the rising edge of the pulse. Figure 1 shows an example contrast trace recorded on a third order autocorrelator.

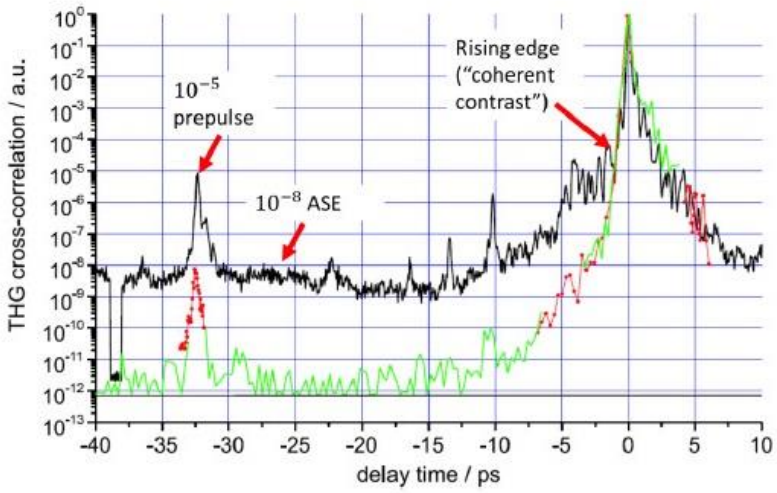

Figure 1 Third order autocorrelator trace of the laser intensity up to 40ps before the main pulse. The black line shows the intrinsic laser contrast and the green line is the contrast after a plasma mirror setup (see section 1.1) The dip at ~ – 38ps is an artefact. Figure taken from [1]

This leading laser radiation can ionise and heat the initially solid density neutral target, which turns into plasma and expands into the vacuum region in front of the surface. This can dramatically alter the nature of the main pulse's interaction. It can be the difference between an interaction with a steep, very dense target to a long, density gradient in front of the surface with a significant amount of underdense plasma. The main parameter used to characterise this "pre-plasma" is the scale length, which is defined as the point in the gradient where the density falls to e^{-1} of the peak electron density. For the relatively steep gradients this lecture is concerned with, this is on the order of a laser wavelength (λ) and below.

1.1 Control of laser contrast

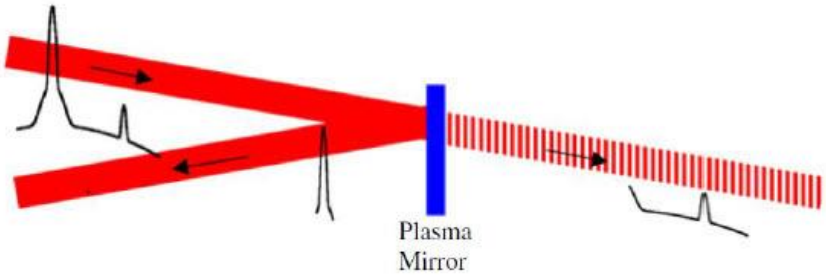

Figure 2 Schematic showing the plasma mirror concept for improving laser contrast. The leading edge of the pulse passes through the anti-reflection coating of the substrate before the main pulse ionises the surface, turning it overdense and hence reflective. The reflected pulse is then "cleaned" of the poor contrast leading edge.

Here we will focus on one main technique for improving the overall contrast of the laser and another technique for introducing a controlled prepulse but note that there are other methods beyond the scope of this lecture.

In figure 2, the use of a plasma mirror as an ultrafast optical switch to improve laser contrast is illustrated. Antireflection (AR) coatings on a glass substrate transmit the lower intensity prepulse/ASE radiation that arrives ahead of the main pulse before the high intensity of the main pulse ionises the surface and forms an overdense plasma. This turns the surface highly reflective (typical reflectivities of 70% to 80%) on an ultrafast timescale allowing only the main pulse to be reflected and carry on to the required interaction region [2,3].

The total improvement in contrast depends on the ratio between the reflectivity of the AR coating (typically <1%) to the plasma reflectivity leading to a single plasma mirror providing anywhere

between 2 and 4 orders of magnitude improvement depending on the AR coating specifications and the optical layout.

For many applications, including high harmonic generation, a perfectly step-like plasma density profile is not always ideal so, once we have a high contrast laser pulse, we need a method to introduce a preplasma in a controlled manner. One effective technique is to use a controlled prepulse as illustrated in figure 3. A mirror reflects a small region of the laser beam earlier than the rest. This will then be focused by the same optic as the full beam but to a larger, lower intensity spot (due to diffraction-limits) which arrives at the target early triggering an expanding plasma. The timing, and has the time the plasma has to expand, is controlled by the position of the prepulse mirror.

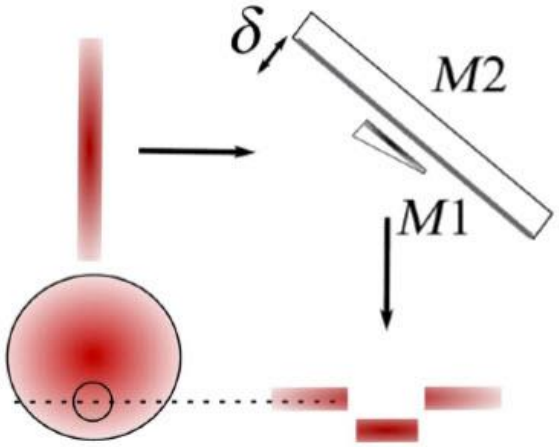

Figure 3 Introducing a controlled prepulse with a small mirror. The laser pulse incident from the left reflects off mirror M2 on its way to the interaction region. A small region of the beam (shown in bottom left cross-sectional view) is, instead, reflected off a smaller mirror M1 placed in front of M2 a distance δ away. The path of the portion of the beam that reflects off M1 will be ahead of the rest of the beam and hence will act as a prepulse whose timing is controlled by varying δ. Figure taken from [4]

2. Attosecond pulse trains

2.1 Time-frequency relationship

The spectral structure of any light pulse is related to the temporal structure of the electromagnetic fields that form the pulse by the Fourier transform. A useful analogy is the relationship between a slit function and the far-field Fraunhofer diffraction pattern that results from diffraction at a slit which can be found by Fourier transforming the slit function. In this case, a top hat slit function results in a sinc^2 function for the angular distribution of the diffracted radiation where the diffraction pattern becomes wider as the slit gets smaller. Likewise, for the spectral domain, a wider frequency bandwidth ($\Delta\nu$) can lead to a shorter pulse (Δt) in the temporal domain according to

$$\Delta\nu\Delta t = \alpha \tag{1}$$

Where α is a constant on the order of unity that depends on the shape of the spectral amplitude function. For a Gaussian function we have $\alpha \approx 0.44$.

This, however, is not the full story. It is not sufficient to have enough bandwidth to support a short pulse, we must also consider the relative phase between different spectral components. A flat phase indicates that all the peaks of each wavelength line up at some point and add together to give a short pulse. In this case, the pulse duration is given by equation (1) and we say the pulse is transform limited.

2.2 Pulse trains and high order harmonics

The output of a laser is not quite as simple as the single pulse discussed so far. We will have a train of pulses separated by the round-trip time of the cavity. In the Fourier domain this will be seen as a frequency comb with a constant frequency spacing. This is analogous to how a diffraction grating relates to a single slit. The diffraction grating pattern will consist of individual diffraction orders with an envelope function determined by the width of each groove. Likewise, a frequency comb in the time domain will (assuming flat phase) be a regularly spaced pulse train as shown in figure 1.

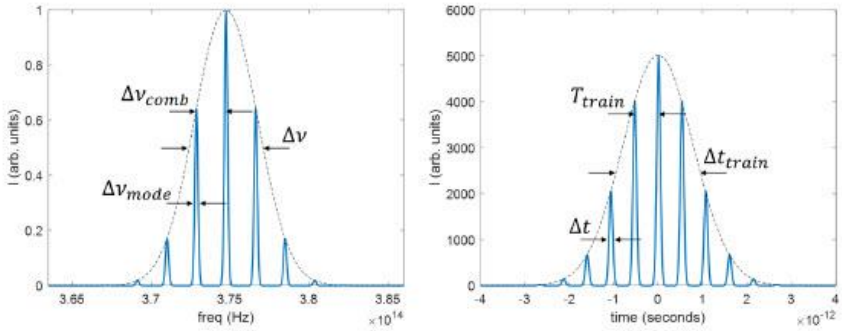

Figure 4 – An equal spacing frequency comb and it's corresponding temporal structure, assuming a flat spectral phase. The width of individual modes and pulses are related to the overall width of the temporal and spectral envelope functions (dashed lines) respectively. The spacing of the frequency comb is also directly related to the spacing of the pulse train.

The spacing of the pulse train will just be the reciprocal of the frequency spacing: $T_{train} = \frac{1}{\Delta\nu_{comb}}$

The width of the envelope function of the frequency comb will be related to the width of each individual pulse according to equation (1) : $\Delta\nu\Delta t = \alpha$ and vice versa for the envelope of the pulse train: $\Delta\nu_{mode}\Delta t_{train} = \alpha$

Harmonics are nothing more than a frequency comb when the spacing of the pulse train is the length of an optical cycle ($T = \lambda/c$). Thus, when we observe harmonics, we know this is the signature of interference of individual attosecond pulses in the same way as a diffraction grating pattern results from interference from individual grooves. This will become important for laser driven XUV sources as the period of the driving laser pattern will result in a series of equally spaced pulses resulting in harmonics that can extend into the XUV regime with an overall broad bandwidth sufficient to support attosecond scale pulses. Any interruption to this equal spacing will modify this harmonic structure, resulting in either a spectral broadening or "splitting" of the individual harmonics due to imperfect interference between successive pulses in the train.

Section 3: High harmonic generation from plasma surfaces

3.1 Intense laser-surface interactions

During very high intensity ($> 10^{18} Wcm^{-2}$) interactions with an initially solid surface we reach a regime where we can effectively assume full ionisation of the target. In this regime, a lot of interesting physics takes place during interactions with initially solid targets which become overdense after ionisation (free electron density greater than the critical density which means the plasma reflects the incident laser).

During these intense interactions, we can also get coherent attosecond XUV radiation emitted in the reflected direction. There are a variety of possible mechanisms [5] but two key contributors are coherent wake emission and the relativistically oscillating mirror.

3.2 Coherent wake emission (CWE)

When the main part of the laser pulse arrives at the target, it will already be ionised due to intense light arriving before the main pulse due the amplified spontaneous emission or prepulses arising in the laser chain. These need only be tiny fractions of the main pulse intensity in order to generate a plasma on the surface of the target. This will then expand to give an exponential density ramp which the main pulse interacts with.

It is the electrons in this plasma ramp that are the key to the CWE mechanism, which can be efficient for intensities starting at $10^{16} Wcm^{-2}$ and for a laser field incident obliquely so that there will be an electric field component normal to the plasma surface. At these intensities, the electrons that are pulled out by the laser field have trajectories that extend significantly into the vacuum region in front of the target. This can be called vacuum heating or the Brunel regime [6].

In an interesting analogy with gas harmonics (although due to a different mechanism) the electrons gain energy in the laser field and return to the plasma density ramp. Here, trajectories of the electrons overlap in space and time inside the ramp and lead to a sharp density spike which is able to strongly perturb the local plasma medium leading to plasma oscillations [7].

These plasma oscillations are then able to couple into electromagnetic modes propagating in the reflected direction. As this process repeats each laser cycle (once per cycle) this radiation is observed as harmonics of the laser frequency. Since the frequency of these plasmas oscillations depends on the electron density via the plasma frequency, different electromagnetic frequencies originate from different parts of the density ramp, resulting in an inherent chirp of the XUV pulse. A critical feature

of this mechanism is then that the maximum XUV frequency observed corresponds to the maximum plasma frequency present in the target which will be given by

$$\omega_m = \sqrt{\frac{n_m}{n_c}}\omega_L \tag{6}$$

Where ω_L is the laser frequency and n_m is the peak electron density. Typical peak densities are about $400n_c$ for a bulk glass target with 800nm laser radiation which corresponds to a maximum CWE harmonic of $\approx 20^{th}$.

3.2.1 Effect of laser contrast on CWE

Unsurprisingly, as a mechanism that relies on plasma oscillations in the density gradient, CWE is dependent on the scale length of the plasma and, hence, on the contrast of the laser. For efficient harmonic generation, CWE requires very clean pulses and scale lengths generally less than $\lambda/10$. Furthermore, the spectral structure of the harmonics is strongly influenced by the scale length.

The origin of this effect is the dependence of the return time of the Brunel bunches on both the instantaneous intensity of the laser and the depth into the density gradient the bunches must travel to trigger the plasma oscillation for a particular harmonic (which is clearly directly dependent on the scale length). The intensity dependence means that, for a typical Gaussian laser intensity temporal profile, the spacing of the individual attosecond pulses will vary during the interaction resulting in imperfect spectral interference (which, as discussed in section 2, is the origin of harmonics) which results in a broadening of the individual harmonics in the spectrum. Fitting the observed width to a simple model allows the scale length to be recovered which has allowed the indirect measurement of scale length on the order of $\lambda/100$ and below [8] which would be extremely challenging to measure directly (scale of a few nms).

3.3 The relativistically oscillating mirror (ROM) mechanism

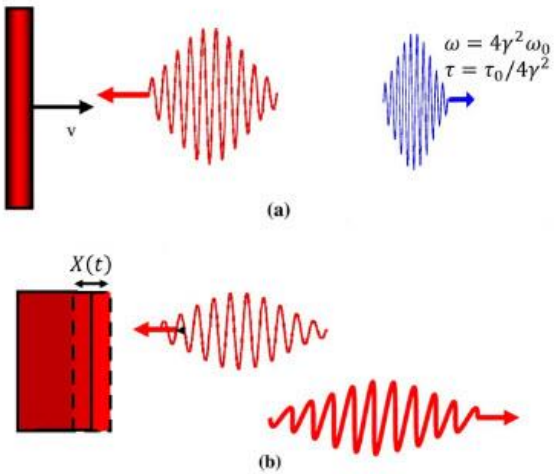

Figure 5 Drawing of (a) a laser pulse upshifted in frequency after reflection from a constant velocity mirror and (b) an oscillating mirror periodically upshifting an incident pulse each laser cycle in a model of the interaction with an overdense plasma at very high intensity [9]

As the intensity of the driving laser is increased beyond $10^{18} W cm^{-2}$, the peak velocity of the electrons approaches the speed of light and relativistic effects become important. Consider the reflection of pulse of light from a perfect reflector counterpropagating with a constant velocity as shown in figure 5. Einstein's relativity theory tells us that the reflected pulse will experience a Doppler upshift in frequency by a factor of $4\gamma^2$ where γ is the Lorentz factor of the mirror. The reflected pulse will also be compressed in time by the same factor.

During the interaction of a laser pulse, the overdense surface can be modelled as a reflector moving periodically with the laser and Doppler upshifting it each cycle but with a time varying velocity. This oscillatory extension to the ideas of Einstein's moving mirror is the ROM model. This model has been supported by the results of both simulations [10] and experimental observations [11]. As the intensity is increased further, this mechanism is seen to dominate the emission.

3.3.1 Effect of laser contrast on ROM

An intense laser pulse can exert a large pressure on the surface of a plasma (radiation pressure). This causes the surface to recede with a velocity that is strongly dependent on the laser intensity. Since the intensity varies in space (finite sized focal spot) and time, this will cause the effective point of interaction for the driving of ROM harmonics to also vary.

In the spatial domain this has signatures in the divergence of the observed harmonics. A spatially varying pressure with a maximum at the centre of the laser focal spot will cause denting of the surface leading to an effective curvature which can focus the harmonics close to the surface and dictate the final divergence of the beam [12,13]. A longer scale length will be more easily dented as the lower densities are less able to respond to the pressure of the laser, hence signatures of the laser contrast appear here as well.

The temporal variation of the pressure leads to a variation in the timing of the individual attosecond pulses, in a similar manner to effect of varying intensity on the return time of Brunel bunches for CWE. Similarly, in this case it can lead to a broadening of the harmonics or even lead to splitting of the harmonics when the denting is particularly severe [14]. This surface recession also tends to lead to an overall red shift in the harmonic frequency [13].

Finally, figure 6 shows a scan of prepulse timing from an experiment on the JETI40 Ti:Sapphire laser system showing the transition from very strong CWE and no ROM for very short scale lengths to weak CWE and a maximum ROM signal for a prepulse arriving about 2ps before the main pulse. This is the typical trend for many parameter ranges with some variation depending on target density, angle of incidence and laser intensity. Hence, the clearest property which can indicate the scale length of the target and, hence, the laser contrast is simply the relative efficiency of each mechanism, which can be distinguished by the CWE cut off frequency.

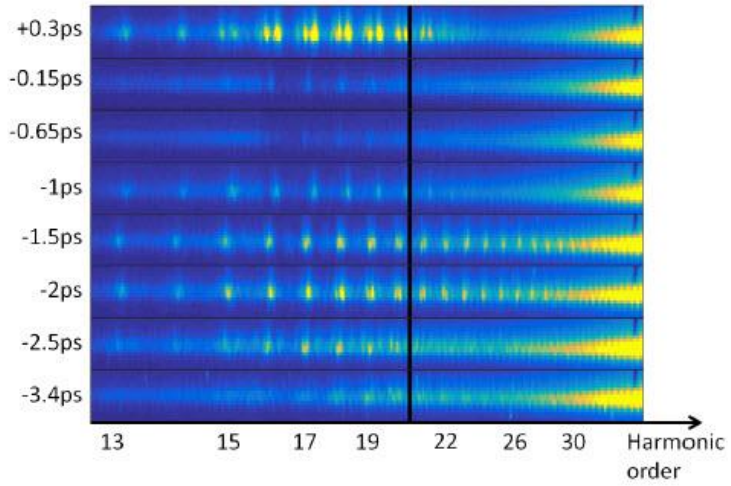

Figure 6 Variation of experimental harmonic spectra for varying prepulse timings (shown on the left). Interaction conditions are 22.5 degrees incidence, 30fs pulse at $\approx 2 \times 10^{19} Wcm^{-2}$. *The black vertical line indicates the CWE cut off frequency. Taken from supplementary information in ref [15]*

References

[1] Rödel *et al.* Appl. Phys B **103**, (2011), 295

[2] Obst *et al.*, Plasma Phys. Control. Fusion, **60**, (2018), 054007

[3] Dromey *et al.* Rev. Sci. Instrum., **75**, (2004), 645

[4] Kahaly *et al.*, PRL **110**, (2013), 175001

[5] Teubner and Gibbon, Rev. Mod. Phys. **81** (2009) 445

[6] Brunel, PRL **59** (1987) 52

[7] Quéré *et al.* PRL **96** (2006) 125004

[8] Malvache *et al.* PRE, **87**, (2013), 035101

[9] M. Zepf *et al.* PPCF **49** (2007) B149

[10] Lichters *et al.* Phys. Plasmas **3** (1996) 3425

[11] Dromey *et al.* PRL **99** (2007) 085001

[12] Dromey *et al.* Nature Phys., **5**, (2009), 146

[13] Vincenti *et al.* Nature Comm., **5**, (2014), 3403

[14] Behmke *et al.* PRL, **106**, (2011), 185002

[15] Yeung *et al.* PRL **115** (2015) 193903

PowerLaPs

Innovative Education & Training in High Power Laser Plasmas

Laser plasma diagnostics - Theory and Experiments

Chapter 8: Atomic physics in plasma diagnostics

M. Benis

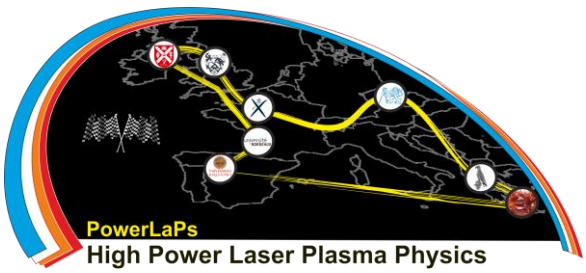

8. 1 Basics on scattering theory

8.1.1 Introduction

In this Chapter, we will provide a brief introduction to the elementary concepts and methodology of scattering theory. The focus lies on the introduction of the description of the scattering process in terms of the Hamiltonian of the scattering projectile at a finite range interaction potential of a single site target by the method of partial waves and the first Born approximation.

8.1.2 Nomenclature

In a typical scattering experiment, a homogeneous well-collimated monoenergetic beam of particles A is colliding with a stationary target containing particles B (the scatterers) as depicted in Fig. 10.17. Particles A can be photons electrons or ions while particles B are usually atoms. Collision experiments are conducted under the condition that each of the particles A collides with only one of the target scaterrers B and this condition will be adopted here (single collision conditions). After the collision particles A are detected by detectors located outside the path of the incident beam.

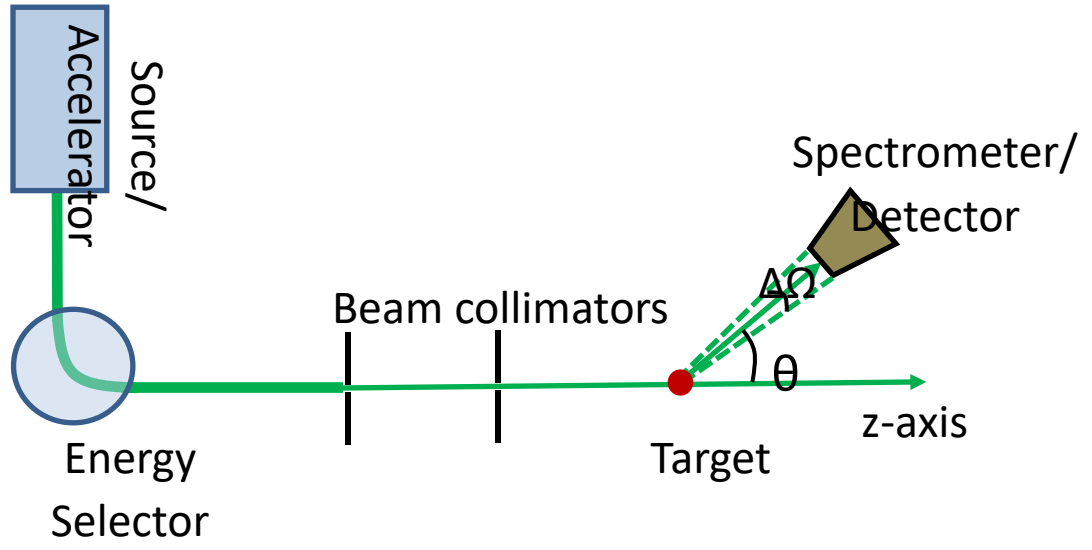

Figure Geometry of a typical scattering experiment.

The collision may result in various final states of the colliders. In this concept we may categorize the processes as

- *Elastic scattering*. The two particles maintain their initial quantum state, i.e.

$$A + B \rightarrow A + B$$

- *Inelastic scattering*. The particles A and/or B change their initial quantum state, for example B left in an excited state B'

$$A + B \rightarrow A + B'$$

- *Reaction*. The collision results into more than two particles, for example a split of particle B in to two particles C and D:

$$A + B \rightarrow A + C + D$$

A *channel* is a possible pathway for a collision system allowed by Quantum Mechanics. However, the various pathways to the final states of a collision depend on the conservations laws (energy, momentum, angular momentum, etc.). A channel is termed *open* for a collision if it is allowed by all the conservation laws, otherwise it is termed *closed*. For example, let us assume the collision of an electron beam with atomic hydrogen. For incidence kinetic energies T < 10.2 eV only the elastic scattering channel is open, i.e.

$$e + H(1s) \rightarrow H(1s) + e$$

Increasing the collision energy to values of 10.2 ≤ T < 13.6 eV the excitation channels to excited hydrogen states are open, i.e.

$$e + H(1s) \rightarrow [H(nl)]^* + e$$
$$e + H(1s) \rightarrow [H(nl)]^* + e$$

Finally, for collision energies T > 13.6 eV the ionization channel opens i.e.

$$e + H(1s) \rightarrow H^+ + e + e$$

The most important measured parameter in collision experiments is the *cross section*. It provides all the necessary information for the experimental feasibility of a certain channel and it is the outcome of the corresponding theoretical calculation. Theoretical results and measurements are compared on the grounds of cross sections. Under the above experimental conditions, and for the case of elastic scattering, we assume a flux of N incident particles[1] on a target of length L having n scatterers per unit volume. Then the elastically scattered flux is dN' to a unit solid angle $d\Omega$ around the scattering angle θ will be

$$dN' = NnL\sigma(\theta, \varphi)d\Omega$$

The proportionality quantity $\sigma(\theta, \varphi)$ is called *differential cross section* and is denoted as

$$\sigma(\theta, \varphi) \equiv \frac{d\sigma}{d\Omega}(\theta, \varphi)$$

By integrating the differential cross section in all angles, results in the total cross section σ or simply cross section. Cross section has units of area and for Atomic

[1] Number of incident particles crossing perpendicular a unit area per unit time.

Physics it is measured in cm^2. Typical cross section values for ion-atom collision lie in the region of $10^{-16} - 10^{-21}\ cm^2$.

In the more general case of inelastic collision where reaction channels are open a more general definition for the cross section can be imposed. Thus, *the cross section for a certain channel is defined as the ratio of the number of events corresponding to the channel per unit time and per unit scatterer, to the flux of the incident particles with respect to the target*. Connecting this experimental approach of definition to its theoretical equivalent we may also state that *the cross section for a certain channel is defined as the transition probability per unit time, per unit scatterer and per unit flux of the incident particles with respect to the target*.

It is also of interest to mention that since differential cross section depends on the scattering angles, its value will depend on the coordinate system, i.e. laboratory of centre of mass. Theoretical results, usually carried out in center of mass system, have to be transformed to the laboratory system for comparison to the experimental results and vice versa.

8.1.3 Potential scattering

In this chapter we shall examine the simplest collision problem, that of a non-relativistic scattering of a spinless particle by a potential $V(r)$. For a real and independent of time potential $V(r)$ the Schrödinger equation is written as

$$\left[-\frac{\hbar^2}{2m}\nabla^2 + V(\boldsymbol{r})\right]\psi(\boldsymbol{r}) = E\psi(\boldsymbol{r})$$

The well defined energy E of the particle is

$$E = \frac{p^2}{2m} = \frac{\hbar^2 k^2}{2m}$$

where k is the wave vector of the particle. Then, after introducing the reduced potential

$$U(\boldsymbol{r}) = \frac{2m}{\hbar^2}V(\boldsymbol{r})$$

The first can be written in the form of

$$[\nabla^2 + k^2 - U(\boldsymbol{r})]\psi(\boldsymbol{r}) = 0$$

In the general and realistic case where the potential $V(\boldsymbol{r})$ vanishes faster than $1/r$, and is reduced to a free-particle Schrödinger equation, i.e.

$$[\nabla^2 + k^2]\psi(\boldsymbol{r}) = 0$$

In this case, i.e. for large distances away from the scattering center, the wavefunction of the scattered particle $\psi_{\boldsymbol{k}}(\boldsymbol{r})$ can be written as the sum of an incident wave $\psi_{inc}(\boldsymbol{r})$ and a scattered wave $\psi_{sc}(\boldsymbol{r})$ as

$$\psi_{\boldsymbol{k}}(\boldsymbol{r}) \sim \psi_{inc}(\boldsymbol{r}) + \psi_{sc}(\boldsymbol{r})$$

Then, the incident beam can be represented by a plane wave since the beam is monoenergetic and propagating towards the direction $\boldsymbol{k}$, along the z axis, therefore

$$\psi_{inc}(\boldsymbol{r}) \sim e^{i\boldsymbol{k}\boldsymbol{r}} \sim e^{ikz}$$

It should be cleared out here that even though a plane wave has infinite wavefront it is appropriate for describing a well collimated particle beam. The reason is that the beam's extent, typically a few mm, is orders of magnitude larger than the atomic dimensions where the scattering process takes place and thus can be considered as having a comparatively infinite extent.

The scattered wavefunction at large distances away from the scattering center should represent an outward flaw of particles originating from the scattering center. This can be described by an outgoing spherical wave the amplitude of which is reduced according to the spherical geometry, thus

$$\psi_{sc}(\boldsymbol{r}) \sim f(k,\theta,\varphi)\ \frac{e^{ikr}}{r}$$

where (θ,φ) are the polar angles with respect to the z axis and $f(k,\theta,\varphi)$ the very important quantity termed *scattering amplitude*. Therefore, the total wavefunction of the collision process for large distances away from the scattering center can be written as

$$\psi_{\boldsymbol{k}}(\boldsymbol{r}) = A\left[e^{ikz} + f(k,\theta,\varphi)\ \frac{e^{ikr}}{r}\right]$$

where A is a normalization constant and the asymptotic solution for the free-particle Schrödinger equation or in other words the asymptotic boundary condition.

It can be proven that the scattering amplitude $f(k,\theta,\varphi)$ is related to the differential cross section by the formula

$$\frac{d\sigma}{d\Omega}(\theta,\varphi) = |f(k,\theta,\varphi)|^2$$

and this is the reason why it is the most important parameter in the study of a scattering process. Its determination is not straightforward, especially in cases of inelastic scattering and reactions. Next, we shall present two popular approaches for the determination of the scattering amplitude in potential scattering.

8.1.4 The partial waves expansion

We shall consider the case of a central potential, i.e. a potential $V(r)$ that depends only on the magnitude of the vector $\boldsymbol{r}$. In centrally symmetric potentials the scattering wavefunction, $\psi(\boldsymbol{r}) = \psi(r, \theta, \varphi)$, as well as the scattering amplitude $f(k, \theta, \varphi)$ must be symmetrical about the axis of incidence (z axis), and hence independent of the azimuthal angle, φ. The method of partial wave expansion is inspired by the observation that a plane wave $e^{i\boldsymbol{kr}}$ can actually be written as a sum over spherical waves

$$e^{i\boldsymbol{kr}} = e^{ikr\cos\theta} = \sum_{l=0}^{\infty}(2l+1)i^l j_l(kr)P_l(\cos\theta)$$

where the radial functions $j_l(kr)$ are the spherical Bessel functions and the angular function $P_l(cos\,\theta)$ are the Legendre polynomials connected to the spherical harmonics $Y_{lm}(\theta)$ as $P_l(cos\,\theta) = \sqrt{4\pi/(2l+1)}\; Y_{l0}(\theta)$. Each term in the series is known as a *partial wave*. Following standard spectroscopic notation, l = 0, 1, 2, ...they are referred to as s, p, d, ... waves.

For centrally symmetric potentials the Hamiltonian operator $H = -\frac{\hbar^2}{2m}\nabla^2 + V(r)$, commutes with the angular momentum operators $\boldsymbol{L}^2$ and L_z and thus the Schrödinger equation is separable in spherical coordinates. Therefore, the wavefunction can be expanded in a similar way to the plane waves as

$$\psi_{\boldsymbol{k}}(\boldsymbol{r}) = \psi(k, r, \theta) = \sum_{l=0}^{\infty}(2l+1)i^l R_l(k,r)P_l(\cos\theta)$$

The radial wavefunctions $R_l(k,r)$ are determined by the solution of the radial Schrödinger equation

$$\left[\frac{d^2}{dr^2} + \frac{2}{r}\frac{d}{dr} - \frac{l(l+1)}{r^2} - U(r) + k^2\right]R_l(k,r) = 0$$

Since in the radial wavefunction has to fulfill the asymptotic boundary condition its asymptotic solution will result from the solution of the radial Schrödinger equation

$$\left[\frac{d^2}{dr^2} + \frac{2}{r}\frac{d}{dr} - \frac{l(l+1)}{r^2} + k^2\right]R_l(k,r) = 0$$

whose solutions are the spherical Bessel functions, similar to the plane wave expansion. The main difference to the plane wave is that the outgoing spherical wave will suffer a phase shift $\delta_l(k)$ that depends on the scattering potential and is recorded in the radial wavefunction. After some lengthy algebra, it can proven that the scattered wave function outside the interaction region, i.e. at large distances, is written as

$$\psi_{sc}(\boldsymbol{r}) = \left[\frac{1}{2ik}\sum_{l=0}^{\infty}(2l+1)\{\exp[2i\delta_l(k)]-1\}P_l(\cos\theta)\right]\frac{e^{ikr}}{r}$$

Thus, the scattering amplitude is straightforwardly obtained as

$$f(\theta) = \frac{1}{2ik}\sum_{l=0}^{\infty}(2l+1)\{\exp[2i\delta_l(k)]-1\}P_l(\cos\theta)$$

and the total cross section is estimated as

$$\sigma = \int \frac{d\sigma}{d\Omega}(\theta,\varphi)d\Omega = \int |f(k,\theta,\varphi)|^2 d\Omega = \frac{4\pi}{k^2}\sum_{l=0}^{\infty}(2l+1)sin^2\delta_l$$

The partial wave expansion method is an accurate method in the sense that if all the partial waves are taken into consideration then the result will be accurate. However, a realistic inclusion of many partial waves is a cumbersome task. Thus, the method is preferably useful in problems involving a few partial waves, a condition that corresponds to low energy collisions.

8.1.5 The Born approximation

We rewrite the Schrödinger equation as

$$(\nabla^2 + k^2)\psi_{\boldsymbol{k}}(\boldsymbol{r}) = U(\boldsymbol{r})\psi_{\boldsymbol{k}}(\boldsymbol{r})$$

in order to explicitly include the wavefunction dependence on the wave vector k. The general solution can be written in an integral form known as the *Lippmann-Schwinger equation*

$$\psi_{\boldsymbol{k}}(\boldsymbol{r}) = \Phi_{\boldsymbol{k}}(\boldsymbol{r}) + \int G_0(k,\boldsymbol{r},\boldsymbol{r}')U(\boldsymbol{r}')\,\psi_{\boldsymbol{k}}(\boldsymbol{r}')d\boldsymbol{r}'$$

where $\Phi_{\boldsymbol{k}}(\boldsymbol{r})$ is the solution for the homogeneous equation

$$(\nabla^2 + k^2)\Phi_{\boldsymbol{k}}(\boldsymbol{r}) = 0$$

that is the known plane wave $e^{i\boldsymbol{kr}}$, and $G_0(k,\boldsymbol{r},\boldsymbol{r}')$ is the *Green's function* satisfying the equation

$$(\nabla^2 + k^2)G_0(k,\boldsymbol{r},\boldsymbol{r}') = \delta(\boldsymbol{r}-\boldsymbol{r}')$$

Requiring that the wavefunction $\psi_{\boldsymbol{k}}(\boldsymbol{r})$ describes outgoing scattering waves, the Green's function can be obtained as

$$G_0(k,\boldsymbol{r},\boldsymbol{r}') = -\frac{1}{4\pi}\frac{e^{ik|\boldsymbol{r}-\boldsymbol{r}'|}}{|\boldsymbol{r}-\boldsymbol{r}'|}$$

which indeed describes outgoing waves generated at the point $\boldsymbol{r}'$ and approximating spherical waves of the form of Eq. 10.65 for large $|\boldsymbol{r}|$, i.e. for $|\boldsymbol{r}| \gg |\boldsymbol{r}'|$, as depicted in Fig.

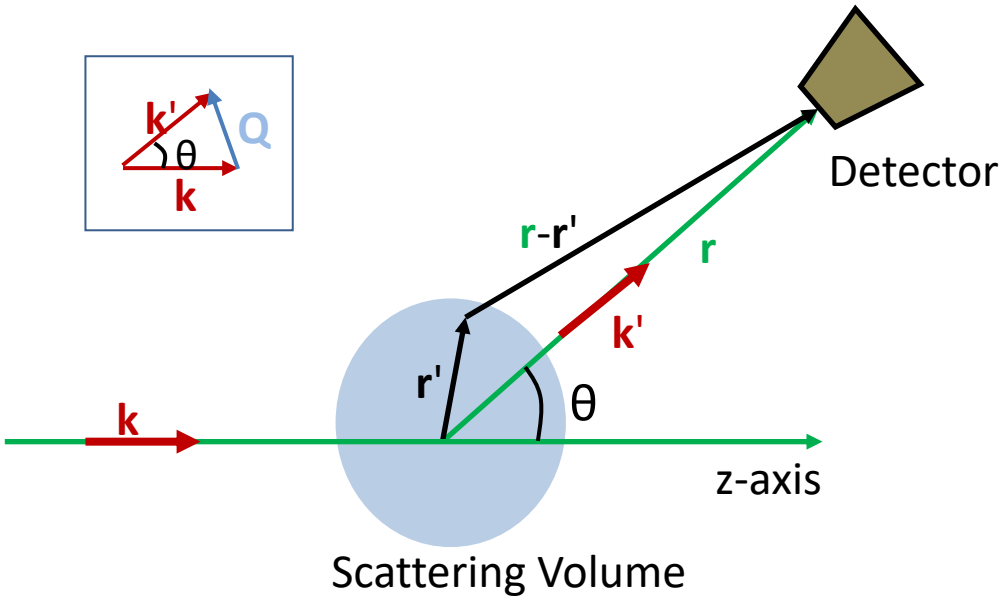

Figure Scattering geometry corresponding to the outgoing waves described by the Green's function.

Then the final form of the integral equation is written as

$$\psi_{\boldsymbol{k}}(\boldsymbol{r}) = e^{i\boldsymbol{k}\boldsymbol{r}} - \frac{1}{4\pi}\int \frac{e^{ik|\boldsymbol{r}-\boldsymbol{r}'|}}{|\boldsymbol{r}-\boldsymbol{r}'|} U(\boldsymbol{r}')\,\psi_{\boldsymbol{k}}(\boldsymbol{r}')d\boldsymbol{r}'$$

which in the asymptotic form of $|\boldsymbol{r}| \to \infty$ (after approximating $\frac{e^{ik|\boldsymbol{r}-\boldsymbol{r}'|}}{|\boldsymbol{r}-\boldsymbol{r}'|} \to \frac{e^{ikr}}{r} e^{-i\boldsymbol{k}'\boldsymbol{r}'}$, where $\boldsymbol{k}' = k\hat{\boldsymbol{r}}$) is reduced to

$$\psi_{\boldsymbol{k}}(\boldsymbol{r}) = e^{i\boldsymbol{k}\boldsymbol{r}} - \frac{1}{4\pi}\frac{e^{ikr}}{r}\int e^{-i\boldsymbol{k}'\boldsymbol{r}'} U(\boldsymbol{r}')\,\psi_{\boldsymbol{k}}(\boldsymbol{r}')d\boldsymbol{r}'$$

Thus, we obtain the scattering amplitude as

$$f(\theta,\varphi) = -\frac{1}{4\pi}\int e^{-i\boldsymbol{k}'\boldsymbol{r}'} U(\boldsymbol{r}')\,\psi_{\boldsymbol{k}}(\boldsymbol{r}')d\boldsymbol{r}'$$

However, the solution is still not reached since the wavefunction $\psi_{\boldsymbol{k}}(\boldsymbol{r})$ is unknown. Its solution can be obtained in a series of iterations. Indeed, starting from an incident plane wave as the zeroth order approximation then the next iterations are structured as follows

$$\psi_{\boldsymbol{k}}^{(0)}(\boldsymbol{r}) = e^{i\boldsymbol{k}\boldsymbol{r}}$$

$$\psi_{\boldsymbol{k}}^{(1)}(\boldsymbol{r}) = e^{i\boldsymbol{k}\boldsymbol{r}} - \frac{1}{4\pi}\frac{e^{ikr}}{r}\int e^{-i\boldsymbol{k}'\boldsymbol{r}'}U(\boldsymbol{r}')\,\psi_{\boldsymbol{k}}^{(0)}(\boldsymbol{r}')d\boldsymbol{r}'$$

$$\psi_{\boldsymbol{k}}^{(2)}(\boldsymbol{r}) = e^{i\boldsymbol{k}\boldsymbol{r}} - \frac{1}{4\pi}\frac{e^{ikr}}{r}\int e^{-i\boldsymbol{k}'\boldsymbol{r}'}U(\boldsymbol{r}')\,\psi_{\boldsymbol{k}}^{(1)}(\boldsymbol{r}')d\boldsymbol{r}'$$

$$\psi_{\boldsymbol{k}}^{(n)}(\boldsymbol{r}) = e^{i\boldsymbol{k}\boldsymbol{r}} - \frac{1}{4\pi}\frac{e^{ikr}}{r}\int e^{-i\boldsymbol{k}'\boldsymbol{r}'}U(\boldsymbol{r}')\,\psi_{\boldsymbol{k}}^{(n-1)}(\boldsymbol{r}')d\boldsymbol{r}'$$

This approach is actually a perturbation expansion in powers of the interaction potential $U(\boldsymbol{r})$ known as the *Born expansion* or *Born series*. The first order term $\psi_{\boldsymbol{k}}^{(1)}(\boldsymbol{r})$ is the *first Born approximation* or simply *Born approximation*, resulting for the scattering amplitude in

$$f^{(1)}(\theta,\varphi) \equiv f_{B1} = -\frac{1}{4\pi}\int e^{-i(\boldsymbol{k}-\boldsymbol{k}')\boldsymbol{r}'}U(\boldsymbol{r}')\,d\boldsymbol{r}'$$

It is interesting to note that the quantity $\boldsymbol{k}-\boldsymbol{k}'=\boldsymbol{Q}$ is the momentum transfer as depicted in Fig. and that the scattering amplitude is the Fourier transform of the potential.

The physical meaning behind the Born series is that each term corresponds to a scattering process inside the scattering volume. The zeroth order corresponds to no scattering, the first order to a single scattering process, and the second order to a double scattering process and so on and so forth. Usually higher orders that the first require arithmetical approaches and even though the convergence is not guaranteed depending on the potential and the collision energy. Thus, only the first Born approximation is taken into account which gives good results for high collision energies and weak potentials as expected.

8.1.6 Electron-atom collisions

In this last subsection, we will describe the approach on a realistic problem that of an electron beam colliding with an atom. We shall examine the elastic scattering from a hydrogen atom for simplicity. Let us call electron 1 the electron of the beam and electron 2 the electron of the atom in its ground state. Then the asymptotic wavefunction for $|\boldsymbol{r}_1| \gg |\boldsymbol{r}_2|$ of the system is written as

$$\psi_{\pm}(\boldsymbol{r}_1,\boldsymbol{r}_2) \sim F_1^{\pm}(\boldsymbol{r}_1)\psi_{100}(\boldsymbol{r}_2)$$

where $\pm$ corresponds to the singlet (+) and triplet (-) spin states of the two electron system. The function $F_1^{\pm}(\boldsymbol{r}_1)$ is the known scattering wavefunction of Eq. 10.66

$$F_1^{\pm}(\boldsymbol{r}_1) = e^{ik_1 z} + f_1^{\pm}(k_1,\theta,\varphi)\,\frac{e^{ik_1 r_1}}{r_1}$$

Due to the symmetry of the wavefunction it can also be written as (interchanging $\boldsymbol{r}_1$ and $\boldsymbol{r}_2$ should not affect the wavefunction)

$$\psi_{\pm}(\boldsymbol{r}_1,\boldsymbol{r}_2) \sim F_1^{\pm}(\boldsymbol{r}_2)\psi_{100}(\boldsymbol{r}_1)$$

Therefore a correctly antisymmetrized wavefunction for the problem of the electron elastic scattering from the ground state of the atomic hydrogen can be written as

$$\psi_{\pm}(\boldsymbol{r}_1,\boldsymbol{r}_2) = \left[F_1^{\pm}(\boldsymbol{r}_1)\psi_{100}(\boldsymbol{r}_2) + F_1^{\pm}(\boldsymbol{r}_2)\psi_{100}(\boldsymbol{r}_1)\right]$$

This is known as the *static exchange method*. In case where the collision energy is high enough to excite or even ionize the hydrogen atom then all the open channels should be included in an appropriately antisymmetrized wavefunction which would be then written as

$$\psi_{\pm}(\boldsymbol{r}_1,\boldsymbol{r}_2) = \sum_{q=1}^{N}\left[F_q^{\pm}(\boldsymbol{r}_1)\psi_q(\boldsymbol{r}_2) + F_q^{\pm}(\boldsymbol{r}_2)\psi_q(\boldsymbol{r}_1)\right]$$

where N is the number of states allowed by the collision conditions. This is also known as the *close coupling approximation*. It is instructive to realize that these wavefunction are actually approximations of the "real" wavefunction and not the only solutions to the problem.

8.2 Electron-ion collisions and related processes

8.2.1 Introduction

Collisions of electrons with ions and atoms are of fundamental nature. The details of the involved processes enhance our understanding on the behavior of nature on the quantum level. Experimental data provide the most stringent tests on atomic collision and structure theoretical models, thus providing detailed knowledge about the structure and the dynamics of atomic systems. Besides their intrinsic relevance, electron collisions are also most important in plasma physics and applications. They determine the charge-state balance of atoms in the plasma and the emitted spectrum of electromagnetic radiation. Understanding and diagnosing the state of a plasma, whether of astrophysical origin or man-made, relies on information about cross sections and rate coefficients for electron–atom and electron–ion interactions. Elastic collisions of ions with cold electrons are used to cool ion beams in storage rings. Inelastic electron interactions with atomic ions are the dominant processes in high temperature plasmas such as stellar coronae. Recombination and scattering of electrons from ions are also important in low temperature plasmas, for example in

photo-ionized gases. Thus, depending on the environment, the different electron collision processes have varying importance and the charge state distributions of atoms in the environment under consideration can span a very wide range between almost neutral and almost fully stripped. A classic application of electron–ion collision data is plasma diagnostics. From the analysis of spectroscopic observations, Doppler shifts, line broadening and line intensity ratios, it is possible to infer plasma parameters such as plasma rotation velocity, ion temperature, electron temperature, and electron density.

8.2.2 The processes

Collision processes of electrons with charged atomic ions, noted hereafter A^{q+}, can be inferred largely from the final ionic state after the electron–ion interaction and followed by the possible relaxations.

Elastic Scattering

An electron scattered from a target ion may change its initial direction while the target ion remains in its original state. It is called *direct elastic scattering* and is the most common case found in textbooks, i.e. the Coulomb scattering or Rutherford scattering which can be described even by classical mechanics in case of structureless ions. The process of direct elastic scattering can be described as

$$e + A^{q+} \rightarrow A^{q+} + e$$

In addition, there is a different two-step pathway by which the final state can be reached and consequently called *indirect elastic scattering*. Here the first step is called *dielectronic capture* (DC) where the incident electron is captured by the ion while simultaneously an electron of the ion is promoted to higher energy levels. It is a process mediated by Coulombic electron-electron interaction and for this reason it can be treated as the time-reversed Auger process, or, more generally, as time-reversed autoionization. Due to the resonant character of the process, DC can only occur if the kinetic energy of the incident electron matches the difference of total binding energies of all electrons in the initial and final states of the ion. The second step is relaxation of the doubly excited intermediate state $\left[A^{(q-1)+}\right]^{**}$ by emission of an electron, following an Auger transition as pictorially shown in Fig. The whole process is then termed *resonant elastic scattering* (RES) and can be described as

$$e + A^{q+} \rightarrow \left[A^{(q-1)+}\right]^{**} \rightarrow A^{q+} + e$$

RES cannot be distinguished from the direct process. As a consequence, interference between the amplitudes of the two routes of elastic scattering can occur.

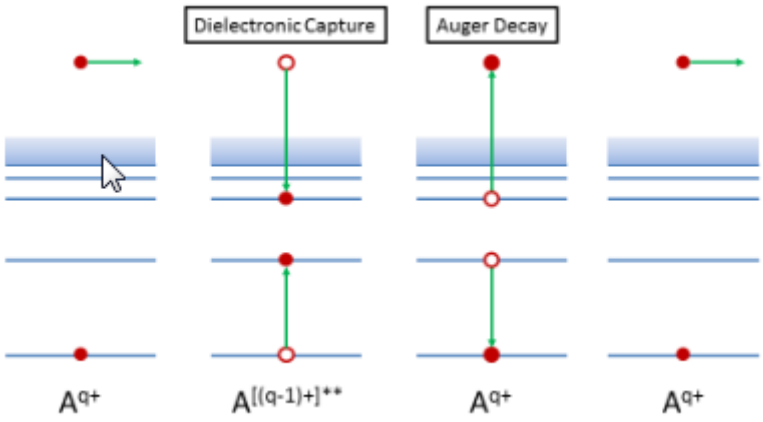

Figure Schematic energy diagram depicting the steps of resonant elastic scattering.

Recombination

When the doubly excited intermediate state $\left[A^{(q-1)+}\right]^{**}$ in a DC process relaxes by the emission of photons, the whole process is termed *dielectronic recombination* (DR). It is a resonant process since it involves DC in the first step. It is schematically depicted in Fig. and can be described as

$$e + A^{q+} \rightarrow \left[A^{(q-1)+}\right]^{**} \rightarrow A^{(q-1)+} + hf_1 + hf_2 + \cdots$$

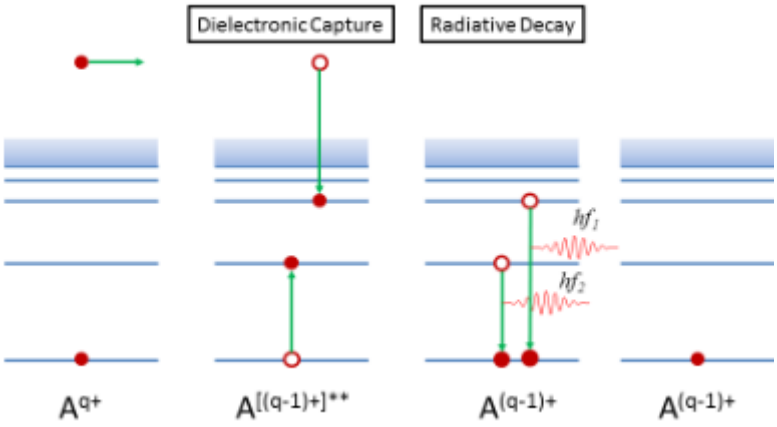

Figure Schematic energy diagram depicting the steps of dielectronic recombination.

Another recombination path that does not involve a resonant first step is the direct or *radiative recombination* (RR). In this case the incident electron is captured in a bound ionic state while the excess of energy is carried away by a photon, i.e.

$$e + A^{q+} \rightarrow A^{(q-1)+} + hf$$

Excitation

The excitation process is an inelastic process where the incident electron is scattered from an ion losing some of its initial kinetic energy, while the ion is left an excited state. The energy lost by the electron is the difference in energy of the initial and final bound states of the ion. This so called process of *electron-impact excitation* can be described by

$$e + A^{q+} \rightarrow [A^{q+}]^{*} + e$$

Similar to the elastic scattering case, the final state can be reached not only directly as described above but resonantly as well. In this case, the first step is a DC process while the second is autoionization to an excited ionic state, as shown in Fig., and described as

$$e + A^{q+} \rightarrow \left[A^{(q-1)+}\right]^{**} \rightarrow [A^{q+}]^{*} + e$$

Again, the result of the resonant excitation cannot always be distinguished from that of the direct process. As a consequence, interference between the amplitudes of the two routes may occur.

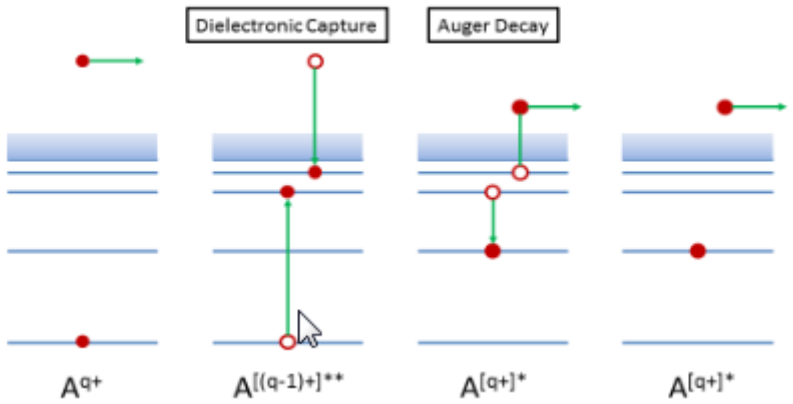

Figure Schematic energy diagram depicting the steps of resonant excitation.

Ionization

Electron impact on an ion with sufficiently high collision energy may result in the removal of one electron of the ion and the process is then termed direct *electron-impact single ionization* is schematically depicted in Fig. and can be described as

$$e + A^{q+} \rightarrow A^{(q+1)+} + e$$

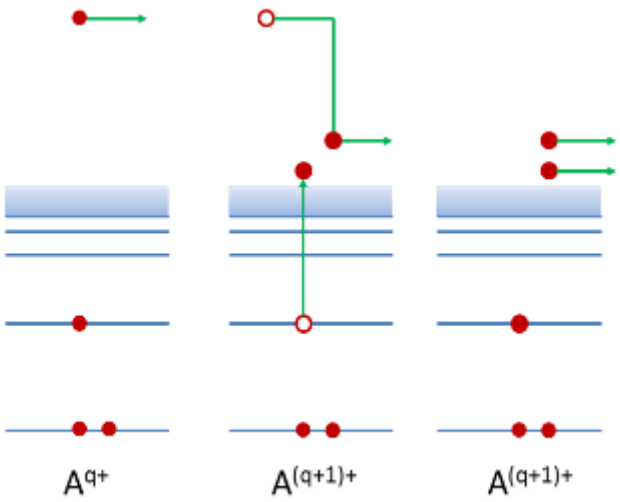

Figure Schematic energy diagram depicting the steps of direct ionization.

In case the electron kinetic energy high enough two or several (n) electrons from the ion can be emitted leading to a process termed direct *electron-impact multiple ionization*, which accordingly can be described as

$$e + A^{q+} \rightarrow A^{(q+n)+} + (n+1)e$$

Besides these direct knock-off processes there are indirect mechanisms. One of these is the excitation of inner-shell electrons of the target ion A^{q+}. As a result, the ion may end up in an excited state with energy that exceeds the ionization threshold for the removal of the outermost electron. Such a state would be autoionizing and the highly excited ion can hence decay by the emission of an electron instead of a photon. The net result of that process is ionization of the parent ion and the processes, shown in Fig., is termed *excitation-ionization* (EA), described as

$$e + A^{q+} \rightarrow [A^{q+}]^* + e \rightarrow A^{(q+1)+} + e + e$$

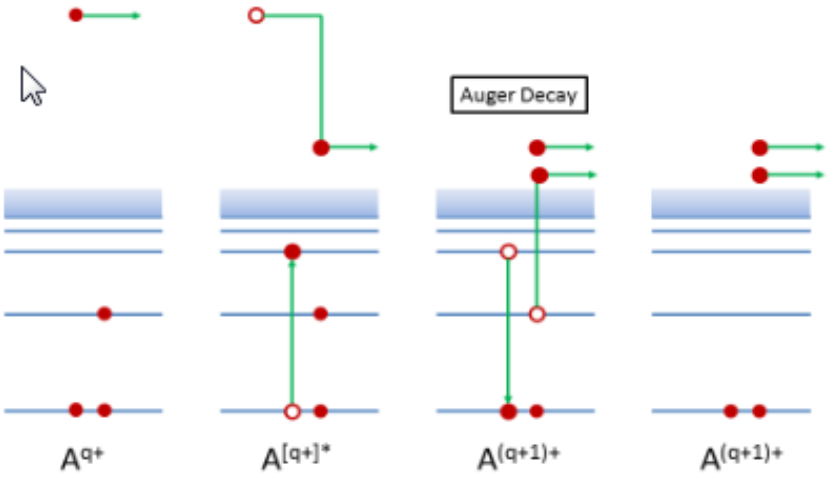

Figure Schematic energy diagram depicting the steps of excitation-ionization.

As before, the first step of EA may proceed via the formation of an intermediate resonance state involving an EA process. The resulting short lived recombined ion state is so highly excited that two electrons can be ejected in the relaxation process. In the end, the ion has lost one electron in the whole process, described as

$$e + A^{q+} \rightarrow [A^{q+}]^{**} \rightarrow A^{(q+1)+} + e + e$$

Higher order processes

Aside from the above fundamental mechanisms there are similar processes of higher order, the probability of which is much lower compared to the above described low order mechanisms. For the sake of completeness we will mention the tri-electronic recombination. Here the electron has enough kinetic energy to excite two of the ions electrons in one step process as depicted in Fig. If the triply excited state of the ion relaxes with photon decays then the process is termed trielectronic recombination.

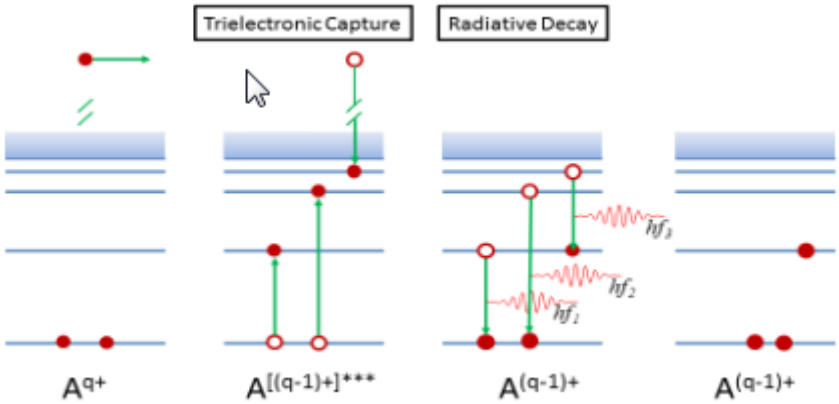

Figure Schematic energy diagram depicting the steps of trielectronic recombination.

Cross sections

Indirect scattering processes may be quite complex in the case of a multi-electron target ion and hence, the cross-section estimation can be quite cumbersome. Next, we shall examine a few indicative and instructive cases.

Resonant processes

For processes associated to resonances associated with resonances the related cross section can be calculated by multiplying the cross section for dielectronic capture with the branching ratio for the particular decay path starting from the intermediate doubly excited state. The cross section for dielectronic capture is

$$\sigma_d^{DC} = 7.88 \cdot 10^{-31} [cm^2 eV^2 s] \frac{1}{E_e} \frac{g_d}{2g_i} \frac{A_a(d \to i) \cdot \Gamma_d}{(E_e - E_{res})^2 + \Gamma_d^2/4}$$

where E_e is the electron energy and $E_{res} = E(|d>) - E(|i>)$ the resonance energy obtained from the total energies of the intermediate resonant state $|d>$ and the initial state $|i>$, respectively. The quantities g_d and g_i are the statistical weights of the states $|d>$ and $|i>$, respectively. $A_a(d \to i)$ is the autoionization rate of $|d>$ for a transition to $|i>$ and Γ_d the total width of $|d>$.

Thus, for the calculation of the cross section for resonant elastic scattering, the cross section for dielectronic capture has to be multiplied by the Auger yield

$$\omega_A = \hbar \frac{A_a(d \to i)}{\Gamma_d}$$

while for the calculation of cross sections for dielectronic recombination it has to be multiplied by the fluorescence yield

$$\omega_r = \hbar \frac{\sum_f A_r(d \to i)}{\Gamma_d}$$

of the intermediate state $|d>$, where the summation index f runs over all states below the first ionization limit of the recombined $A^{(q-1)+}$ ion that can be reached from $|d>$ by radiative transitions. Resonances in other reaction categories are treated accordingly.

Excitation

The total cross section for direct excitation of ions can be approximated as

$$\sigma = 2.36 \cdot 10^{-31} [cm^2 eV^2] \frac{f_{ij} \bar{g}}{E_e E_{ij}}$$

where f_{ij} is the optical oscillator strength for the transition from excited state $|j>$to ground state $|i>$, E_{ij} the related excitation energy, E_e the electron energy and $\bar{g}$ the

effective Gaunt factor. In the vicinity of the threshold this is reasonably well approximated by $\bar{g}$ = 0.2. At higher energies $E_e \geq 2E_{ij}$, it scales as $\bar{g} = 0.28\ln(E_e/E_{ij})$.

The cross section has an energy dependence that is characterized by a finite maximum at the excitation threshold and a slow, smooth decrease with increasing electron energy. Along with indirect resonant channels of excitation and neglecting the possibilities of interference between them, the generic shape of the total cross section is shown in Fig.

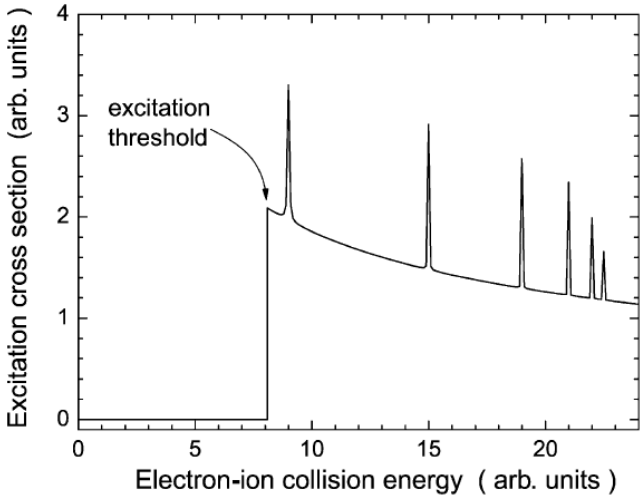

Figure Generic energy dependence of the total cross section for electron-impact excitation. The resonances are assumed to show no interference with the direct excitation channel (A. Müller, Advances in At., Mol. Opt. Phys. 55, 2008).

Single Ionization
The cross section for direct excitation of ions can be approximated as

$$\sigma_\nu = 4.5 \cdot 10^{-14}[cm^2 eV^2]\frac{\xi_\nu}{I_\nu E_e} ln\frac{E_e}{I_\nu}$$

where ξ_ν is the number of equivalent electrons in the νth subshell, I_ν the ionization potential of that subshell, and E_e the electron energy. The total cross section has to summed over all the subshells that may contribute to the process. The energy dependence is similar to the excitation case showing a finite maximum at the ionization threshold and a slow decrease with increasing electron energy, much like the one shown in Fig.

8.2.3 Experimental setups and techniques

Although plasma observations with careful diagnostics of electron temperature and particle densities can be a source of information about plasma rate coefficients, there are numerous other types of experiments that provide data about rate coefficients for electron–atom or electron–ion collisions. The most popular ones are listed below.

Electron gun beams

One of the oldest techniques to determine cross sections for electron collisions is that of producing an electron beam passing through a target of particles that are essentially at rest. Various type of electron guns (e-guns) were developed for these purposes including the e-guns for CRT screens and SEM/TEM electron microscopes. A typical CRT-type e-gun and a custom made high current e-gun are shown in Fig.

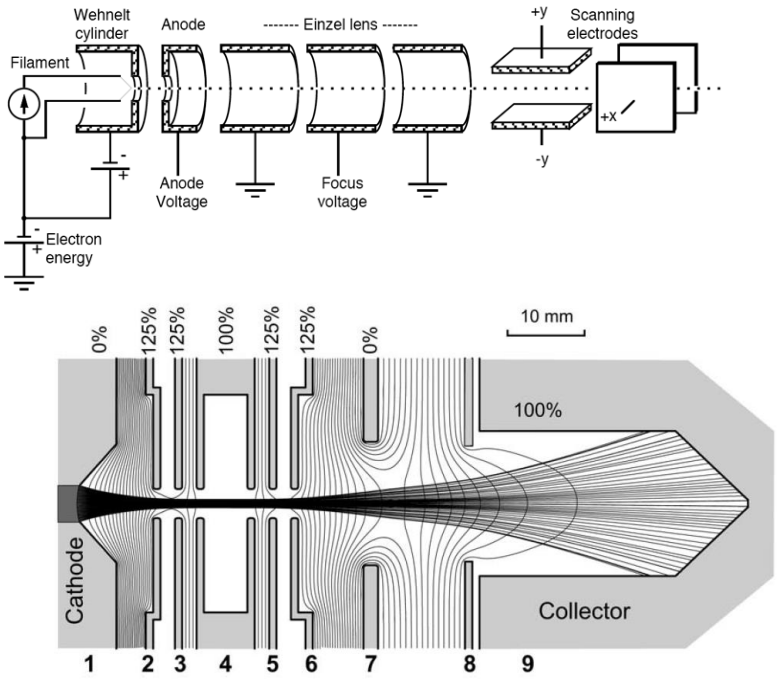

Figure [Top] a typical CRT-type e-gun. [Bottom] Computer simulation of an electron gun for electron–ion crossed-beams experiments. In the interaction region (electrode 4) the density of equipotential lines is low indicating at most small electric fields (A. Müller, Advances in At., Mol. Opt. Phys. 55, 2008).

Traps

Trapped-ion techniques for the determination of electron–ion collision cross sections are based on the observation of spatially confined ions that are exposed to electron impact. The state of the art in use of traps for electron–ion collision studies was initiated by the development of the electron beam ion source (EBIS). EBIS employs a very dense magnetically guided electron beam for trapping and for sequential ionization of highly charged ions. A substantial extension of the technique became possible with the development of a modified EBIS, the electron beam ion trap (EBIT) which facilitates the observation and spectroscopy of electromagnetic radiation emitted by the trapped ions. In both cases the electron energy is ramped over a selected range of interest providing signatures of electron–ion collisions either in the number of extracted ions of a given charge state or in the differential photon yield at a fixed angle relative to the electron beam. A typical design of the EBIS is sketched in Fig.

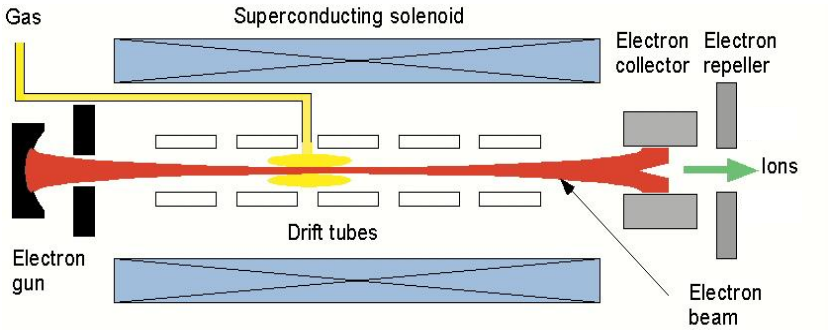

Figure Schematic of an electron beam ion source

Quasi-free electrons

Targets of charged particles are difficult to prepare because of space-charge limitations. As a consequence, the investigation of interactions between free electrons and ions often suffers from low signal rates. The most efficient scheme of this kind is the use of electrons bound in atoms. Under certain conditions electron–ion interactions can be studied by passing an ion beam through neutral gas. The gas atoms or molecules provide a dense target of quasi-stationary electrons which interact with the incident ions. At sufficiently high projectile velocities ($V_P \gg v_0$, with V_P the velocity of the incident ion and v_0 the orbital electron velocity) the electrons bound in target atoms can be treated as free particles (therefore the term "quasi free"). The active bound target electrons as seen from the rest frame of the incident ion are considered to behave like free electrons with a given momentum distribution along the collision axis z, $J(p_z) = \iint |\psi(\boldsymbol{p})|^2 dp_x dp_y$, known as the Compton profile. Thus, the measured cross section for the ion–atom collision process $\sigma_{ion-atom}$ can be expressed as an average over the related electron–ion cross section σ_{e-ion} with the momentum distribution of the electrons $\sigma_{ion-atom} = \int \sigma_{e-ion} J(p_z)\, dp_z$. This is known as the electron scattering model.

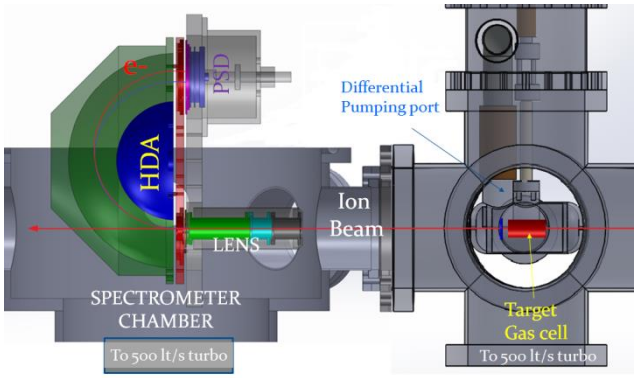

Figure 9 Zero-degree electron spectrometer used for the measurement of electron scattering cross sections by employing the quasi-free-electron approach. The ion beam interacts with the gas target and traverses the spectrograph. The electrons emitted from the target area in the forward direction are energy analyzed by the hemispherical deflector analyzer (HDA) and recorded by the two-dimensional position sensitive detector (PSD) (J. Atom. Mol. Cond. Nano Phys. 3 (2016) 125).

Colliding beams

The optimum experimental conditions for electron–ion studies are those of colliding-beams experiments providing unambiguous information about electron–ion collisions. The experimental setups can be in geometries of inclined or merged-beams arrangements as schematically shown in Fig. 10.29. Each beam is individually produced and characterized and then mutually colliding. The merged beams geometry is particularly favorable for energy resolution measurements. In that case, the two beams can interact over distances up to several meters where the intense electron beam is axially guided by magnetic fields as shown in Fig. 10.29. It is important to note that the merged beams setup shown in Fig. 10.29 is is actually an indispensable part of storage rings used for cooling the ion beams through elastic collisions of ions with cold electrons.

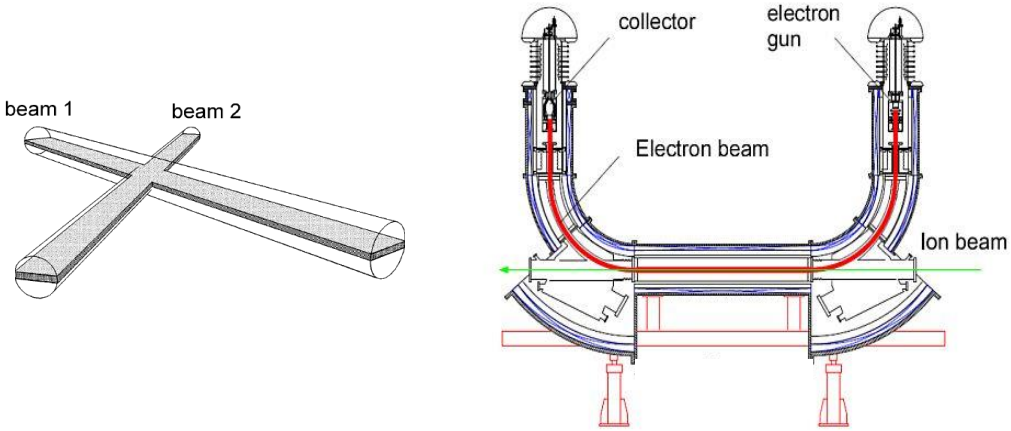

Figure [Left] Principle of inclined beams colliding with one another at an angle. [Right] Typical setup for merged electron-ion beams experiments.

8.3 References

The following bibliography is only indicative containing books, chapters and review articles. The reader is referred to the references within for further reading.

1. B. H. Bransden, C.J. Joachain
   Physics of Atoms and Molecules
   Longman Group Limited, 1983. ISBN 0-582-44401-2
2. M.Scully and S.Zubairy
   Quantum Optics
   Cambridge University press, 2008. ISBN 0521434580
3. J. H. Posthumus
   The dynamics of small molecules in intense laser fields
   Rep. Prog. Phys. 67 (2004) 623–665
4. F. Krausz and M. Ivanov
   Attosecond Physics
   Rev. Mod. Phys. 81 (2009) 163-234
5. S. Blüegel
   Scattering Theory: The Born Series
   Lecture Notes of the 43rd IFF Spring School, 2012. ISBN 978-3-89336-759-7
6. A. Müller
   Electron-Ion Collisions: Fundamental Processes in the Focus of Applied Research
   Advances in Atomic, Molecular and Optical Physics, Vol. 55, (2008) 293-417, Elsevier Inc.
7. N. Stolterfoht, R. D. DuBois, R.D. Rivarola
   Electron Emission in Heavy Ion-Atom Collisions
   Springer-Verlag Berlin Heidelberg 1997, ISBN 978-3-642-08322-8
8. R. K. Janev
   Atomic and Molecular Processes in Fusion Edge Plasmas
   Springer Science+Business Media, LLC, 1995. ISBN 978-1-4757-9321-5
9. Y. Itikawa
   Molecular Processes in Plasmas. Collisions of Charged Particles with Molecules
   Springer, 2007. ISBN 978-3-540-72609-8
10. G.B. Rybicki, A.P. Lightman
    Radiative Processes in Astrophysics

WILEY-VCH Verlag GmbH & Co. KGaA, 2004. ISBN-13: 978-0-471-82759-7

PowerLaPs

Innovative Education & Training in High Power Laser Plasmas

Laser plasma diagnostics - Theory and Experiments

Chapter 9: Experimental measurement of shock waves generated by intense laser-plasma interaction

J. Pasley

9.1 Introduction

Investigating extremely strong shock waves in the laboratory generated by application of ultra-high intensity short pulse laser pulses is complicated by three factors. The first of these is the fact that the shock waves weaken rapidly once the laser pulse has ended, and therefore persist only fleetingly at maximum strength. The second issue is one of spatial scale: the shock waves form around the focus of the laser. In order to achieve such high intensities as we have discussed earlier, the laser is typically focused to a spot of around 5 μm diameter. Finally the interaction between the laser and the dense plasma generates a range of energetic particles including relativistic ions and electrons, as well as electromagnetic radiation over an exceptionally broad range of frequency space from radio to gamma-rays. This calls for a diagnostic that has exceptionally high temporal and spatial resolution, and which can discriminate the desired signal a bright background. The diagnostic must also be capable of functioning in the environment of the target chamber, where electromagnetic pulses (EMP) generated by the laser-plasma interaction can disable some diagnostics.

In addition to the difficulties of making measurements on such shock waves, the short pulse laser based method for shock wave generation renders the shock waves so produced inappropriate for some applications. Material ahead of the shock wave may be preheated by energetic particles and hard x-ray radiation generated by the interaction. Furthermore, at early times, the shock waves will tend to be irregular, and non-planar in character. This renders them poor candidates for equation of state studies, and for drawing inferences about more general strong shock physics; it may, for example, be challenging to determine, whether preheating is driven by thermal radiation from behind the shock front, or by radiation generated directly by the laser-plasma interaction.

Most measurements of shock waves generated by short pulse laser systems have therefore focused upon measuring blast waves that have evolved for many tens of picoseconds, or even nanoseconds, after the laser-plasma interaction has occurred [1, 2]. Measurements of shock-wave dynamics at earlier times are scarcer. Some data may be gleaned from x-ray spectroscopy

[3], however such data are challenging to analyze, and there is a reliance upon substantial modelling for interpretation.

It is clear that in order to better understand the hydrodynamics associated with the short pulse laser interaction that takes place in a fast ignition target, additional measurements, and more detailed simulations will be required. Experimental data is particularly scarce at early times, for the reasons mentioned. In this section we discuss a promising new diagnostic approach which might enable substantial data on the process of shock wave formation and propagation in the first few picoseconds of an intense short-pulse laser plasma interaction to be extracted. This in turn will support modelling efforts, by providing data suitable for bench-marking of simulation codes, for instance codes like that described in the preceding section.

9.2 The Doppler spectroscopy diagnostic

A recent experiment performed at the Tata Institute for Fundamental Research (TIFR) in Mumbai, demonstrated a novel diagnostic approach to investigating short pulse laser generated shock waves [4]. This approach, illustrated alongside sample data in figure 1, relies upon the Doppler shift of a short pulse of probing laser light reflecting off the shock generated by a higher energy “pump” pulse at earlier times. In this case the focused intensity of the pump laser was $5 \times 10^{18} W/cm^2$, at a frequency of 800nm, with a pulse length of 30fs and the target is 0.5mm thick optically polished aluminum. By selecting a probe wavelength shorter than that of the laser which drives the shock, it is possible to view the dynamics in plasma that is over-dense with respect to the pump pulse. In this experiment we chose to use a second harmonic probe (400nm). Using a probe of a different wavelength also enables more ready disambiguation from the scattered light of the pump pulse. As may be seen in figure 1, the frequency doubling results in a probe beam with a spectral width of around 2nm.

This diagnostic has a number of interesting advantages. The probe laser pulse can have a very short duration, and be timed precisely with respect to the pump pulse, enabling plasma dynamics to be resolved at very early times. The probe laser is also bright enough that self-emission from the background plasma can

be readily over-come, yielding a clean signal. Furthermore, the probe laser can be focused down to dimensions similar to that of the pump laser, thereby effectively achieving spatial resolution on the scale of a few microns. Using multiple shots on similar targets enables excellent resolution of comparatively small Doppler shifts, in this experiment data from around 100 shots was averaged at each time point. The major drawback is that the diagnostic can only function when the shock wave is moving in plasma that is under-dense with respect to the probe.

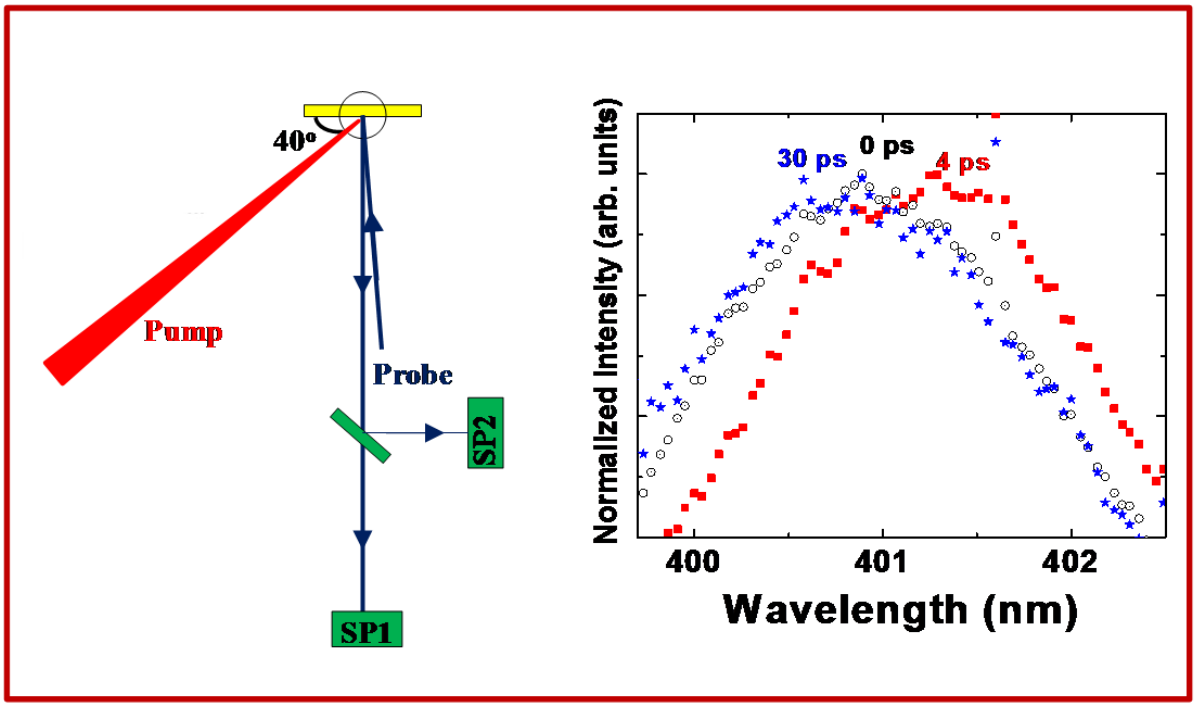

Figure 1. Showing the layout of the Doppler Spectroscopy experiment described in reference 11. The 5 × 10^{18}W/cm^2, 800nm, 30fs pump pulse drives hydrodynamics in the aluminium target. A 400nm probe pulse interrogates the region illuminated by the pump pulse. The reflected probe light is then directed onto two spectrometers which record the Doppler shift of the probe due to the motion of the target plasma as induced by the pump pulse.

Since this diagnostic relies upon the Doppler Effect, it provides an unambiguous measurement of shock wave velocity. The degree of frequency shifting corresponds exactly to the velocity at which the critical surface for the probe pulse is moving through the plasma. As shown in figure 2, the match between measurements made using this diagnostic at TIFR and a coupled 1D PIC-hydrodynamics simulation of the experiment is impressive. The diagnostic

provides detailed time resolved information about the plasma dynamics that can be readily compared with simulation output. This makes it possible to accurately constrain computational models used in this and other computational modelling codes.

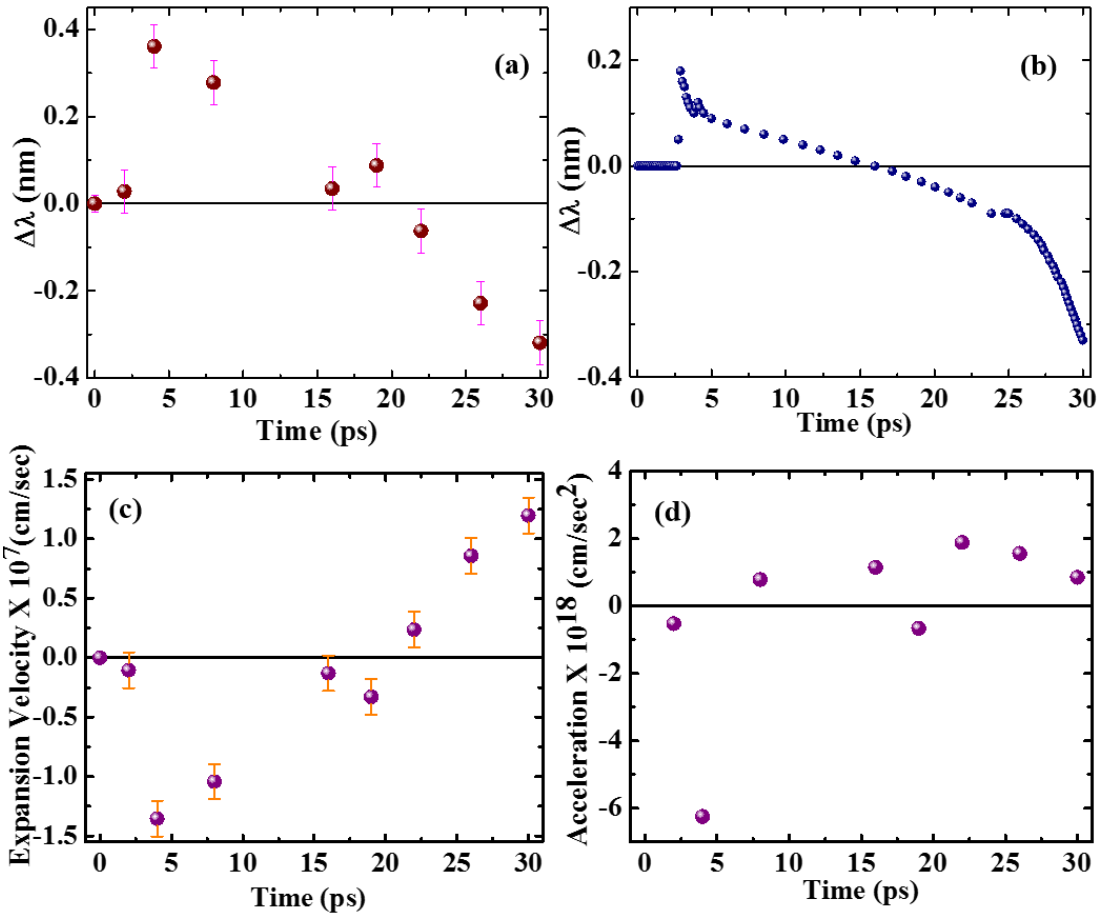

Figure 2. (a) experimental data and (b) hybrid simulation that uses a 1-D electromagnetic PIC simulation for the initial evolution and a hydrodynamics code for the later times. Calculated (c) expansion velocity and (d) acceleration from Doppler shift. The strong negative acceleration and associated high velocity around 4ps corresponds to the passage of the shock wave into the target launched by the high intensity laser plasma interaction

The experimental results, taken in combination with the simulations, suggest that the pump pulse induces rapid heating of the intermediate density plasma blow-off that has previously been created by the laser pre-pulse. This heating rapidly launches a pressure disturbance, which is observed shortly thereafter propagating into the target by the Doppler Spectrometry diagnostic. After this pressure disturbance (which it is expected would take the form of a strong

shock wave) has passed, the rarefaction wave that must follow it causes the fluid motion to reverse. Other more recent publications explore the hydrodynamics of intense-short pulse laser pulses with dense plasmas in more detail [5-10].

9.3 References

[1] T. Ditmire, K. Shigemori, B. A. Remington, K. Estabrook and R. A. Smith, ApJS, 127, 299, (2000)

[2] M. J. Edwards, A. J. MacKinnon, J. Zweiback, K. Shigemori, D. Ryutov, A. M. Rubenchik, K. A. Keilty, E. Liang, B. A. Remington, and T. Ditmire, Phys. Rev. Lett. 87, 085004 (2001)

[3] K. U. Akli, S. B. Hansen, A. J. Kemp, R. R. Freeman, F. N. Beg, D. C. Clark, S. D. Chen, D. Hey, S. P. Hatchett, K. Highbarger, E. Giraldez, J. S. Green, G. Gregori, K. L. Lancaster, T. Ma, A. J. Mackinnon, P. Norreys, N. Patel, J. Pasley, C. Shearer, R. B. Stephens, C. Stoeckl, M. Storm, W. Theobald, L. D. Van Woerkom, R. Weber and M. H. Key, Phy. Rev. Lett., 100, 165002 (2008)

[4] S. Mondal, A. D. Lad, S. Ahmed, V. Narayanan, J. Pasley, P. P. Rajeev, A. P. L. Robinson, G. Ravindra Kumar, Phys. Rev. Lett., 105, 105002 (2010)

[5] A. Adak, Blackman, D. R., Chatterjee, G., Kumar Singh, P., Lad, A. D., Brijesh, P., Robinson, A. P. L., Pasley, J. & Kumar, G. R., Physics of Plasmas. 21, 6, 062704, (2014)

[6] A. Adak, Robinson, A. P. L., Singh, P. K., Chatterjee, G., Lad, A. D., Pasley, J. & Kumar, G. R., Physical Review Letters 114, 11, p. 1-5 5 p., 115001, (2015),

[7] A. Adak, Singh, P. K., Blackman, D. R., Lad, A. D., Chatterjee, G., Pasley, J., Robinson, A. P. L. & Ravindra Kumar, G., Physics of Plasmas. 24, 7, 072702, (2017)

[8] Lancaster, K. L., Robinson, A. P. L., Pasley, J., Hakel, P., Ma, T., Highbarger, K., Beg, F. N., Chen, S. N., Daskalova, R. L., Freeman, R. R., Green, J. S., Habara, H., Jaanimagi, P., Key, M. H., King, J., Kodama, R., Krushelnick, K., Nakamura, H., Nakatsutsumi, M., MacKinnon, A. J. & 4 othersMacPhee, A. G., Stephens, R. B., Van Woerkom, L. & Norreys, P. A., Physics of Plasmas. 24, 8, 6 p., 083115, (2017)

[9] K. Jana, Blackman, D. R., Shaikh, M., Lad, A. D., Sarkar, D., Dey, I., Robinson, A. P. L., Pasley, J. & Ravindra Kumar, G., Physics of Plasmas. 25, 1, 5 p., 013102, (2018)

[10] Shaikh, M., Jana, K., Lad, A. D., Dey, I., Roy, S., Sarkar, D., Ved, Y., Robinson, A. P. L., Pasley, J. R. & Kumar, G. R., Phys. Plasmas 25, 5 (2018).

PowerLaPs

Innovative Education & Training in High Power Laser Plasmas

Laser plasma diagnostics - Theory and Experiments

Chapter 10: Diagnostics for Inertial Fusion

D. Batani

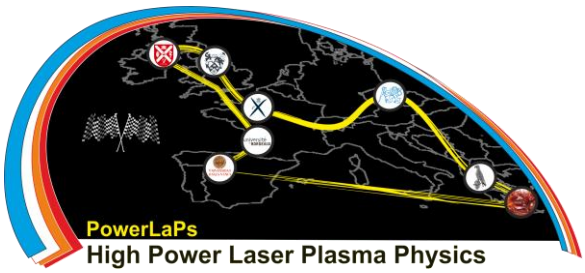

10.1 Introduction to diagnostics for inertial fusion

The voyage of nuclear fusion has started about 70 years ago (Sacharov, Teller, …) and despite progress has provided many disillusions…60 years ago the laser was invented, opening the field of "Inertial Fusion" (Basov, Nuckolls, …). Today we still facing great difficulties but also we are probably close to the demonstration of ignition, the scientific feasibility of fusion, which will conclude the first part of this travel.

Principle of Inertial Confinement (direct drive):

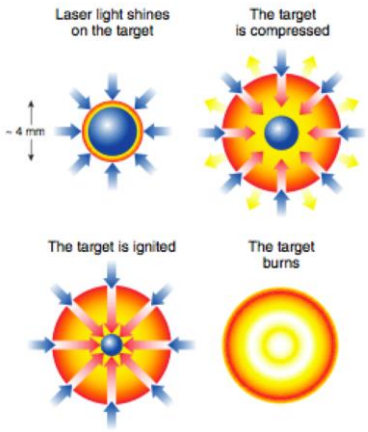

Thermonuclear Fusion:

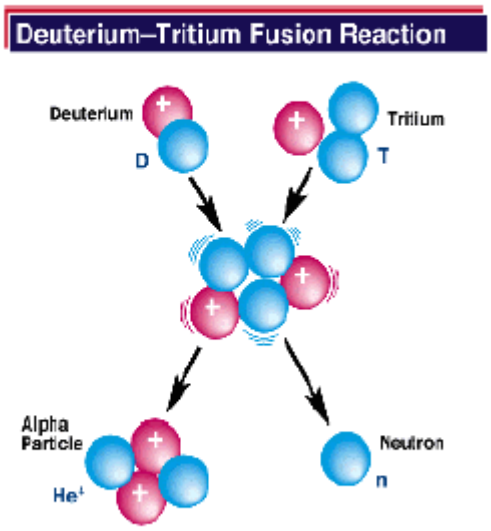

- Need to have high temperatures to overcome Coloumb repulsion

  $T_{min} \approx$ 5 - 10 keV

- Need to have many fusion reactions to allow for energy gain, i.e. large number of particles and/or long confinement time.
  Lawson's criterium

  $n_e \tau \approx 1.5\ 10^{14}$ s cm^{-3}

"Triple product" $n_e \tau\ T \geq 8\ 10^{14}$ s cm^{-3} keV

Lawson's criterium for inertial fusion

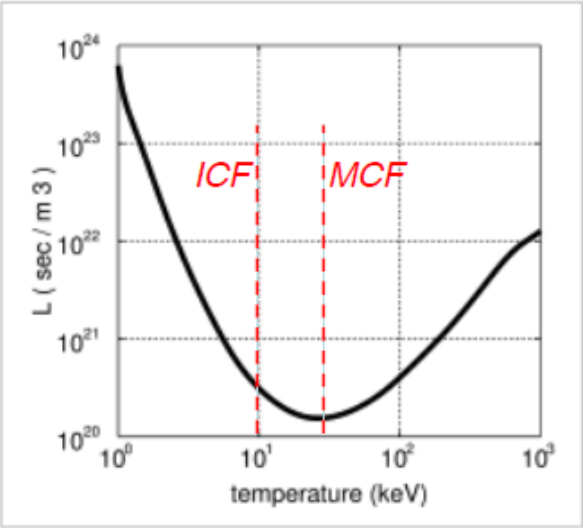

$n_e \tau \approx 1.5\ 10^{14}$ s cm^{-3}

is a minimum point

In general case:

$n_e \tau > L(T)$

In ICF we cannot reach 25 keV. Then: $n_e \tau \approx 3\ 10^{14}$ s cm^{-3}

Creating conditions for fusion:

Gravitational Confinement

Heating Mechanisms:
* Compression (gravity)
* Fusion Reactions (such as the p-p chain)

Magnetic Confinement

* Electromagnetic Waves
* Ohmic Heating (by electric currents)
* Neutral Particle Beams (atomic hydrogen)
* Fusion Reactions (D+T)

Inertial Confinement

* Compression (implosion driven by laser, or by X-rays from laser, or by ion beams)
* Fusion Reactions (primarily D+T)

Creating conditions for fusion:

The secondary system (H-bomb) is ignited by the explosion of a "conventional" nuclear bomb

For controlled nuclear fusion:
- Need to ignite small mass of fuel
- Need to ignite with different tools!

Isothermal expansion of a gas

Rarefaction (expansion) wave
Self-similar model

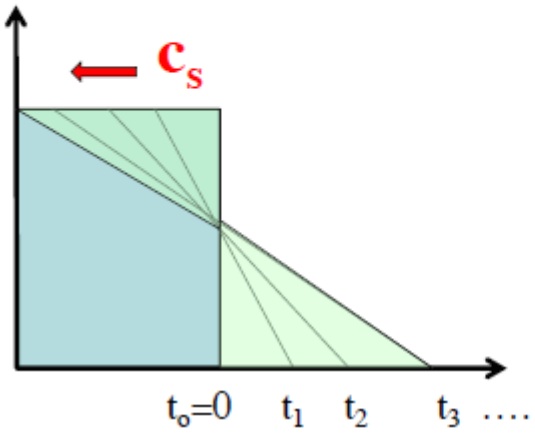

$$n(x) = n_o \exp(-x / L)$$

$$L = c_s \, t$$

$$c_s = \left(\gamma ZkT / m\right)^{1/2}$$

Lawson's criterium for inertial fusion

$\mathbf{n_e \tau \approx 3\ 10^{14}\ s\ cm^{-3}}$

Disassembly time determined by the fuels inertia

$$\tau < R / c_s \quad \Rightarrow \quad \text{we take } \tau = R / 4c_s$$

ion sound velocity in a plasma

$$c_s = \left(\gamma Z k T_e / m_i\right)^{1/2} = 9.8 \quad 10^5 \left(\gamma Z \; T_e(eV) / \mu\right)^{1/2} cm / s$$

$$\approx 7 \quad 10^7 \quad cm / s \quad (\text{for } \mathrm{T} = 10 \text{ keV})$$

Notice:

in magnetic fusion the time τ expresses the *confinement of energy*

In inertial fusion it refers to the *confinement of mass*

Lawson's criterium for inertial fusion

$\mathbf{n_e \tau \approx 3\ 10^{14}\ s\ cm^{-3}}$

Disassembly time determined by the fuels inertia

$$\tau = R / 4c_s \qquad c_s \approx 7 \quad 10^7 \quad cm / s \quad (\text{for } \mathrm{T} = 10 \text{ keV})$$

$$n_e = n_i = \frac{\rho(\mathrm{g/cc})}{2.5} \; 6.022 \quad 10^{23} cm^{-3} = 2.4\rho \quad 10^{23} cm^{-3}$$

$$n_e \tau = \quad 3 \quad 10^{14} = \left(2.4\rho \quad 10^{23}\right)\left(R / 4 \times 7.6 \quad 10^7\right)$$

For typical ICF conditions

$$\Rightarrow \rho R = \quad 3 \; 10^{14} \times 4 \times 7 \; 10^7 / \; 2.4 \; 10^{23} \approx 0.3 \text{ g/cm}^2$$

Burning fraction in ICF

H_B "combustion parameter" for a DT plasma fuel

$$\phi = \frac{\rho R}{\rho R + H_B} \approx \frac{\rho R}{\rho R + 6}$$

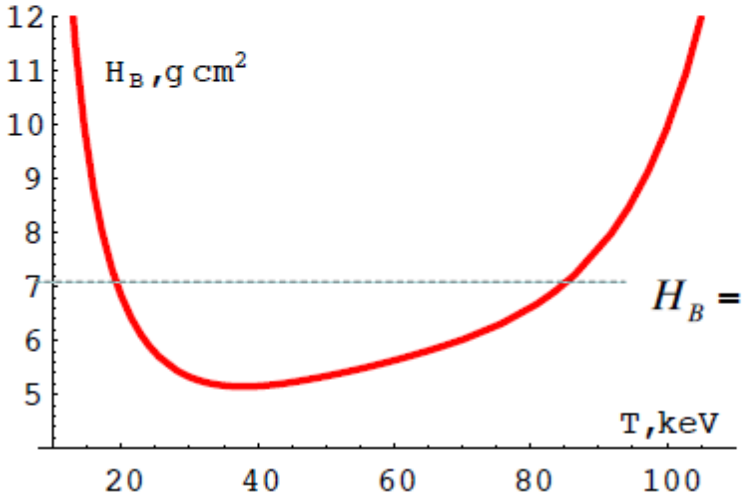

$$H_B = \frac{8 m_i c_s}{\langle \sigma v \rangle} \approx 6 \ \ g/cm^2$$

Lawson's criterium for inertial fusion

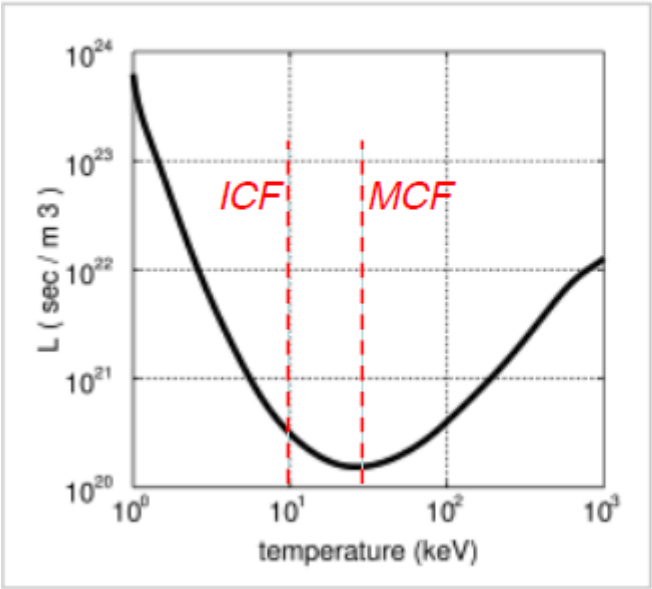

Lawson's Criterium for ignition (D-T): $\rho R > 0.3$ gcm^{-2}

Burning criterum: $\rho R > 3$ gcm^{-2}

In ICF we cannot reach 25 keV. Then: $\mathbf{n_e \tau \approx 6\ 10^{14}\ s\ cm^{-3}}$

10.2 Targets for fusion

ICF typical targets

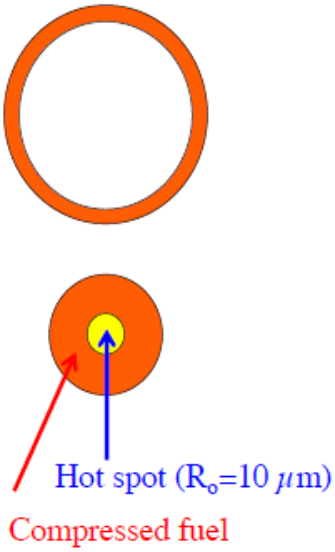

INITIAL CONDITIONS
CRYOGENIC SHELL
- $R_{in} \approx$ 2 mm, $\Delta r \approx$ 33 μm
- $A = R_{in} / \Delta r \approx 60$
- $V_{in} \approx 4 \pi R_{in}^2 \Delta r \approx 1.6\ 10^{-3}$ cm^3
- $\rho_{in} \approx 2.5 \times$ 0.1 g/ cm^3, M ≈ 0.41 mg

FINAL CONDITIONS
- $\rho_{fin} / \rho_{in} \approx 1000$
- $\rho_{fin} \approx 250$ g/ cm^3
- $V_{fin} \approx 4/3 \pi (R_{fin}^3 - R_o^3) \approx 1.6\ 10^{-6}$ cm^3
- $R_{fin} \approx$ 72 μm
- $\Delta r \approx 60\ \mu$m (A =1.2)
- $\rho_{fin} R_{fin} \approx 1.8$ g/ cm^2

ICF typical targets

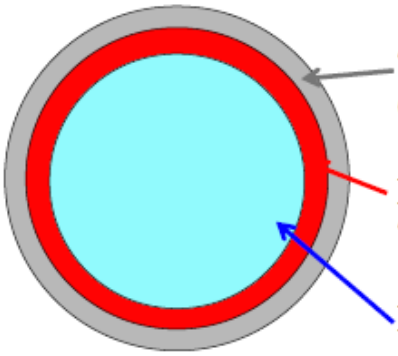

"Ablator"
(plastics, SiO_2, Be, Diamond)

DT ice ($\rho = 0.25$ g/cm^3)
"Fuel" "Shell"

DT gas

External radius ≈ mm

DT mass ≈ mg

Some orders of magnitude

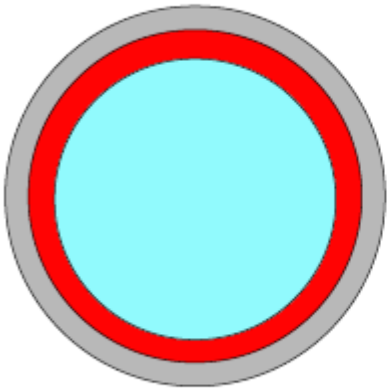

If

$t_{laser} \approx t_{implosion} \approx 10$ ns

$I_L \approx 3\ 10^{14}$ W/cm^2

$R \approx 2$ mm

Then

$S = 0.5$ cm^2

$E_{laser} = I_L t_{laser} S = 1.5$ MJ

$V_{implosion} = 2$ mm/10 ns

$= 200\ \mu$m/ns $= 200$ km/s

(in reality up to 400 μm/ns before "stagnation")

Space-time plot

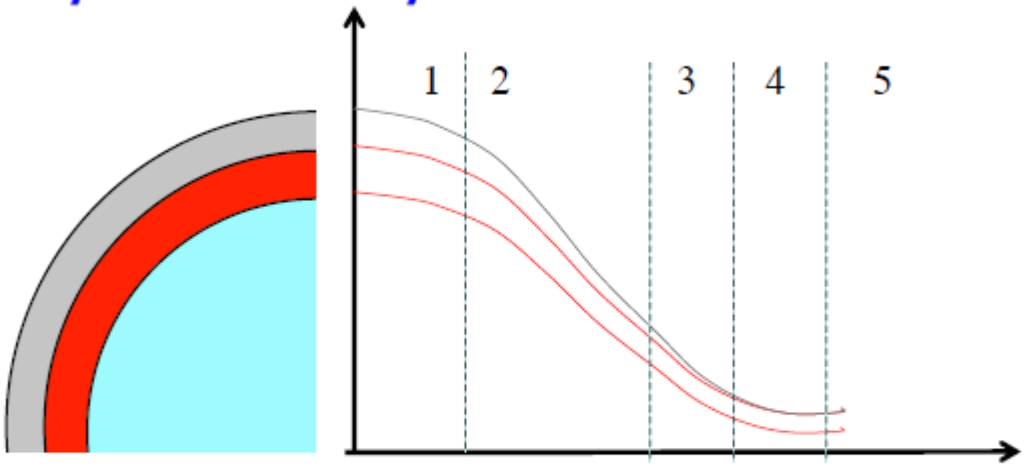

1 ablation and acceleration
2 implosion (almost constant velocity)
3 deceleration
4 stagnation (creation of hot spot)
5 explosion

"Isobaric" approach to ICF

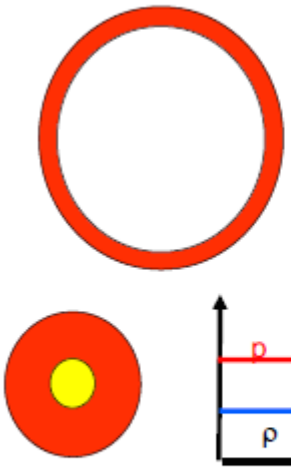

Stagnation is reached as the pressure of the internal fuel increases and gradually slows the shell down.
At stagnation $P_{shell} \approx P_{central\ spot}$

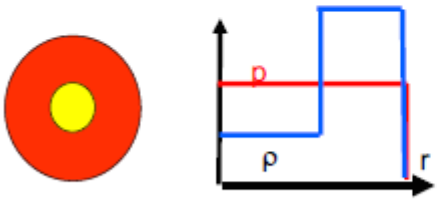

Kinetic Energy of (remaining) imploding shell is converted in:
- Compression of the fuel in the shell
- Heating of the central has

Produces an Isobaric fuel assembly
Need for High Aspect ratio target and high implosion velocities
V ~400 km/s

Why do we need a hot spot?

INITIAL CONDITIONS
CRYOGENIC SHELL
- $R_{in} \approx$ 2 mm, $R_{in} / \Delta r \approx 60$ ($\Delta r \approx 33$ μm)
- $V \approx 4 \pi R_{in}^2 \Delta r \approx 1.6\ 10^{-3}$ cm³
- $\rho_{in} \approx 2.5 \times 0.1$ g/ cm³, M ≈ 0.41 mg
- $N_{moli} = 0.8\ 10^{-4}$

Total number of ions $N_{DT} \approx 2\ 10^{21}$
If $T_{fin} \approx 10$ keV, total thermal energy in fuel $E \approx 2\ (3/2\ N_{DT}\ T) \approx 10$ MJ !!

"Volume ignition" is NOT achievable !

Conversion efficiency from laser light to thermal energy of the fuel is extremely low ≈ 5 %

Spherical geometry

Notice:

Ablation Pressure P ≈ 50 MBar

Pressure at stagnation P ≈ 500 Gbar

Amplification of a factor × 10000 due to convergence.

Spherical geometry is essential for ignition

NIF-like target (1 MJ)

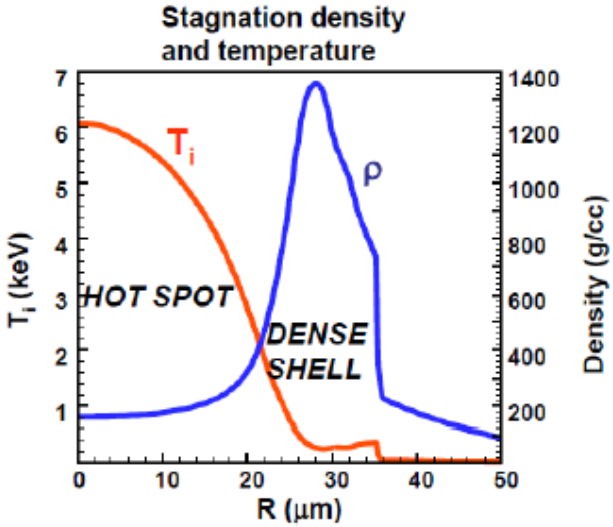

$$n_e = n_i = 2.4\rho \quad 10^{23} cm^{-3}$$

$$P(Bar) = 1.8 \quad 10^{-18} \quad n_{TOT}(cm^{-3})\, T_e(eV)$$

SHELL

$-\rho_{fin} R_{fin} \approx 10^3$ g/ cm^3 × 40 μm
= 4 g/ cm^2

$-n_i = n_e \approx 2.5\ 10^{26}$ cm^{-3}

HOT SPOT

$-\rho_{fin} R_{fin} \approx 130$ g/ cm^3 × 22 μm
= 0.3 g/ cm^2

$-n_i = n_e \approx 3\ 10^{25}$ cm^{-3}

PRESSURE (hot spot)

-P ≈ 600 GBar

Driving ICF targets with lasers is a very inefficient

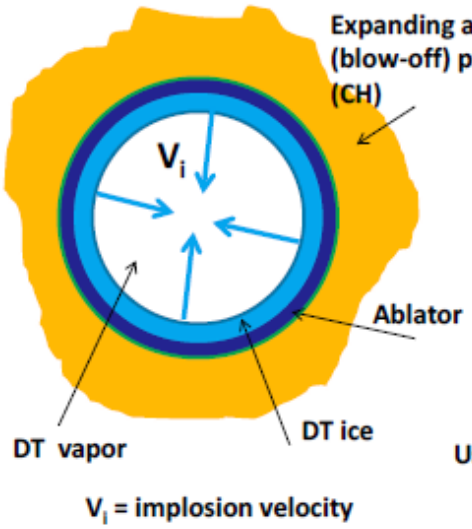

Examples:

NIF Indirect Drive
Laser energy = 1.8MJ
Shell final kinetic energy = 10-14kJ
Total efficiency = 0.6-0.8 %

NIF Direct Drive
Laser energy = 1.8MJ
Shell final kinetic energy = 70-90kJ
Total efficiency = 4-5 %

Useful kinetic energy = $\frac{1}{2} M_{unablated}^{shell} V_i^2$

V_i = implosion velocity

Only a small fraction of the driver energy is converted into useful implosion energy

Useful kinetic energy $\frac{1}{2} M_{unablated}^{shell} V_i^2$

- ~50% → **Compression and heating of the central hot spot**
- ~50% → **Compression of the dense shell to provide the "inertial" confinement**

10.3 Characteristic instabilities

Rayleigh-Taylor Instability:

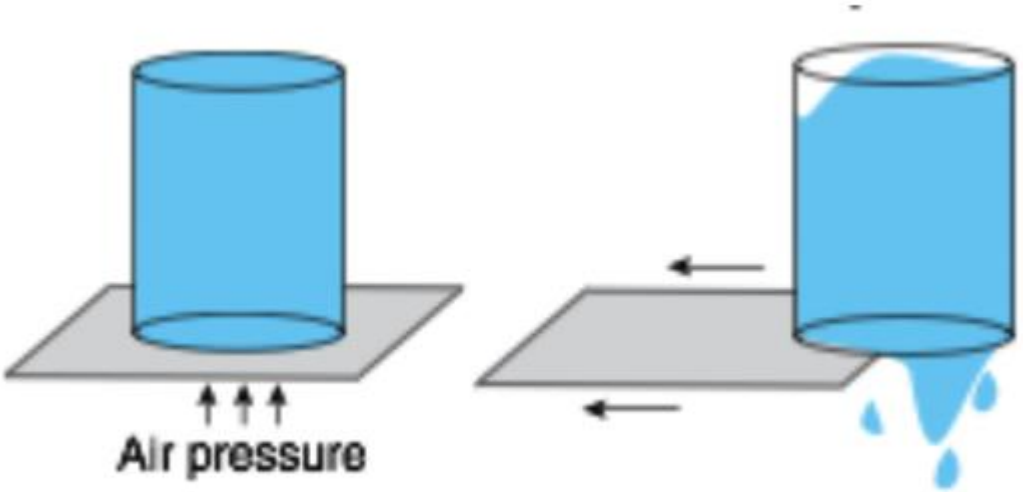

$$\gamma = \sqrt{Akg} \qquad A = \frac{\rho_1 - \rho_2}{\rho_1 + \rho_2}$$

Rayleigh-Taylor Instability – spherical implosions / explosions

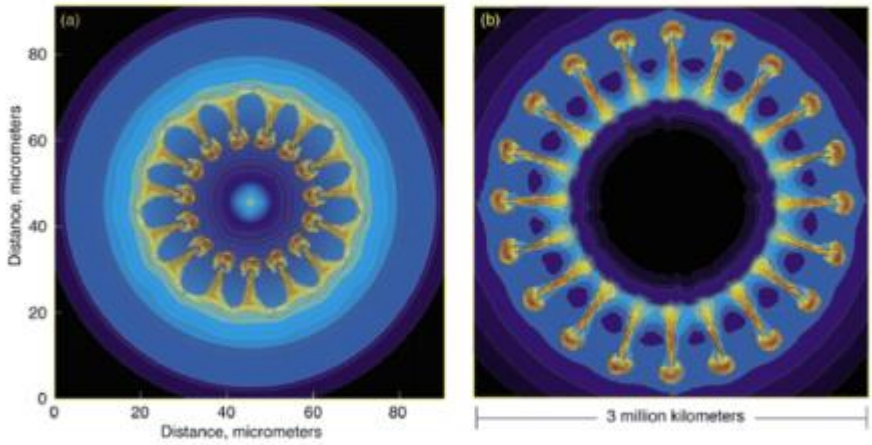

Striking similarities exist between hydrodynamic instabilities in (a) inertial confinement fusion capsule implosions and (b) core-collapse supernova explosions. [Image (a) is from Sakagami and Nishihara, *Physics of Fluids B* **2**, 2715 (1990); image (b) is from Hachisu et al., *Astrophysical Journal* **368**, L27 (1991).]

Energy must be delivered as sysmmetric as possible!

Rayleigh-Taylor Instability:

In ICF, Rayleigh Taylor instability is partially stabilised due to

- the presence of a density gradient ($\rho(x)=\rho_o \exp(-x/L)$) (less space for growth)
- plasma expansion (the "seeded instability" is transported away)

$$\gamma = \sqrt{\frac{Akg}{1+kL}} - \beta k v_{abl}$$ ***Takabe's formula***

- Short modes are stabilised ($\lambda << L$, i.e. $kL >> 1$)
- Large modes are not stabilised but they grow very slowly (λ is big and then k and γ are small)

The most dangerous modes are the intermediate ones

Rayleigh-Taylor Instability:

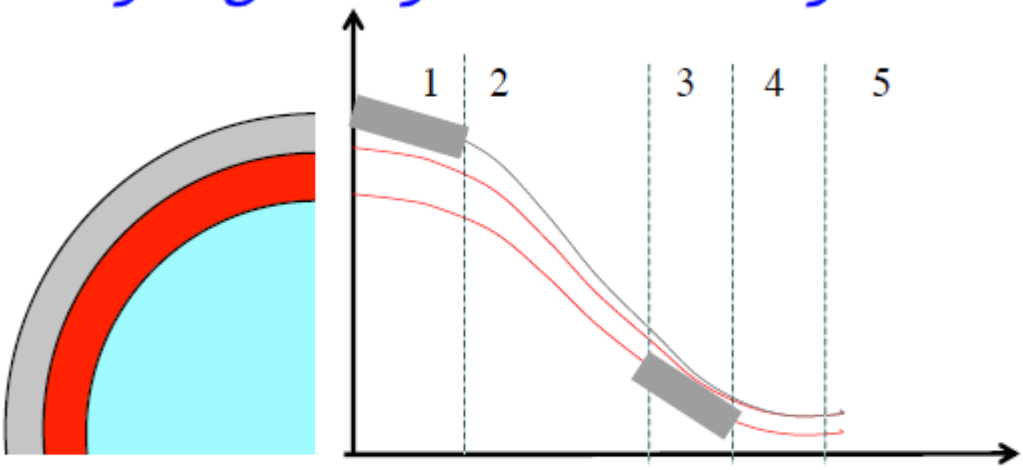

In ICF Rayleigh Taylor instabilities may develop:
1) during the acceleration phase (1) at the ablation front [the less dense plasma corona "pushes" the denser shell]
2) During the deceleration phase (3) at the shell/fuel inner interface [the less dense gas in the core pushes the imploding shell]

Good and bad news:

Experiments with GEKKO XII laser, Institute of Laser Engineering, University of Osaka, Japan

- **Experimental demonstration of compression of DT up to 600 × solid density** (Azechi et al., Las. Part. Beams, 1991)

- WE ARE ABLE TO OBTAIN DENSITIES DIRECTLY RELEVANT FOR ICF!
  However: number of neutrons much smaller than expected: The central hot spot was not generated
  WE ARE NOT ABLE TO COMPPRESS UNIFORMILY

Inertial confinement: direct vs. indirect drive

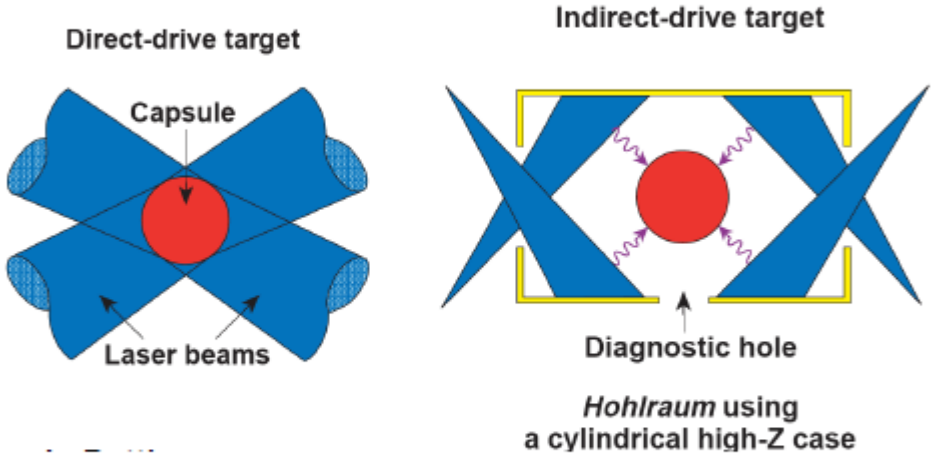

Direct: higher efficiency, more problems with uniformity
Indirect: better uniformity but reduction of efficiency

In both case you need MJ-class laser systems

National Ignition Facility (NIF) - layout

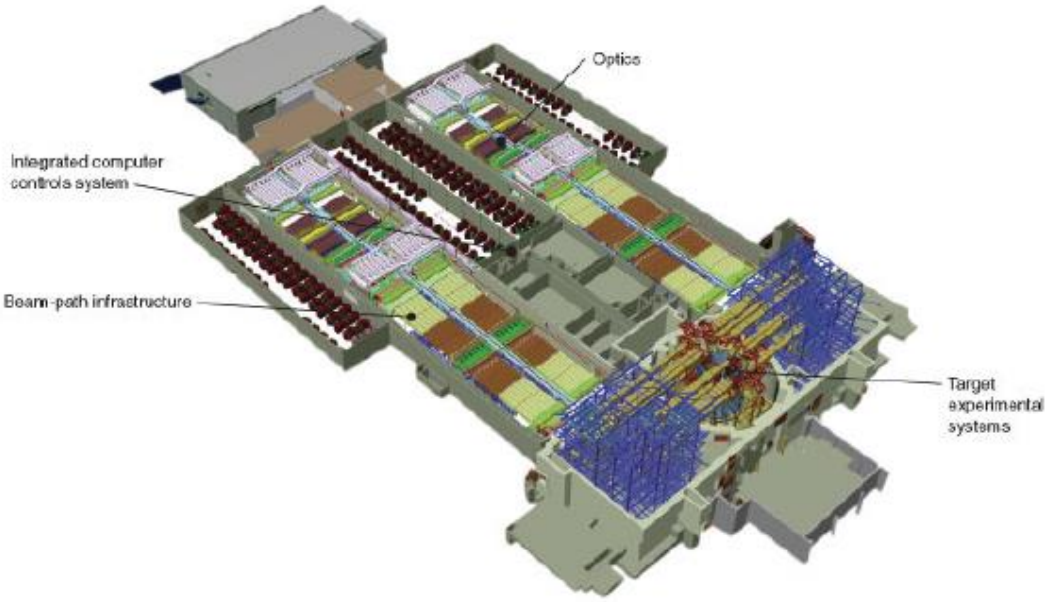

National Ignition Campaign (2009-2012)

- NIF @ 1.5 MJ. Designed for $G=E_{fusion}/E_{laser}$ =20
  $G=1$ implies $N_{neutron} \approx 5\ 10^{17}$ (but they only got $\approx 10^{15}$)

Problems:

- Incomplete EOS data of materials at high pressures in hydrodynamics simulations
- Incomplete data on opacities
- Underestimation of the impact of parametric instabilities in the gas inside the holhraum
- Significant problem on how to keep the pellet inside the holhraum
- Underestimation of impact of Rayleigh Taylor instability [Measured convergence ratio lower than predicted (using the implosion velocity extracted from experiment). The shell breaks before end of the implosion]

National Ignition Campaign (2009-2012)

- NIF @ 1.5 MJ. Designed for $G=E_{fusion}/E_{laser}$ =20
  $G=1$ implies $N_{neutron} \approx 5\ 10^{17}$ (but they only got $\approx 10^{15}$)

This clearly shows that the goal of achieving ignition is still a scientific challenge rather than a technological challenge.
As such it is somewhat "umpredictable"

(and this is true for MCF too...)

We finally have an implosion where a large fraction of the total fusion output is from α-particle self-heating

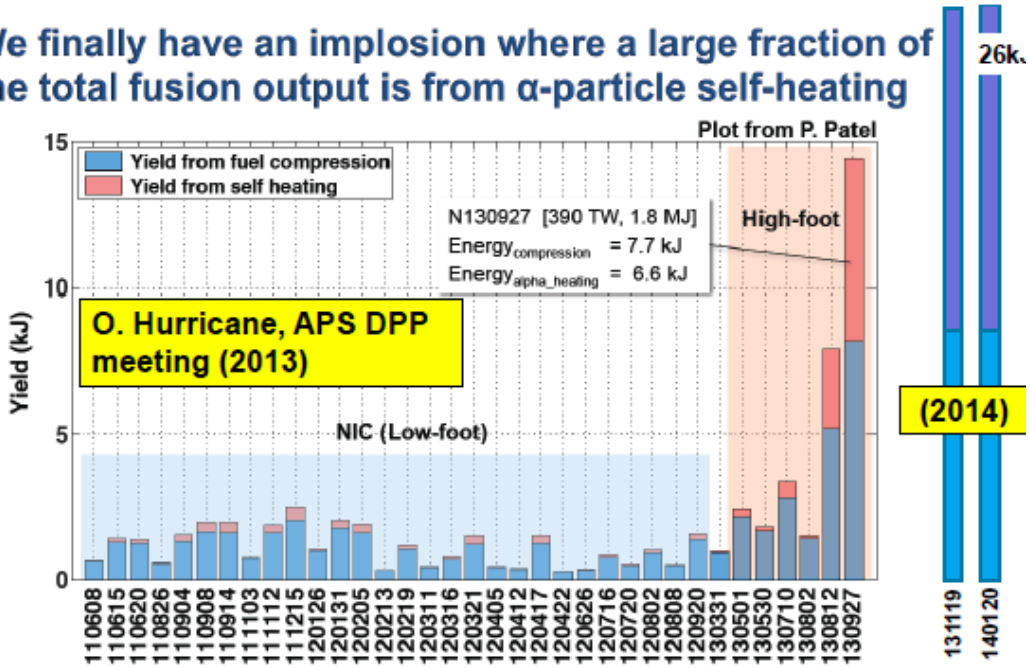

Joint WCI/NIF Team:
D. Callahan, E. Dewald, T. Dittrich,T. Doeppner, D. Hinkel, L. Berzak Hopkins, O. Hurricane, P. Kervin, J. Lee Kline (LANL), S. LePape, T. Ma, J. Milovich, J. Moody, A. Pak, H.-S. Park, B. Remington, H. Robey, J. Salmonson, NIF operations, NIF cryo, NIF targets, GA, LLE, & M.I.T.

Extremely interesting results after NIC (and bad pubblicity)

High-foot implosions (O.Hurricane, et al. Nature 2014) have allowed entering a novel "α-heating regime"

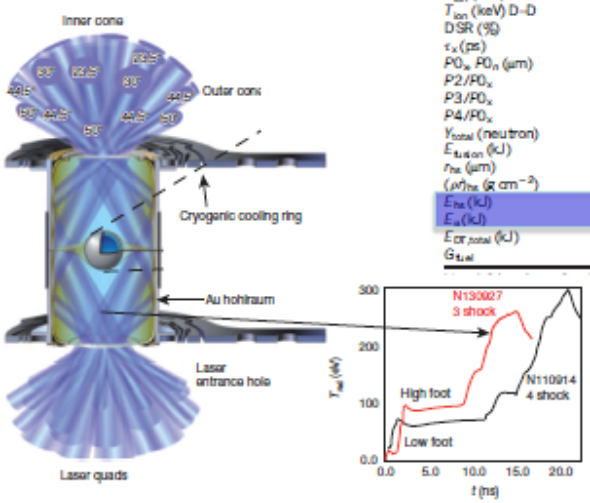

Quantity	N131119	N130927
Y_{13-15} (neutron)	$(5.2 \pm 0.097) \times 10^{15}$	$(4.4 \pm 0.11) \times 10^{15}$
T_{ion} (keV) D–T	5.0 ± 0.2	4.63 ± 0.31
T_{ion} (keV) D–D	4.3 ± 0.2	3.77 ± 0.2
DSR (%)	4.0 ± 0.4	3.85 ± 0.41
τ_x (ps)	152.0 ± 33.0	161.0 ± 33.0
$P0_x$, $P0_n$ (μm)	35.8 ± 1.0, 34 ± 4	35.3 ± 1.1, 32 ± 4
$P2/P0_x$	−0.34 ± 0.039	−0.143 ± 0.044
$P3/P0_x$	0.015 ± 0.027	−0.004 ± 0.023
$P4/P0_x$	−0.009 ± 0.039	−0.05 ± 0.023
Y_{total} (neutron)	6.1×10^{15}	5.1×10^{15}
E_{fusion} (kJ)	17.3	14.4
r_{hs} (μm)	36.6	35.5
$(\rho r)_{hs}$ (g cm^{-2})	0.12–0.15	0.12–0.18
E_{hs} (kJ)	3.9–4.4	3.5–4.2
E_{α} (kJ)	2.2–2.6	2.0–2.4
$E_{CR,total}$ (kJ)	8.5–9.4	10.2–12.0
G_{tot}	1.8–2.0	1.2–1.4

This also shows that the MAIN problem towards ignition is REALLY the impact of hydro instabilities related to non-uniformities

The best NIF implosions used the High-Foot laser pulse that drives stronger shocks in the "foot"

O. Hurricane, APS DPP meeting (2013)

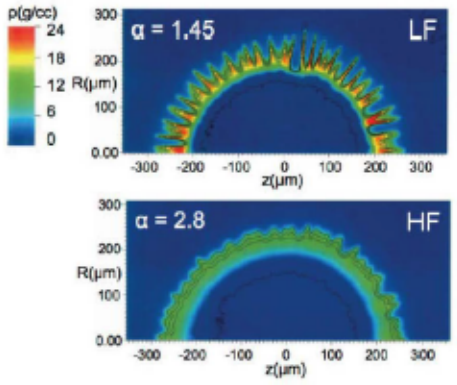

The high foot pulse set the imploding shell on a higher isentrope α (nothing to do with α-particles) because it launches stronger shocks in the "foot" of the pulse

$$\gamma = \sqrt{\frac{Akg}{1+kL}} - \beta k v_{abl}$$

Increase with α

High-foot growth-factor calculations and simulations are consistent with the expectation of less instability

Very recent results on NIF

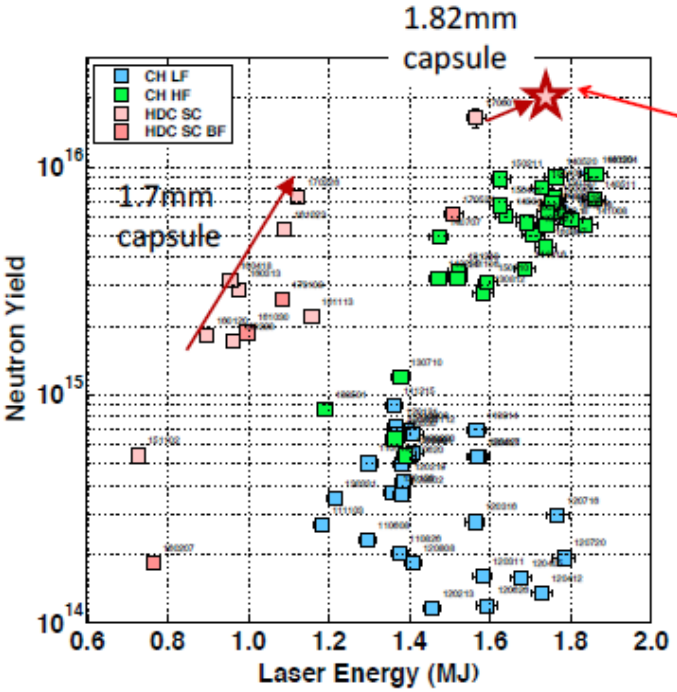

W-doped HDC capsule driven in a low-gas-fill hohlraum 390 km/s, 2e16, 57 kJ of fusion yield, more than 2x α-heating

Near Vacuum Hohlraums reduce Laser-Plasma-Instabilities

HDC (diamond) or Beryllium Ablator have greater hydrodynamic efficiency allowing a more massive (and more stable) shell to be imploded

Rugby holhraum

NIF and indirect drive

The National Ignition Facility (NIF) maybe able to demonstrate the scientific feasibility of nuclear fusion. This will be an enormous scientific achievement !
However.... NIF is based on INDIRECT DRIVE which does not seem compatible with requirements for fusion reactors:

- Complicated targets
- Massive targets (lot of high-Z material in chamber)
- Above all: intrinsic low gain due to X-ray conversion.

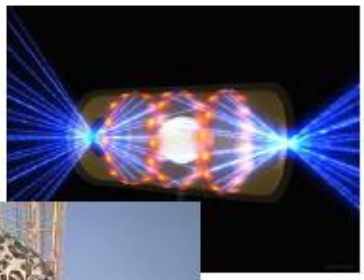

In addition, indirect drive poses "political" problems...
Therefore we need DIRECT DRIVE

Shock ignition: a final laser spike launches a converging shock

Conventionnal direct drive

450 TW, 1.5MJ pulse

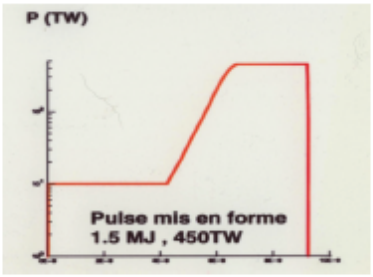

High Aspect ratio target
V ~400 km/s

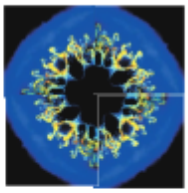

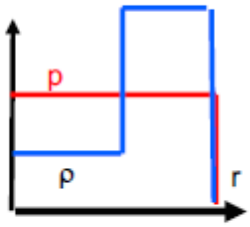

Produces an Isobaric fuel assembly

Low velocity drive

220 TW
Ignition spike

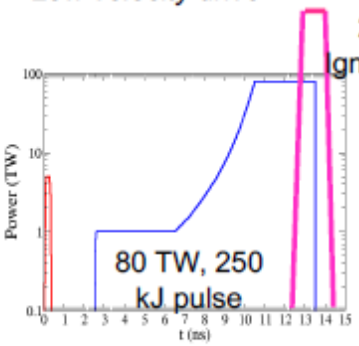

Low AR V~240 km/s

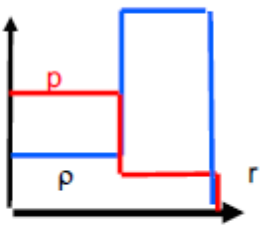

Fuel assembly is non isobaric

Physics of laser-driven proton acceleration

Fast electrons are produced by the laser and escaping from the target rear create a space charge which ionizes the material and accelerate protons

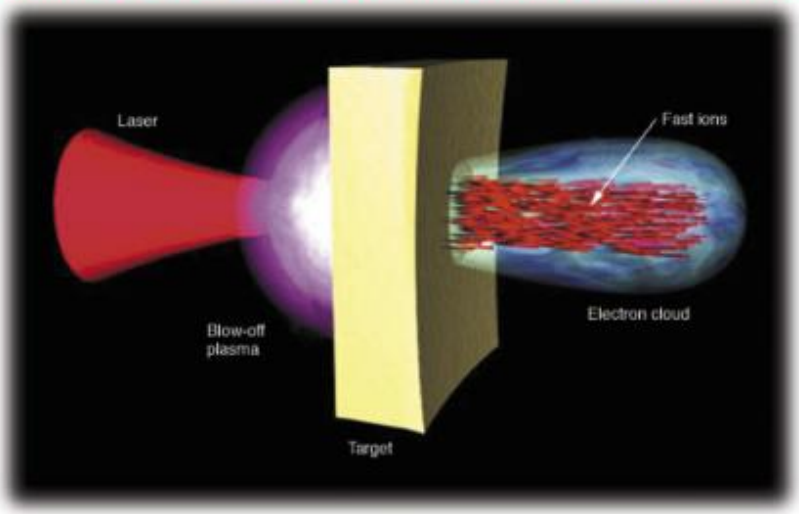

TNSA (Target Normal Sheat Acceleration) Mechanism

Role of CH / H_2O contamination

In laboratory experiments, the Petawatt laser's tremendous power produced intense beams of protons, proving the laser to be a powerful ion accelerator.

Radiochromic films

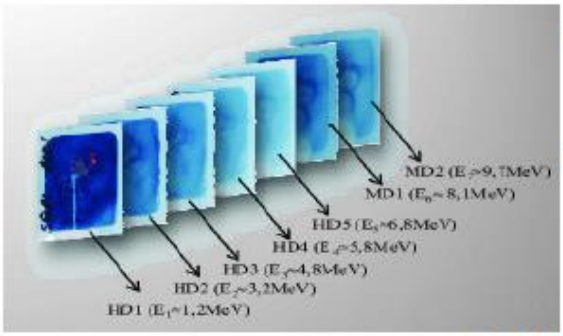

- The detector is made by a series of active layers placed one after each other
- The final (OD) profiles across a given layer is MAINLY due to the protons with Bragg peak corresponding to that layer

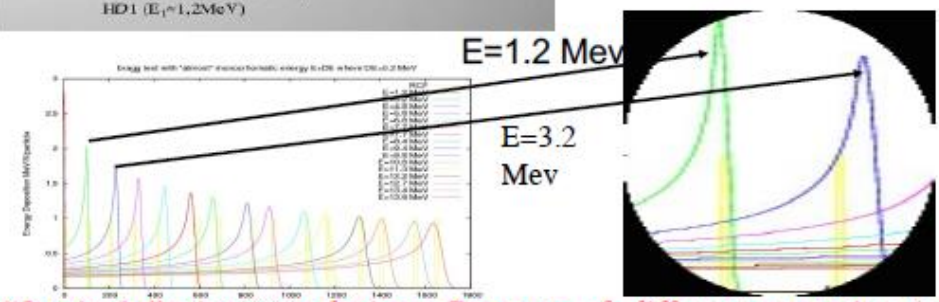

"Intrinsic" time resolution: Protons of different energies (non monochromatic spectrum!) travel at different velocities and hence probe the plasma at different times

Principle of Proton radiography

- Protons deposit most of energy at the end of their travel
- Protons with different energy arrive at different time to the cylinder and at different position inside the detector
- Different time delay for each shot

$$\tau = delay + TOF$$

$$TOF = \frac{d}{V} = \frac{d}{\sqrt{\frac{2E_p}{m_p}}}$$

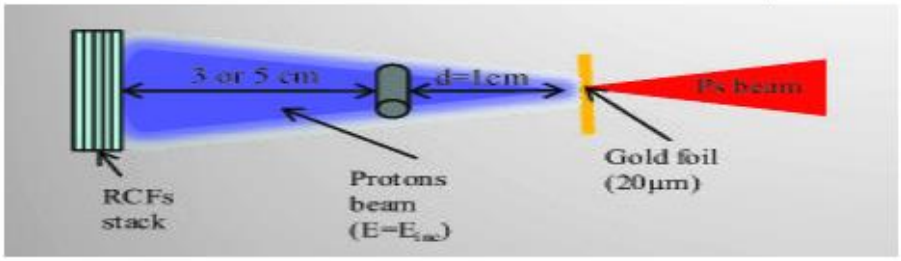

$$E_1 < E_2 < .... < E_N$$

$$\tau_1 > \tau_2 > .... > \tau_N$$

(pioneering works by M.Borghesi et al.)

Protons: diagnostics of electric and magnetic fields

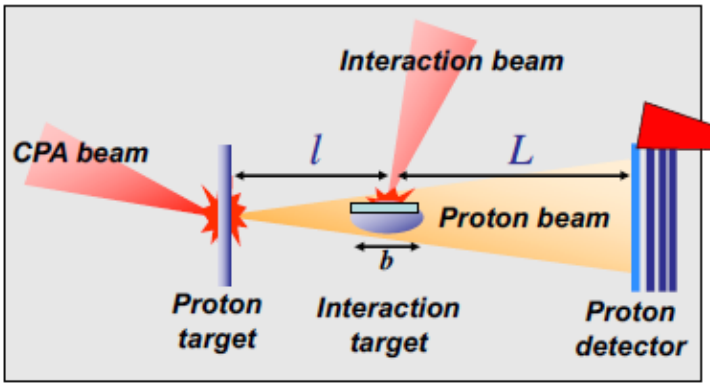

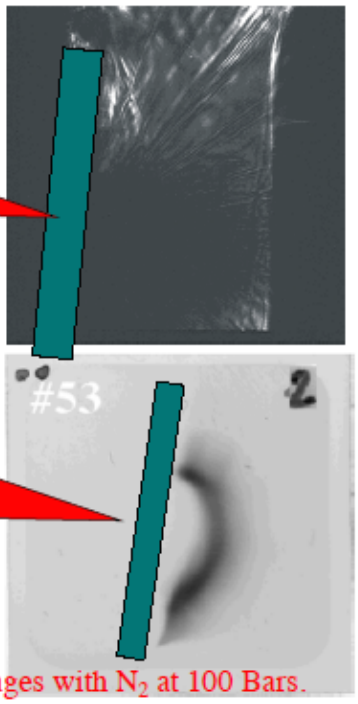

Comparison of shadowgraphy image and proton image

Electric fields localised at ionisation front moving in the gas

Proton images with N_2 at 100 Bars.

43

Protons: diagnostics of electric and magnetic fields

PHYSICS OF PLASMAS 16, 033104 (2009)

Laser-driven fast electron dynamics in gaseous media under the influence of large electric fields

D. Batani,[1] S. D. Baton,[2] M. Manclossi,[1] D. Piazza,[1] M. Koenig,[2] A. Benuzzi H. Popescu,[2] C. Rousseaux,[3] M. Borghesi,[4] C. Cecchetti,[4] and A. Schiavi[5]

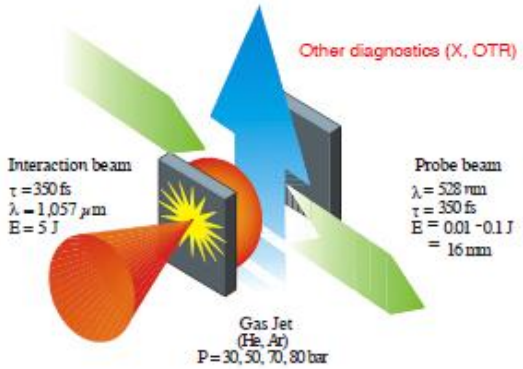

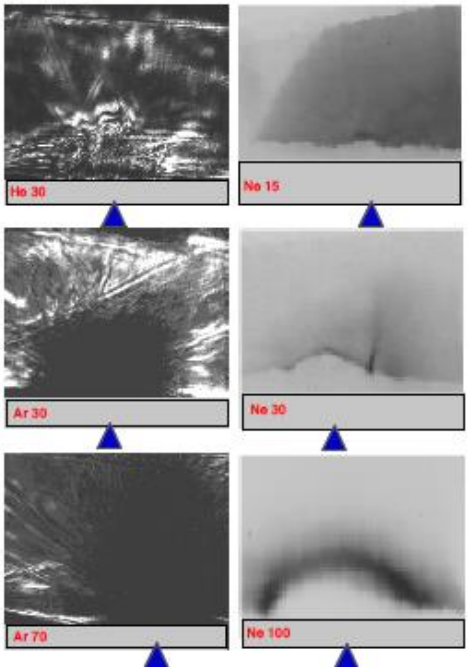

44

Proton radiography of shock propagation

PHYSICAL REVIEW E 82, 016407 (2010)

Proton radiography of a shock-compressed target

A. Ravasio,[1] L. Romagnani,[2] S. Le Pape,[3] A. Benuzzi-Mounaix,[1] C. Cecchetti,[2] D. Batani,[4] T. Boehly,[5] M. Borghesi,[2] R. Dezulian,[4] L. Gremillet,[6] E. Henry,[6] D. Hicks,[3] B. Loupias,[1] A. MacKinnon,[3] N. Ozaki,[1] H. S. Park,[3] P. Patel,[3] A. Schiavi,[7] T. Vinci,[1] R. Clarke,[8] M. Notley,[8] S. Bandyopadhyay,[8] and M. Koenig[1]

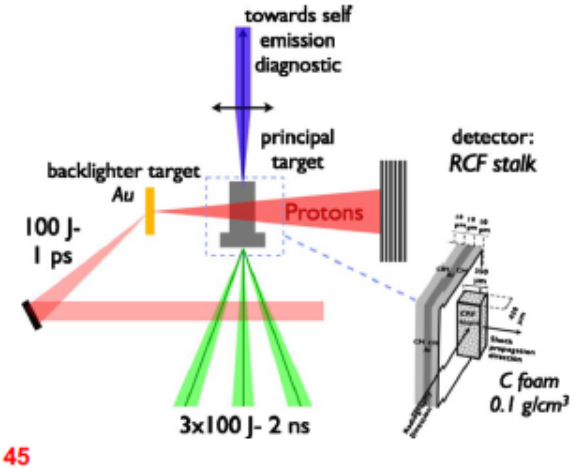

Radiography from ≈7 MeV protons

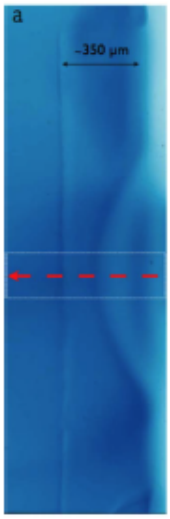

45

Proton radiography of imploding targets

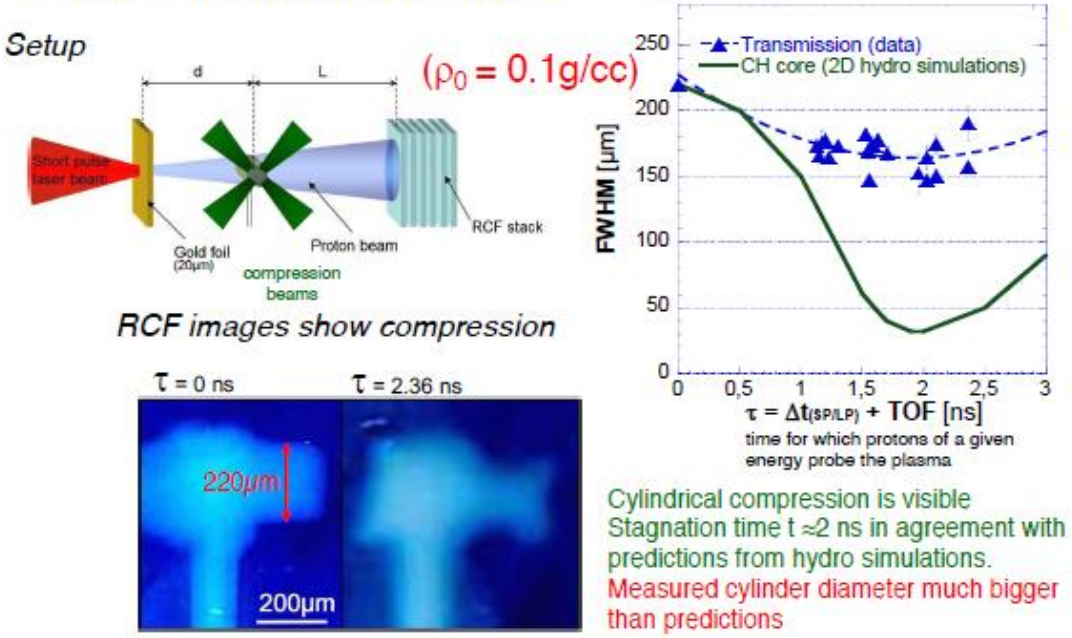

Cylindrical compression is visible
Stagnation time t ≈2 ns in agreement with predictions from hydro simulations.
Measured cylinder diameter much bigger than predictions

- Protons seem not to be able to probe the dense region. Should we trust results?

46

Simulations with MCPNX

Proton radiography has been simulated with MCNPX taking into account plasma effects in the extended corona and image mixing

Uncompressed cylinder target (Reference case)

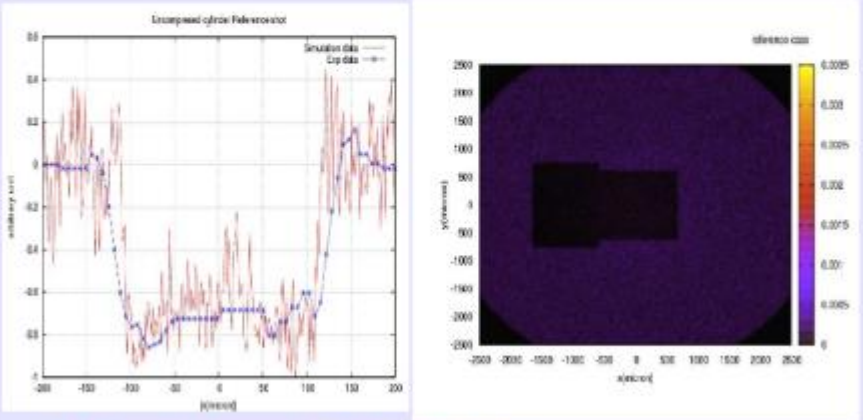

- Very good agreement with reality
- diameter(detector)=diameter(real)*magnification

Simulations with MCPNX

For compressed cylinders, there is ***severe multiple scattering and proton energy loss in the target producing image mixing***. Detailed comparison with synthetic images produced by codes is needed

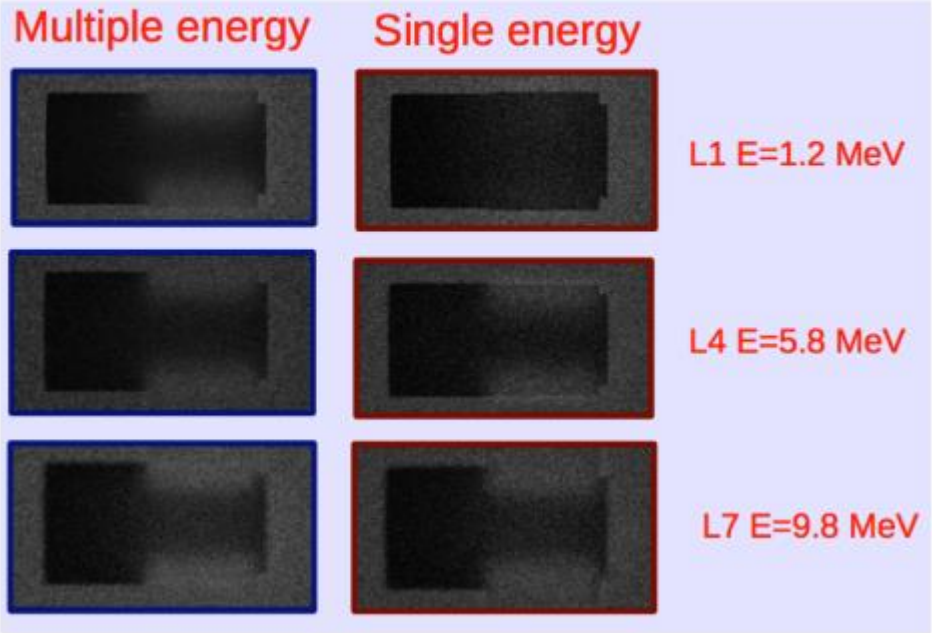

3

Proton radiography of imploding targets

PHYSICS OF PLASMAS 18, 012704 (2011)

Proton radiography of laser-driven imploding target in cylindrical geometry

L. Volpe,[1] D. Batani,[1,2] B. Vauzour,[3] Ph. Nicolai,[3] J. J. Santos,[3] C. Regan,[3] A. Morace,[4] F. Dorchies,[3] C. Fourment,[3] S. Hulin,[3] F. Perez,[5] S. Baton,[5] K. Lancaster,[6] M. Galimberti,[6] R. Heathcote,[6] M. Tolley,[6] Ch. Spindloe,[6] P. Koester,[7] L. Labate,[7] L. A. Gizzi,[7] C. Benedetti,[8] A. Sgattoni,[8] M. Richetta,[8] J. Pasley,[9] F. Beg,[10] S. Chawla,[10] D. P. Higginson,[10] and A. G. MacPhee[11]

- Scattering in dense matter causes loss of resolution
- Energy loss in dense matter produces "mixing" of protons emitted at different times

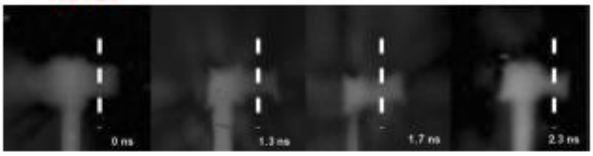

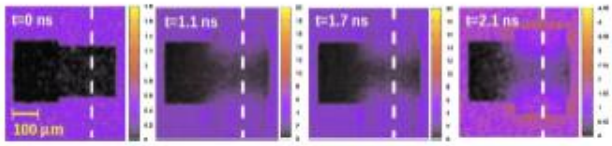

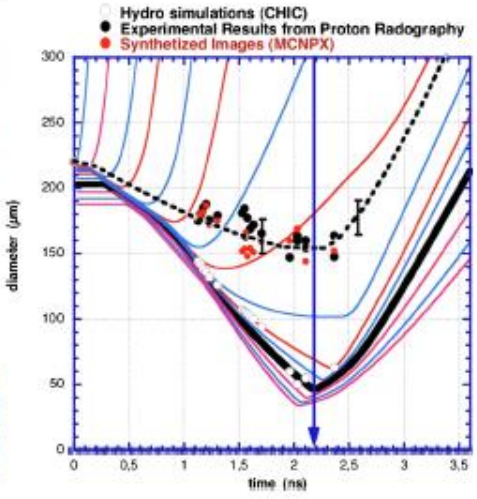

Simulations with MCPNX

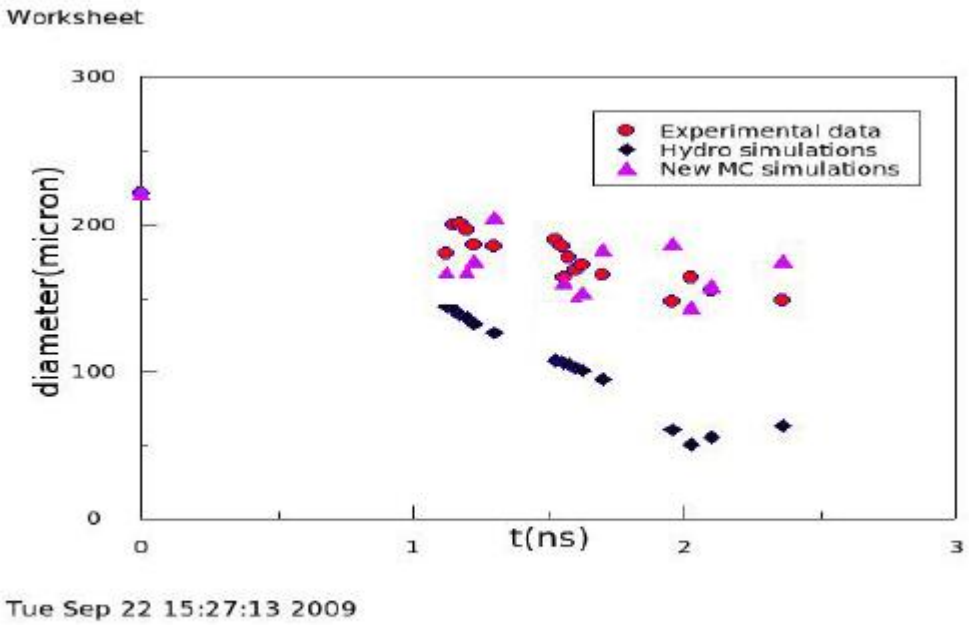

Experimental data are well reproduced by MC (MCNPX) simulations without the need of including *exotic* effects

Pin-hole Camera

A small hole in an opaque screen produces an image (in the limit of very small holes only 1 ray from each point source passes, creating the image)

$$M = \frac{A'B'}{AB} = \frac{p}{q}$$

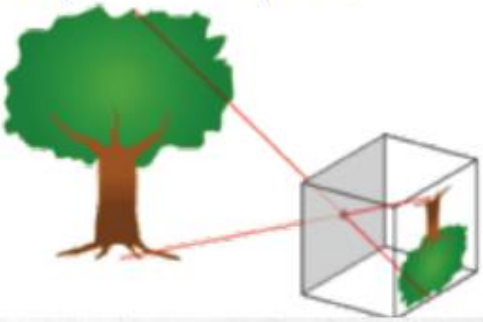

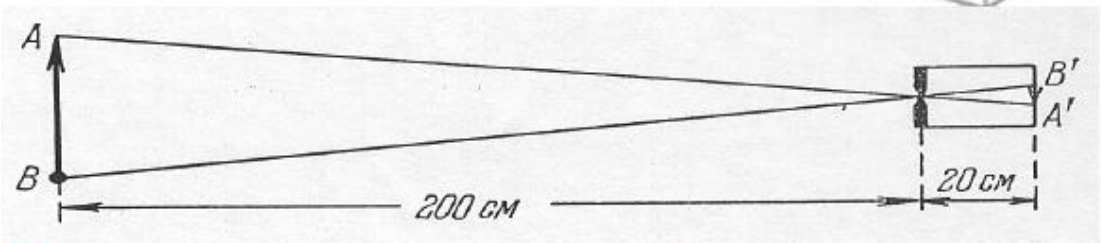

52

q

2D plasma image

Plasma size increases with laser energy

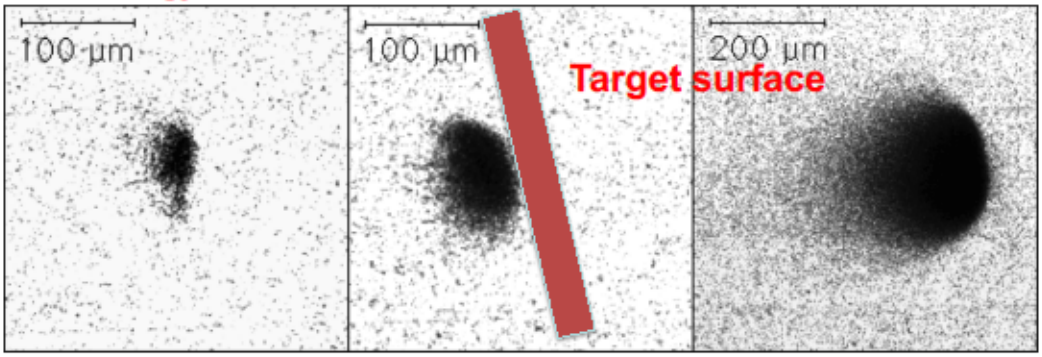

- **Non monochromatic images**
- **Need to place an X-ray filter on pin-hole to stop visible light and XUV**
- **Need to take the viewing angle into account**
- **Resolution implies small pin-hole which means very low flux**

53

Spherically bent crystal

X-ray reflection, in the energy range 1-10 keV, is achievable using crystals following the well known Bragg law of reflection

$$2d \sin\Theta = n\lambda$$

Spherically bent crystals allow 2D spatial resolution of the x-ray source,

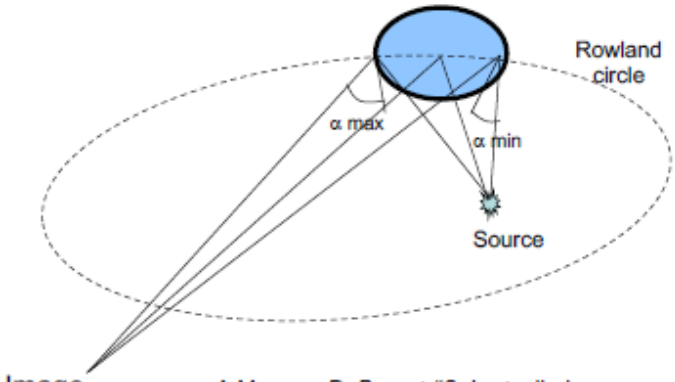

Some suitable crystals

Quartz 211, 3.082 Å, Cu Ka

Quartz 203, 2.749 Å, Ti Ka

Quartz 203, 2.749 Å, Sc Lya

A.Morace, D. Batani "Spherically bent crystal for X-ray imaging of laser produced plasmas" Nuclear Instruments and Methods in Physics Research A , 623:22, 797-800, Elsevier BV, 11 (2010)

54

Experiment on fast electron propagation at RAL (laser Vulcan)

"Fast ignition" approach to ICF

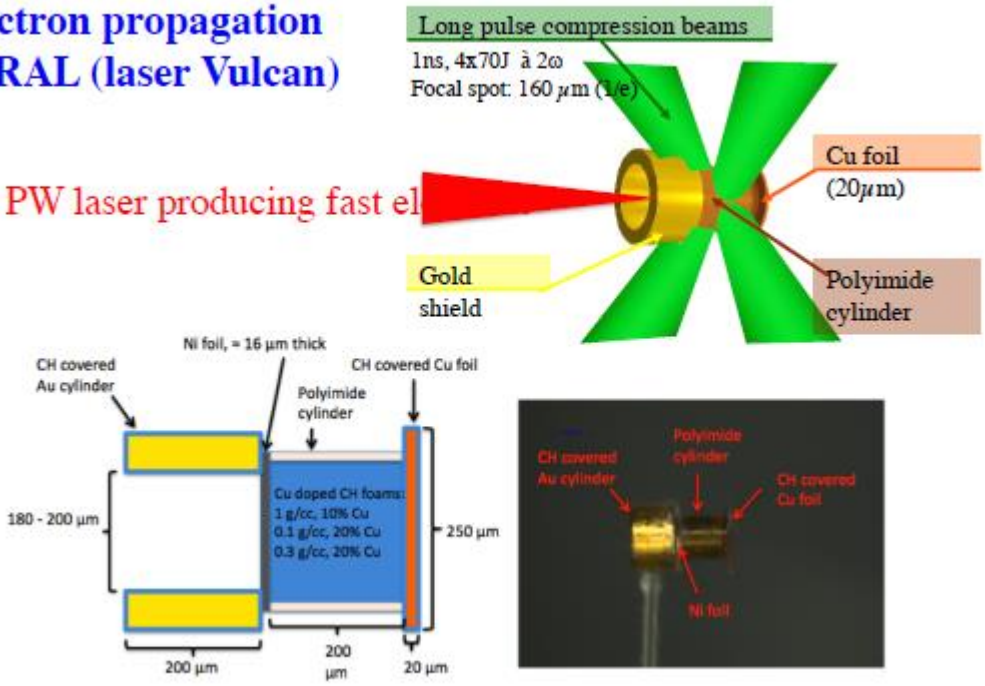

Cross section Actual Target

K-shell ionization and K-α emission

The Kα emission from the target tracks the fast elctron beam transport

A fast electron ionizes the inner shell of an atom in the propagation medium

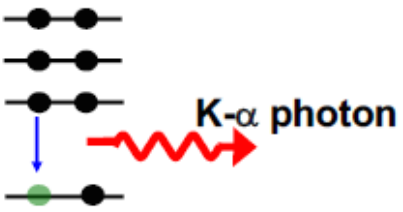

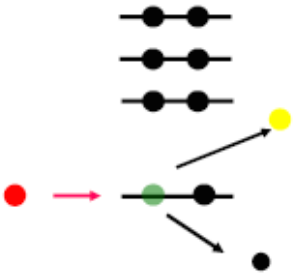

The atom in the subsequent recombination process emits a photon called Kα photon, the emission is completely isotropic

Is therefore possible, by imaging the x –ray source, to get spatial information on the fast electron beam propagation into the target

Cu Kα images

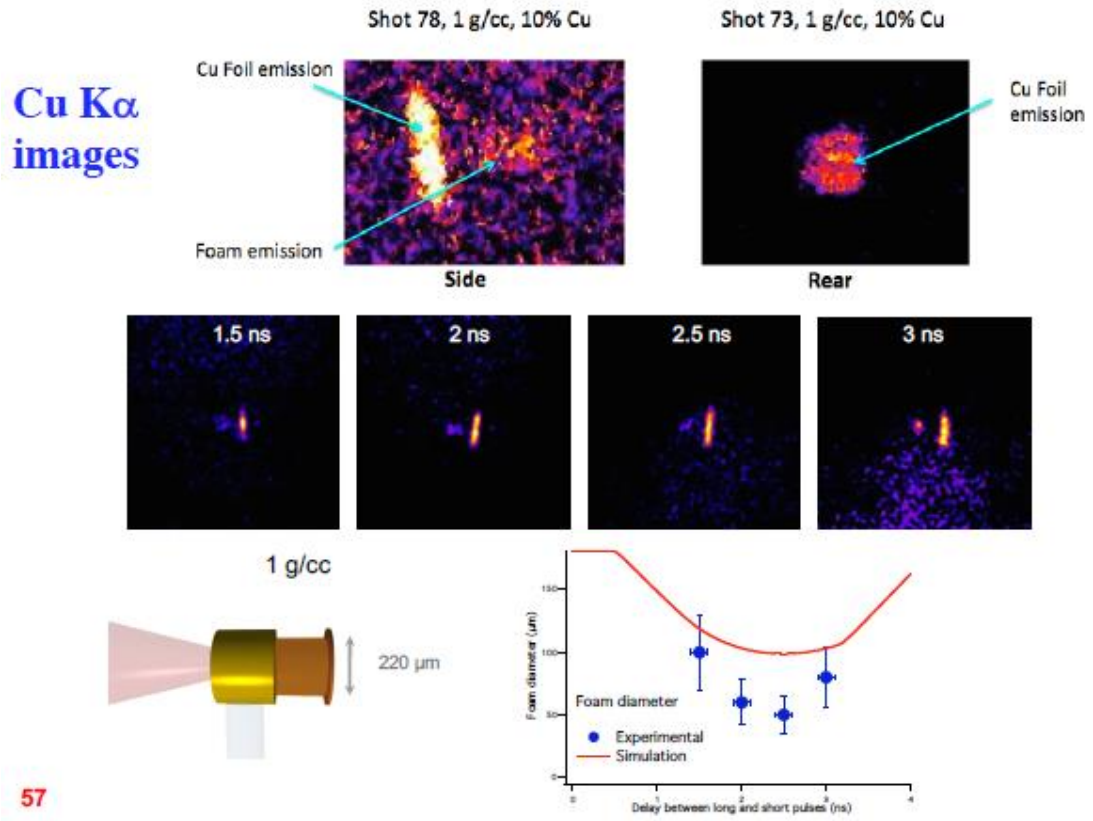

57

Cone-wire targets

Cone-wire targets from "fast electron transport" experiment at TAP

The wires are 400 μm long

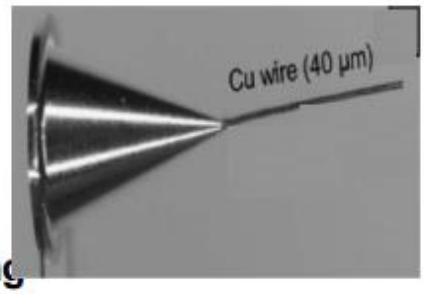

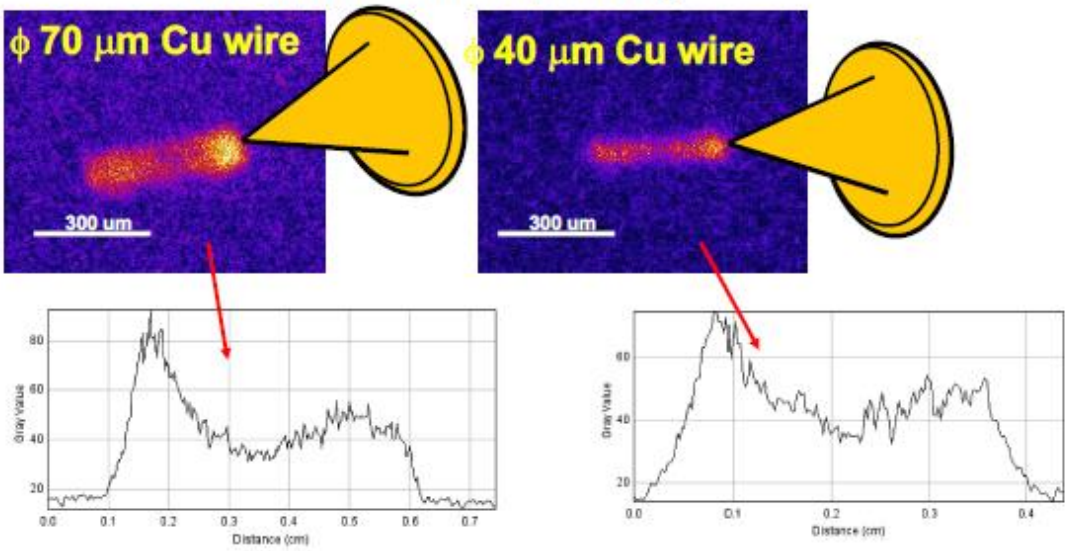

Bandwidth

The bandwidth collected by the crystal is limited by geometrical factors as magnification M, curvature radius R and aperture D

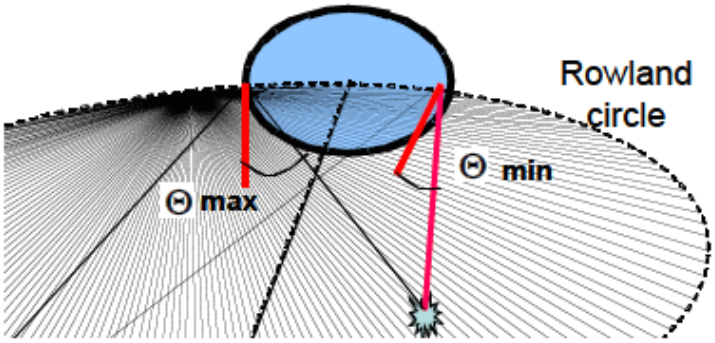

For example, R=38 cm, M= 7.8 and D=16 mm (Cu alignment 1.37) the minimum angle is ~ 0.3° and the maximum 2.25°

This corresponds to a spectral bandwidth of 6 eV, from 8046 to 8052

Actually the bandwidth is usually less that the width of the Kα line !

See for example : Akli et al. Phys. Plasmas **14**, 023102 2007

Bandwidth

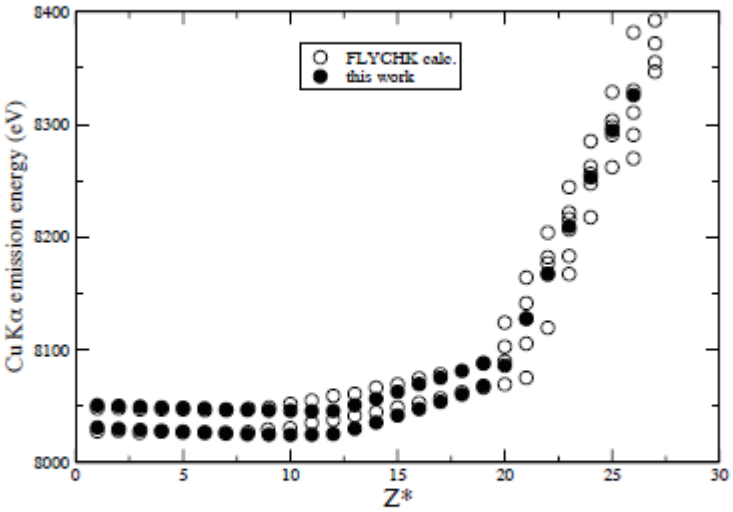

Target heating induces a blue shift of the Kα line and this corresponds to a reduction of the collected signal

See for example : Akli et al. Phys. Plasmas **14**, 023102 2007

Limits to resolution

The dominant factor that influences the resolution is the bending process

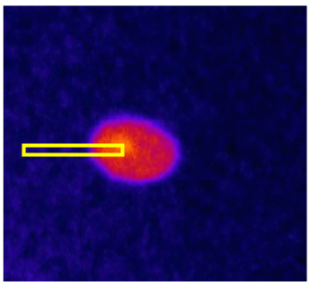

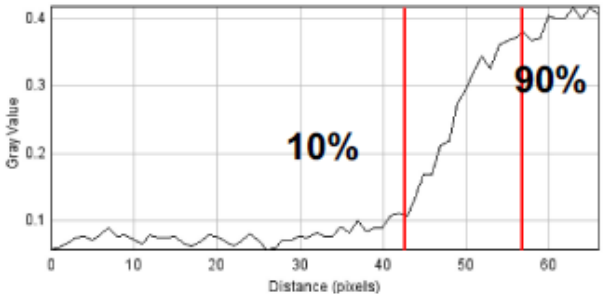

Take the lineout from the 10% to the 90%

$$\frac{d}{dx} f(x)$$

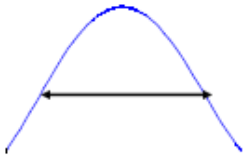

61 **Or fit the hard edge profile, calculate the derivative and take its FWHM**

Astigmatism

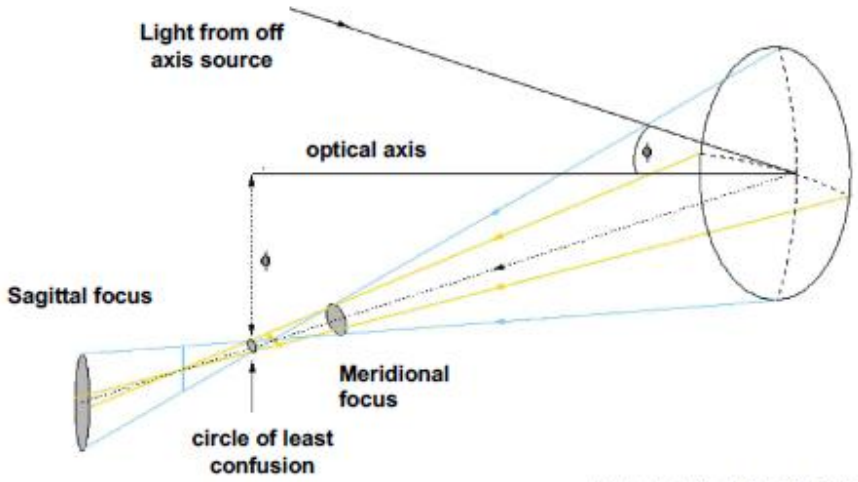

Koch et al. Appl. Opt. 37, 1784 (1998)

Koch et al. Rev. Sci. Inst. 74, 2130 (2003)

A resolution of 3 μm has been demonstrated by Aglitskji

PALS: accurate hot electron characterization

Simultaneous characterisation by: i) X-ray imaging, ii) X-ray spectroscopy, iii) Bremsstrahlung cannon

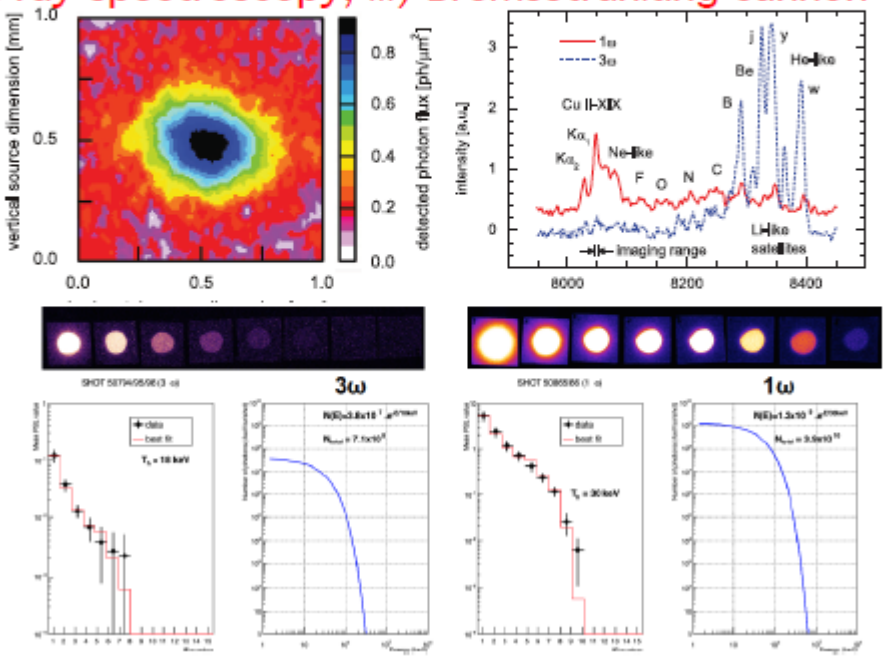

Astigmatism free imaging

It is possible to avoid almost completely the astigmatism using thoroidally bent crystals for imaging, these were not available 10 years ago

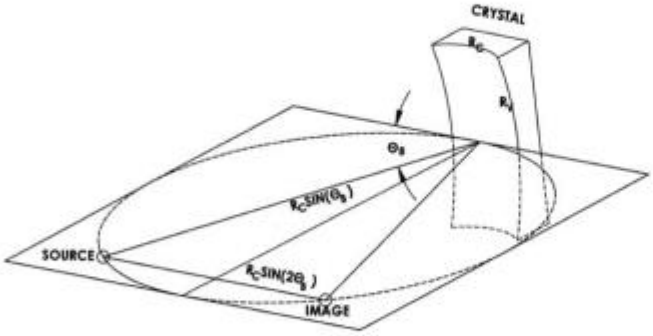

Thoroidal crystal can correct the astigmatism providing two different curvature radii for meridional and sagittal planes

Alignment procedure is much more complex because it introduces constraints on all the 6 degrees of freedom and its quite expensive: 20 k$

PALS: accurate hot electron characterization

Hot electrons: results

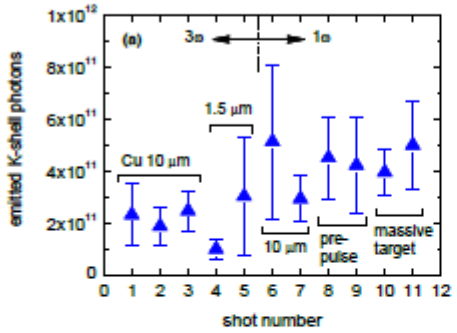

Photon fluxes reconstructed from x-ray images for ΔE=100

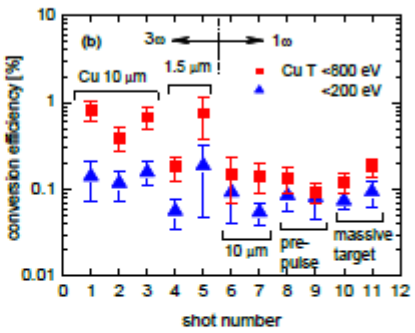

Laser energy conversion efficiency into hot electrons. Diverse Cu targets were irradiated by 1ω and 3ω lasers focused to diameter 100 μm.

HE characteristics at 3ω and 1ω irradiation deduced from this work.

	3ω, $E_{laser} \approx 200J$	1ω, $E_{laser} \approx 650J$
T_{e-} (keV)	20^{+15}_{-8}	38^{+57}_{-12}
$\varepsilon_{laser \rightarrow e-}$ (%)	$0.14^{+0.14}_{-0.03}$	$2.66^{+3.45}_{-0.13}$

Laser Megajoule

≥ 20% of shots will be allocated for civilian academic research oriented towards fusion for energy

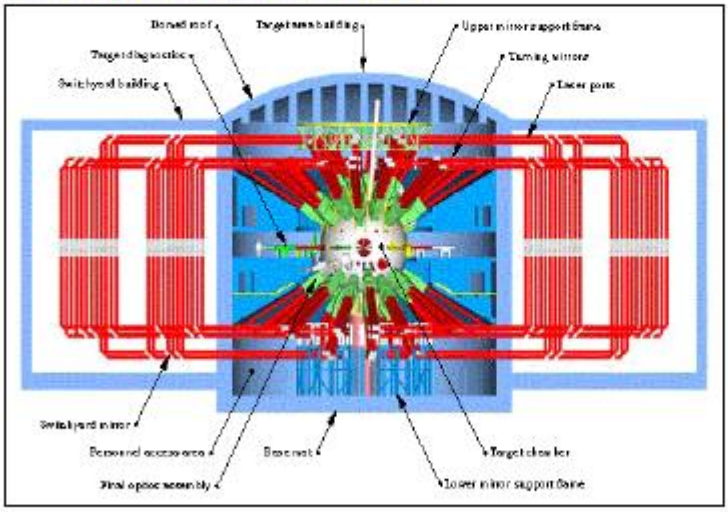

Nd:glass
2 MJ
10 ns
160 beams

Goal:
Performing shock ignition demonstration experiments

LMJ/PETAL: Configuration 2019

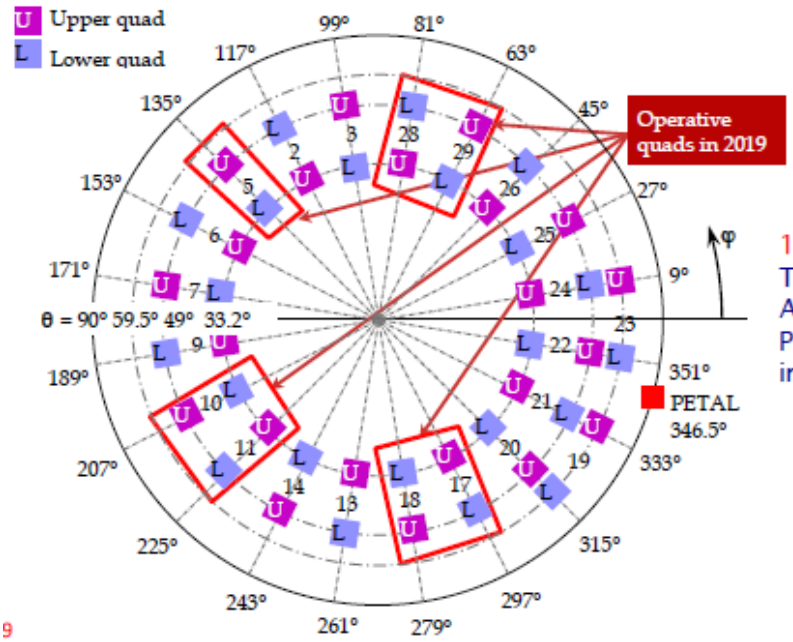

14 Quad LMJ
Total Energy normally Available ≈ 200 kJ,
Possibility of different irradiation geometries

9

LMJ/PETAL

PETAL
Energy ≈ 3.5 kJ,
Wavelength: 1053 nm,
Duration: 0,5 ps to 10 ps,
Intensity: > 10^{20} W/cm^2
(in a first phase energy delivered to TCC is ≈ 1 kJ)

Quad LMJ
Energy ≈ 30 kJ, Wavelength: 351 nm,
Duration: a few ns,
Intensity on target: > a few 10^{15} W/cm^2

Configuration 2017

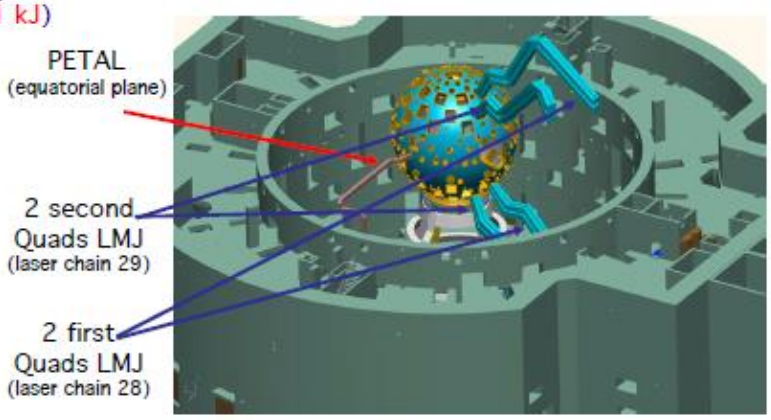

68

PETAL, a laser for Academic research

"PETAL" stands for "PETawatt Aquitaine Laser", a petawatt laser coupled with LMJ facility for civilian research

The development of the system has been funded by "Région Aquitaine" with contribution from the French national government and the E.U. (total budget 54.3 M€)

The Region Aquitaine is the contracting owner of the PETAL facility

CEA is the prime contractor of the PETAL system which is constructed on the CESTA site of Le Barp (near Bordeaux)

The laser system

The pre-amplification module of PETAL

Characteristics of the PETAL laser system

- Energy * 3.5 kJ,
- Wavelength : 1053 nm,
- Duration 0,5 ps - 10 ps,
- Intensity on target 10^{20} W/cm^2,
- Intensity contrast : 10^{-7} at -7 ps,

* Limited to 1 kJ at the moment due to damage threshold of mirros

PETAL, a laser for Academic research

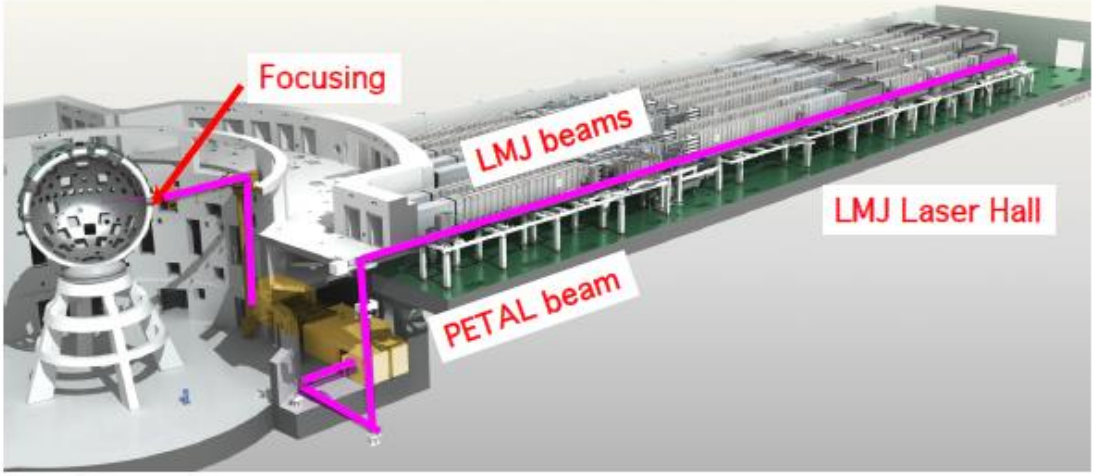

PETAL

- PETAL: coupling a PW laser to LMJ

The pre-amplification module of PETAL

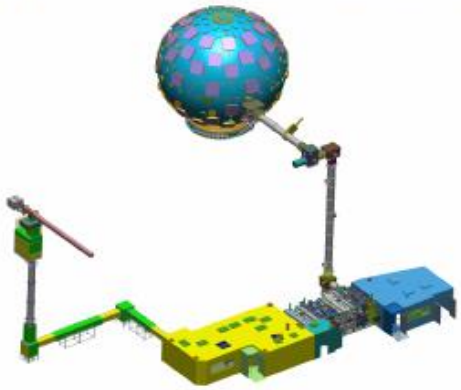

SID: Diagnostics inserter on LMJ/PETAL

Need for remote handling & remote control…

Example of insertion system (SID) on LMJ interaction chamber

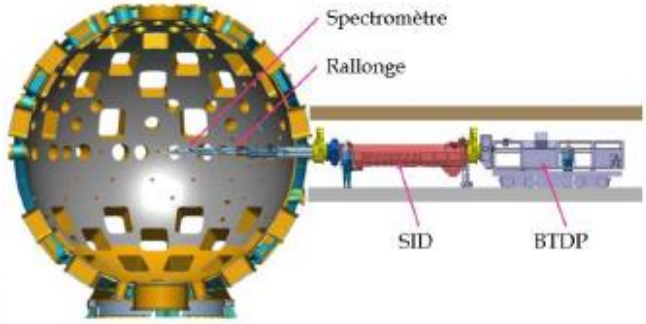

5

EquipEx PETAL+ "Realisation of first plasma diagnostics for LMJ/PETAL"

SEPAGE: A Thomson Parabola for:
- Ions/protons in the 100 keV – 200 MeV range
- Electrons in the 100 keV-100 MeV range

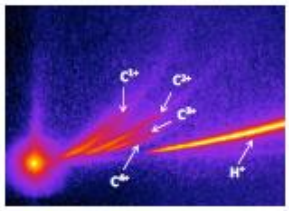

SESAME:
Electron spectrometers for 0.1 – 150 MeV with 10% Spectral resolution

SPECTIX: Crystal cylindrical crystal transmission X-ray spectrometer for 5-100 keV with $\Delta\lambda/\lambda$ = 1/300 (Cauchois geometry)

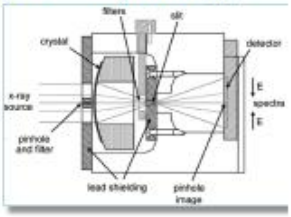

CRACC: radiographic cassette Stacks of radiochromic films or IP for proton / X-ray radiography using PETAL as a backlighter source

74

Generation of protons

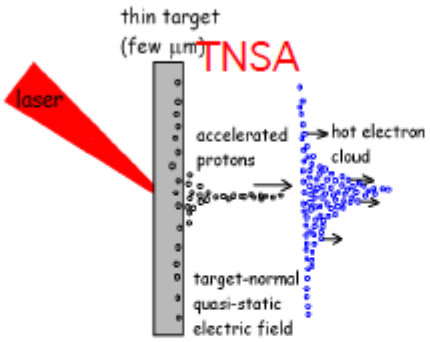

Estimation of Proton emission from a 10-μm plastic target irradiated with PETAL from 2D PIC simulations using the code PICLS

Proton divergence distribution for protons with an energy > 40 MeV in the forward direction

(Comparable to the 50 MeV obtained on Omega EP by K. Flippo et al. with 1kJ but with a longer pulse duration)

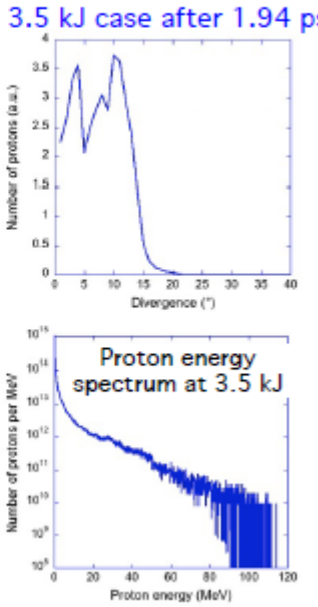

Radiographic cassette

- Functions: measurement of the divergence of the proton beam as a function of energy on ~45° (100 mm from TCC).
- Stacks of radiochromic films or IP for proton / X-ray radiography using PETAL as a backlighter source
- Hole in the centre to allow for proton spectroscopy
- Dimensions : 100x100 mm²
- 20 radiochromic films separated by filters in Aluminum and tungsten to cover the energy range between ~1 MeV and 200 MeV.

- Mass : 5 kg (without suppport, total allowed mass 10 kg)

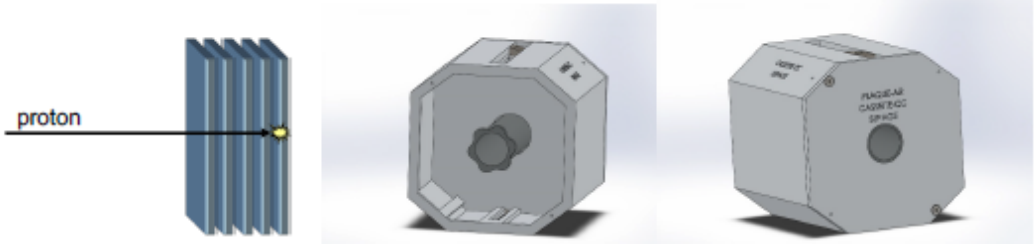

First PETAL shots (400J) Radiography

Target 25 µm Au 30 mm rom TCC + 2 µm Au + grid at TCC
LASER 400 J / 1000 fs / focal spot to be improved
PETAL shot on 24/10/2017

SESAME

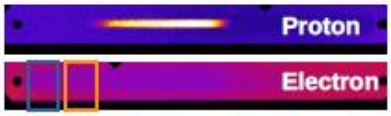

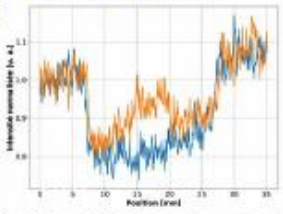

Electron signal very weak but present

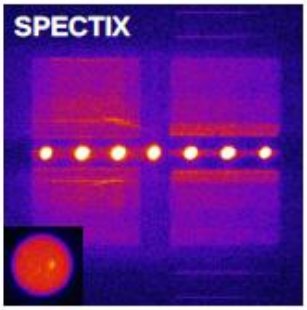

CRACC

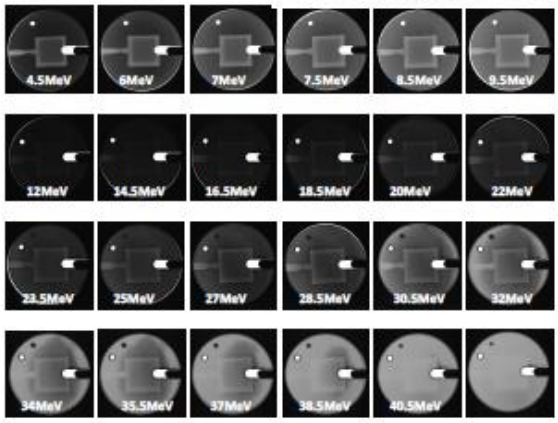

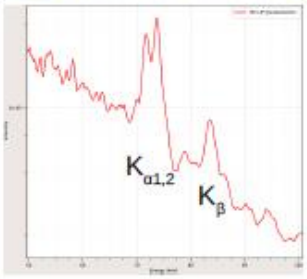

IP in position 2 to improve spectral resolution at high photon energy

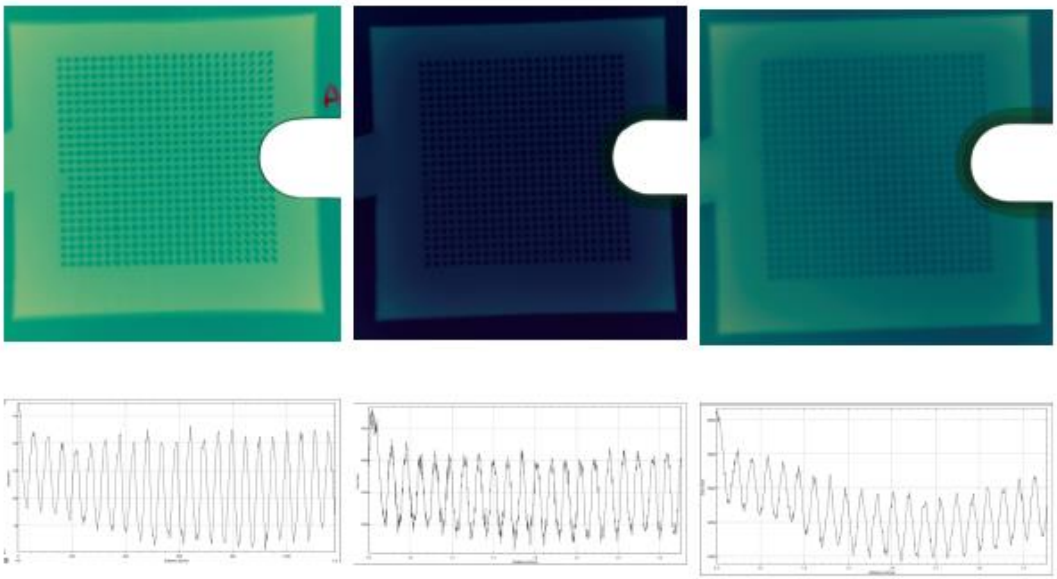

9,5 MeV **18,5 MeV** **30,5 MeV**

First PETAL shots (400J) Radiography

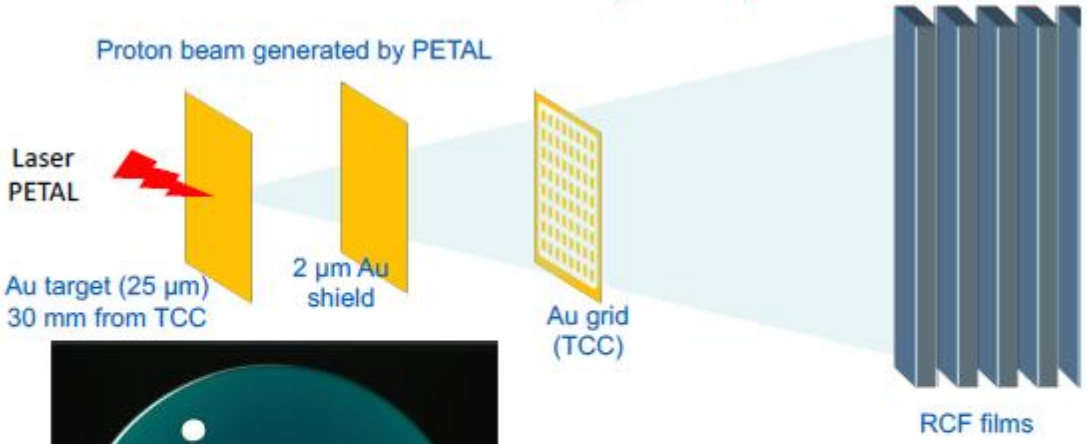

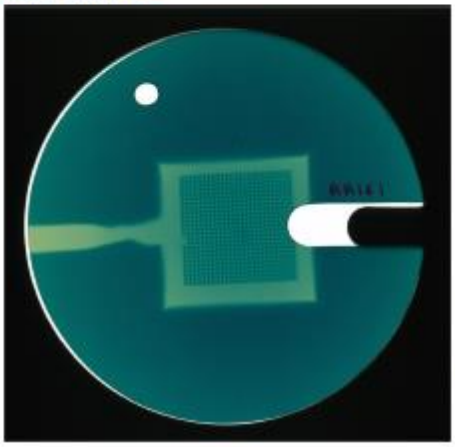

Grid:
Surface 7x7 mm^2
Thickness 50 μm
Pitch 200 µm
Wire size 100 μm

SEPAGE

A Thomson Parabola for:
- Ions/protons in the 100 keV – 200 MeV range
- Electrons in the 100 keV-100 MeV range

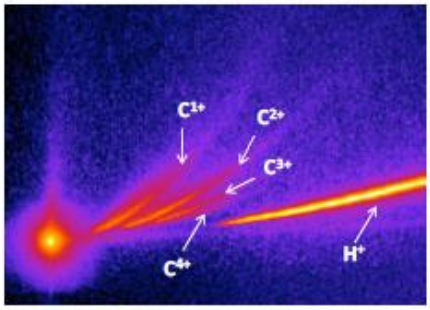

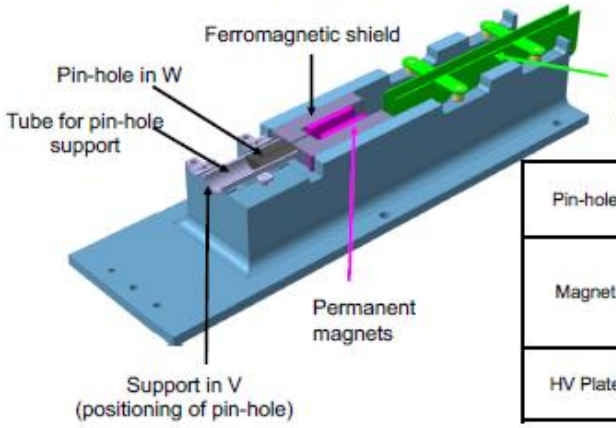

		Low Energy	High Energy
Pin-hole	diameter	200 µm	500 µm
	length	4 mm	40 mm
Magnet	B field	0,05 T	0,5 T
	Material	Ferrite	NdFeB
	Gap	33 mm	12 mm
HV Plate	E field	1,3 kV/mm	2,5 kV/mm
	Voltage	± 25 kV	± 13 kV

Calibration of the low-energy channel Thomson parabola of PETAL+/SEPAGE

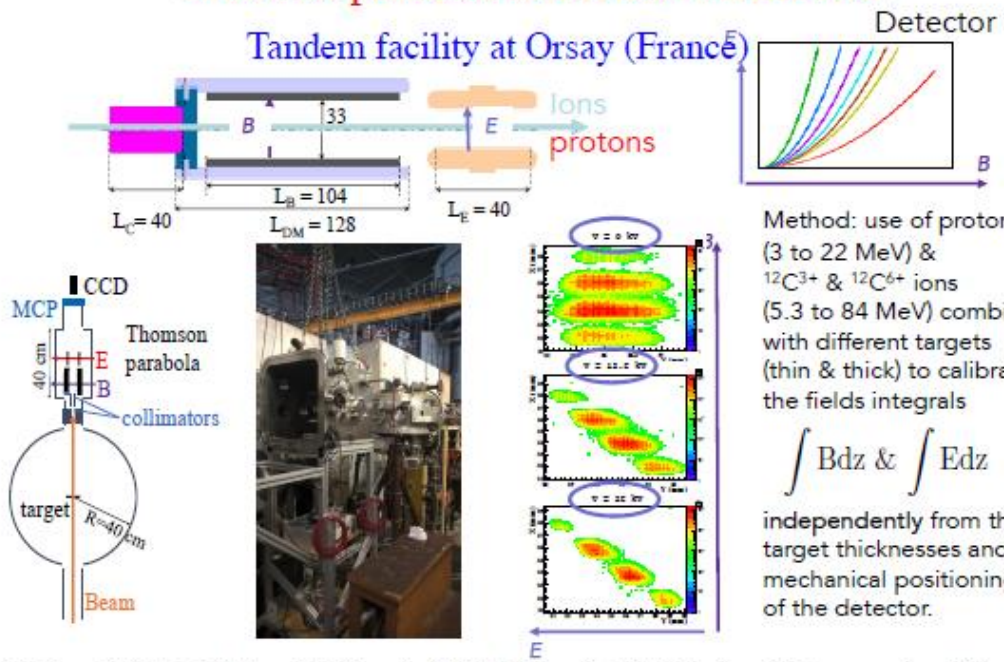

Method: use of protons (3 to 22 MeV) & $^{12}C^{3+}$ & $^{12}C^{6+}$ ions (5.3 to 84 MeV) combined with different targets (thin & thick) to calibrate the fields integrals

$$\int Bdz \;\&\; \int Edz$$

independently from the target thicknesses and the mechanical positioning of the detector.

J.-E. Ducret, D. Batani, G. Boutoux, K. Jakubowska, N. Rabhi, L. Serani, et al., "Calibration of the low-energy channel Thomson parabola of the LMJ-PETAL diagnostic SEPAGE with protons and carbon ions" Review of Scientific Instruments **89**, 023304 (2018)

Manip Q_Sepage (Avril 2018): CH 50 μm + flash Al, 450 J / 610 fs

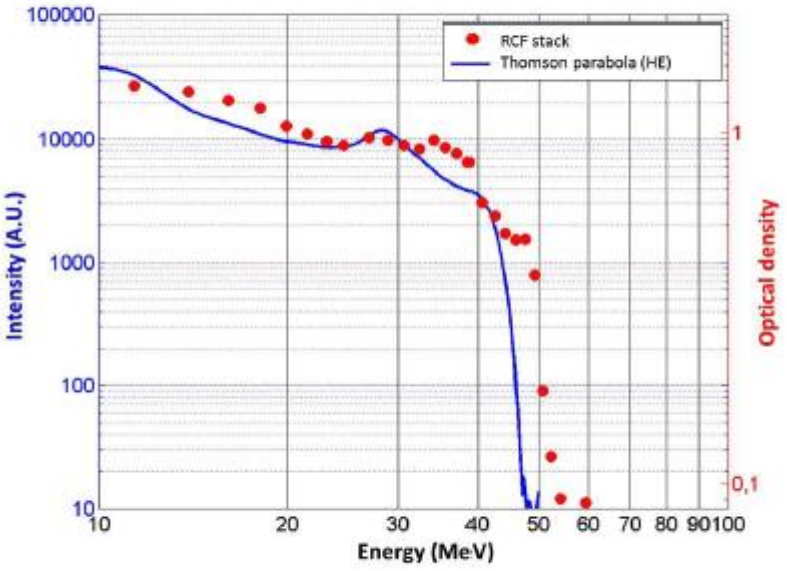

Preliminary comparison of a proton spectrum obtained with the RCF stack and the HE Thomson Parabola.

EquipEx Petal+: SPECTIX

X-ray spectrometer
Detection of X-rays in the range 5 – 100 keV
With spectral resolution $\Delta\lambda/\lambda$ = 1/300
Principle: Cylindrical crystal in transmission

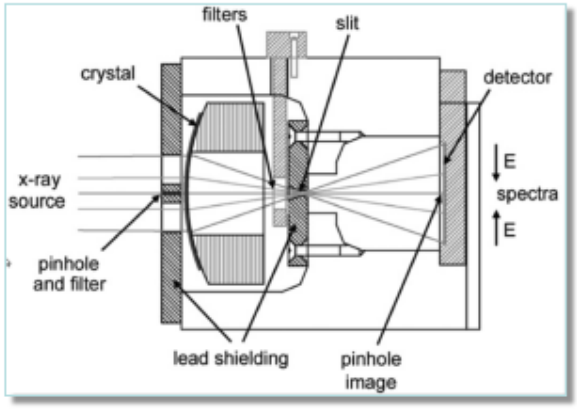

HXS, HENEX, DCS → Naval Research Laboratory

TCS → OMEGA EP
LLCS → LLNL
LCS → LULI
C2S → CELIA

Y. Cauchois, Journal de Physique 3, 320 (1932)

84 J.F. Seely et al., High Energy Density Physics 3, 263 (2007)

SPECTIX: X-ray spectrometer

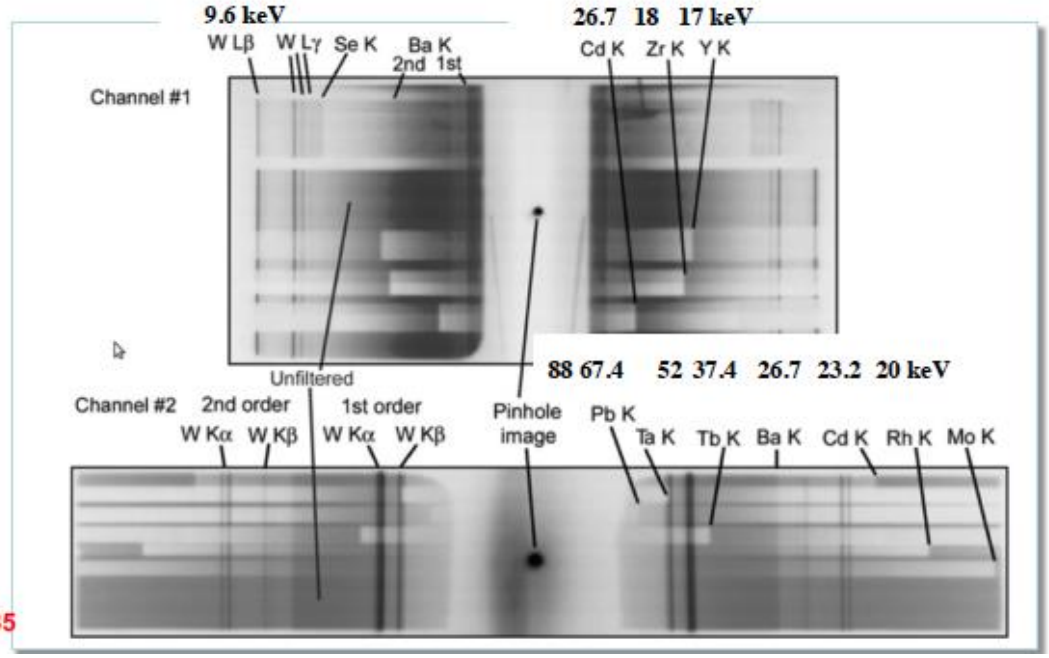

85

SPECTIX in the SID

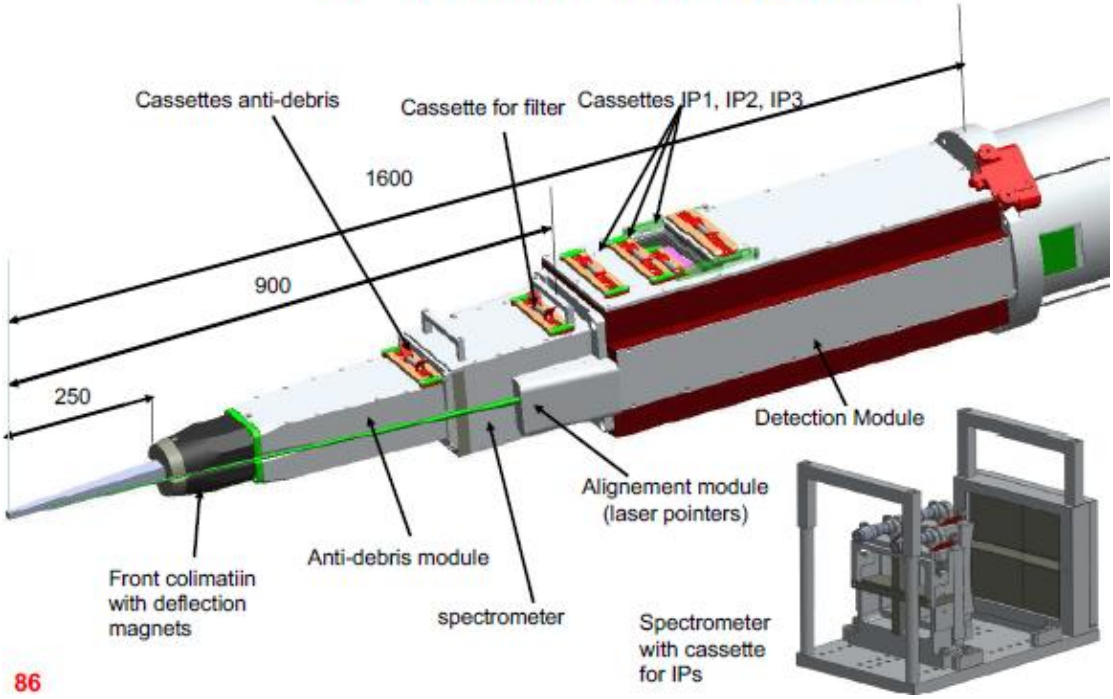

86

SPECTIX: first shots at LMJ

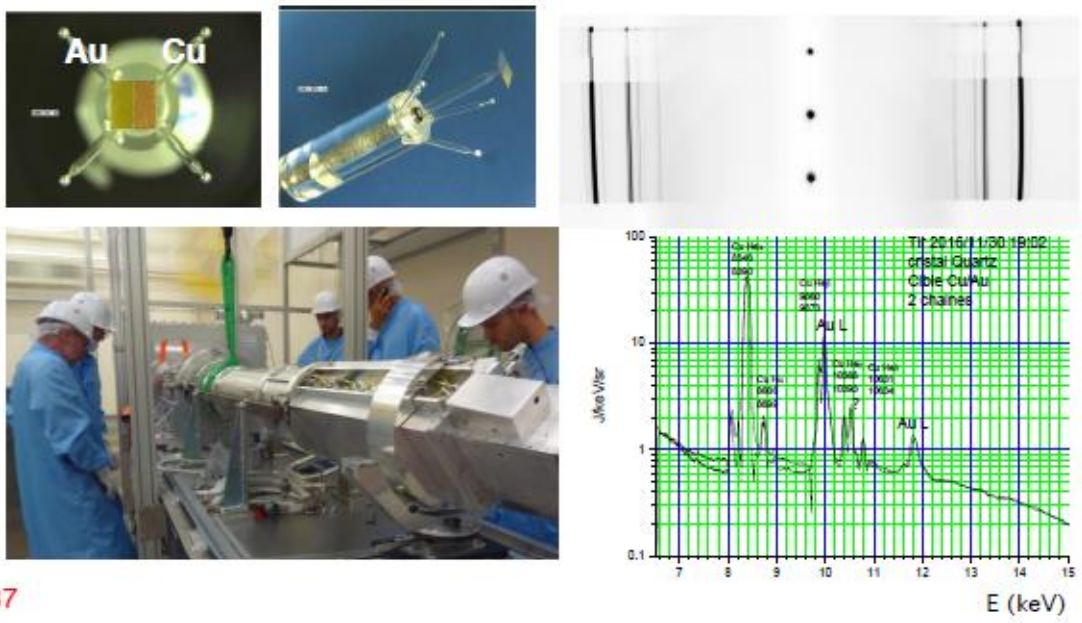

87

Manip Q_Sepage (Avril 2018):
Tir 1 : W Φ2 mm, 430 J / 660 fs

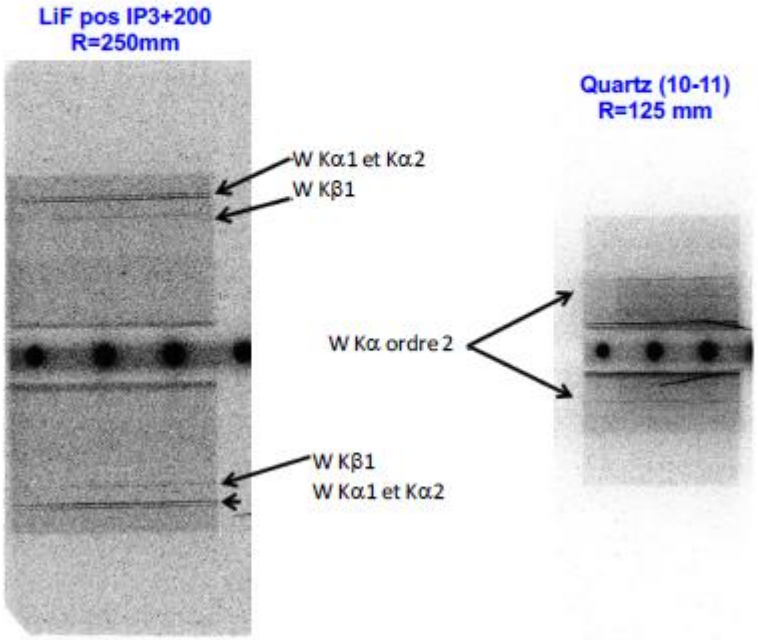

SESAME

SESAME is a passive magnetic spectrometer.

It is made of an entrance slit and two coupled permanent magnets.
Electron spectra are recorded on IP

Characteristics:

- Spectral range 0.1 – 150 MeV
- Spectral resolution □□□
- Field of vision 1 mm
- Construction - October 2016

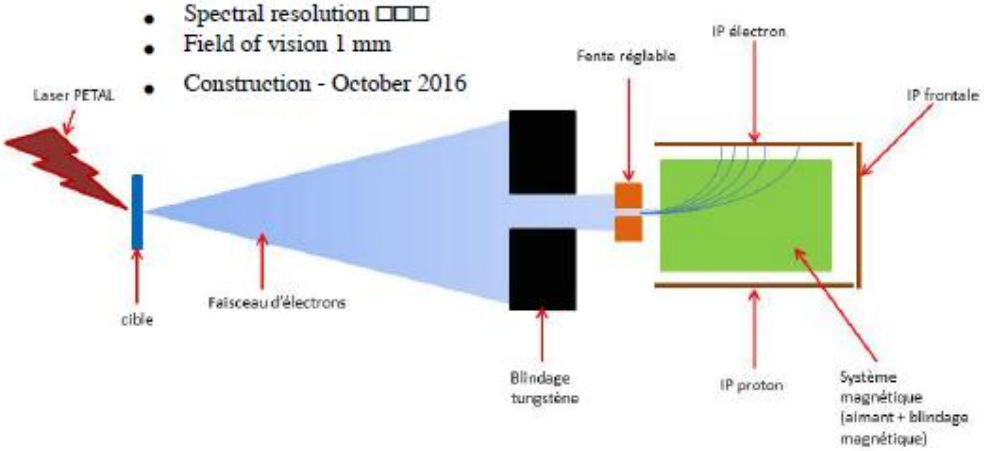

Manip Q_Sepage (Avril 2018):
CH 50 μm + flash Al, 450 J / 610 fs

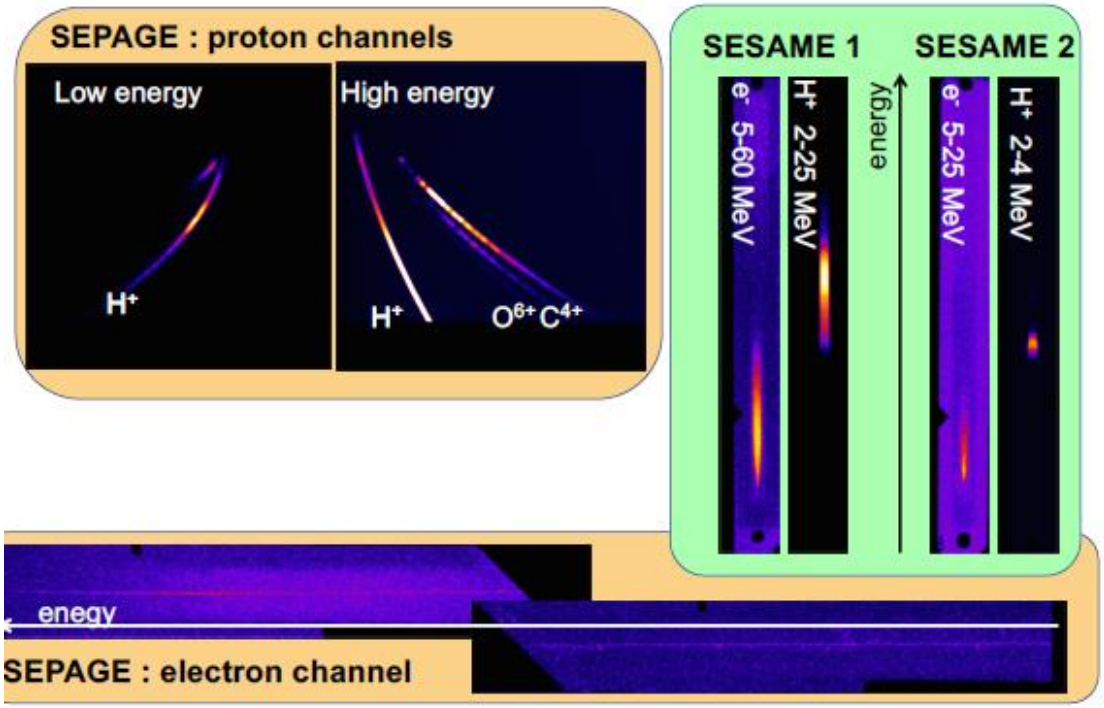

PETAL+ "Spin-offs"

Projet PETAPHYS «Preparation of the high power laser system PETAL for experimental studies of inertial confinement fusion and high energy density states of matter»

TwIST: «Two (or Three) ω Imaging SysTem»
- Measurement of PETAL focal spot shot-by-shot
- Characterisation of PETAL performance

ASPIX: Spectrometer Bremsstrahlung compact (filters/IP)
Inserted by means of a insurable cylinder to 3600 mm from TCC and "out of chamber" (5 mm Al interface).
Measurement of X-ray spectra in the range 10 keV-20 MeV, Temperature of fats electrons produced by PETAL

Photo of spectrometer:

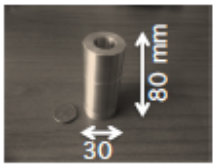

The insertable rod

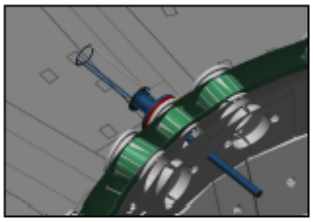

Problems related to EMP

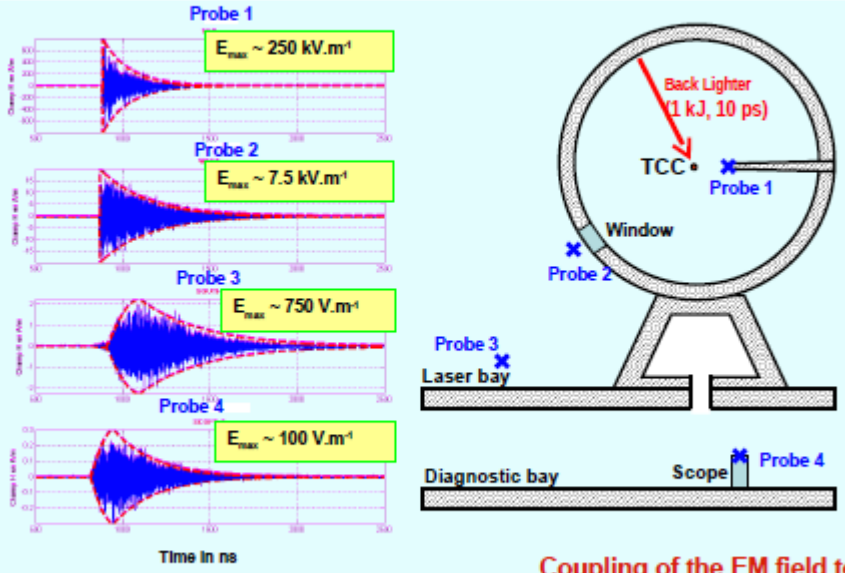

OMEGA measurements on May 2011

Coupling of the EM field to cables may induce volt-level disturbances in the data acquisition electronics

EMP from PETAL ≈1 MV/m

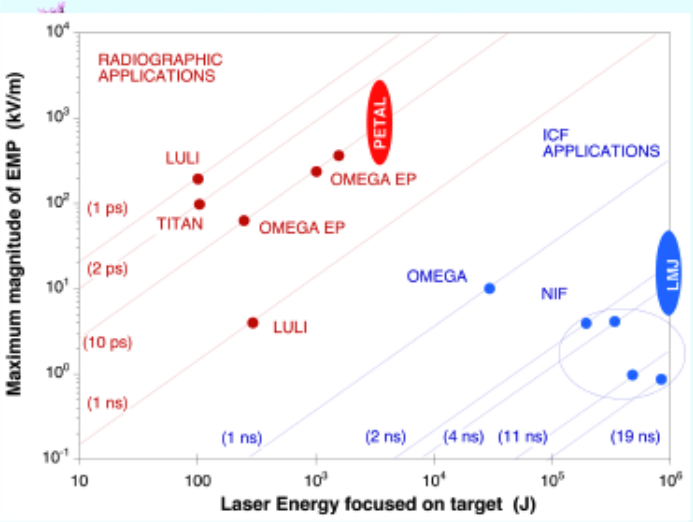

PETAL ps shots could produce more perturbations than the LMJ ns shots

EMP measurements performed by CEA on laser facilities :

2000 – 2004 : LLE – **Omega**

2006 : LULI – **Nano2000**

2007 – 2009 : LULI – **Pico2000**

2009 – 2010 : LLE – **Omega EP**

US feedback on NIF :

EMP measurments on **TITAN**

National Ignition Campaign

EMP features depends on :

the application

the **laser power/intensity**

the target, focal spot size, etc.

Specifications :

ICF : 100 kV.m^{-1} @ 1 GHz

Radio. : 1 MV.m^{-1} @ 10 GHz

Origin of EMP

EMP is produced by
1) Electric and magnetic fields due to relativistic current propagating in solid targets
2) Fields due to $\nabla n \times \nabla T$ mechanism in the plasma

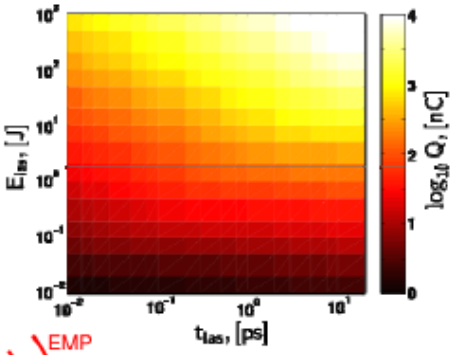

Target charge prediction for various laser energy and duration.

Charging and de-charging

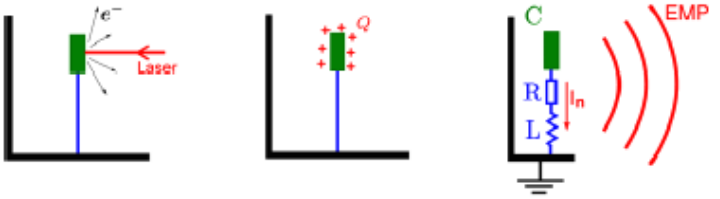

The laser pulse ejects some electrons

The target is charged

The neutraisation current oscillates and emits the EMP

- J-L Dubois et al, Phys Rev E 2014
- A Poye et al, Phys Rev E 2015

Modelling EMP (simuls & expts)

Simulation chain covers scales from 0.1 µm to 10 m:
CHIVAS (preplasma) → CALDER (laser plasma interaction) → MCNPX (electron transport and X-ray generation) → SOPHIE (EM generation)

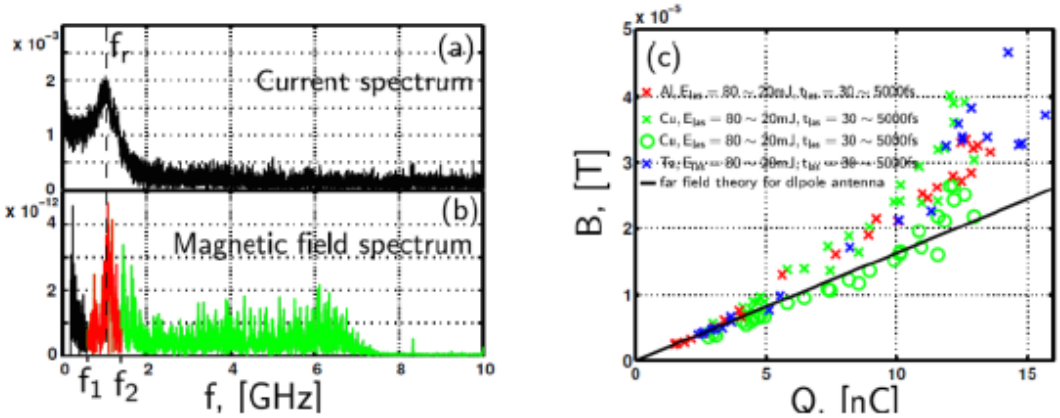

Experimental measurements of the recharge current and the EMP signal on lasers ECLIPSE (CELIA) and EQUINIOX (CEA)

Mitigating EMP at source

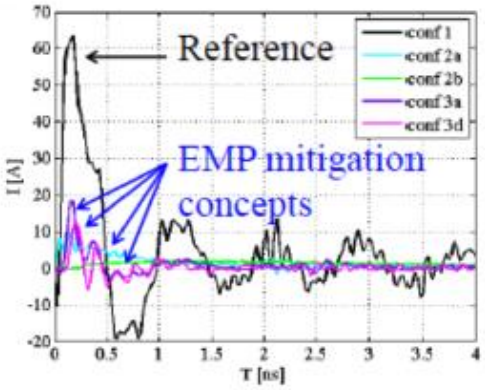

This work allowed proposing mitigation schemes

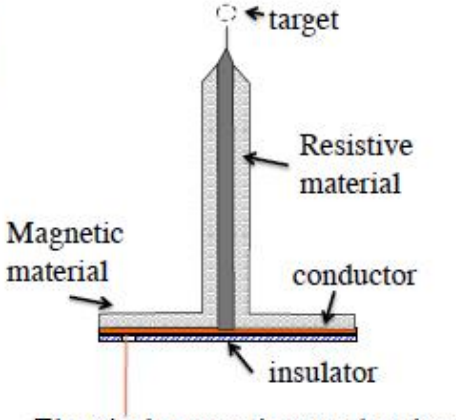

Predicting EMP on PETAL

PETAL shots may produce electromagnetic pulses inside the chamber with

E > 1 MV/m at 1 m

Spectrum: 100 MHz - 10 GHz

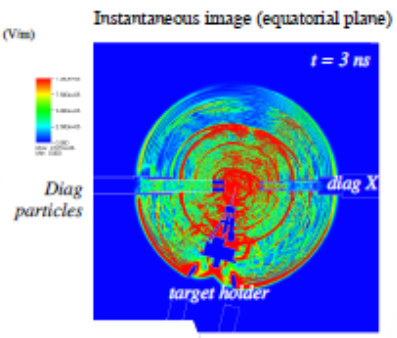

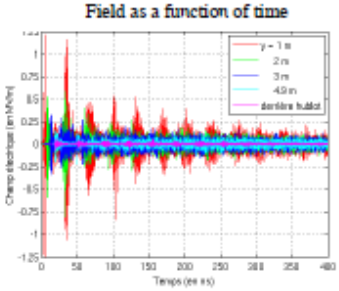

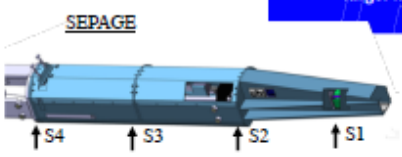

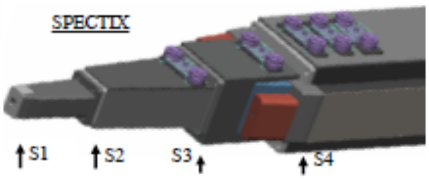

Diagnostics	*Openings*	S1	S2	S3	S4
SEPAGE	E_{max}	**1 MV/m**	**500 kV/m**	**250 kV/m**	**200 kV/m**
	Measuerd at:	75 cm	145 cm	220 cm	290 cm
SPECTIX	E_{max}	**5 MV/m**	**2 MV/m**	**1 MV/m**	**600 kV/m**
	Measuerd at	20 cm	40 cm	65 cm	91 cm

Predicting EMP on PETAL

Max levels during a standard PETAL shot

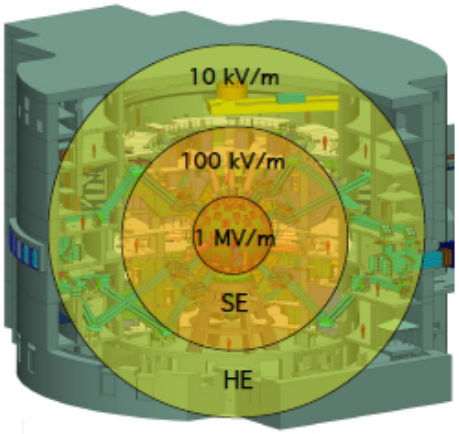

Confirmed by CALDER-SOPHIE numerical simulations and and in-situ transmission measurements

vulnerability threshold (typical values)

Damaging :	1 – 10 kV/m
Malfunctioning :	0.1 – 1 kV/m

Objectives :

Attenuate EMP by controlling the currents flow at origin: objective = factor 10

⇒ EMP (chamber) ≤ 100 kV/m < OMEGA-EP

⇒EMP(HE) ≤ 1 kV/m

- Reduce EMP at source
- Good grounding and shielding
- Develop EMP resistant electronics
- Use passive detector

Generation of radiation

Production of high-energy particles (γ, p, n) in experiments on PETAL:

1) Type I: interaction on thick solid target → production of hard x-rays
2) Type II: interaction on thin solid target → production of high-energy ions
3) Type III: interaction on deuterated targets → neutrons

High doses are produced by firing PETAL on solid or gas targets.

i) Studies on developments of "secondary sources" of particles and radiation
ii) Test of irradiation doses of future LMJ experiments (activation problem)
iii) Impact on the "nuclearization" of the LMJ/PETAL facility

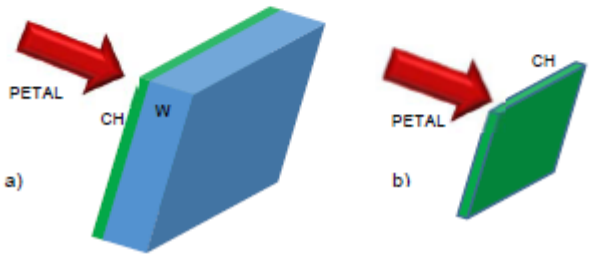

Generation of radiation

In all cases the "driving motor" if the relativistic interaction of the laser beam with the target generating fast electrons

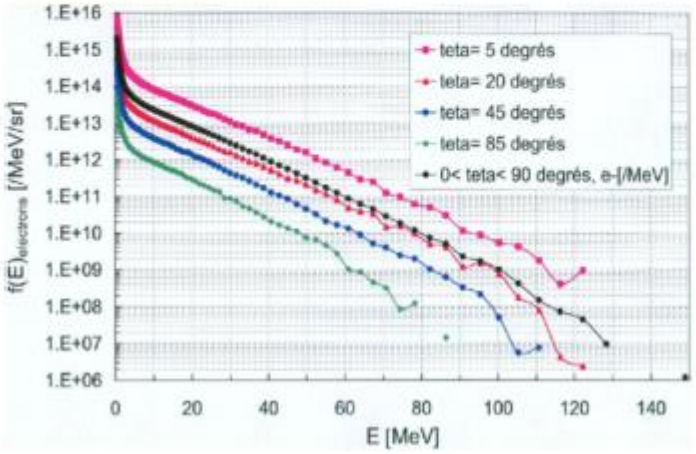

CALDER results
I_{max}~ 3 x 10^{20} W/cm²

Type I: interaction on thick solid target → production of hard x-rays

Electron-photon conversion from 2mm W foil simulated with MCNP
Electrons data obtained at the Calder box edges in 2D injected in MCNP (3D)

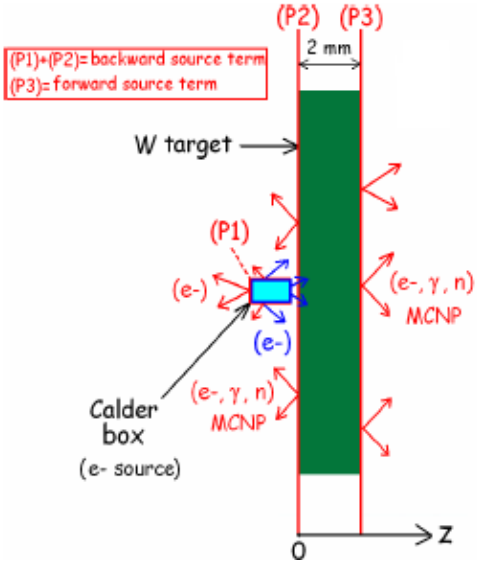

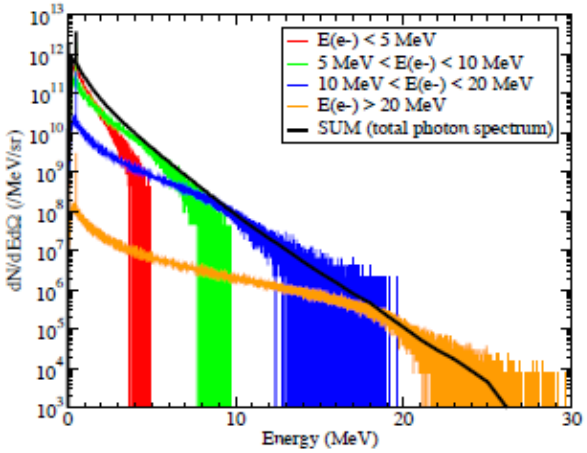

Type I: interaction on thick solid target → production of hard x-rays

Electron-photon conversion from 2mm W foil simulated with MCNP

Electrons data obtained at the Calder box edges in 2D injected in MCNP (3D)

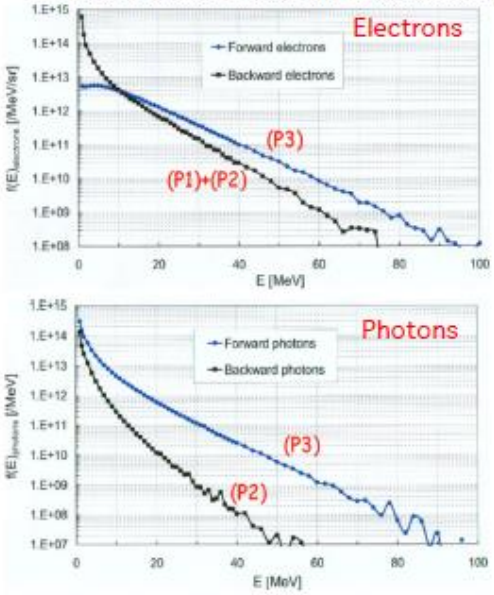

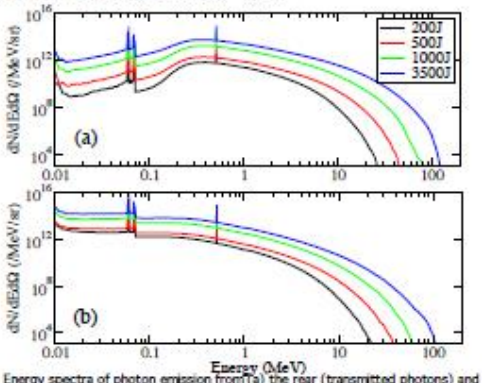

Energy spectra of photon emission from (a) the rear (transmitted photons) and (b) front side (reflected photons) of the target for laser energy of 200, 500, 1000 and 3500 J

Laser energy, J	200	500	1000	3500
Hot electron temperature, MeV	1.63	3	5	7.6
Fraction of reflected electrons, %	47.8	37.9	37.3	32.9
Temperature of reflected electrons, MeV	1.2	2.2	3.5	4.8
Fraction of transmitted electrons, %	0.02	0.52	2.09	8.5
Temperature of transmitted electrons, MeV	1.8	2.8	4.5	6.5
Electron/photon conversion ratio R_{γ}, %	7.4	20.4	42.5	70.0
Maximum energy of transmitted photons $E_{max-\gamma}$, MeV	25	45	84	105
Temperature of transmitted photons T_{γ}, MeV	1.3	2.3	3.5	5.7

Type II: interaction on thin solid target → high-energy ions

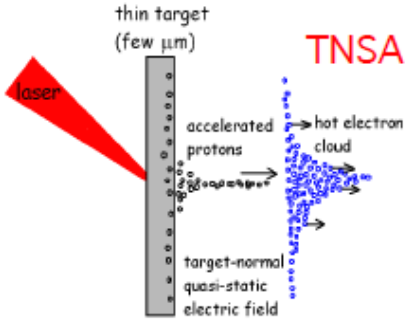

Estimation of Proton emission from a 10-μm plastic target irradiated with PETAL from 2D PIC simulations using the code PICLS

Proton divergence distribution for protons with an energy > 40 MeV in the forward direction

(Comparable to the 50 MeV obtained on Omega EP by K. Flippo et al. with 1kJ but with a longer pulse duration)

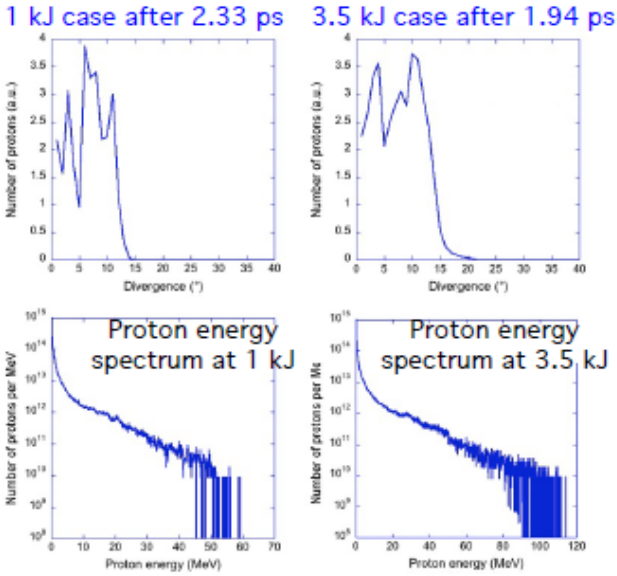

Prompt doses

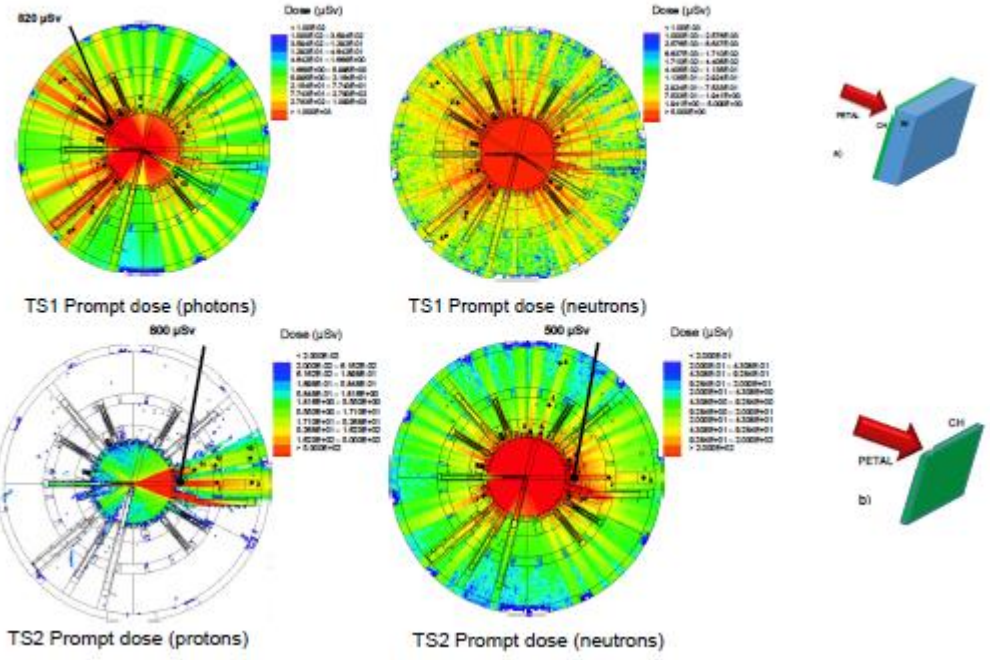

Type II: interaction on thin solid target → high-energy ions

Total laser energy, J	200	500	1000	3500
Hot ion temperature, MeV	5	7	11.3	14.3
Number of accelerated protons > 1 MeV	2.5×10^{13}	3.5×10^{13}	5.7×10^{13}	7.2×10^{13}
Cut-off proton energy, MeV	32	53	60	114
Total hot proton energy, J	20	31	102	163

Table 2. Characteristics of accelerated protons.

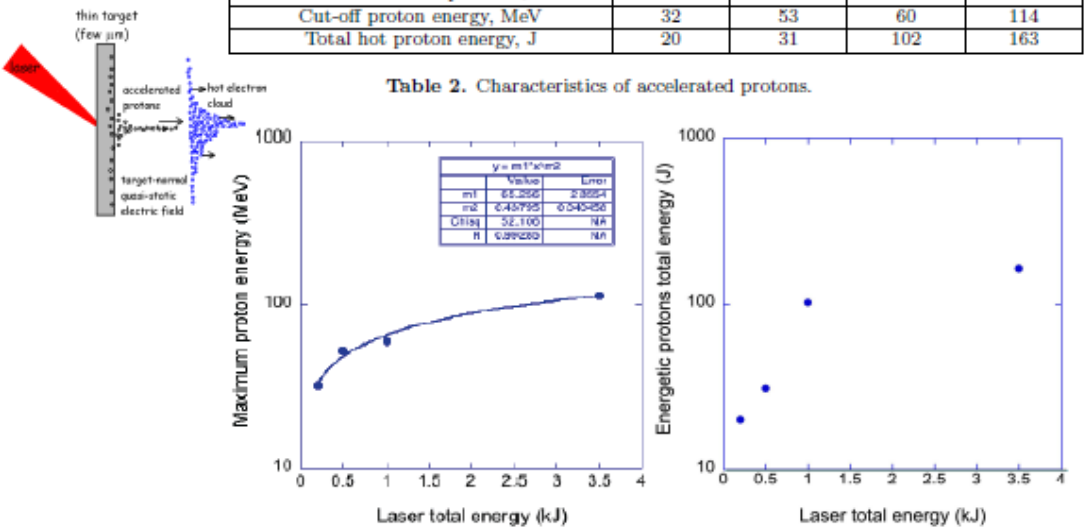

Problems related to radioactivity dose

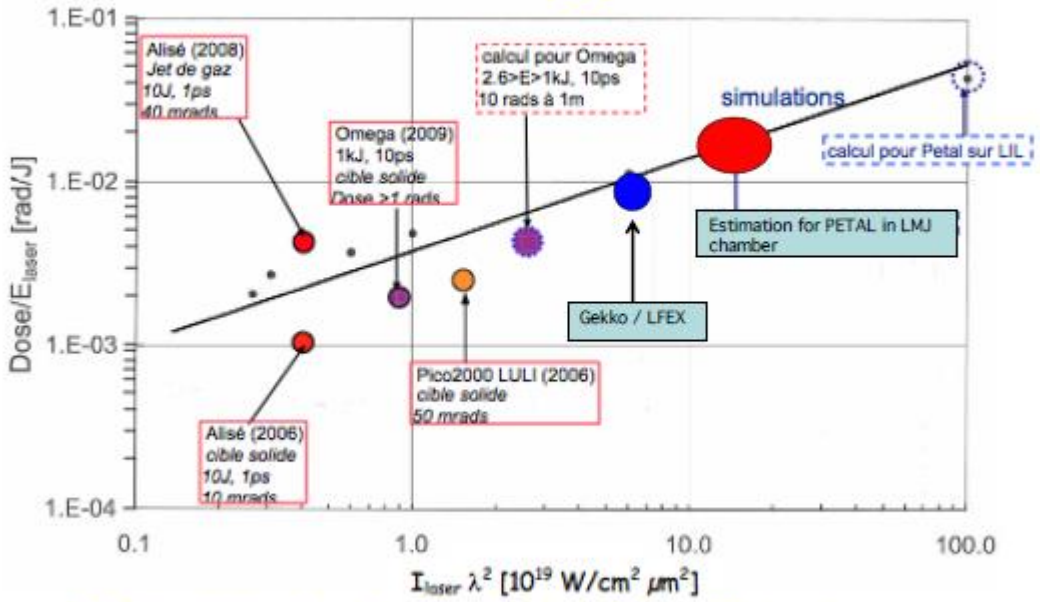

Radioactivity calculated 1 m behind a 2mm W target

Institute of Laser Engineering, Osaka University

Calculated dose per LFEX shot (500 J/shot)

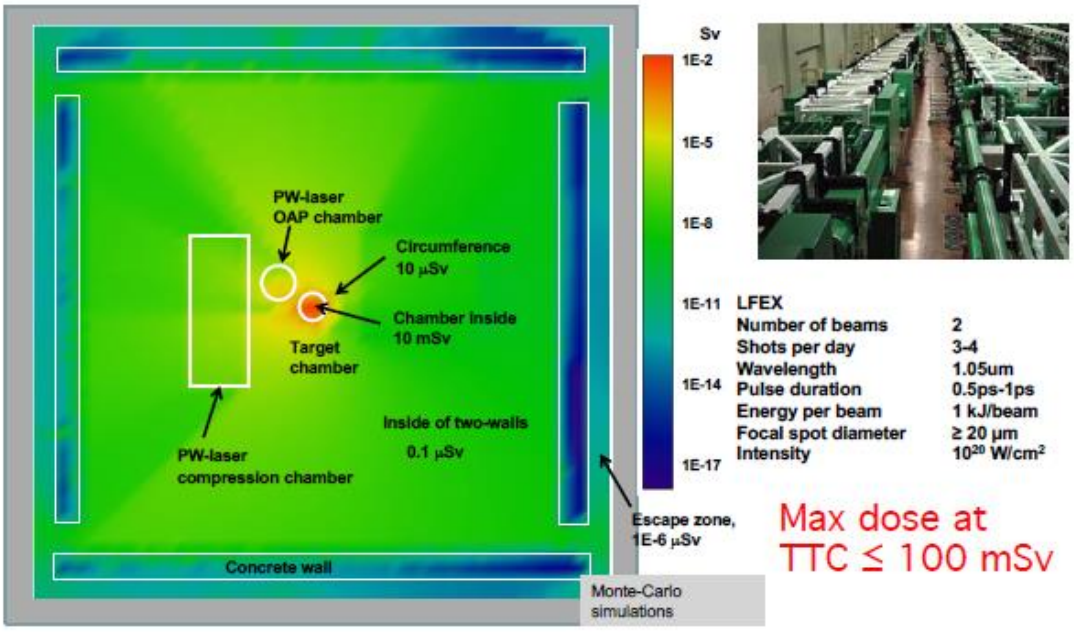

Max dose at TTC ≤ 100 mSv

Activated nucleides

Laser energy 200 J		Laser energy 500 J		Laser energy 1 kJ		Laser energy 3.5 kJ	
Isotopes	Activity, Bq	Isotopes	Activity, Bq	Isotopes	Activity, Bq	Isotopes	Activity, Bq
W183m	1.41×10^{2}	Al26m	4.00×10^{4}	Al26m	2.70×10^{5}	Al26m	3.40×10^{7}
Al28	9.11×10^{1}	W183m	1.28×10^{4}	Al28	4.30×10^{5}	Al28	4.34×10^{6}
Al26m	7.89×10^{1}	Al28	1.15×10^{4}	W183m	3.79×10^{5}	W183m	3.50×10^{6}
Ta180	1.83×10^{1}	Ca39	6.89×10^{3}	Si27	1.64×10^{5}	Mg23	2.31×10^{6}
W185m	1.16×10^{1}	Rh104	2.23×10^{3}	Mg23	1.52×10^{5}	Si27	2.14×10^{6}
Ca39	9.54	Si27	2.10×10^{3}	O15	9.21×10^{4}	O15	1.24×10^{6}
Rh104	6.53	Mg23	1.68×10^{3}	Rh104	8.80×10^{4}	Rh104	9.17×10^{5}
O15	2.41	Ta180	1.34×10^{3}	Ca39	7.76×10^{4}	Al25	7.87×10^{5}
Se77m	1.34	W185m	1.32×10^{3}	W185m	4.78×10^{4}	Ca39	5.52×10^{5}
Mg23	1.19	O15	1.29×10^{3}	Ta180	4.14×10^{4}	W185m	4.45×10^{5}
Total	4.19×10^{2}	Total	8.46×10^{4}	Total	4.33×10^{5}	Total	5.20×10^{7}

Table 5. Radiological inventory of the ten most important contributors to the activity at the time $t_0 = 1$ s for the TS1 source and for several incident laser energies.

Laser energy 200 J		Laser energy 500 J		Laser energy 1 kJ		Laser energy 3.5 kJ	
Isotopes	Activity, Bq	Isotopes	Activity, Bq	Isotopes	Activity, Bq	Isotopes	Activity, Bq
Si27	1.85×10^{1}	Si27	9.49×10^{1}	Si27	3.48×10^{2}	Al26m	1.04×10^{7}
Al26m	2.44×10^{5}	Al26m	2.76×10^{7}	Al26m	1.52×10^{8}	Si27	1.02×10^{7}
Al28	2.77×10^{5}	Mg23	3.55×10^{6}	Mg23	2.16×10^{7}	Mg23	1.94×10^{6}
Mg23	2.19×10^{5}	Al28	2.46×10^{6}	Al25	8.80×10^{6}	Al25	1.11×10^{6}
Na21	1.61×10^{5}	Al25	1.61×10^{6}	Na21	4.51×10^{6}	Na21	2.15×10^{5}
Al25	1.45×10^{5}	Na21	9.59×10^{5}	W179	2.54×10^{6}	W179	1.55×10^{5}
Rh104	4.60×10^{4}	W179	4.36×10^{5}	W179m	9.62×10^{5}	Hf178m	9.69×10^{5}
W179	4.01×10^{4}	Rh104	4.26×10^{5}	Hf178m	7.74×10^{5}	Na25	7.05×10^{5}
Hf178m	3.19×10^{4}	N16	3.50×10^{5}	Si26	7.14×10^{5}	Ta178	6.85×10^{5}
N16	1.86×10^{4}	Si26	1.84×10^{5}	Na25	2.94×10^{5}	Si26	6.07×10^{5}
Total	2.20×10^{7}	Total	1.34×10^{8}	Total	5.63×10^{8}	Total	2.68×10^{7}

Table 6. Radiological inventory of the ten most important contributors to the activity at the time $t_0 = 10$ s for TS2 source and for several incident laser energies.

Dose Problem

Calculated data can allow to calculate the delivered dose.

It can be compared to other measurements (performed by CEA and CELIA researchers or published in the scientific literature)

PETAL Max dose/shot ≈ 70 rad

70 rad : 3.5 kJ = 0.02 rad/J

Conclusions:

Petal experiments do not imply the "nuclearisation" of the facility below 300 J (TS2) and 1kJ (TS1) for 500fs laser duration.

Conservative assessments spot 30 μm vs. 50 μm (nominal)

Special attention should be made to target design

EMP and DOSE problem

The problem of developing diagnostics and materials which can survive in a «harsh environment», i.e. which are resistant to high irradiation doses and very strong EMP, is common to several branches of physics and technology:

- Inertial Fusion
- Magnetic Fusion
- Development of advanced fission reactors
- Space missions
- ...

PowerLaPs

Innovative Education & Training in High Power Laser Plasmas

Laser plasma diagnostics - Theory and Experiments

Chapter 11: Shock dynamics and diagnostics

D. Batani

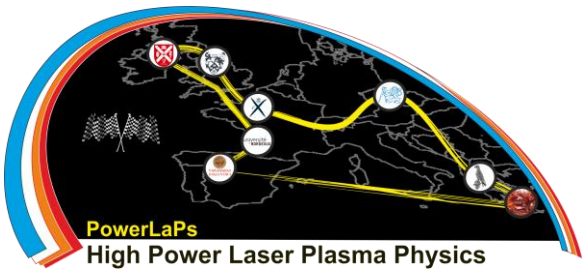

11.1 Introduction to diagnostics of shock dynamics

- Principle of shock generation with lasers and dynamics of shocks
- Diagnostics of shocks: SOP and VISAR
- Diagnostics of shocks: radiography

Laser-solid interaction

Ablation (removal) of material
Formation of a Plasma
Creation of accelerated particles

Emission of radiation
Plasma and material diagnostics
Developing pulsed radiation sources

Redeposition of ablated material on substrates
Thin film production (PLD)

Hot dense Plasmas
Inertial Confinement Fusion

Creation of extreme states of matter:
Compression of matter by shocks
Isochoric heating of matter

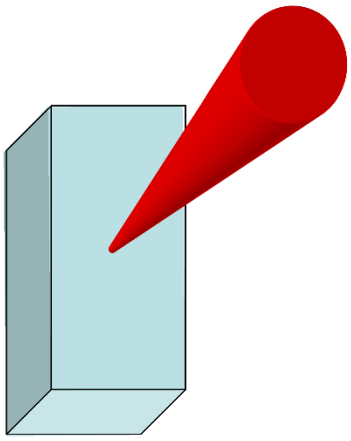

WDM: solids at high temperature ($0.01<\rho<100$ g/cm3 $T_e \approx$ eV)
HED: P>1MBar

3

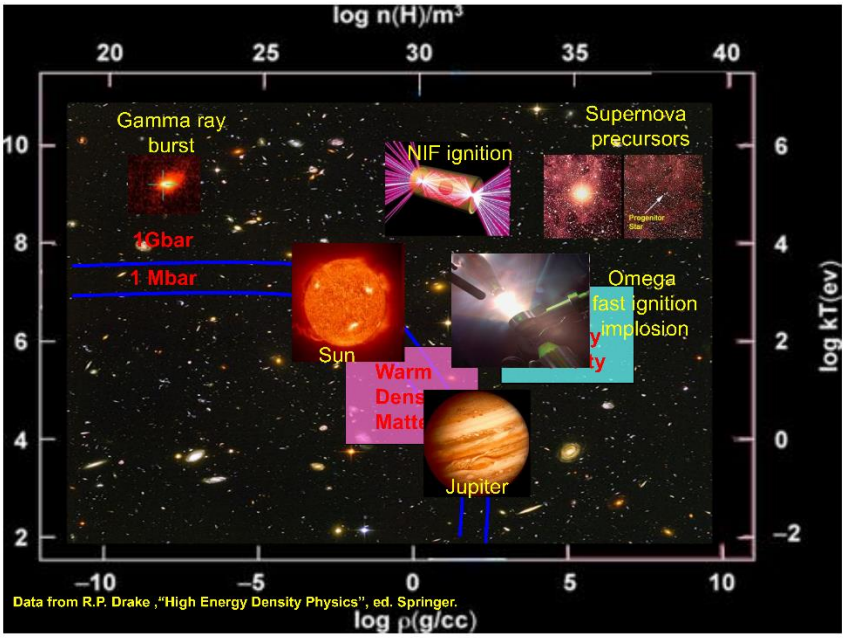

Astrophysical context

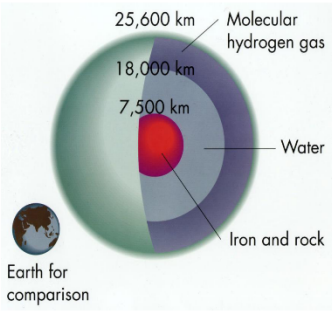

Neptune's internal structure

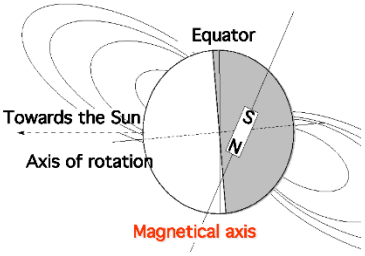

Magnetic field of Uranus

- Mantle of Uranus and Neptune = «hot ices» of H_2O, NH_3, CH_4
- Intense, assymetrical magnetic field

Existence of a fluid, conducting region ?

6

Iron EOS by laser-shocks

Very high Pressures (> 10 Mbars)

- Several experimental points from nuclear explosions theoretical calculations

  Trunin et al., *Physics-Uspekhi* 37, 1123 (1994).

- Planetology

  Rocky cores of giant planets
  Impact phenonema (e.g. formation of the earth-moon system)
  Impact of "planetesimals" to form earth core

Intermediate pressures (1-5 Mbars)

Fusion point in compressed iron (T~ 6000° K at P~3.3 Mbar)

Important issue for terrestrial planets (earth)
Occurs between outer core (liquid) and inner core (solid)

Brown and McQueen, *J. Geophys Res.* 91, 7485 (1986)
Anderson & Ahrens, *J. Geophys Res.* 99, 4273 (1994)

5

Carbon

1) Transition between solid-insulator to liquid semi-metal in carbon compressed at megabar pressures by laser driven shocks

2) Melting curve of carbon at Megabar pressures

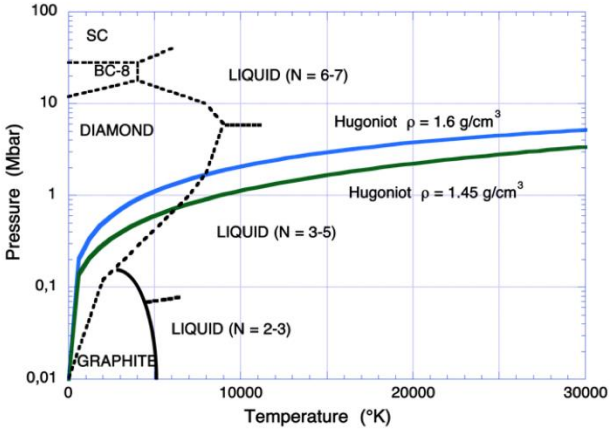

Water at very high pressures

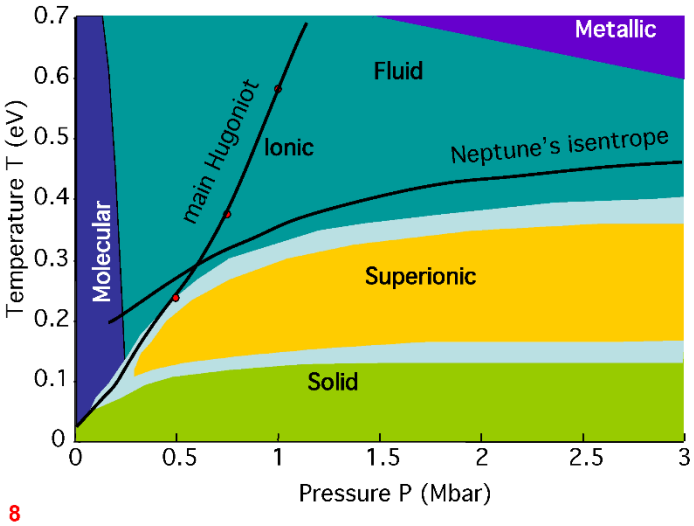

Ab-initio Molecular dynamics simulations

C.Cavazzoni et al., Science, 283, 44 (1999)

8

"Extreme" states of matter

WDM: solids at high temperature ($0.01<\rho<100$ g/cm^3 $T_e \approx$ eV)
HED: P>1 MBar

High-energy lasers allow reaching WDM and HED states:

1) By means of laser-driven shock waves

2) By using short laser pulses to heat matter using laser-generated X-rays, fast electrons, protons, ...
   ➪ ISOCHORIC HEATING OF MATTER

Dimitri Batani «Matter in extreme conditions produced by lasers» Perspective, Europhysics Letters 114, 65001 (2016)

9

"Regions" of Laser-produced plasmas

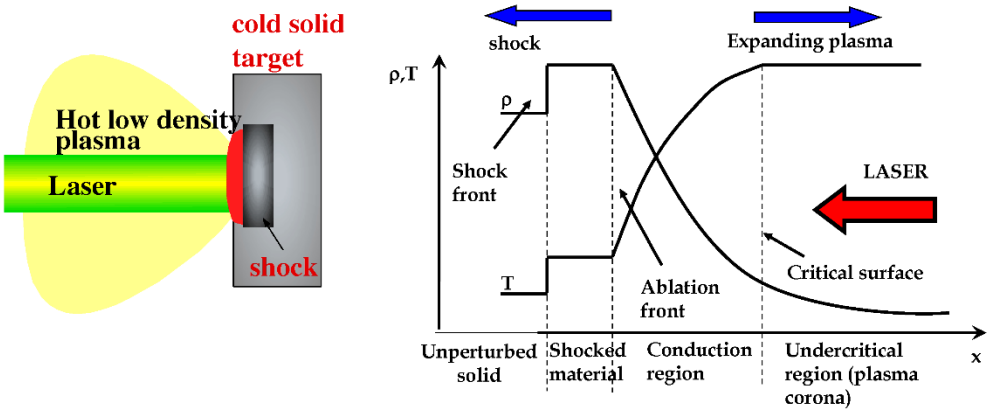

$$n_{cr}\ (cm^{-3}) = 1.1 \quad 10^{21} / \lambda^2\ (\mu m)$$

10

Challenges of diagnostics for laser-plasmas

The plasma is small (μm to mm)
=> High spatial resolution (μm to sub-μm)

The plasma lifetime is short (≈ laser pulse duration)
=> High temporal resolution (fs to ns)

There are several orders of magnutide differences in density and temperature simultaneously present ($n_e \approx 10^{17}$ to 10^{24} cm^{-3}, $T_e \approx$ 1eV to 10 keV, or more in the case of "hot electrons")
=> Need for very large dynamics
=> Need to use different diagnostics approaches and tools simultaneously

11

From sound waves to shock waves

$$c_s = \sqrt{\gamma \frac{P_o}{\rho_o}} = \sqrt{\gamma T_o}$$

$$D = \sqrt{\frac{\gamma + 1}{2} \frac{P}{\rho_o}}$$

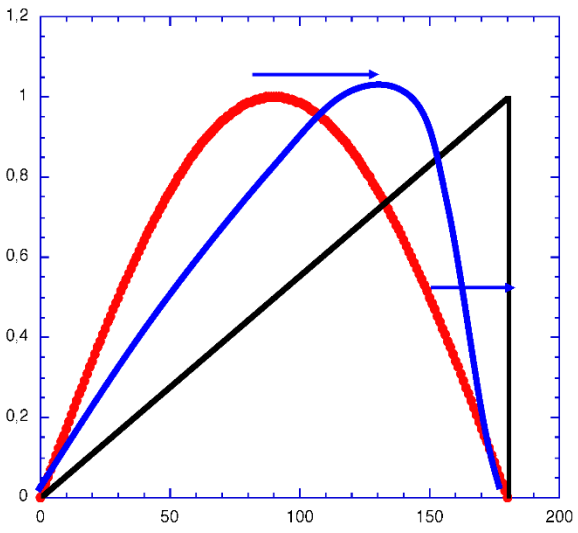

12

The "classical" model of laser-plasma interaction

The temperature at the critical layer is

$$T_e(eV) = 10^{-6}(I\,(W/cm^2)\,\lambda(\mu m)^2)^{2/3}$$

The pressure is

$$P = n_e T_e = \frac{10^{21}}{\lambda^2} 10^{-6} (I_L \lambda^2)^{2/3} = \frac{10^{15}}{\lambda^2} (I_L \lambda^2)^{2/3}$$

and in practical units

$$P(MBar) = 10 \left(\frac{I_L(W/cm^2)}{10^{14}} \right)^{2/3} \lambda(\mu m)^{-2/3}$$

13

1D hydro simulations (MULTI)

CELIA

Laser intensity 5 10^{12} W/cm^2 (no plasma creation on rear side)
Temporal flat-top laser profile

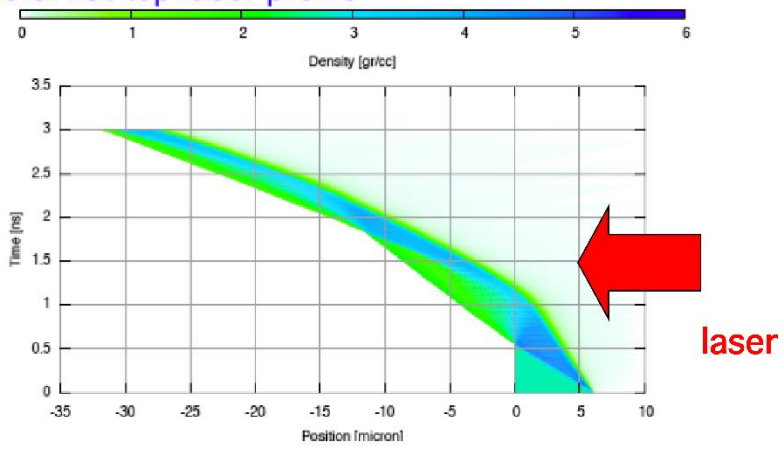

14

1D hydro simulations (MULTI)

CELIA

Laser intensity 5 10^{12} W/cm^2 (no plasma creation).
Temporal flat-top laser profile

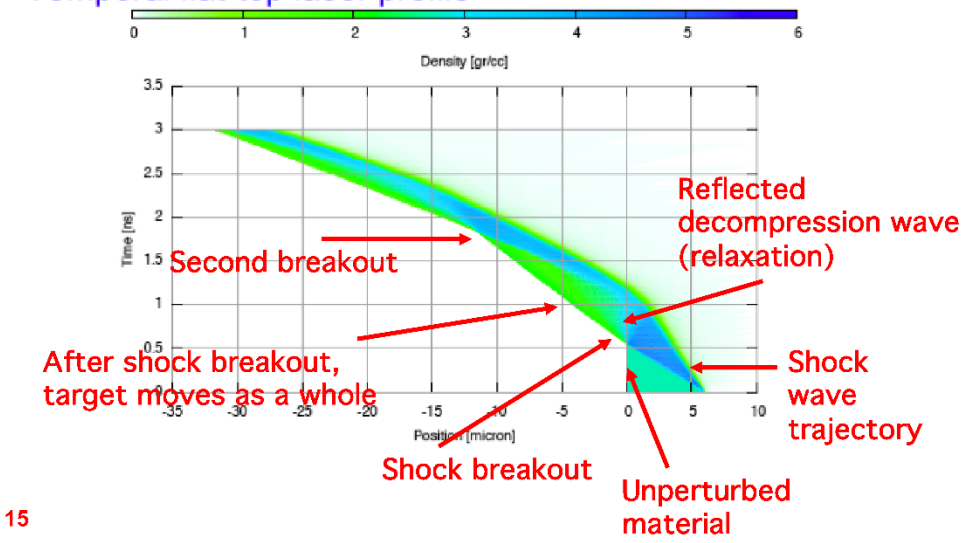

15

2D simulations:

Interaction of a 6 μm foil Al target with laser radiation with τ = 3 ns at 800 nm and 5 10^{12} W/cm^2

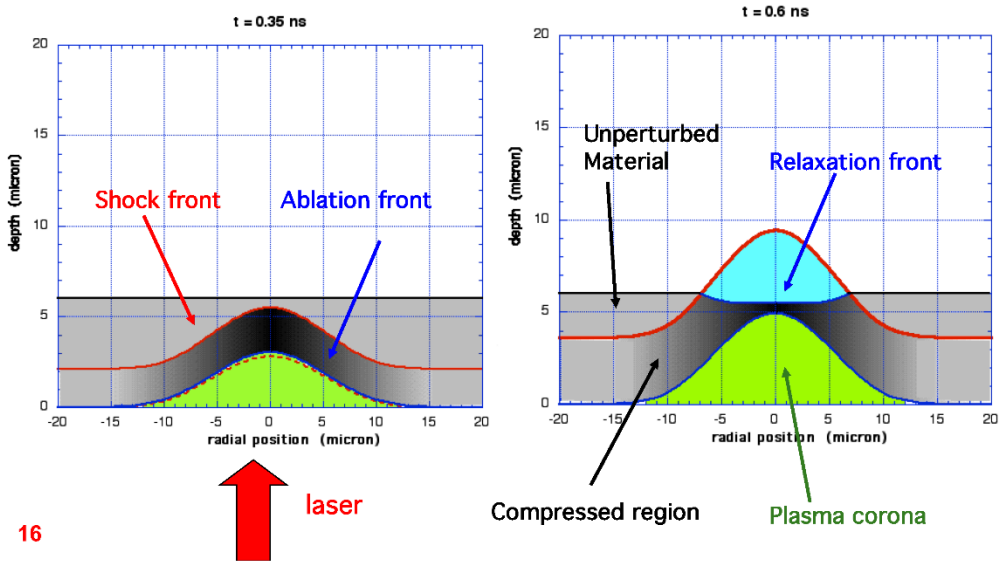

16

We use shock to compress matter and measure EOS

Conservation laws:

Mass
$\rho_o D = \rho\,(D-U)$

Momentum
$\rho_o DU = P-P_o$

Energy
$\rho_o D(E-E_o+U^2/2) = PU$

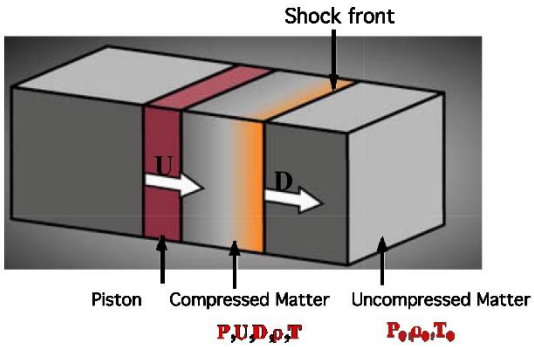

3 equations, 5 unkown parameters ρ, D, U, P, E
Measurement of 2 parameters to get an EOS point.
This point lies on the principal Hugoniot curve (i.e. the ensemble of all states that can be reached with a single shock)

17

Hugoniot and shock polar curves

$$\rho = \rho_0 \frac{(\gamma+1)p + (\gamma-1)p_0}{(\gamma-1)p + (\gamma+1)p_0}.$$

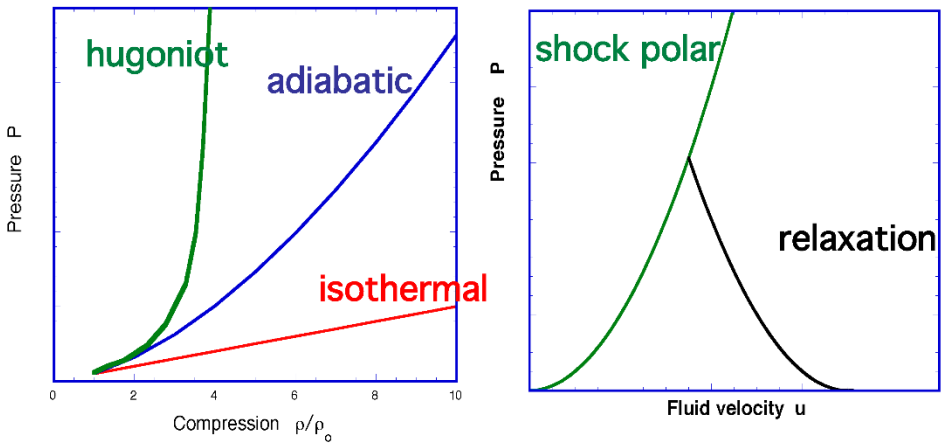

Single shock compression cannot exceed a factor 4. The rest of the work done by pressure goes into heating

18

Hugoniot and shock polar curves

For a perfct gas the shock polar is

$$P = \frac{\gamma + 1}{2} \rho u^2$$

For most solid material, the hugoniot can be expressed as a linear relation between D and U

$$D = c_s + Su$$

where c_s is the sound velocity (phase transitions correspond to changes of the parameters c_s and S). Then the shock polar is

$$P = \rho_o u \, (c_s + Su)$$

19

Passage of the shock between two media

- From low density to high density

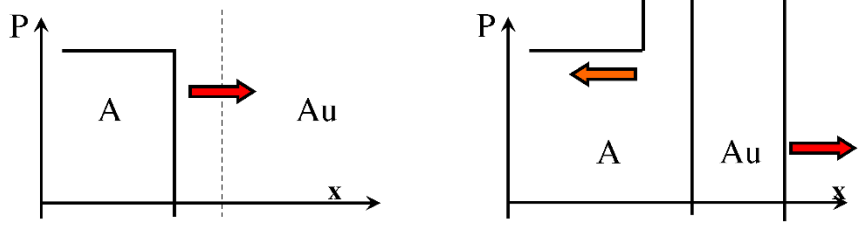

- From high density to low density

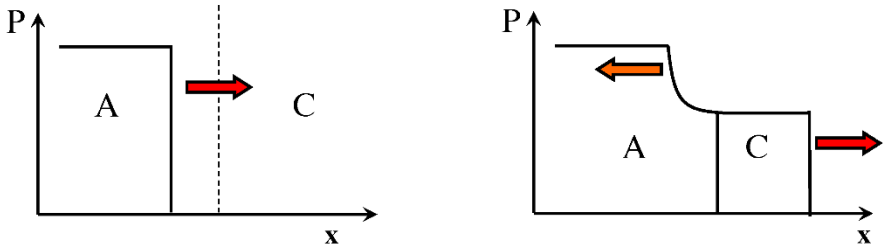

20

Impedance Matching Conditions

Interface Shock Dynamics:
Impedance Mismatch Boundary Conditions
Fluid velocities $U_{Al} = U_C$

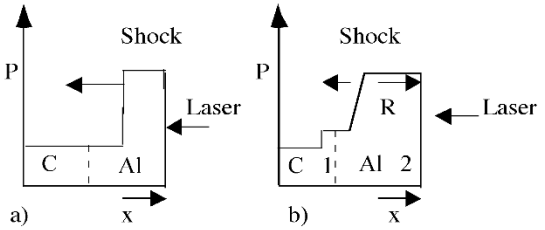

A describes conditions of shocked material in Al before the shock reaches the interface
B describes the conditions in Al and C after shock transmission

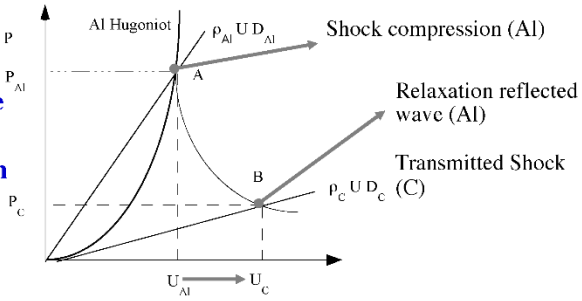

21

"Transmission" to Vacuum

The system virtually relaxes to zero pressure

The target moves as a whole

It is possible to show that if the shock is not too strong, the velocity of the "free surface" is ≈ 2u

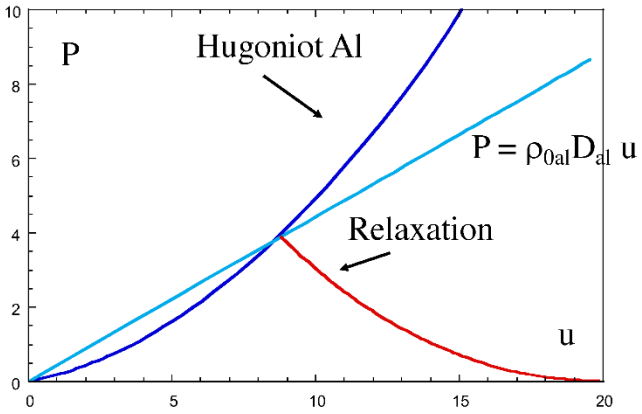

22

The Hugoniot is a «2-parameters» curve

The Hugoniot curve does NOT represent a transformation on the phase plane of the material. It is simply the ensemble of the point which can be reached by (out-of-equilibrium) shock compression.

Therefore (for instance) the final density does not only depend on the applied pressure but also on the initial state

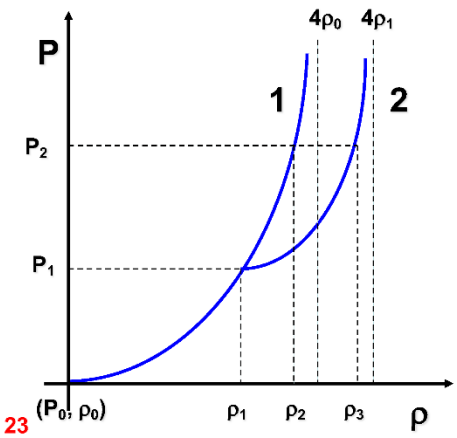

1 - "Principal" Hugoniot curve of the material (starting from (P_0,ρ_0) at normal conditions)

ρ_1 – Density reached with a first shock of pressure P_1

ρ_2 – Density reached by applying the pressure P_2 along the main Hugoniot, i.e; starting from (P_0,ρ_0)

2 - "secondary" Hugoniot curve of the material (starting from (P_1,ρ_1)

ρ_3 – Density reached by applying the final pressure P_2 starting from (P_1,ρ_1)

$4\rho_0$ – compression limit along the main Hugoniot

$4\rho_1$ – compression limit along the secondary Hugoniot

23

Approximating the isentrope

A series of shock compressions can approximate the isentropic curve as well as we want…

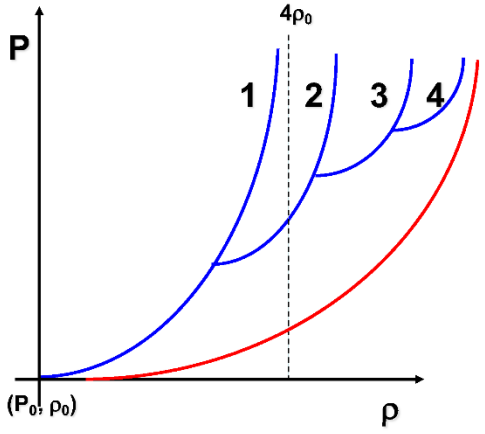

isentropic (adiabatic) compression

24

Reliable EOS measurements have become possible in recent years thanks to:

Optical Smoothing (Phase Zone Plates, KPP, ..)

Control of shock steadiness

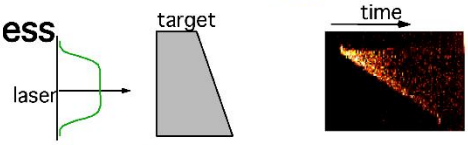

Control of preheating

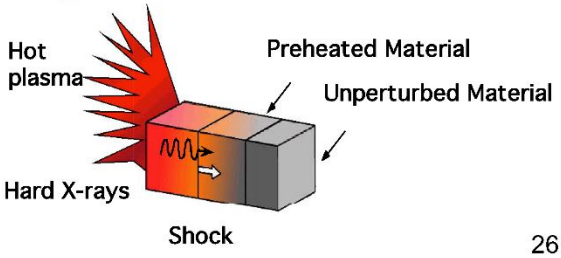

26

Can we uniformly deposit energy on target in direct drive?

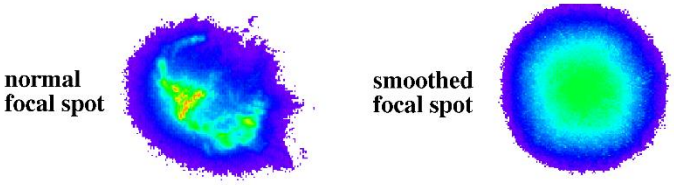

Optical smoothing principle

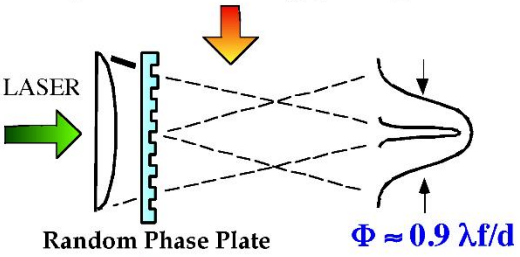

2D square elements with 0 or π dephasing

Kato, PRL (1984)

Result on shock breakout

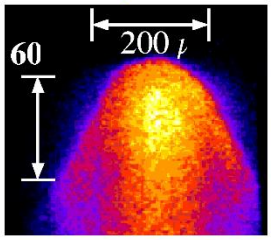

Target :Al, e = 18 μm

27

Phase Zone Plates (PZP)

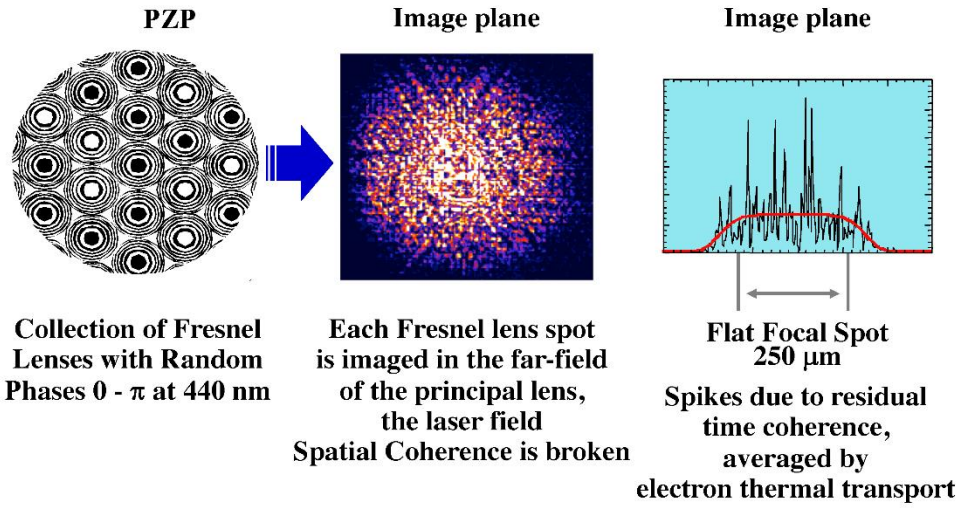

Planar Shocks are Produced

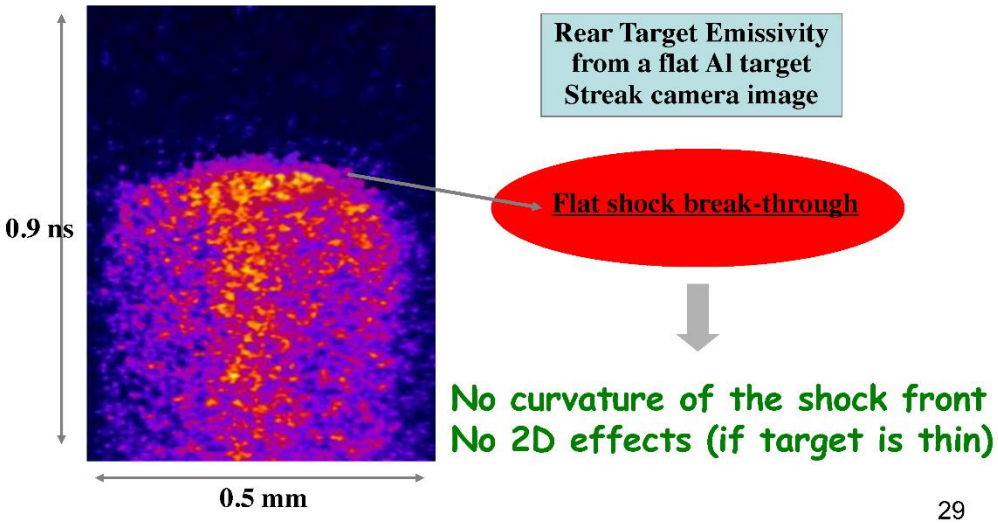

29

DIAGNOSTICS

WORKING PRINCIPLE OF A STREAK CAMERA

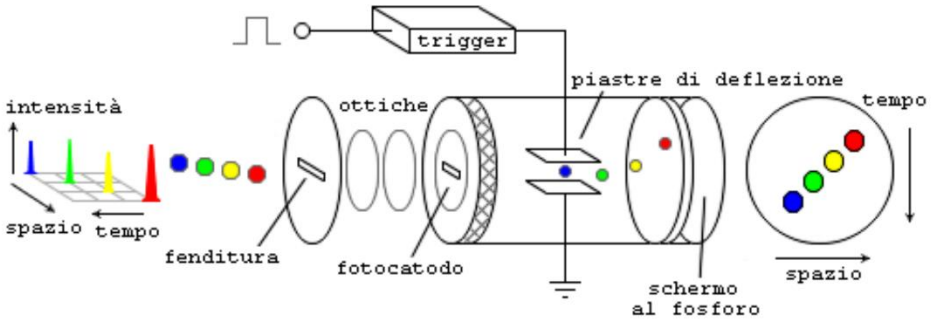

30

STEPPED TARGETS

Stepped targets ⇒ Emissivity ⇒ measurement of shock velocity in Al

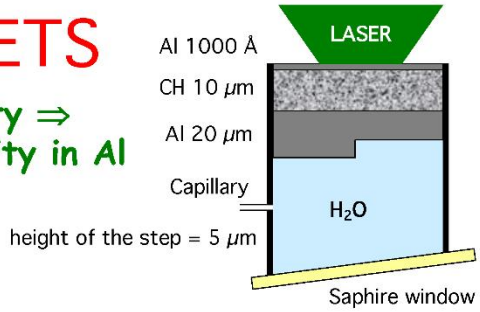

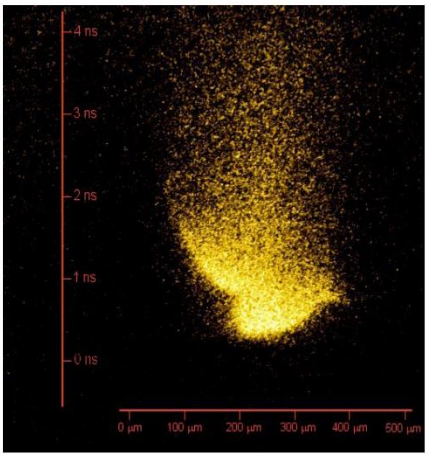

- Shock breakout times at the base and at the top of the step ⇒ shock transit time in the Aluminum step
- Here, 44 pixels = 470 ps.
- Height of the step = 11 μm
- Shock velocity in Aluminum

$$D_{Al} = 11\ \mu m / 470\ ps = 23.4\ km.s^{-1}$$

- Pressure in Aluminium = 9 Mbar
- Pressure in Water = 4.8 Mbar

31

Relative EOS measurements for Iron

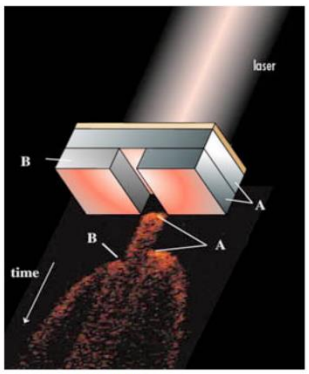

Laser Phebus

P > 10 Mbar

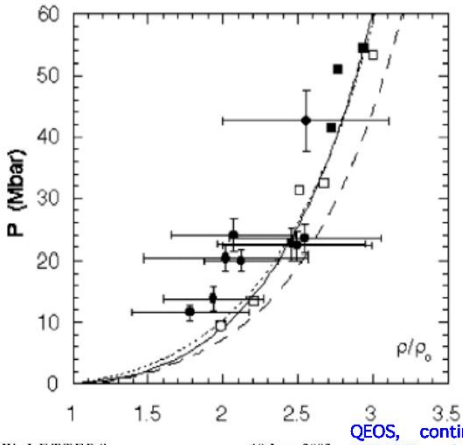

QEOS, continuous line;
SESAME, dashed line;
Trunin, dotted line.

VOLUME 88, NUMBER 23 PHYSICAL REVIEW LETTERS 10 JUNE 2002

Equation of State Data for Iron at Pressures beyond 10 Mbar

D. Batani,[1] A. Morelli,[1] M. Tomasini,[1] A. Benuzzi-Mounaix,[2] F. Philippe,[2] M. Koenig,[2] B. Marchet,[3] I. Masclet,[3] M. Rabec,[3] Ch. Reverdin,[3] R. Cauble,[4] P. Celliers,[4] G. Collins,[4] L. Da Silva,[4] T. Hall,[5] M. Moret,[6] B. Sacchi,[7] P. Baclet,[8] and B. Cathala[9]

Carbon targets

Produced at "General Atomics"
Carbon density ρ = 1.6 gr/cm^3
Aluminum density ρ = 2.7 gr/cm^3 Thickness measured with: profilometer, SEM, FIB

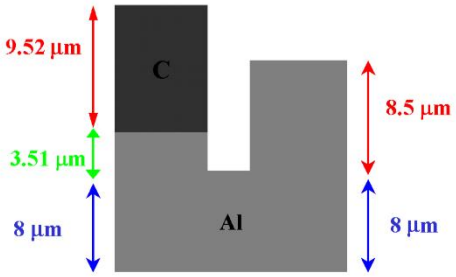

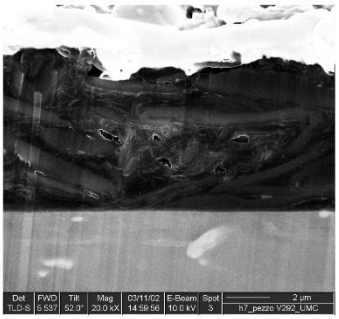

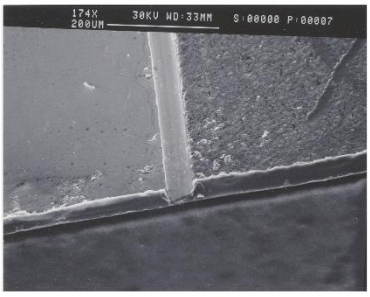

Two steps C / Al target E=108 J

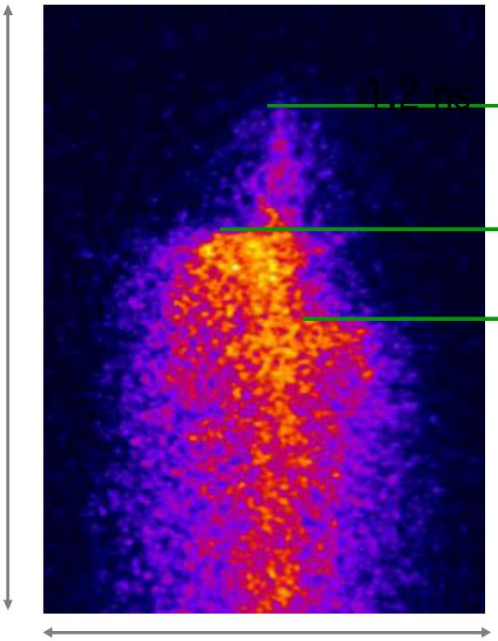

EXP ON PALS LASER, PRA
AND LULI LASER, PARIS

Al step:
$t_1 - t_0 = 205$ ps
$D_{Al} = 38.8$ km/s
$P_{Al} = 33$ Mbar

C step:
$t_2 - t_0 = 295$ ps
$D_c = 32.2$ km/s
$P_c = 18$ Mbar

34

Experimental results for carbon

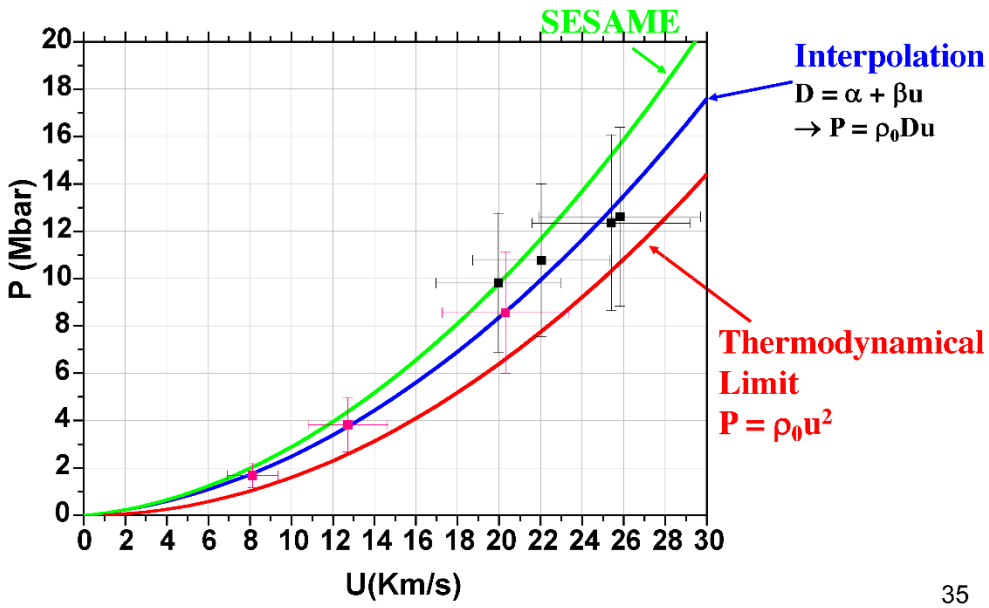

35

Carbon EOS: experimental results

Experimental EOS results from shock experiments:

Only data with pressures P ≥ 1.5 Mbar and corresponding Hugoniot are shown.

Our points:
full squares, 1.45 g/cm³ LULI;
empty circles, 1.6 g/cm³ LULI;
full circles, 1.6 g/cm³ PALS.

Previous points:
empty diamond, 1.85 g/cm³ Pavlovskii et al.;
triangles, 2.2 g/cm³ Nellis;
full diamond, 2.23 g/cm³ Pavlovskii et al.;
empty squares, 3.51 g/cm³ (diamond) Pavlovskii.

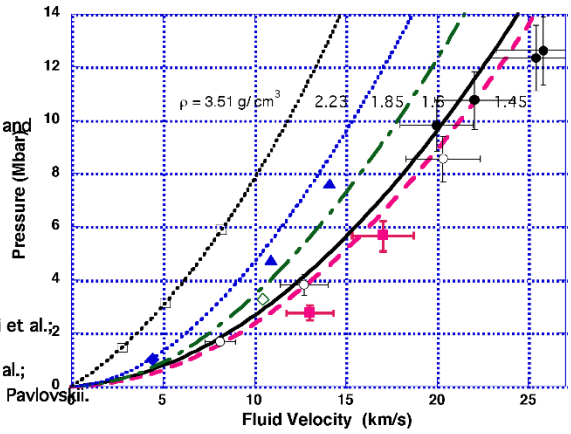

D.Batani, H.Nishimura, J.Ullschmied et al. "Hugoniot Data for Carbon at Megabar Pressures" Physical Review Letters, 92, 065503 (2004)

Laser experiments give the possibility of very high pressures and "*huge*" statisti
Carbon more compressible than what predicted by theoretical models

Pirometric temperature Measurement

Need for absolute calibration of diagnostics

- Brightenss temperature
  Stefan Boltzman' s law ≈ σT^4
- Emissivity temperature
  Emission at a given wavelenghth λ
  Need for relative calibration
- Spectral temperature
  Fit to a blackbody spectrum
- Color temperature
  Emission ratio of in two channels I_b / I_r
  (possibly on *the same* detector)

TARGET
--> 12 μm Al coated with
1000 Å Au on laser side

$I \approx 6\ 10^{13}$ W/cm²

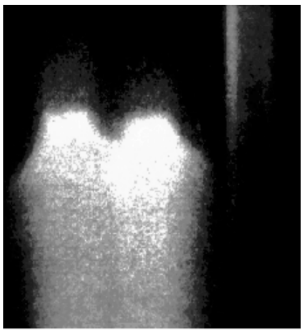

In ALL cases: 1) Blackbody hypothesis f(λ)
2) Need to measure reflectivity to get real temperature through Kirchoff' s law $\varepsilon(\lambda)/(1-r(\lambda)) = f(\lambda)$ (as obtained by VISARS)

Example of emissivity temperature

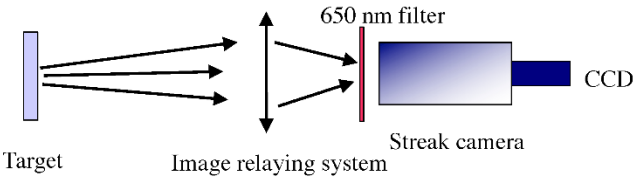

We measure:

- The transmission efficency of the image relaying system at 650 nm
- The response of the system (streak camera + CCD) at 650 nm

We can then map the counts on the CCD to the radiance B_{target} of the target at 650 nm.
In this way, we can measure a black-body temperature T_{BB} by assuming:

$$B_{target} = B_{Planck}(T_{BB}, 650nm)$$

We correct this value for a grey body with the absorption coefficient a = 1 – R, where R is measured at 532 nm *(it should be measured at 650 but at 532 we can use the VISAR)*

The measured temperature T comes from $B_{target} = a(532nm) \cdot B_{Planck}(T_{BB}, 650nm)$

38

VISAR (Velocity Interferometer for Any Reflector)

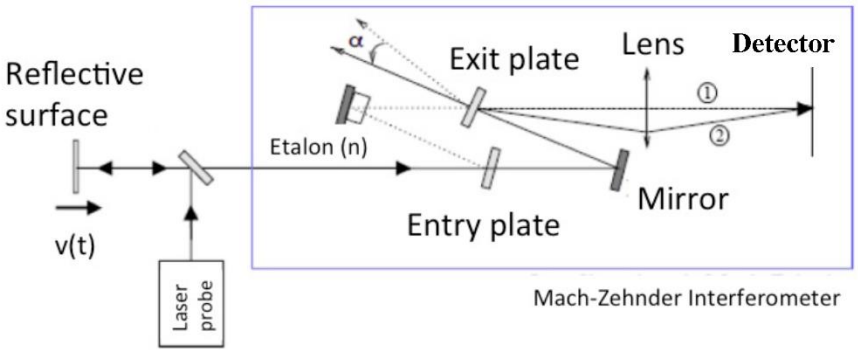

Doppler Effect

$$\frac{d\lambda}{\lambda} = \frac{2V}{c}$$

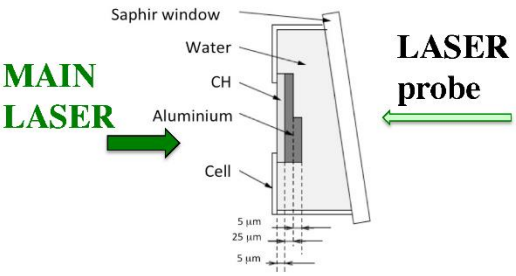

39

ETALON

Uses the "swimming pool" effect to introduce a time delay while preserving the spatial coherence. The delay introduced by the etalon is

$$\tau = 2e / c(n - 1/n)$$

The fringe shift and the measured velocity are related through the VISAR equation

$$F = \frac{2\tau V}{\lambda_O(1+\delta)} = \frac{Vn_O}{S}$$

Due to Doppler effect one must consider the dispersion in the etalon

$$n(\lambda) = n(\lambda_O) + (dn/d\lambda)(\lambda(t) - \lambda_O)$$

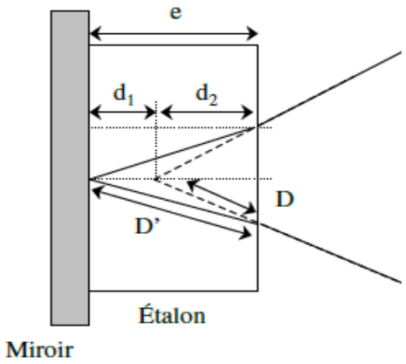

For fused silica with 10 mm thickness τ = 52 ps and δ = 3.15%

You need two VISARs to resolve the fringe jump !

Interpretation of VISAR shift

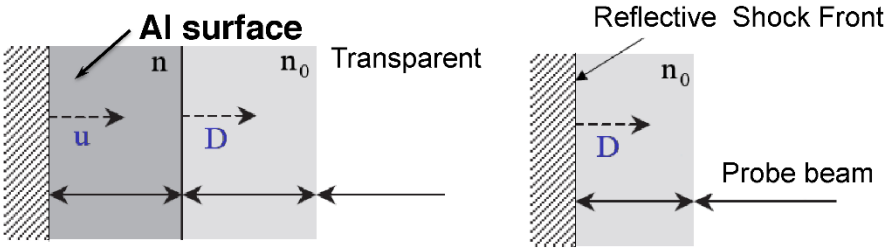

- ✓ **Not-so-compressed:** $n_O U = SF$
- ✓ **Metallized:** $n_O D = SF$
- ✓ **Compressed not metallized:** $n_O D - n(D-U) = SF$

D - shock velocity, n_0 - refractive index of non-shocked transparent medium
S - sensitivity of the VISAR, F - shift of the fringes, n - refractive index of shocked transparent medium, U – fluid velocity.

Detected VISAR signal

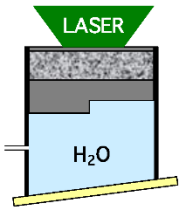

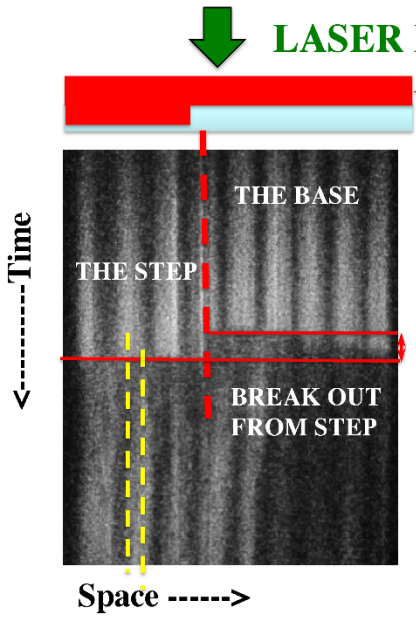

BREAK OUT FROM BASE

Δt

- **Shock velocity** in Al via the step size (d_{step})

$$D_{Al} = \frac{d_{step}}{\Delta t}$$

- **Velocity of the reflecting surface** (D) via the fringe shift (F) and the VISAR sensitivity (S):

$$D = \frac{S}{n_o} F$$

42

Detected VISAR signal

Phase Transition in water at Mbar pressures

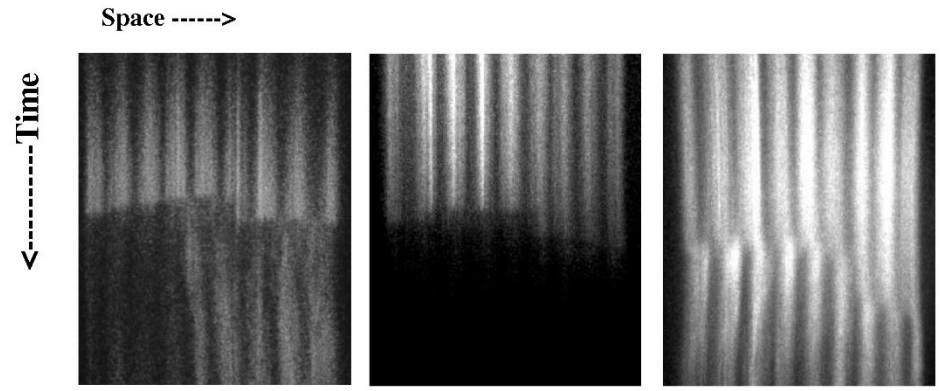

Transparent water
P ~ 0.27 ÷ 0.4 [Mbar]
ρ ~ 2 ÷ 2.2 [g/cm³]

Opaque water
P ~ 0.6 ÷ 1.0 [Mbar]
ρ ~ 2.3 ÷ 2.7 [g/cm³]

Reflecting water
P ~ 1.1 ÷ 3.0 [Mbar]
ρ ~ 2.8 ÷ 3.6 [g/cm³]

43

Precompressed targets

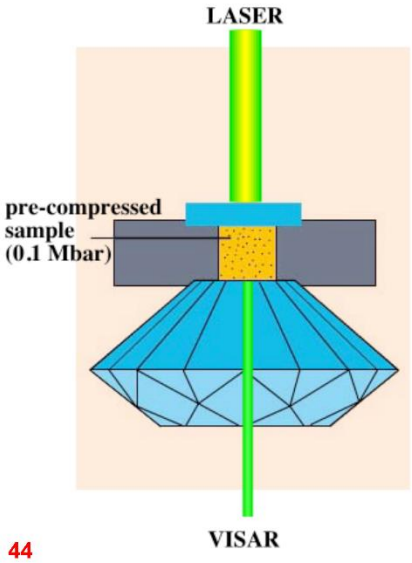

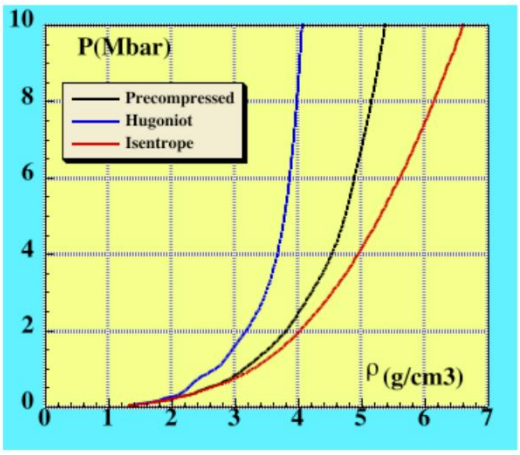

44

Optical properties of water

D. Batani,
K. Jakubowska, et al.,
EPL, 112 (2015)
36001

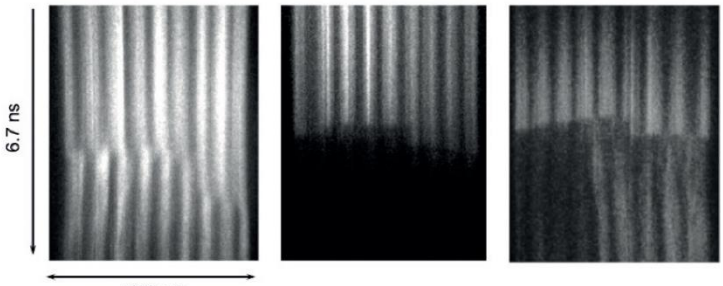

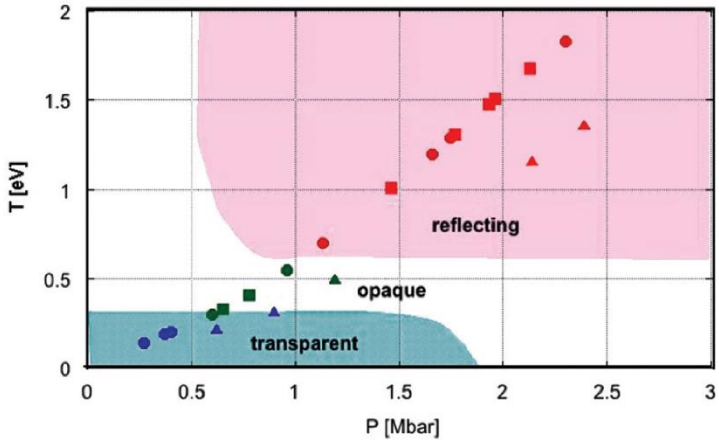

45

Phase Zone Plates (PZP)

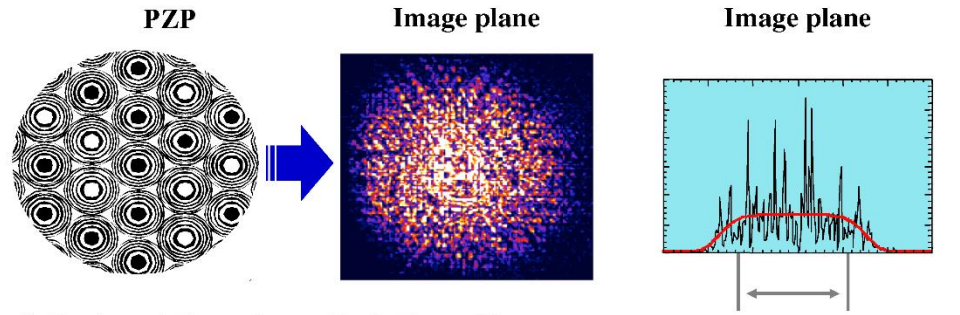

Collection of Fresnel Lenses with Random Phases 0 - π at 440 nm

Each Fresnel lens spot is imaged in the far-field of the principal lens, the laser field Spatial Coherence is broken

Flat Focal Spot 250 μm

Spikes due to residual time coherence, averaged by electron thermal transport

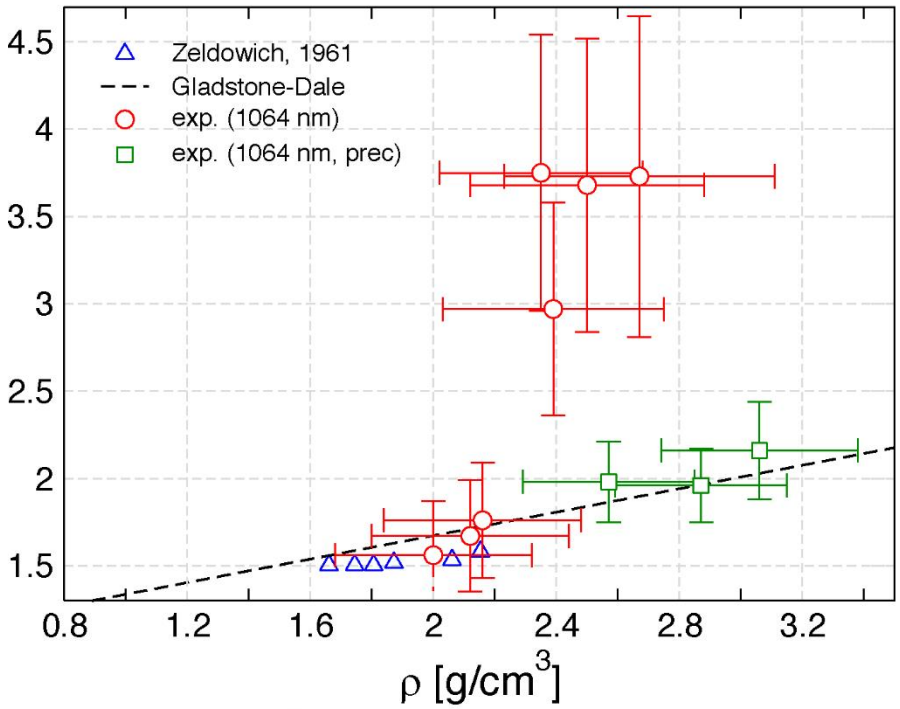
Zeldowich, 1961
Gladstone-Dale
exp. (1064 nm)
exp. (1064 nm, prec)
4.5
4
3.5
3
2.5
2
1.5
0.8
1.2
1.6
2
2.4
2.8
3.2
ρ [g/cm3]

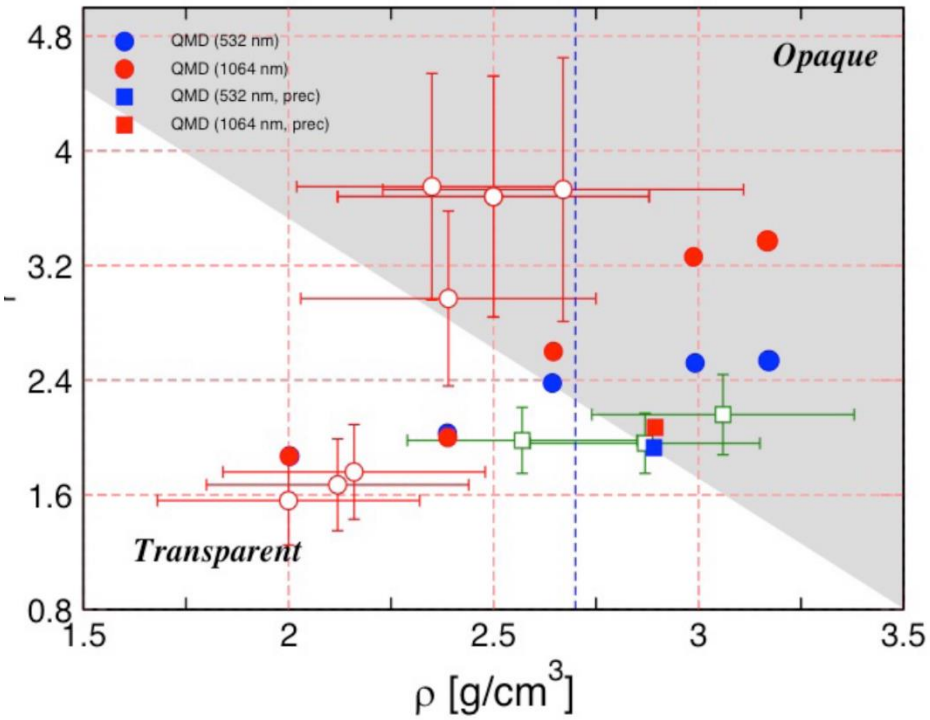
QMD (532 nm)
QMD (1064 nm)
QMD (532 nm, prec)
QMD (1064 nm, prec)
Opaque
Transparent
4.8
4
3.2
2.4
1.6
0.8
1.5
2
2.5
3
3.5
ρ [g/cm3]

Limits of VISAR and SOP
(Experiment at LIL)

$E_{LIL}(3\omega) = 9700$ J

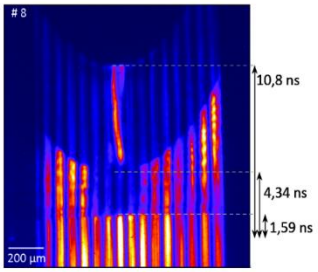

AR @532nm on rear side

$E_{LIL}(3\omega) = 9900$ J

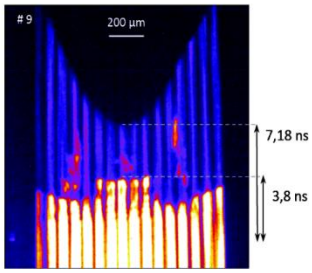

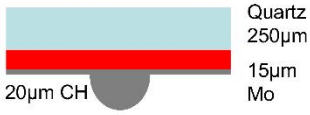

CH Hemisphere
500 µm diameter

- *Blanking of VISAR (and SOP)*
- *Need to measure density directly*

VISAR in inertial fusion

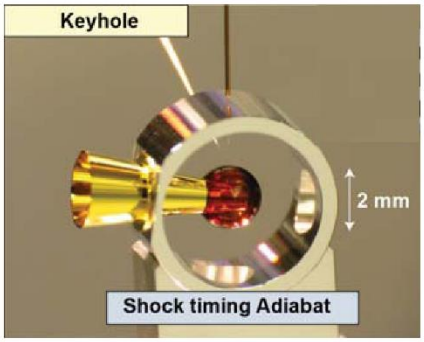

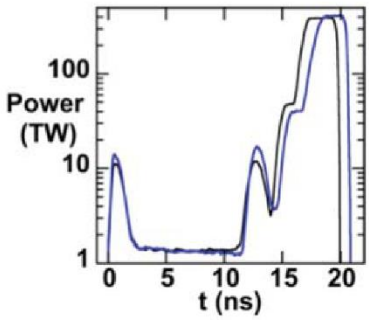

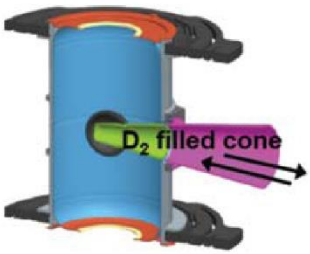

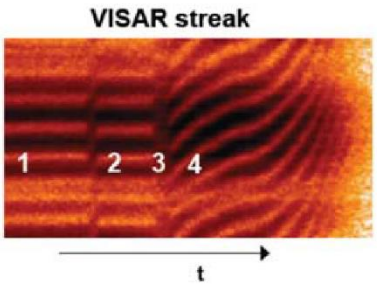

47

Examples of results (VISAR - SOP)

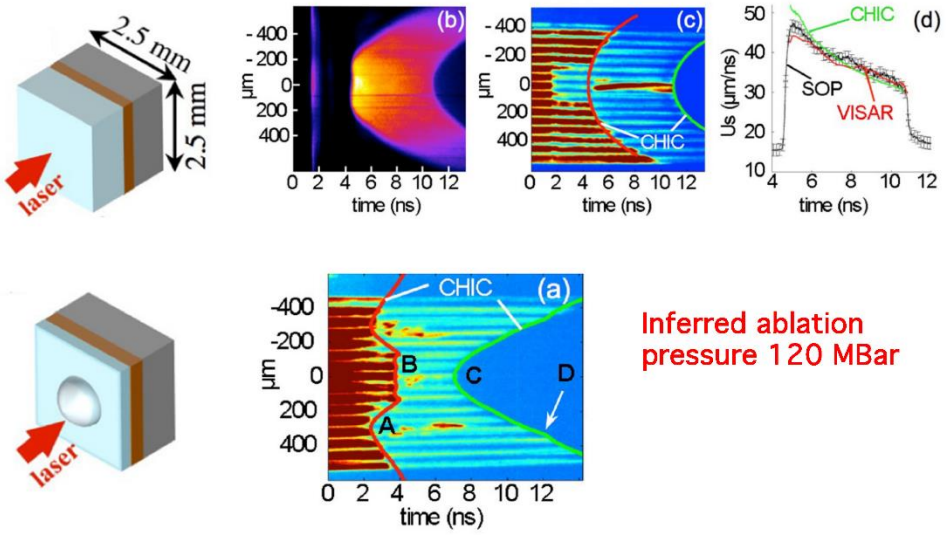

Inferred ablation pressure 120 MBar

"Shock generation comparison with planar and hemispherical targets in shock ignition relevant experiment" S. D. Baton, et al. PHYSICS OF PLASMAS 24, 092708 (2017)

11.2 Diagnostics with radiography

2D time-resolved X-ray radiography

Using small X-ray source and point-projection

Shocking materials to create WDM and HED states and radiography them by hard x-ray radiography

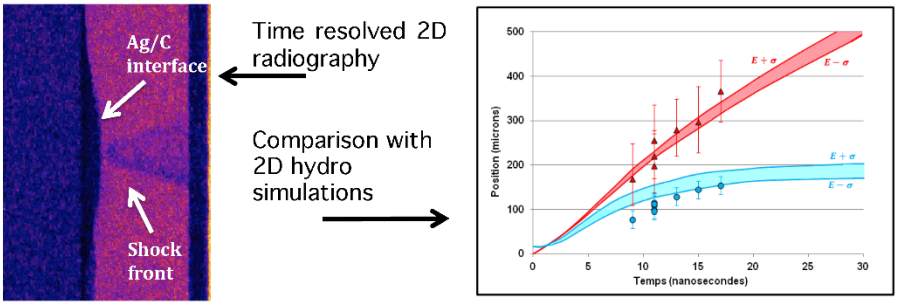

Experimental results obtained at LULI (A.Morace et al.). Motion of shock front and material interface are followed by X-ray (Ka) radiography.
Shock diagnostics at very high pressure when other diagnostics (e.g. VISAR) can be blinded (e.g. shocks produced in the context of "shock ignition")
EOS experiment (detection of D and U allows to obtain the equation of state of material)

53

2D time-resolved X-ray radiography

Using extended X-ray source and imaging system

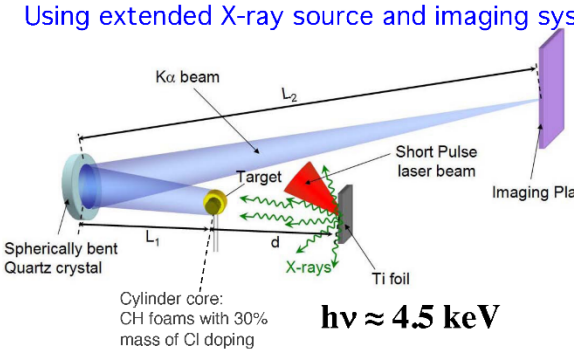

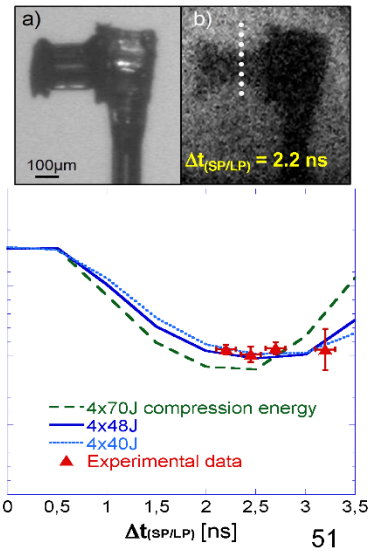

➡ Cylindrical compression is visible

➡ Stagnation time τ = 2.5ns and diameter in fair agreement with predictions from hydro simulations

Expt performed at RAL

51

51

2D time-resolved X-ray radiography

Using small X-ray source and point-projection

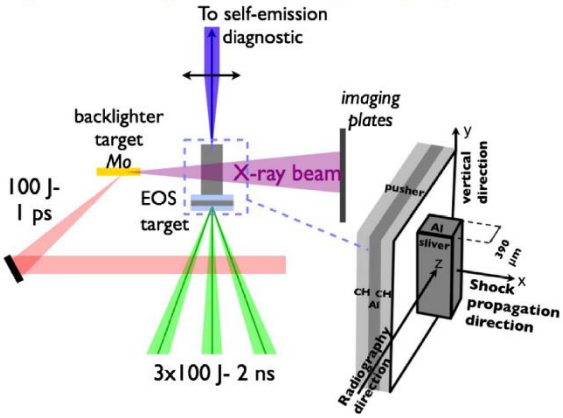

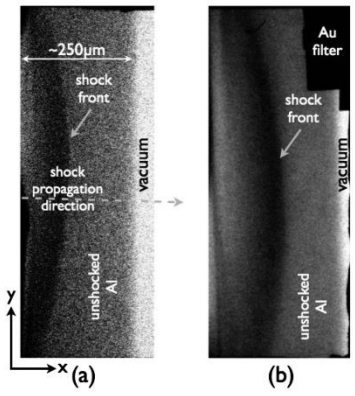

FIG. 2. Radiographs of a shock wave propagating in Al samples taken at 5 ns (a) and 8 ns (b) after the shock driver beams maximum intensity.

A.Ravasio, M.Koenig, S.Le Pape, A.Benuzzi-Mounaix, H.S.Park, C.Cecchetti, P.Patel, A.Schiavi, N.Ozaki, A.Mackinnon, B.Loupias, D.Batani, T.Boehly, M.Borghesi, R.Dezulian, E.Henry, M.Notley, S.Bandyopadhyay, R.Clarke, and T.Vinci «Hard x-ray radiography for density measurement in shock compressed matter» PHYSICS OF PLASMAS 15, 060701 □2008□

52

1D radiography with ns beam

X ray radiography for time-resolved imaging of shock propagation
Laser GEKKO
Osaka Univ

Shock produced inside Beryllium target (100 µm)

Ti foil used as X-ray backlighter

Image is time resolved by an X-ray streak camera coupled to a pin-hole

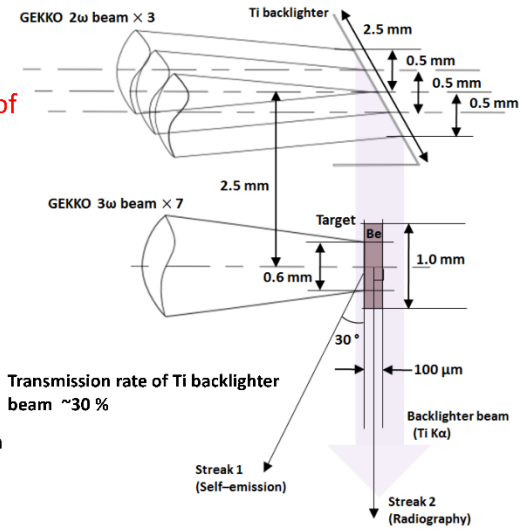

Transmission rate of Ti backlighter beam ~30 %

54

1D radiography with ns beam

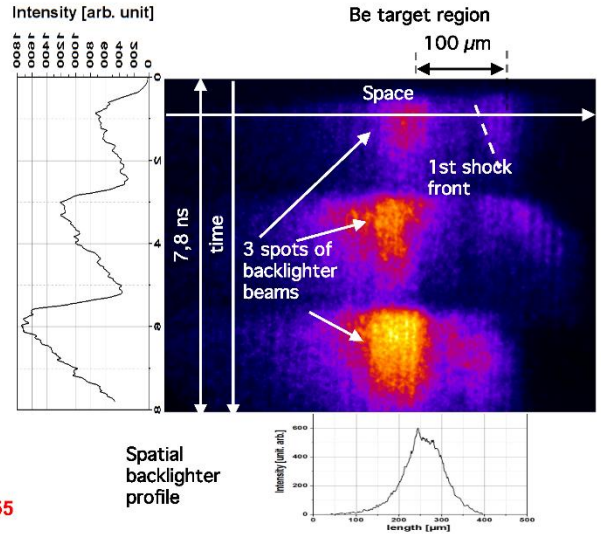

Radiography image (raw)

The knowledge of the spatial and temporal profiles of the X-ray backlighting source allow for image deconvolution

55

1D radiography with ns beam

The image is normalized using spatial and temporal profiles of backlighter emission.

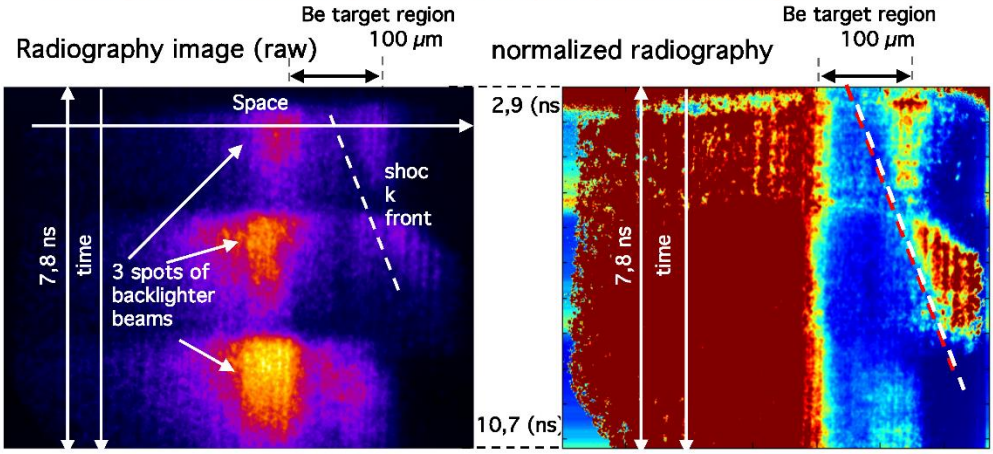

Average shock speed 19 km/s in agreement with hydro simulations

56

X-ray radiography at LULI

2D time-resolved radiography with ps beam
Shock dynamics & Density

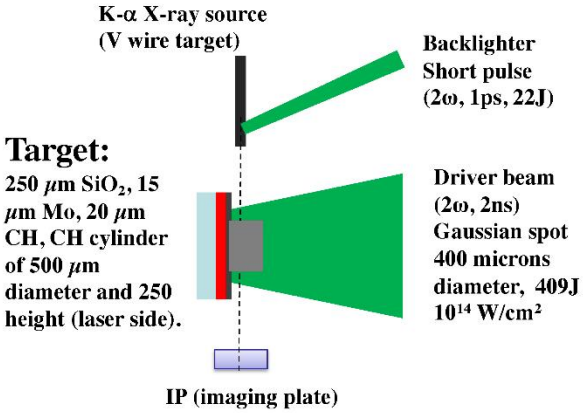

L. Antonelli, et al. «Laser-driven shock waves studied by X-ray radiography» PRE 95, 063205 (2017)

57

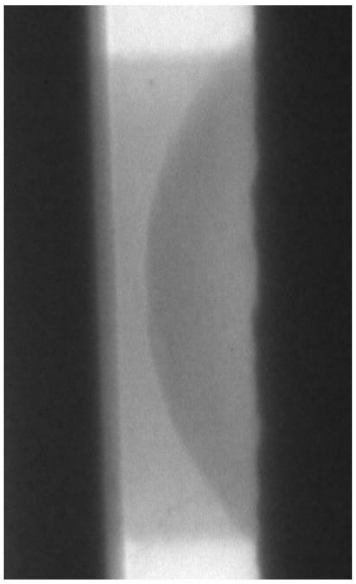

Radiography 4.7ns after shock creatio

Conventional treatment: Abel inversion

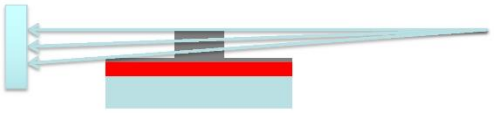

Problems:
- Very noisy
- Does not take into account source size

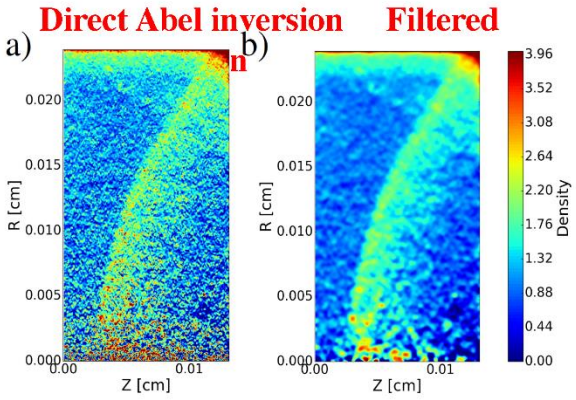

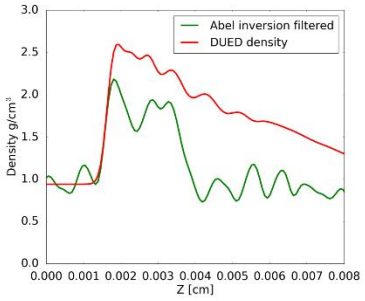

58

Synthetic radiography

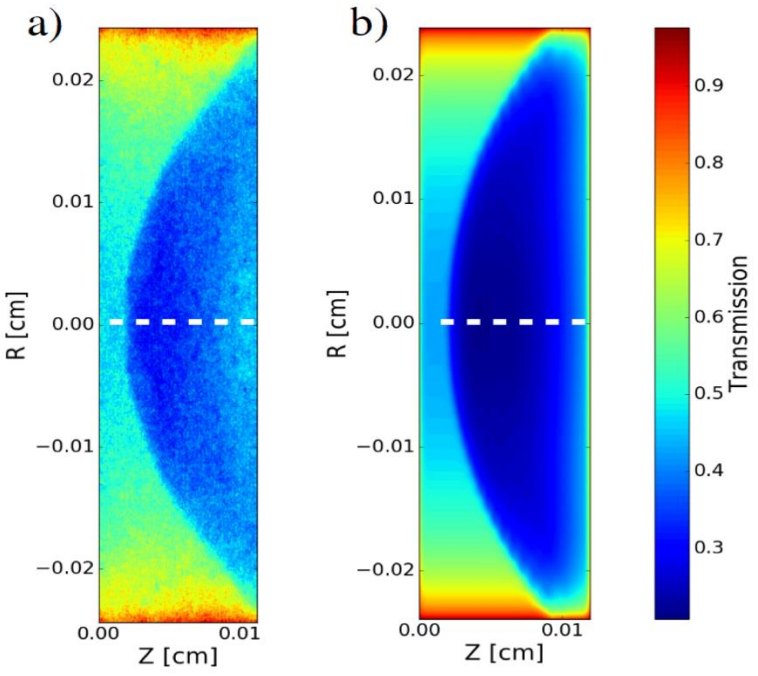

L.Antonelli, et al., « Laser-driven shock waves studied by x-ray radiography » PHYSICAL REVIEW E 95(6) · June 2017

59

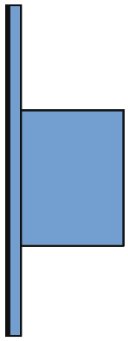

Cylindrical
Target,
t= 4.7 ns

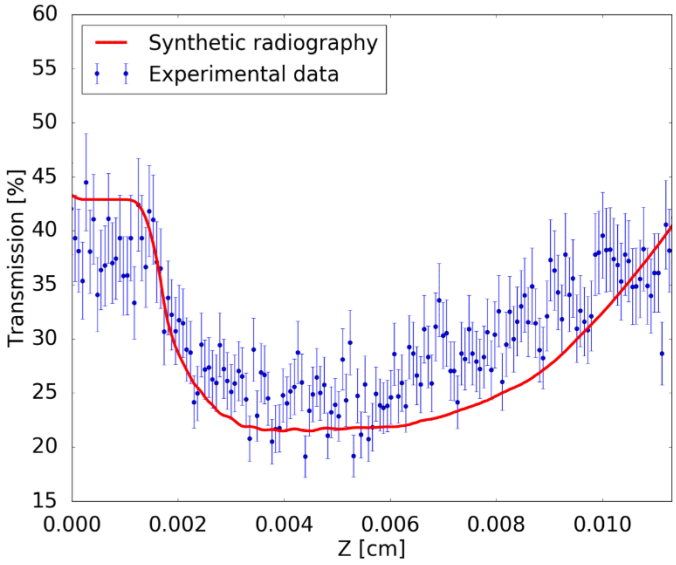

Limitations of X-ray radiography

Development of X-ray Phase Contrast Imaging

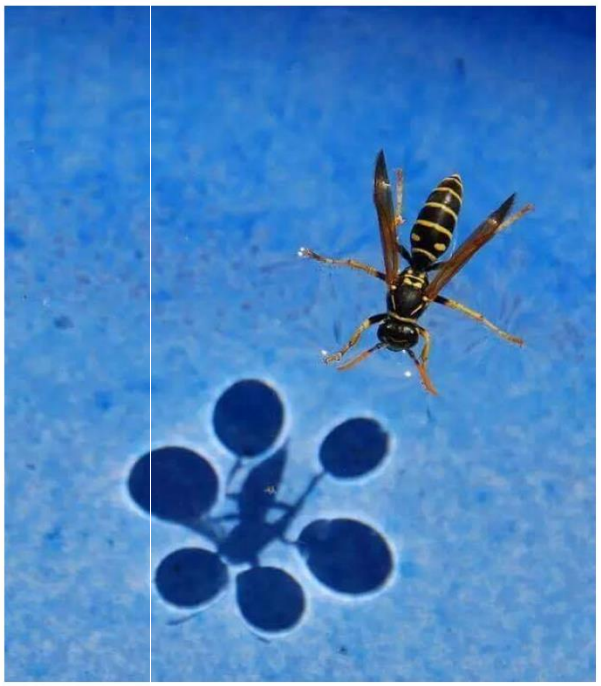

Developing diagnostics: phase contrast

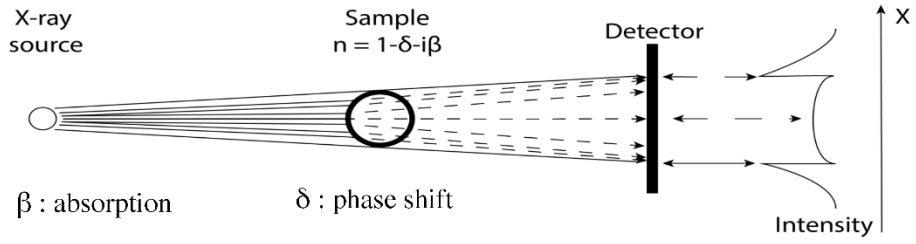

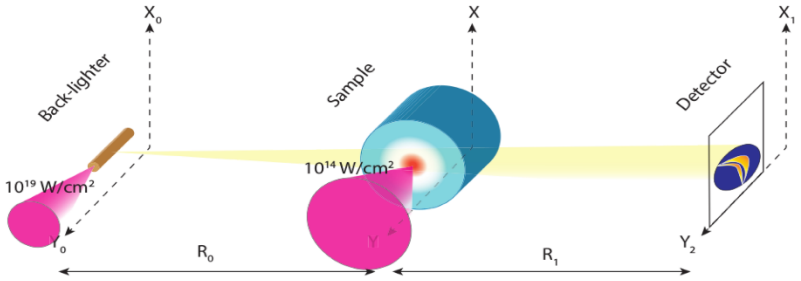

61

Developing diagnostics: phase contrast

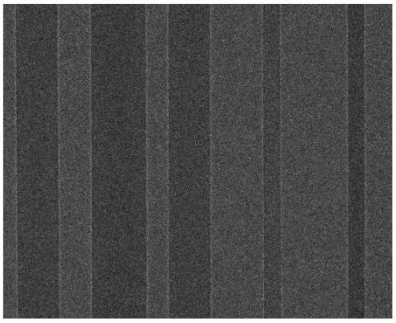

Static objects test:
Nylon wires

Phase contrast with
a single shot (Phelix)

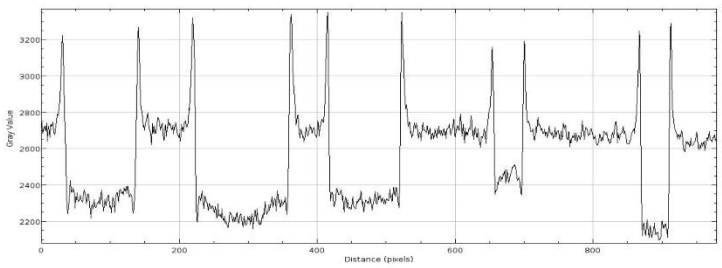

62

Developing diagnostics: phase contrast

EXPERIMENT FROM PHELIX

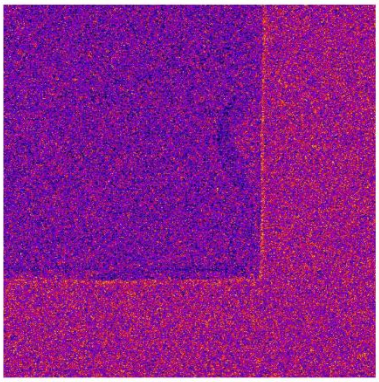

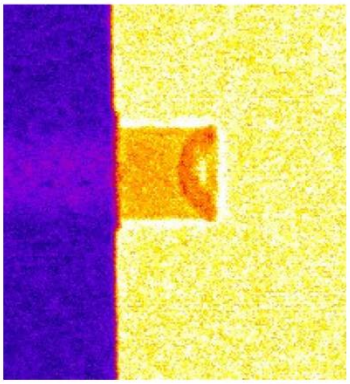

Dynamic test:

E_{tot} = 30 + 30 J

t=4 ns
Imaging Plate
Cylindrical target (Scitech)

t = 10 ns
X-ray CCD
PMMA target

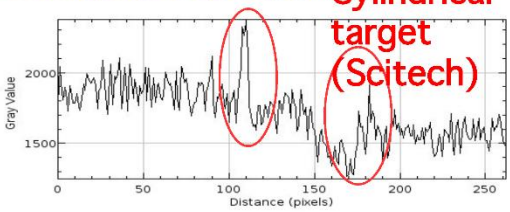

63

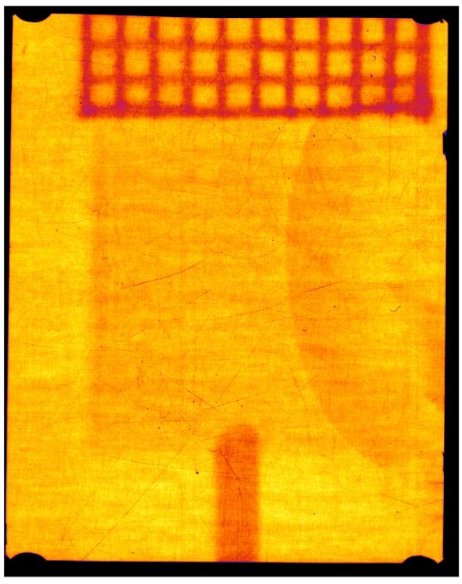

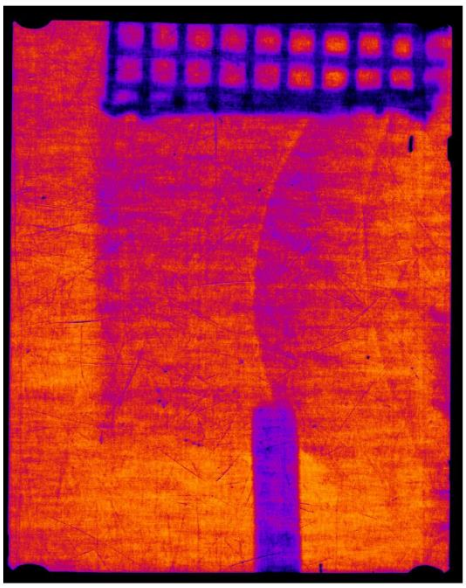

Absorption measurements

Measuring K-edge shift in shock-compressed materials

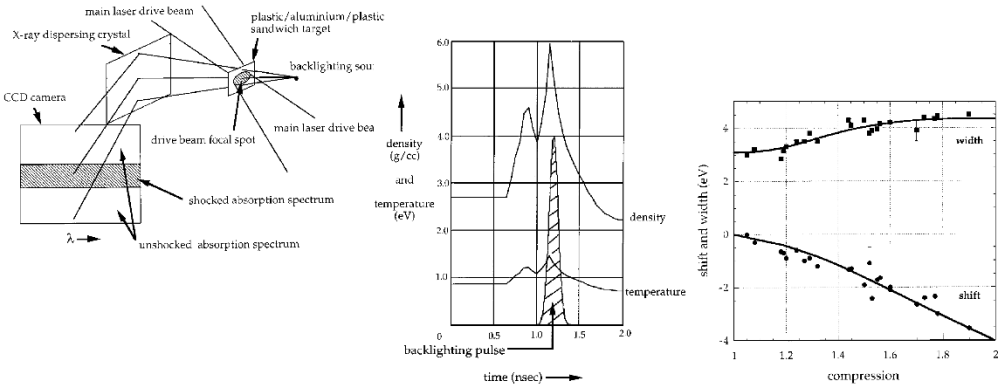

T.A.Hall, J.Al-Kuzee, A.Benuzzi, M.Koenig, J.Krishnan, N.Grandjouan, D. Batani, S. Bossi and S. Nicolella «Experimental observation of the shift and width of the aluminium K absorption edge in laser shock-compressed plasmas» Europhys. Lett., 41 (5), pp. 495-500 (1998)

66

Absorption measurements

Measuring K-edge shift in shock-compressed materials

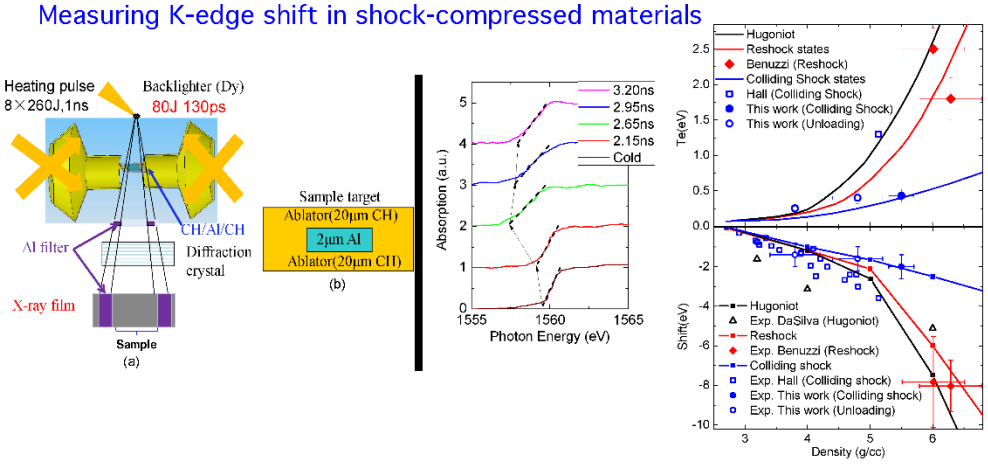

Yang Zhao, Zhiyu Zhang, Bo Qing, Jiamin Yang, Jiyan Zhang, Minxi Wei, Guohong Yang, Tianming Song, Gang Xiong, Min Lv, Zhimin Hu, Bo Deng, Xin Hu, Wenhai Zhang, Wanli Shang, Lifei Hou, Huabing Du, Xiayu Zhan and Ruizhen Yu «K-Shell Photoabsorption Edge of Strongly Coupled Aluminum Driven by Laser-Converted Radiation» EPL 2017

67

11.4 Conclusions

- High Energy Density Physics is a growing field at the crossing of plasma physics, material science, astrophysics, inertial fusion
- High-energy ns-lasers are an important tool in HED physics, expecially if coupled to PW systems
- X-ray diagnostics are essential to HED
- A large effort for development of diagnostics is going on

68

O4 –Experiments

PowerLaPs

Innovative Education & Training in High Power Laser Plasmas

Laser plasma diagnostics - Theory and Experiments

EXP 1: Charged particle detectors:Time-of-flight technique

V. Ospina

1 Physical principle

Physical principle: particle acceleration

$t = t_0$

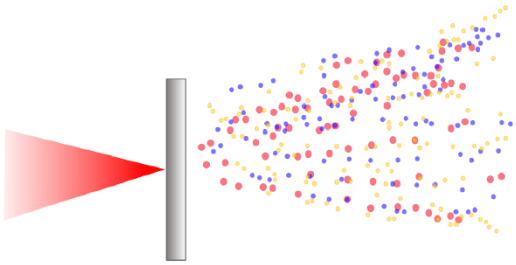

$t = t_0 + \delta$

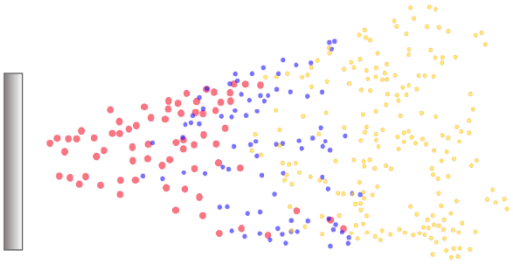

- The kinetic energy of the particles is given by:

$$E_k = \frac{m_p v_p^2}{2} \qquad v_p = \frac{d}{t}$$

Physical principle: signal detection

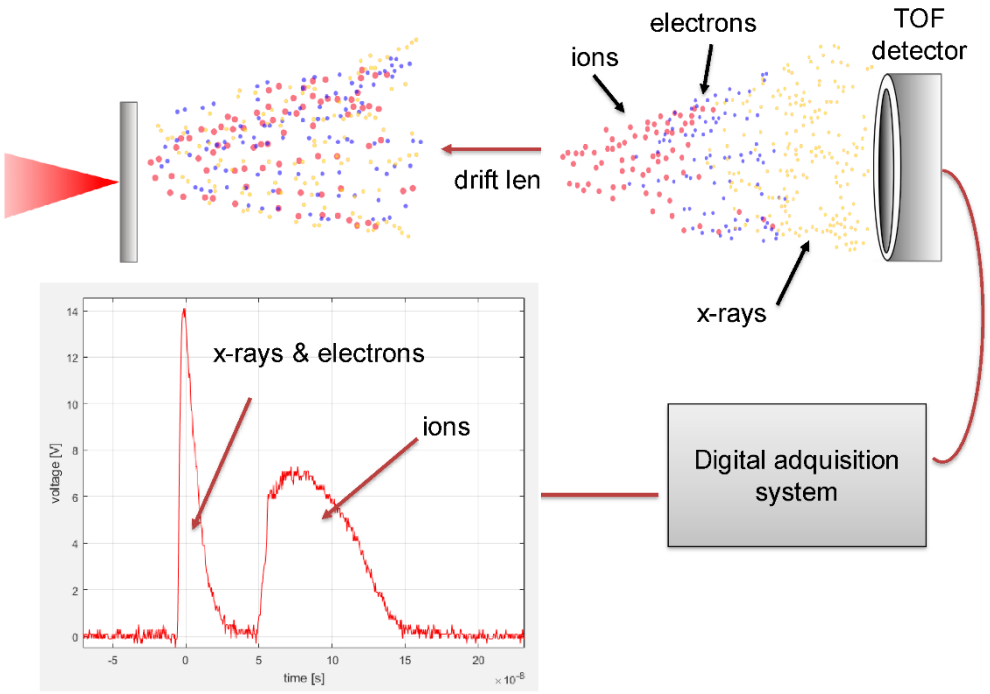

2 Types of detectors

Type of detectors: PIN diode

- Semiconductor based detector

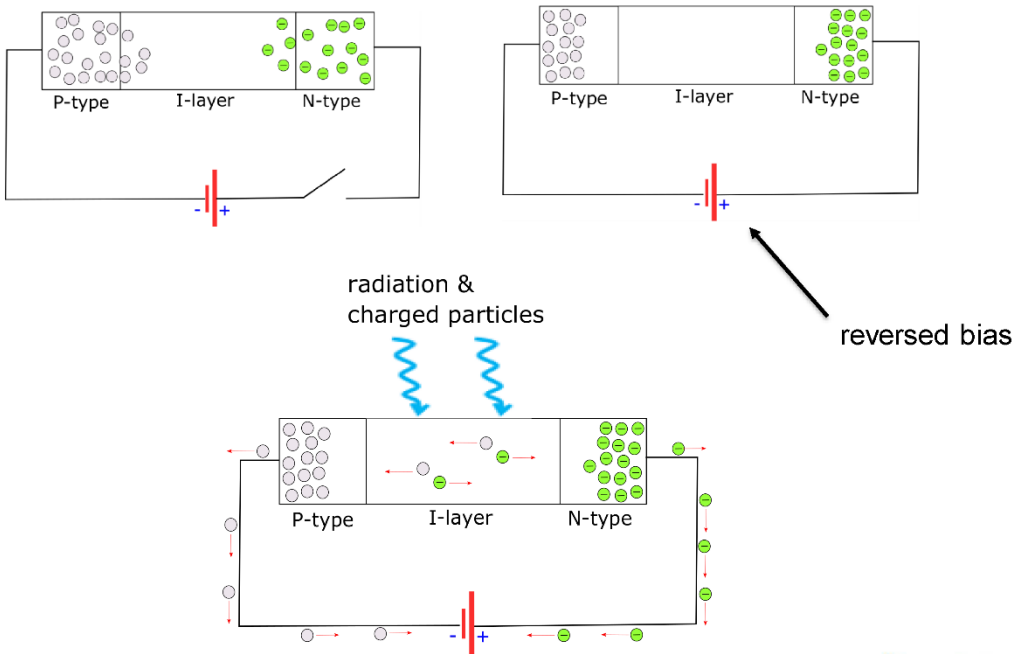

Type of detectors: PIN diode

- Semiconductor based detector: I-layer importance

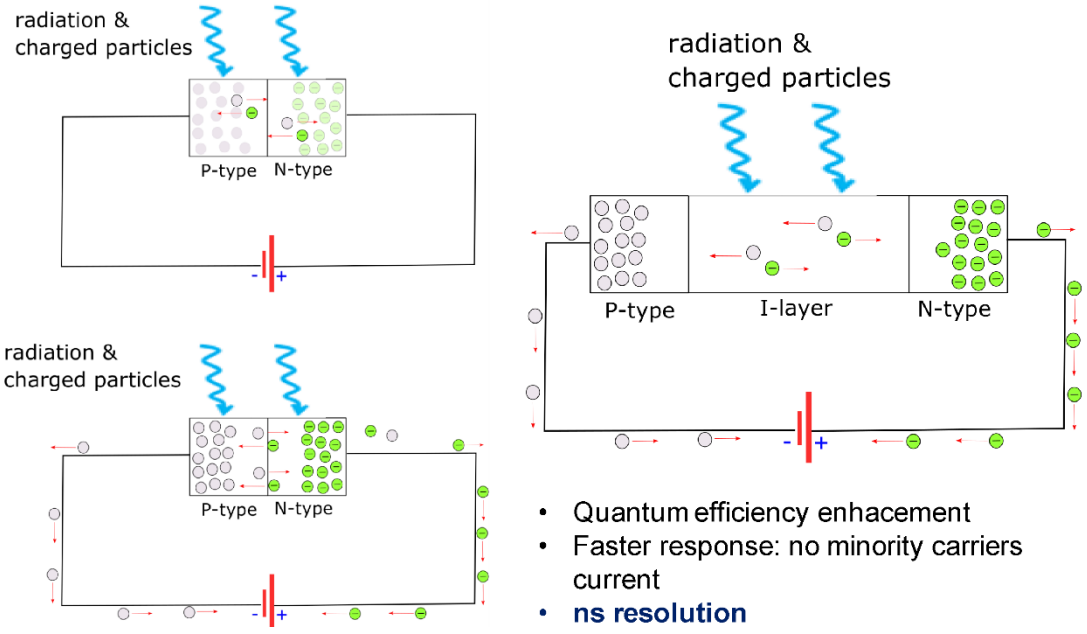

- Quantum efficiency enhacement
- Faster response: no minority carriers current
- **ns resolution**

- Chemical vapor deposition technique (CVD): low cost diamond sheets of higher purity and controlled characteristics
- Temporal properties:
  - Highest e-/hole mobilities & high electrical resistivity → high drift velocities
  - Low dielectric constant, low capacitance → less noise in the measure

$$c = \frac{k\varepsilon_0 A}{d}$$

  - Where k is the relative permittivity of the dielectric, ε_0 is the vacuum permittivity (8.854E-12 F/m), A is the area of the plates and d the separation between them
- **Tens of picoseconds resolution**
- Mechanical hardness & thermal conductivity → high ion fluxes
- High band gap (5.45 eV), good insulator → no PN junction is needed
- Very high radiation hardness (1 MGy)

Type of detectors: Diamond detector

- Detectors principle: creation on e-/hole pairs due to radiation and charged particle impact
- Diamond sample metalized on both side (Al, Au,…) and 90 µm to 500 µm diamond sample → parallel capacitor scheme. Generated charges are atracted to the electrodes

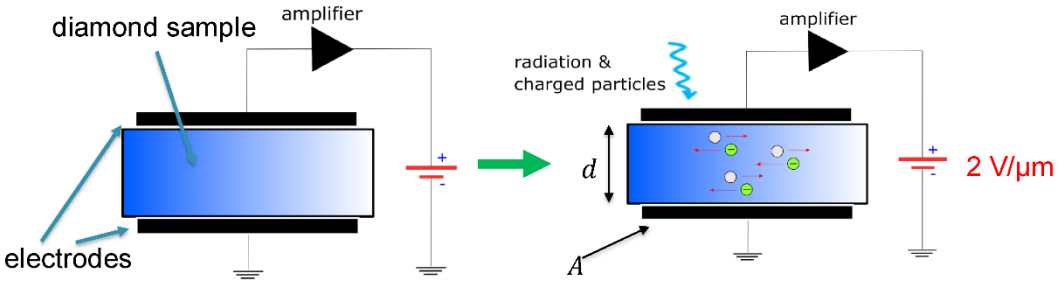

Type of detectors: Micro-channel plate

- Array of miniature electron multipliers oriented parallel to one another
- Parallel electric connections: metallic coating, electrodes
- Electron multiplication factors of 10^4 – 10^7 (Thorium or Barium)
- **Time resolution of hundreds of ps**
- Characteristics: shape and open area ratio (OAR) 60% - 80%

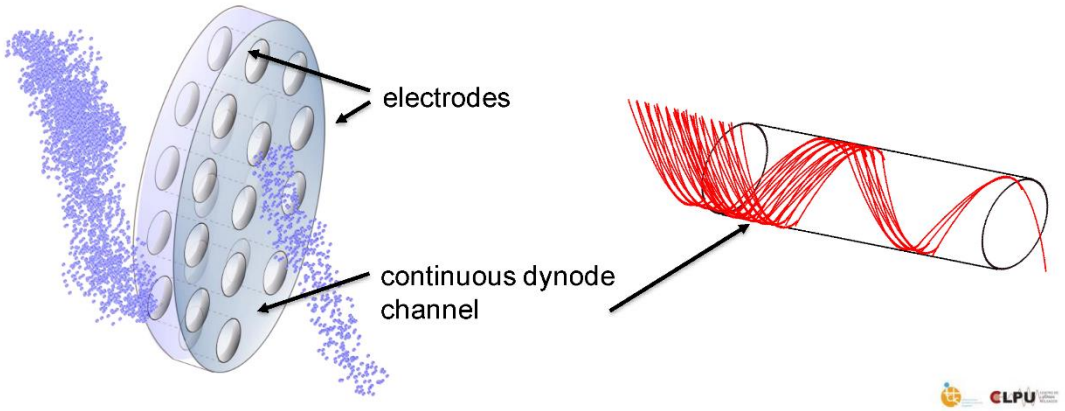

Type of detectors: Micro-channel plate

- Bias angle α = 5º - 15º to optimize detection efficiency and prevent incident particles from passing through

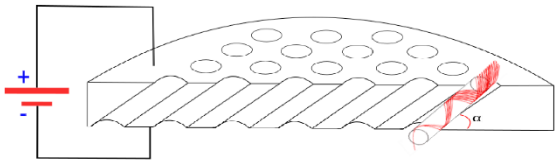

- Gain of the MCP where G is the gain factor (characteristic of the material) and β the length to diameter relation of each channel (40 - 60)

$$g = e^{G \cdot \beta}$$

$$\beta = \frac{L}{d}$$

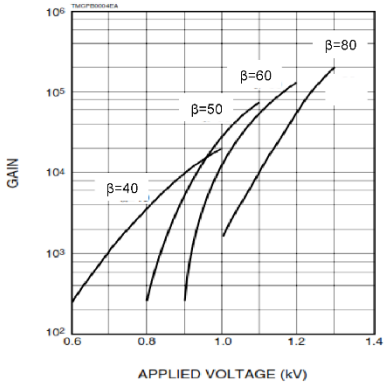

Hamamatsu MCP assembly Technical information

Type of detectors: Micro-channel plate

- When the gain increases to a certain level, self-generated noises caused by ion feedback effects become a problem
- To minimize this phenomenon two (chevron) or three (z-stack) MCP stages are stacked together
- The first MCP stage is polarized with an increasing (e- & UV) or decreasing (ions & UV) voltage depending on the charge of the particles that want to be detected

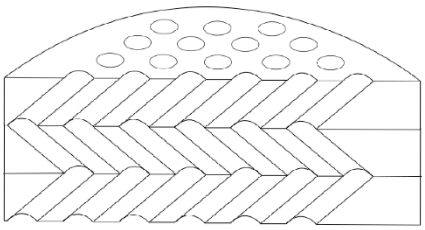

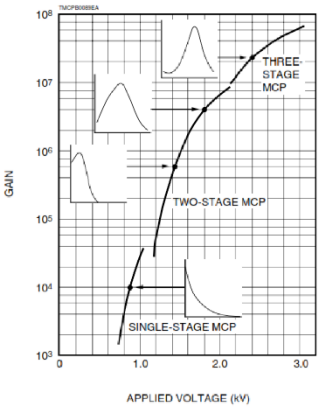

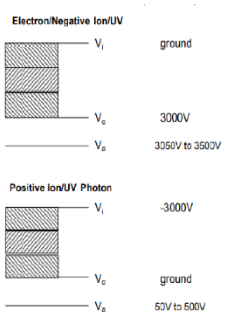

Hamamatsu MCP assembly Technical information

3 Experimental set-up

Experimental setup

- Acceleration mechanism (TNSA, Coulomb explosion,…) → detector's location
- Effective detection area vs. cone of emission → solid angle

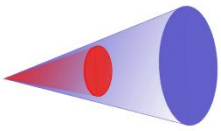

- Filter (Al, Cu, mylar,..)
- Temporal resolution of the measure

$$max.energy \rightarrow E_2 \qquad energy\ increment \rightarrow \Delta E \qquad E_2 = E_1 + \Delta E$$

$$\Delta t_{resolution} = \sqrt{\frac{m_p}{2}} \cdot x_{TOF} \cdot \left(\frac{1}{\sqrt{E_2}} - \frac{1}{\sqrt{E_1}} \right) \geq \Delta t_{system}$$

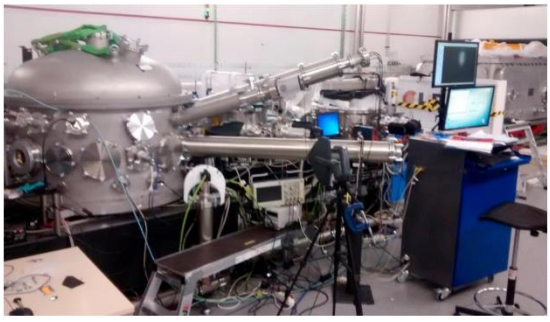

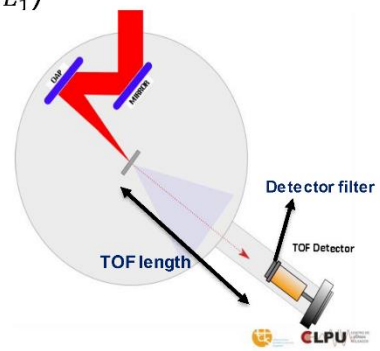

Experimental setup: working around the system resolution

$$\Delta t_{system} = 0.2\ ns$$

- TOF length variation

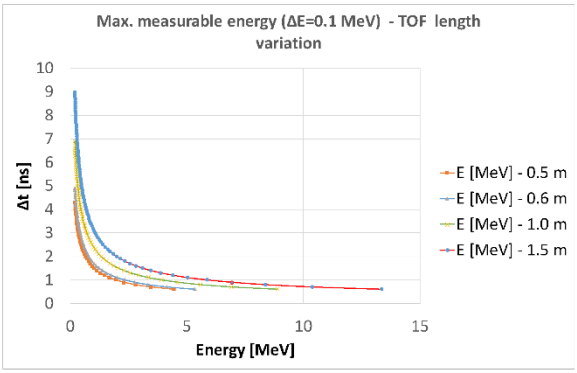

- ΔE variation

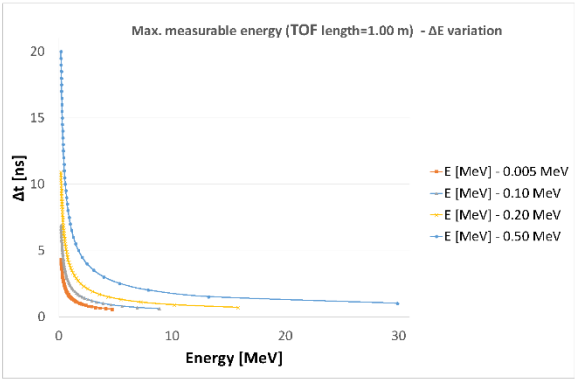

CLPU

4 Data analysis

Data analysis procedure

- Deconvolution of output signal knowing the detectors response function:

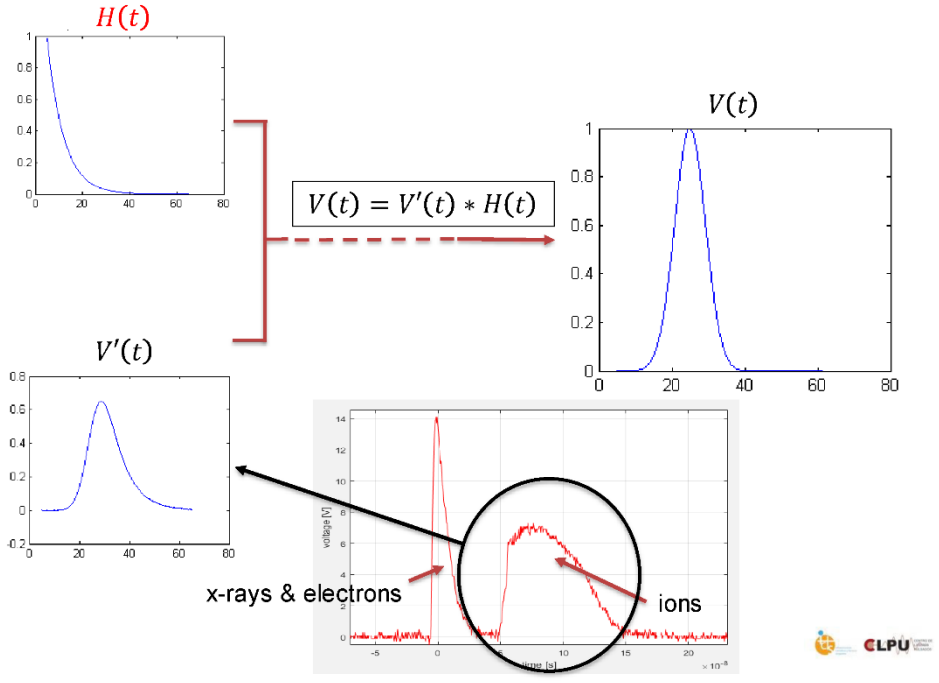

CLPU

Data analysis procedure

- Obtention of the derivative of the charge in each interval:

Y axis $I(t) = \frac{dQ(t)}{dt} = \frac{V(t)}{R_{OUTPUT\ SYSTEM}}$; $\frac{dQ}{dE} = \frac{dQ}{dt} \cdot \frac{dt}{dE}$

X axis $E(t) = \frac{m_p \cdot x_{TOF}^2}{2} \cdot \frac{1}{t^2}$

$\frac{dQ}{dE} vs. E$ → $\int$ → $Q\ vs. E$

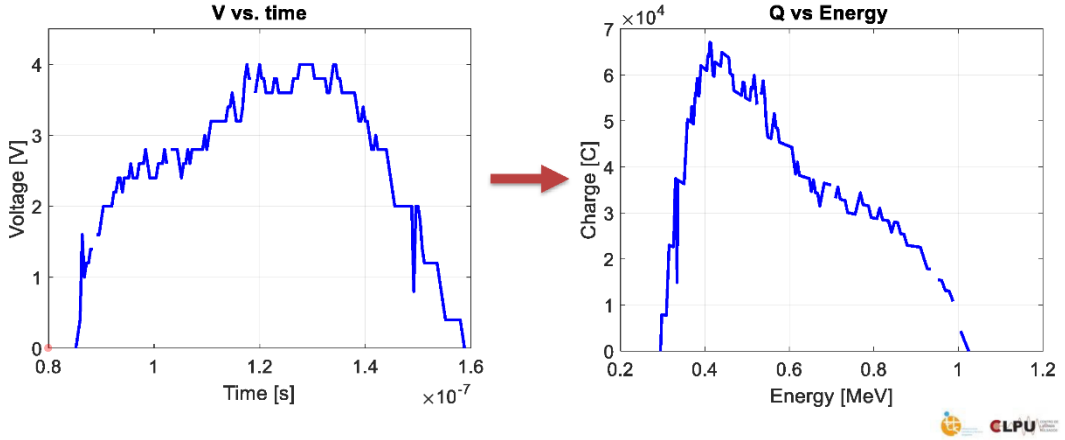

Data analysis procedure

- Distribution of the detected particles $F(E)$:

$F(E) = \frac{dQ}{dE} \cdot C(E)$

$F(E) = Q \cdot C(E)$

Calibration function to obtain a spectrum

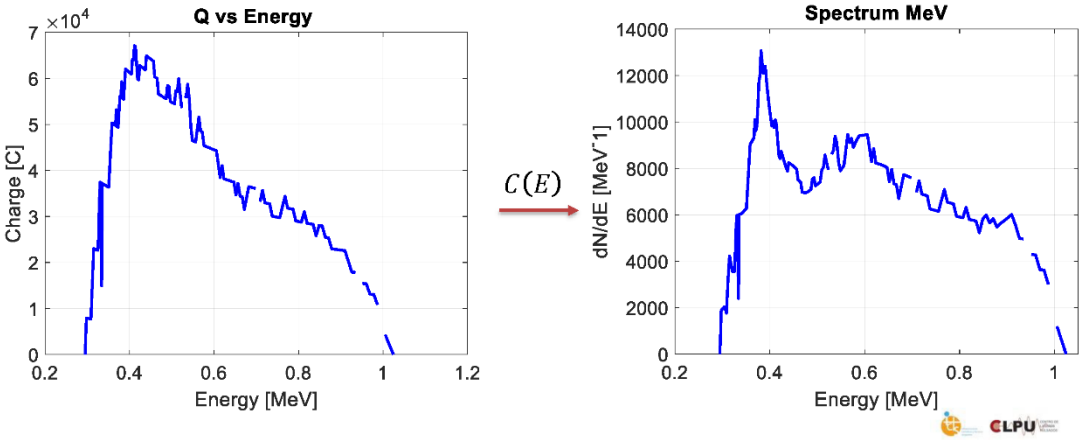

Detector characterization: response & calibration functions

- **Response function:** output signal when an impulse input signal is introduced to the system

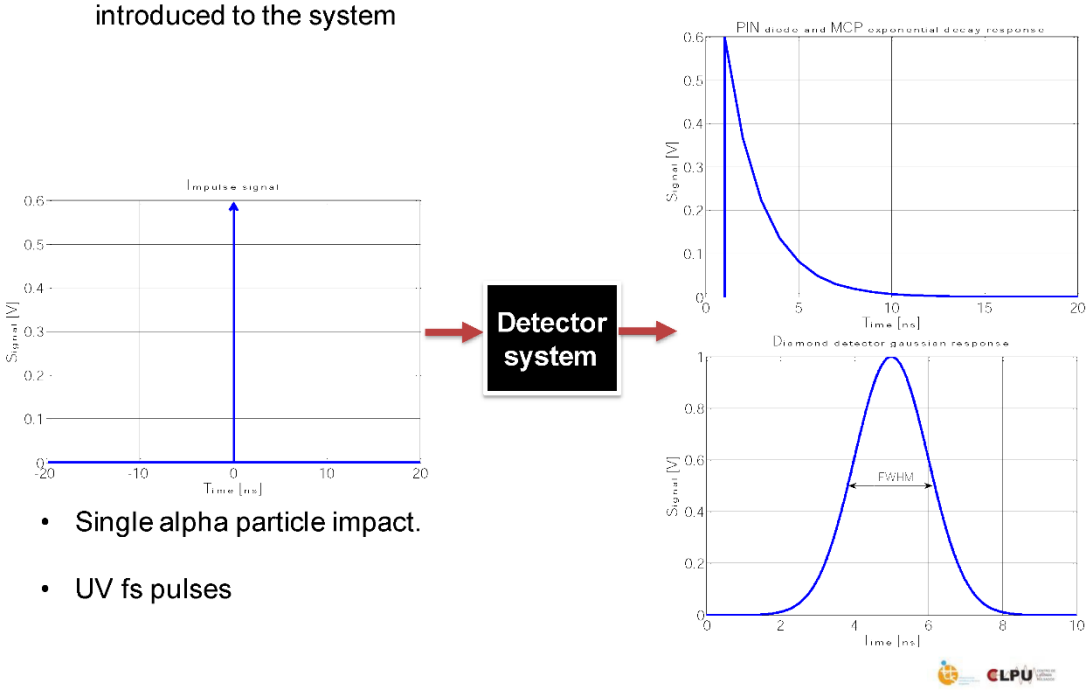

- Single alpha particle impact.
- UV fs pulses

Detector characterization: response & calibration functions

- **Calibration function:** charge deposited in the detector as a function of the particle energy
  - PIN diodes: linear behaviour can be considered. Calibrations in literature are mostly done for x-rays but can be used as a first aproximation for charged particles
  - Diamond detector: energy dependent calibration functions

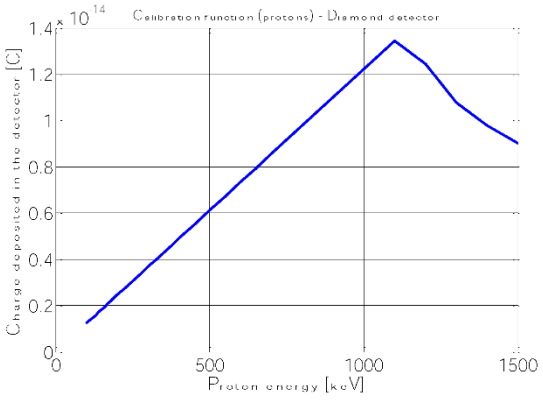

Claudio Verona - University of Rome

- **Calibration function:** charge deposited in the detector as a function of the particle energy
  - Micro-channel plate (MCP) can be proportionally calibrated by installing it as a detector in a Thomson parabola spectrometer. Same material and bias angle

Detector characterization: response & calibration functions

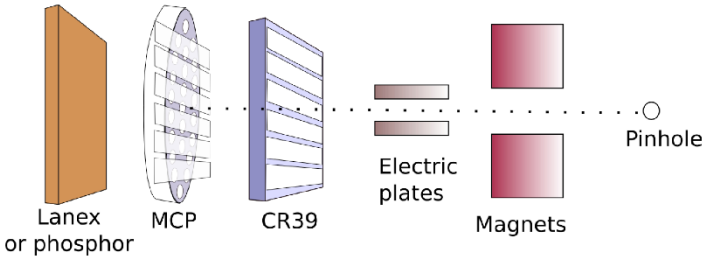

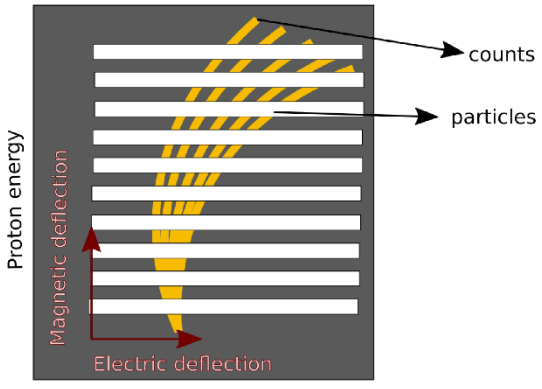

Time-of-flight at CLPU

- Long focalization in gas jet targets – November 2017

  VEGA 2 (200 TW) was focused by a F/13 parabolic mirror on a gas-jet placed at 30 cm far from the TCC. Two PIN diodes were located at 130.7 cm and 135.7 cm. Max. energies of 2.5 MeV

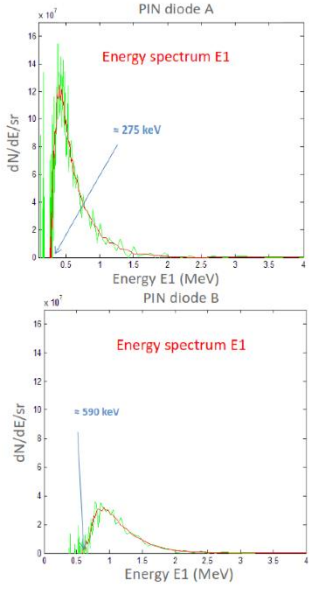

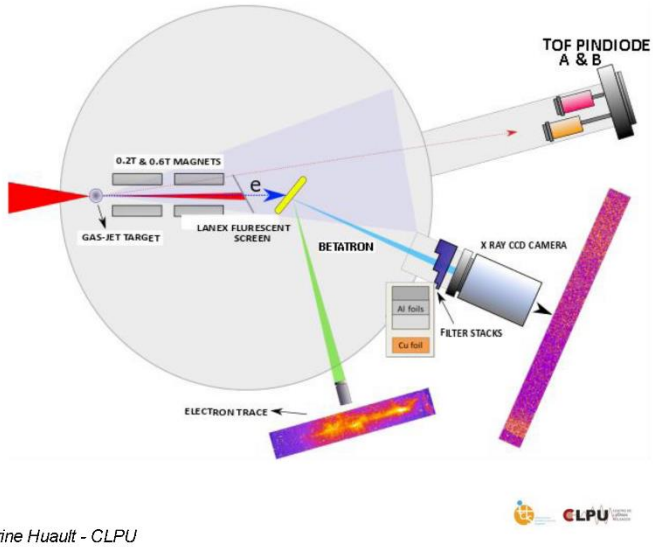

Marine Huault - CLPU

Time-of-flight at CLPU

- Short focalization in solid targets – February 2018

  VEGA 2 was focused by a F/4 gold coated parabolic mirror on a 5 µm thick Al foil with an angle of 10 degrees with respect to the normal of the foil. Max. energies of around 7 MeV

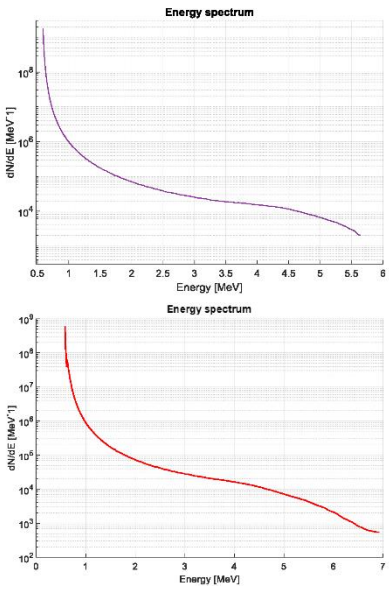

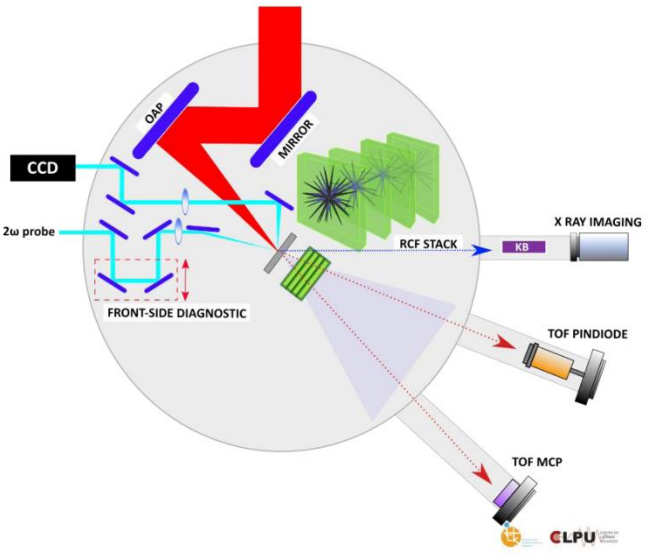

Time-of-flight at CLPU

- Ion stopping power measurements in moderately coupled and degenerate plasma target: characterization of the proton source – May 2018

  VEGA 2 (200 TW) was focused by a F/13 parabolic mirror on a 6 μm Al solid target. TOF diagnostics were installed in the perpendicular trajectory with the help of a vacuum interface

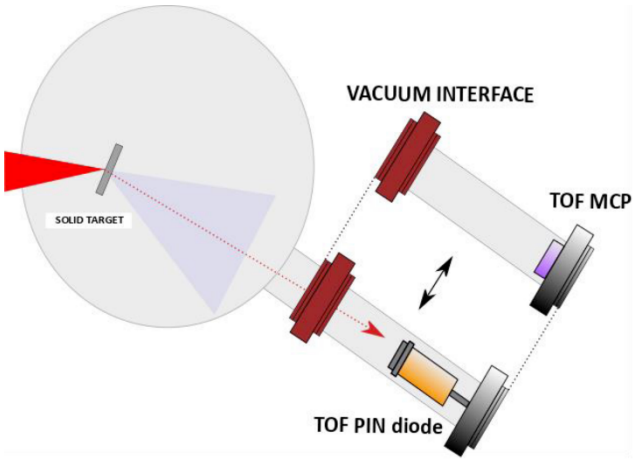

Time-of-flight at CLPU

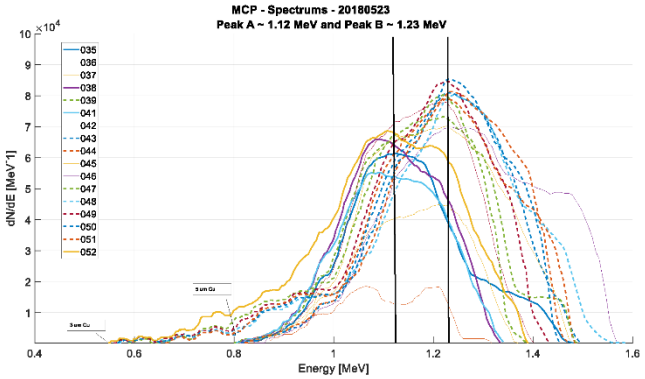

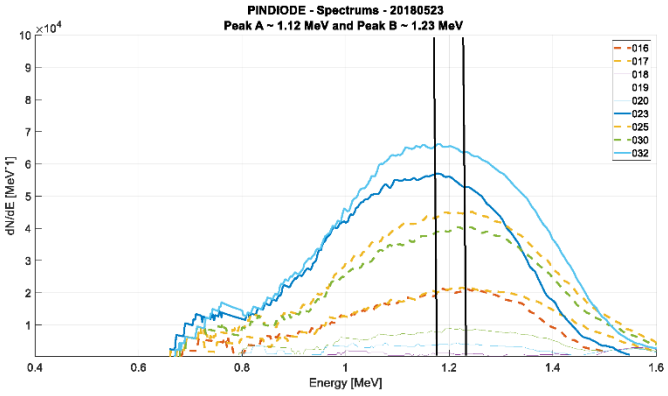

- Statistical analysis

E_mean	Sigma	E_max	dN/dE_peak	E_peak
1.12	0.276	1.39	6.28E+04	1.10

The time-of-flight (TOF) technique has been used to characterize charged particle bunches for more than a decade → what is new?

- TOF technique has considerably gain importance due to the rise of high repetition rate (HRR) facilities capable of producing ion bunches at 1 – 10 Hz rates
- Development of new solid state detectors almost immune to electromagnetic pulses (EMP)
- TOF has become a fundamental tool for online single-beam characterization at HRR, allowing to perform statistical measurements of laser-accelerated ion beams that inherently present shot-to-shot variations

Bibliography

PIN diode

L. Simms, *Hybrid CMOS SiPIN Detectors as Astronomical Imagers* (2009)
Skyworks Solutions Inc., *Design with PIN diodes* (2012)
T.S. Francis *et al., Introduction to optical engineering* (1997)
K. Green *et al.,* Opt. Photonics News **9**, 64 (1998)
M. Davidovic, Proc. Of SPIE **8791**, 879110R (2013)
A. Yogo *et al*., Phys. Plasmas **14**, 043104 (2007)

MCP

T. Gys *et al*., Nucl. Instrum. Methods Phys. Res. **787**, 254 (2015)
J.G. Tymothy, *Observing photons in space* (2013)
J. Martin et al., *Characterization of microchannel plate photomultiplier tuve with high sensitivity GaAs Photocathode*, Signal **35**, 40 (2002)
S.Schemelinin *et al.,* Nucl. Instrum. Methods Phys. Res. **438**, 447 (1999)
Hamamatsu, MCP Assembly technical information (2006)
R. Prasad *et al.,* Rev. Sci. Instrum. **84,** 053302 (2013)
T. Jeong *et al.,* Rev. Sci. Instrum. **87**, 083301 (2016)
R. Prasad *et al.,* Nucl. Instrum. Methods Phys. Res. **623**, 712 (2010)

Diamond detector

F. Foulon *et al.,* IEEE Transactions on Nuclear Science **41**, 927 (1994)
D.R. Kania *et al*., Diamond radiation detectors **2**, 5 (1993)
M. Cipriano *et al*., Journal of Instrumentation **14**, C01027 (2019)
G. Milluzzo *et al*., arXiv:1812.01357 (2018)
W. Cayzac *et al.,* Nature Communications **8**, 15693 (2017)

PowerLaPs

Innovative Education & Training in High Power Laser Plasmas

Laser plasma diagnostics - Theory and Experiments

EXP 2: Introduction to particle spectrometry

J. I. Apiñaniz

1 Time of flight spectrometry

Schemes can be very different depending on:

- Particle charge
- Mass
- Energy spectrum
- Beam characteristics

Typical situations: time resolved spectroscopy

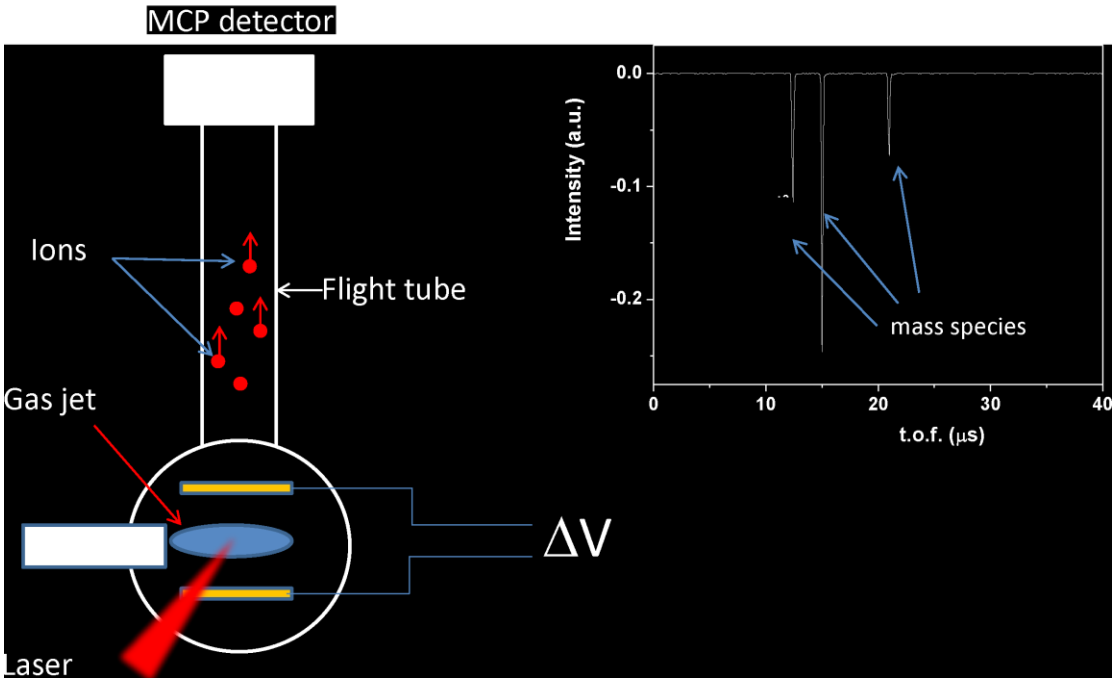

The simplest and most robust technique is Time of flight

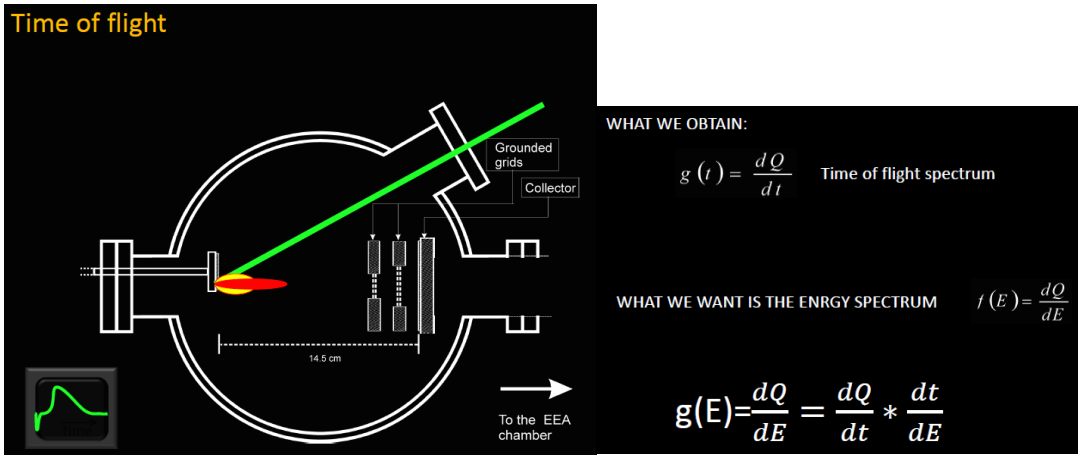

2 Beam deflection spectrometry

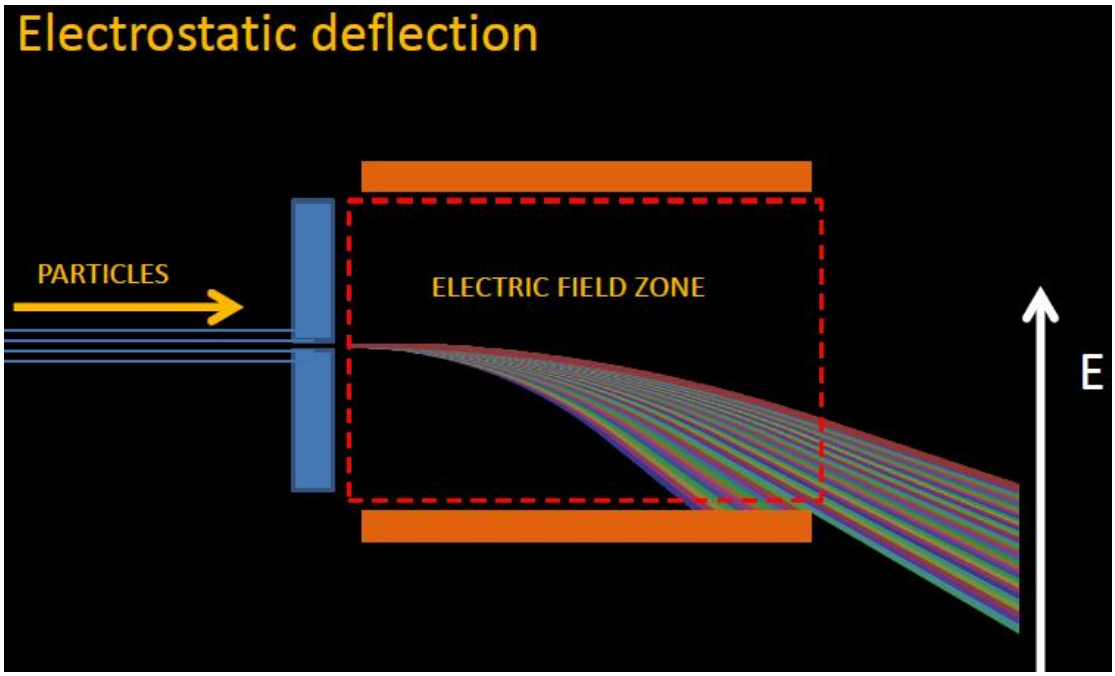

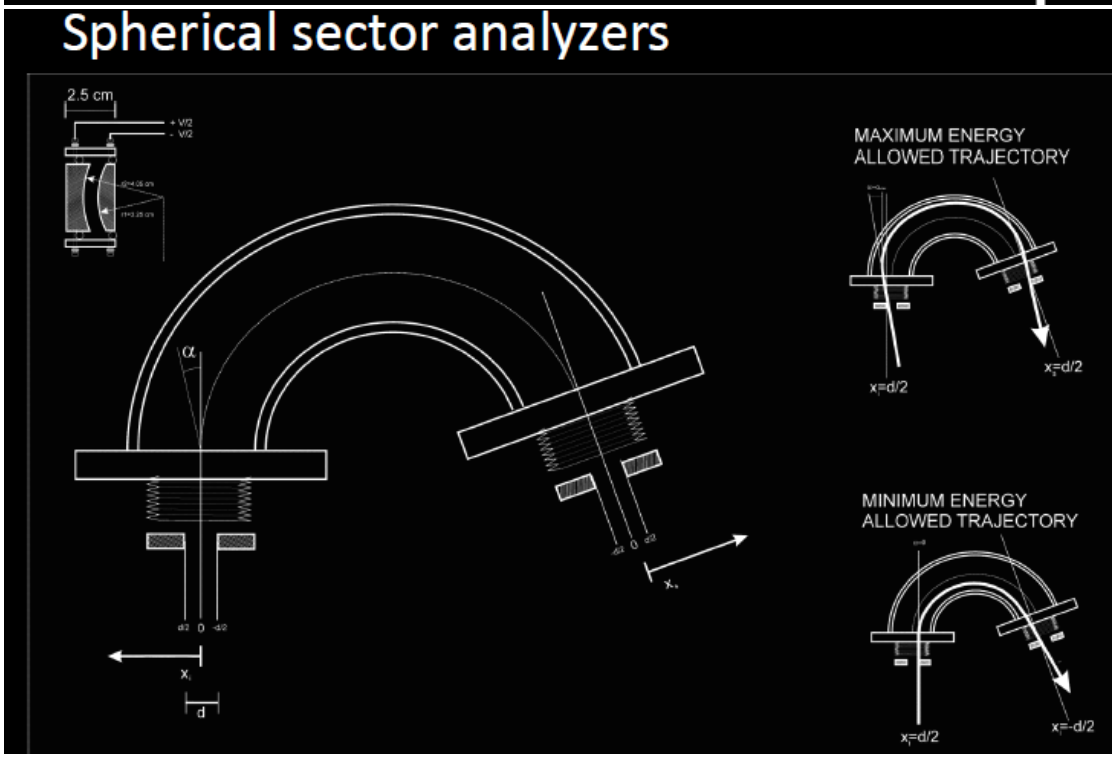

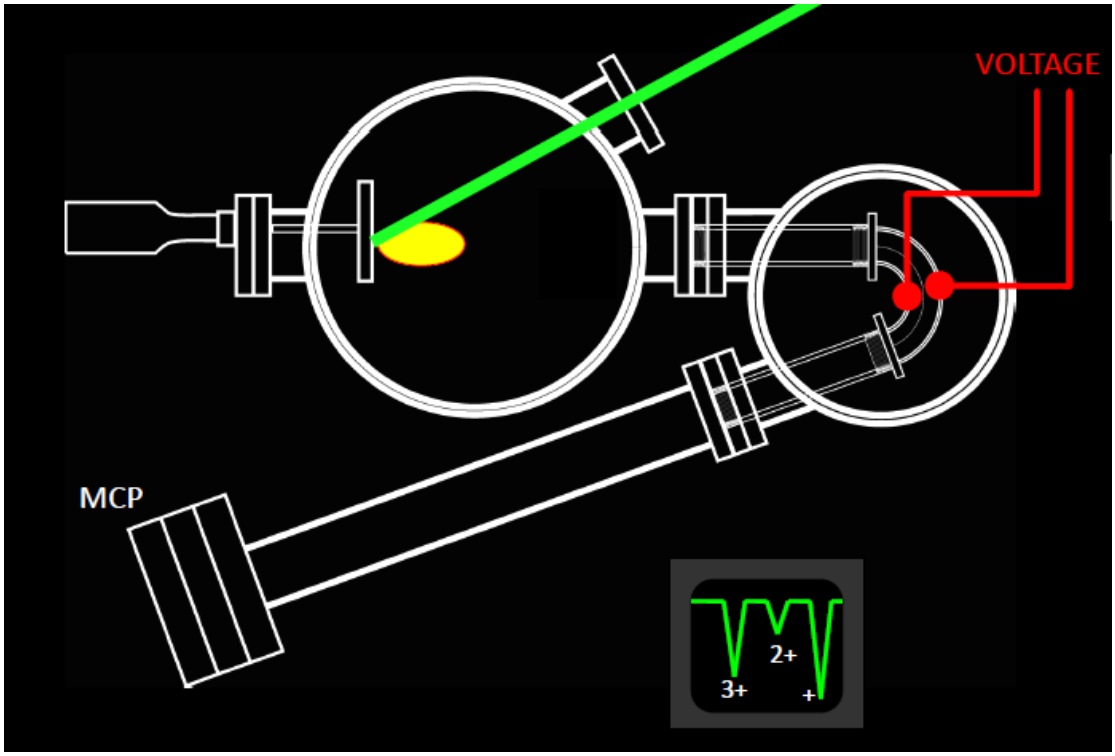

Spherical sector analyzers

Advantages:

- high energy resolution
- with TOF attached can measure spectra of each charge species

Drawbacks:

- Fixed axis of measurement and very low solid angle
- Only for low energy particles (<1MeV)
- No full spectrum per shot

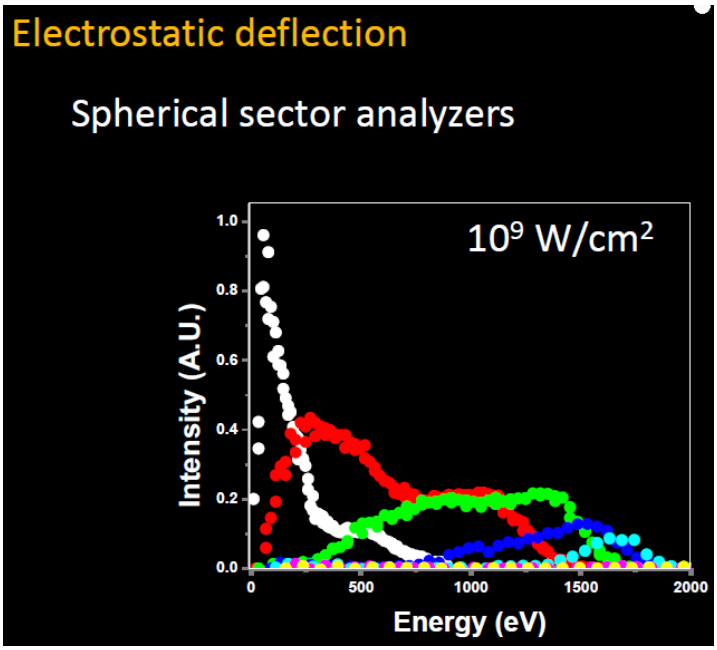

Magnetic deflection

Magnetic sector analyzers

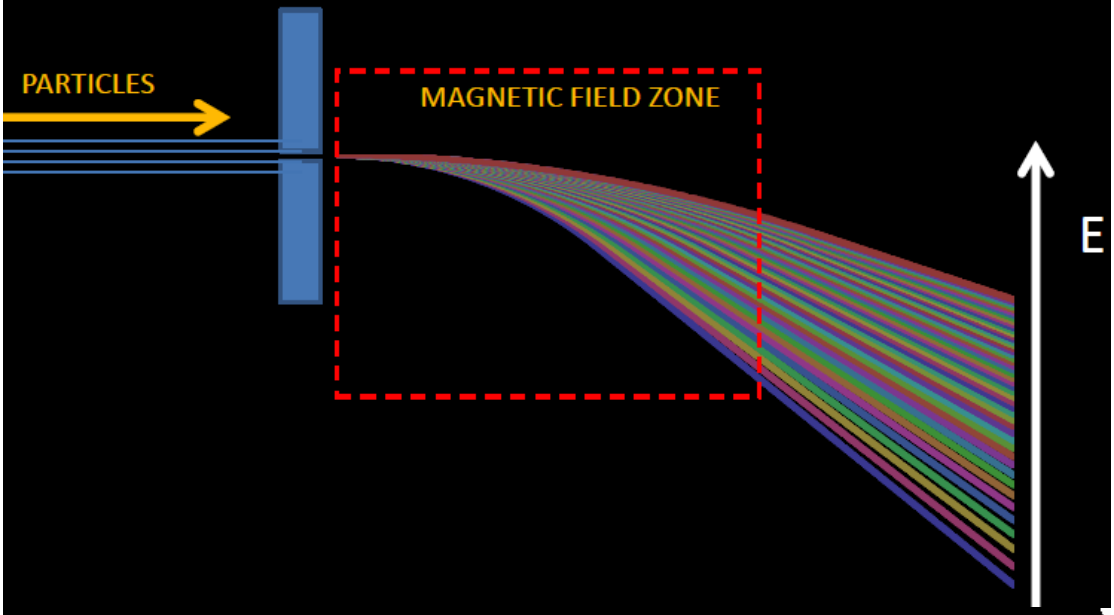

EVERY TYPE OF SPECTROMETER HAS:

COLLIMATING ELEMENT (AT LEAST ONE)

DEFLECTOR FIELD ZONE

SHIELDINGS

PARTICLE DETECTOR

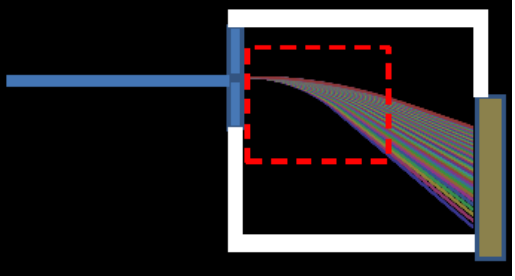

3 Thomson parabola

IN HIGH INTENSITY LASER-PLASMA PHYSICS:

- WE MIX MAGNETIC AND ELECTRIC DEFLECTION
- TAKE ADVANTAGE OF MAGNETIC FIELD:
- MAIN DEFLECTION IS MAGNETIC
- THICK SHIELDING
- HIGH SENSITIVITY AND SURFACE DETECTORS

THOMSON PARABOLA IS THE MOST STANDARD NON TOF SPECTROMETER IN HIGH ENERGY BEAMS

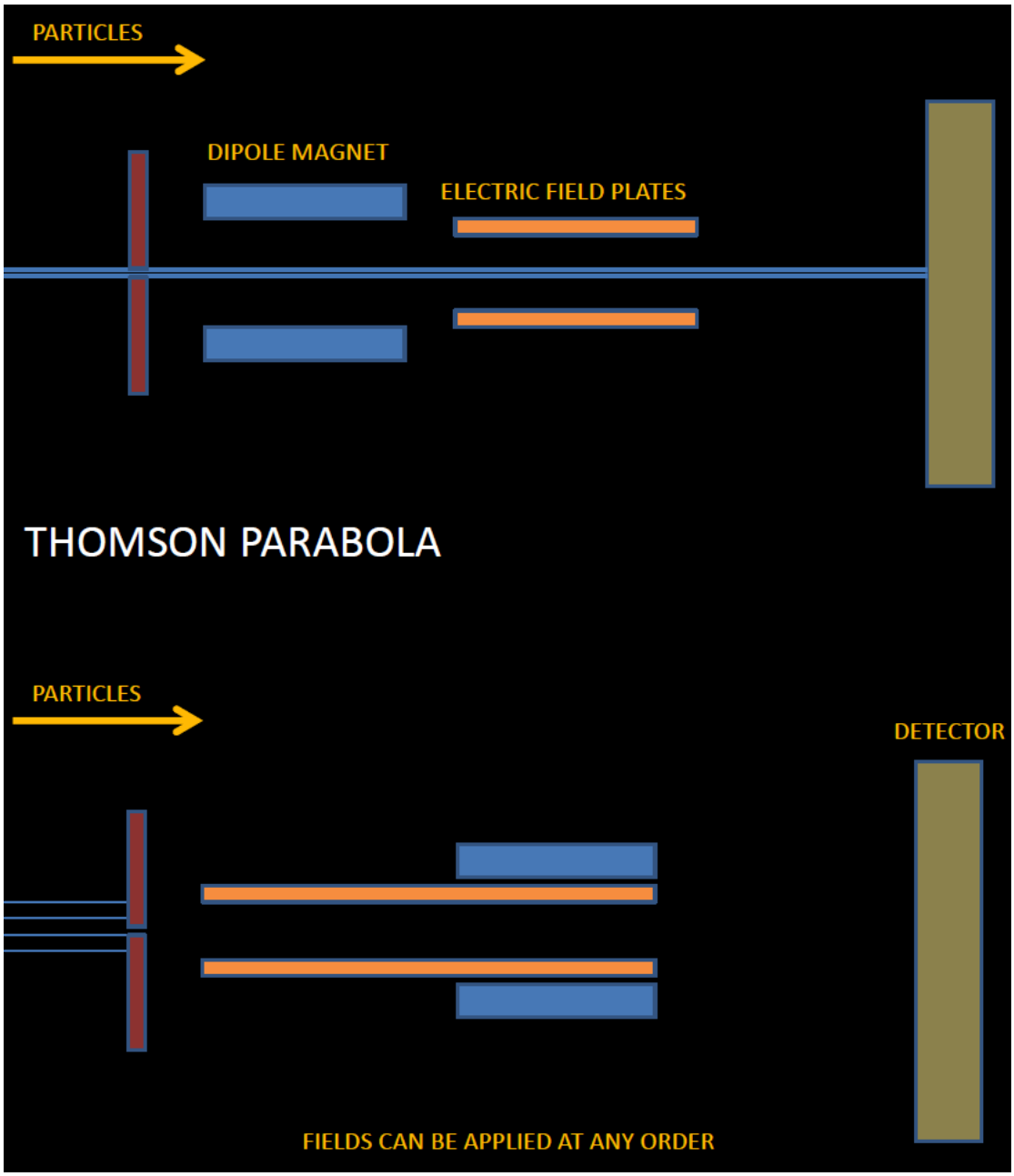

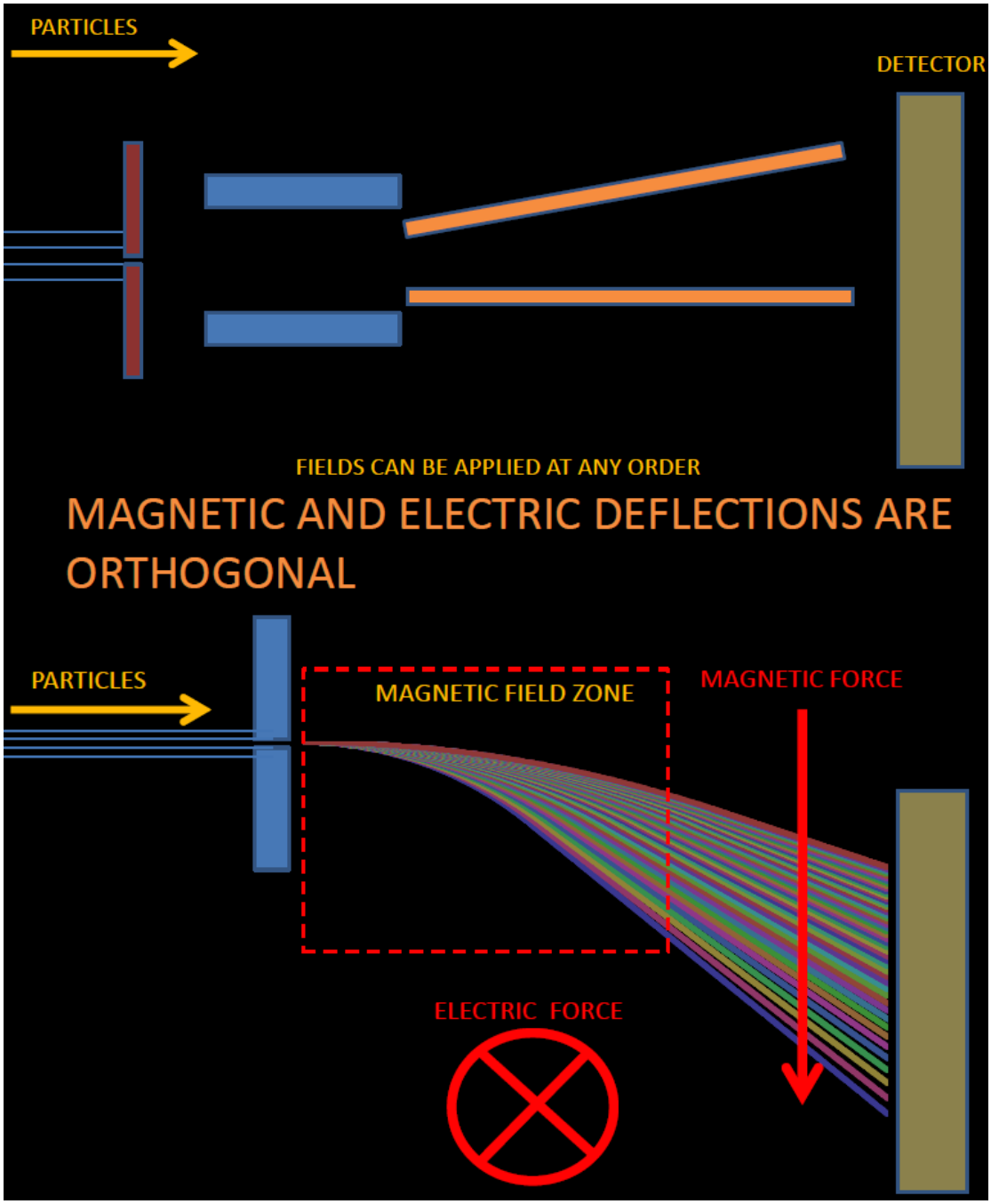

THE DETECTOR MUST OFFER 2D INFORMATION CAN BE PASSIVE OR ACTIVE, ONLINE OR NOT DOESN´T NEED TO BE FAST

THOMSON PARABOLA

TYPICAL IMAGES IN THE DETECTOR

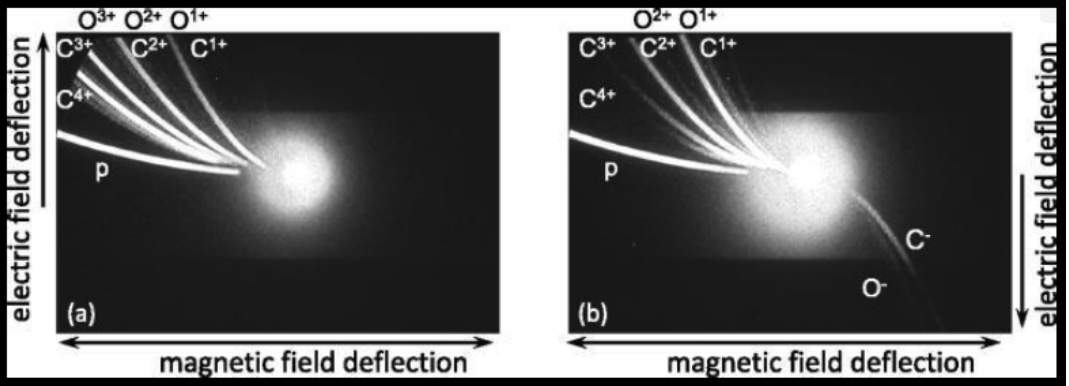

Physics of Plasmas 20(11):113105

THOMSON PARABOLA

CLPU THOMSON PARABOLA MODEL

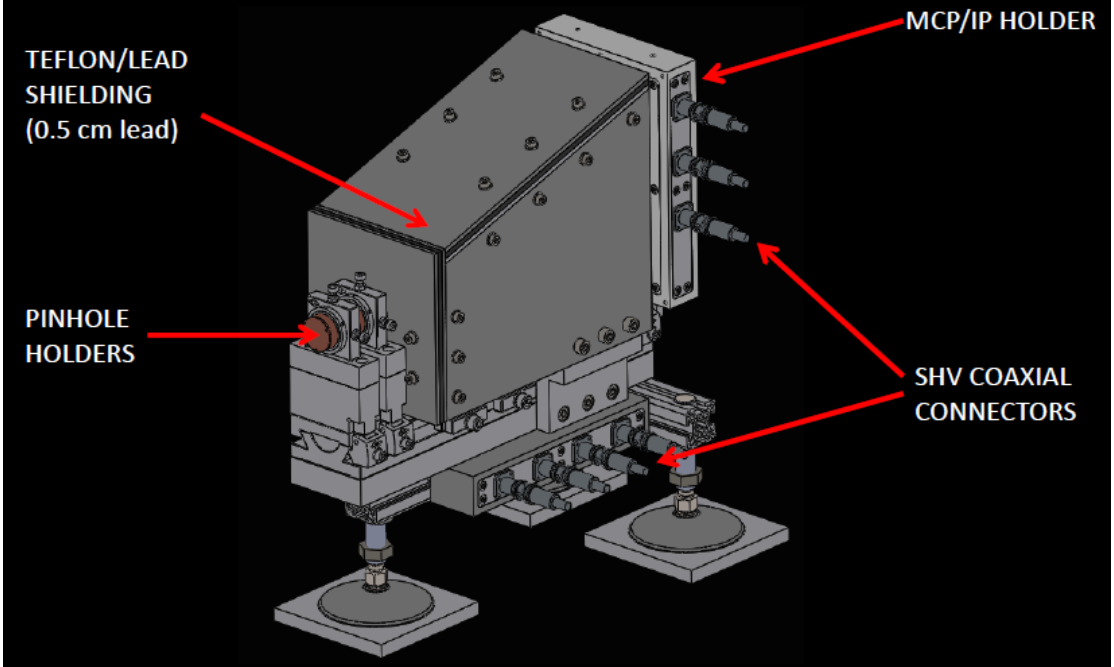

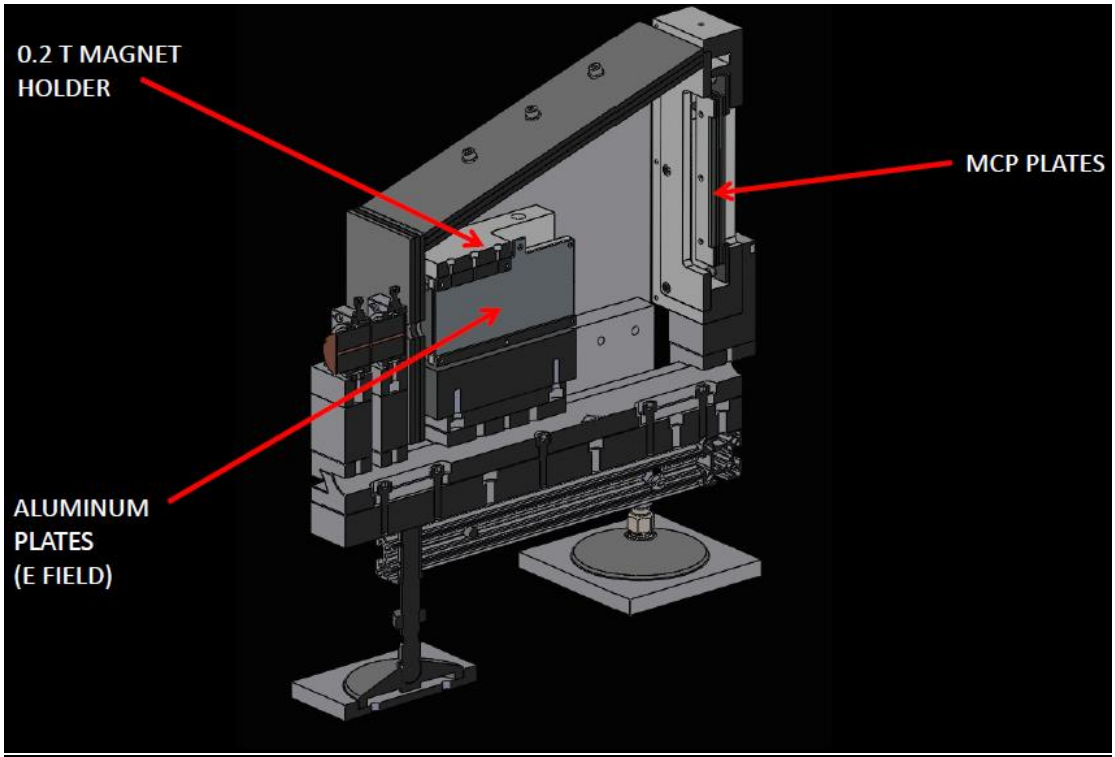
0.2 T MAGNET
HOLDER
MCP PLATES
ALUMINUM
PLATES
(E FIELD)

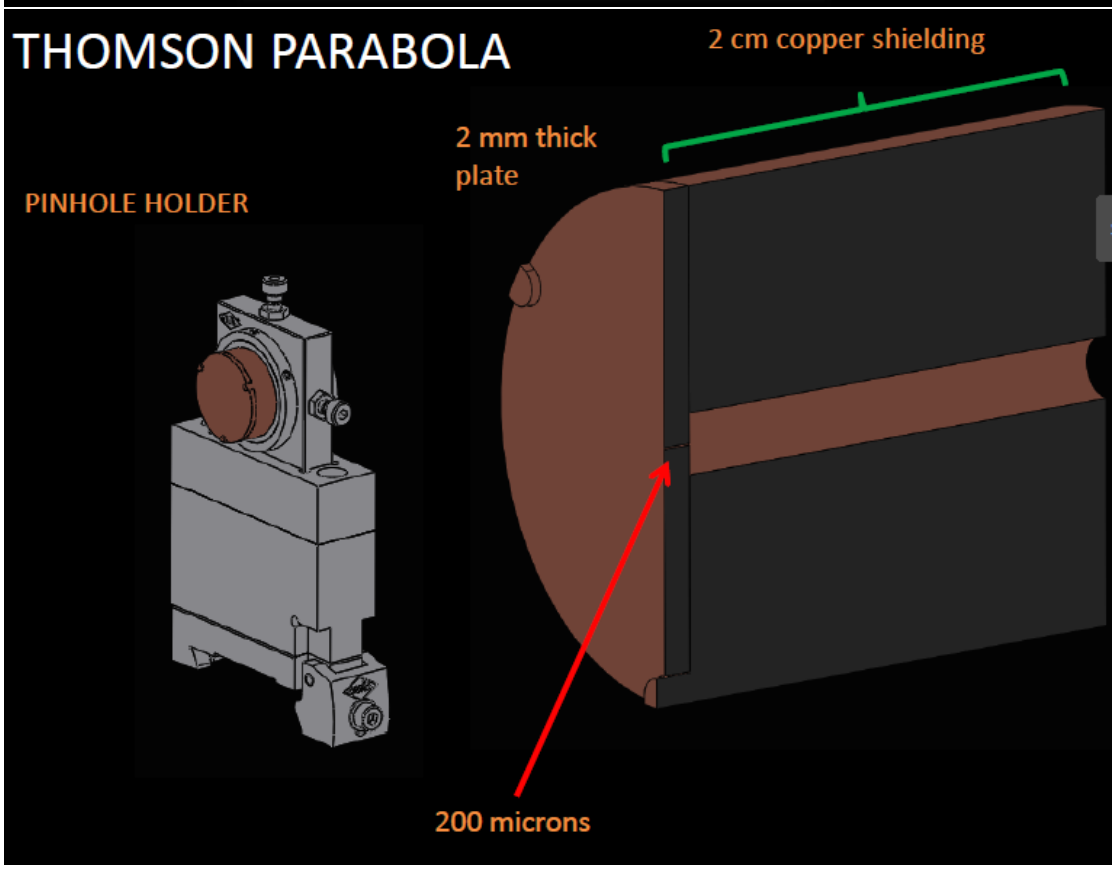
THOMSON PARABOLA
2 cm copper shielding
2 mm thick
plate
PINHOLE HOLDER
200 microns

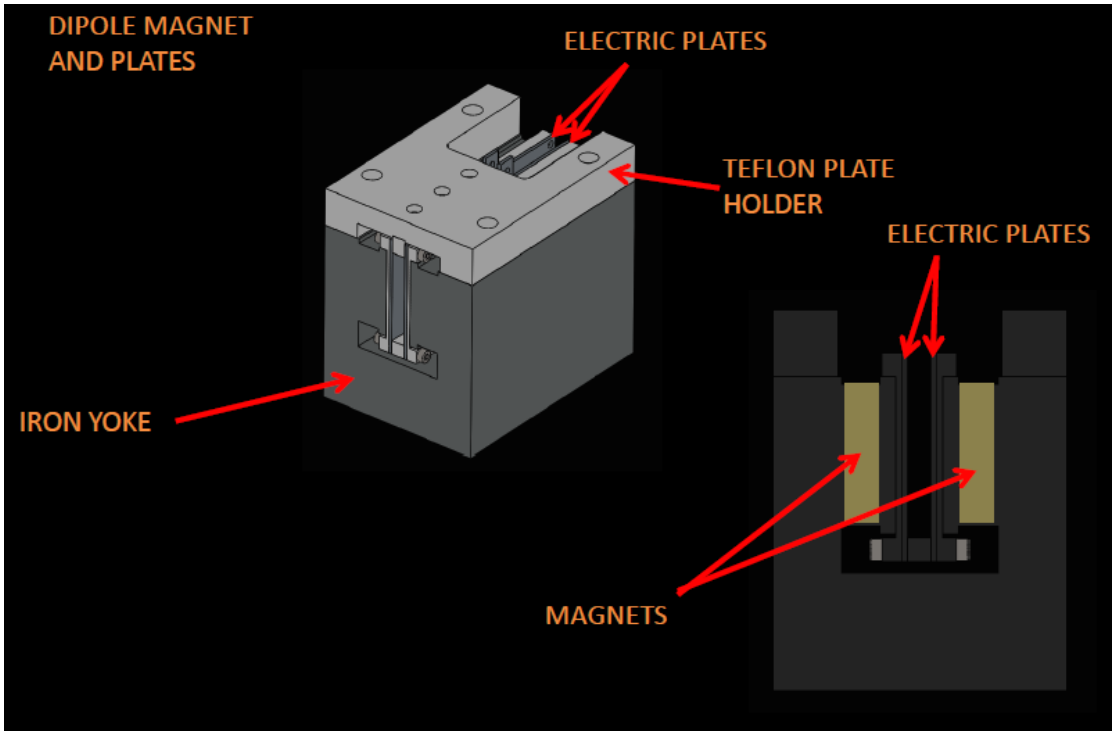
DIPOLE MAGNET
AND PLATES
ELECTRIC PLATES
TEFLON PLATE
HOLDER
ELECTRIC PLATES
IRON YOKE
MAGNETS

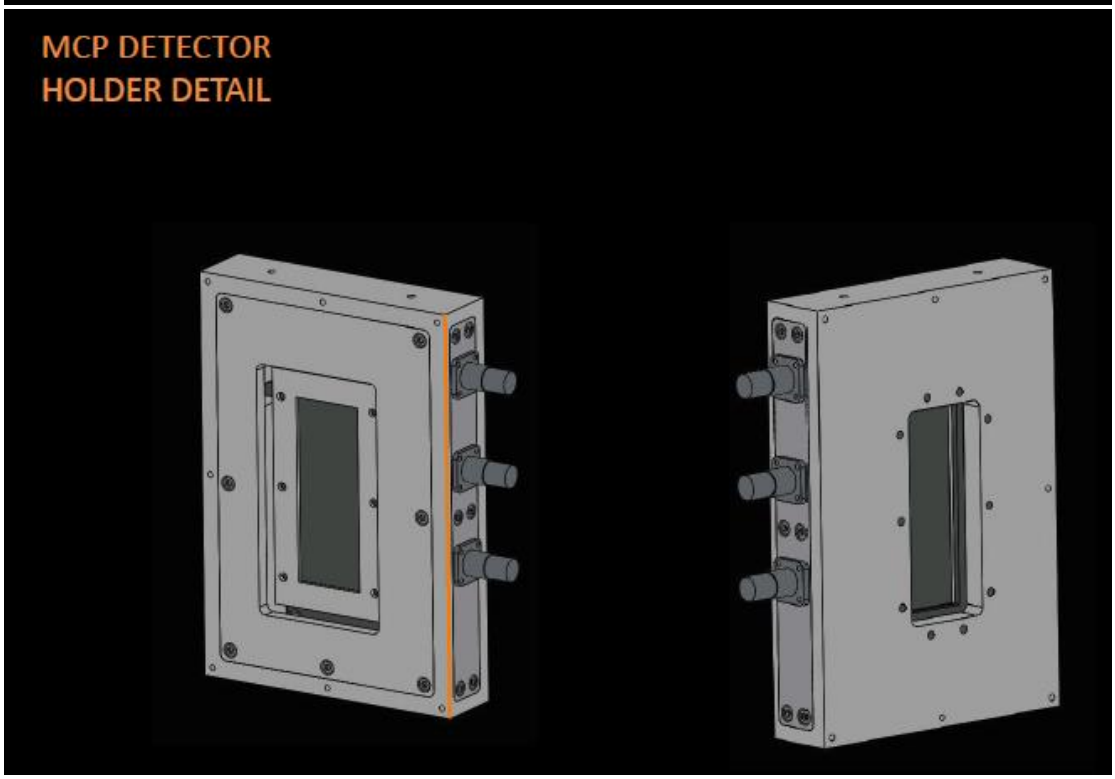
MCP DETECTOR
HOLDER DETAIL

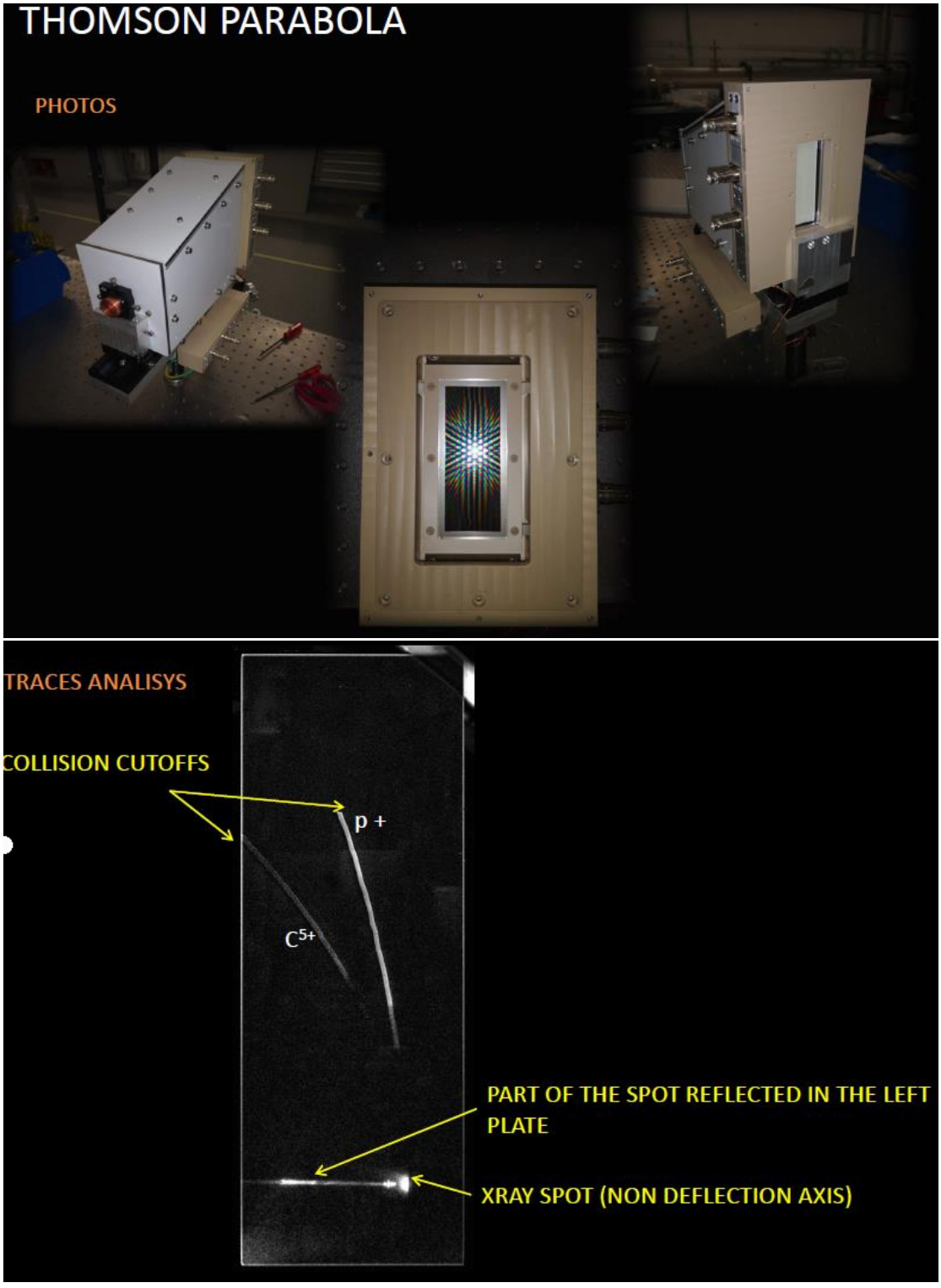
THOMSON PARABOLA
PHOTOS
TRACES ANALISYS
COLLISION CUTOFFS
p +
C5+
PART OF THE SPOT REFLECTED IN THE LEFT PLATE
XRAY SPOT (NON DEFLECTION AXIS)

TRACES ANALISYS

SPECTRUM RETRIEVAL

WE NEED TRAJECTORY CALCULATIONS (NUMERICAL OR ANALYTICAL)

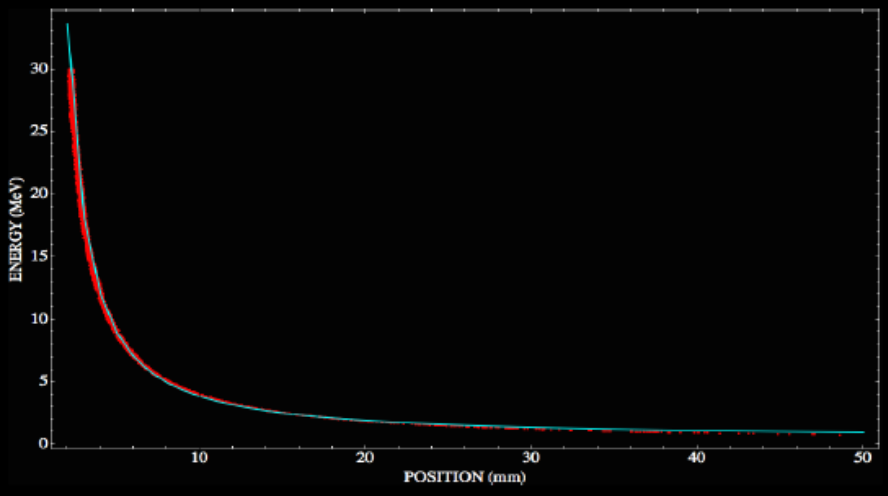

VERTICAL COORDINATE IN SCREN

TRACES ANALISYS

SPECTRUM RETRIEVAL

FOR SIMPLE CASES ANALYTICAL CALCULATIONS ARE EASY

UNIFORM AND PERFECLY SPACE DELIMITED FIELDS

PERFECLY PARALELL INCIDENT BEAMS

NON RELATIVISTIC CASE

$$x = \frac{q \cdot E \cdot Len \cdot D}{2 \cdot E_{kin}} \qquad y = \frac{q \cdot B \cdot Len \cdot D}{\sqrt{2m \cdot E_{kin}}}$$

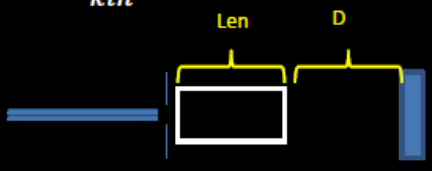

Q=Z*e (charge)
m=mass
Ekin=Kinetic energy (J)
E= electric field modulus (V/m)
B=magnetic field modulus (T)

Len= both fields length
D=free flight distance (from fields to detector)

PARTICLE TRACING SIMULATIONS

WHEN SIMPLE CASE CONDITIONS ARE NOT FULLFILLED (ALLWAYS)

- **REAL FIELDS (NON UNIFORM)**
- **REAL BEAMS (WITH DIVERGENCE)**

NUMERICAL SOLUTIONS OF EQUATIONS OF MECHANICS ARE NECESSARY:

1.- INITIAL POSITION

2.- INITIAL VELOCITIES

3.- 3D MAPS OF THE FIELDS

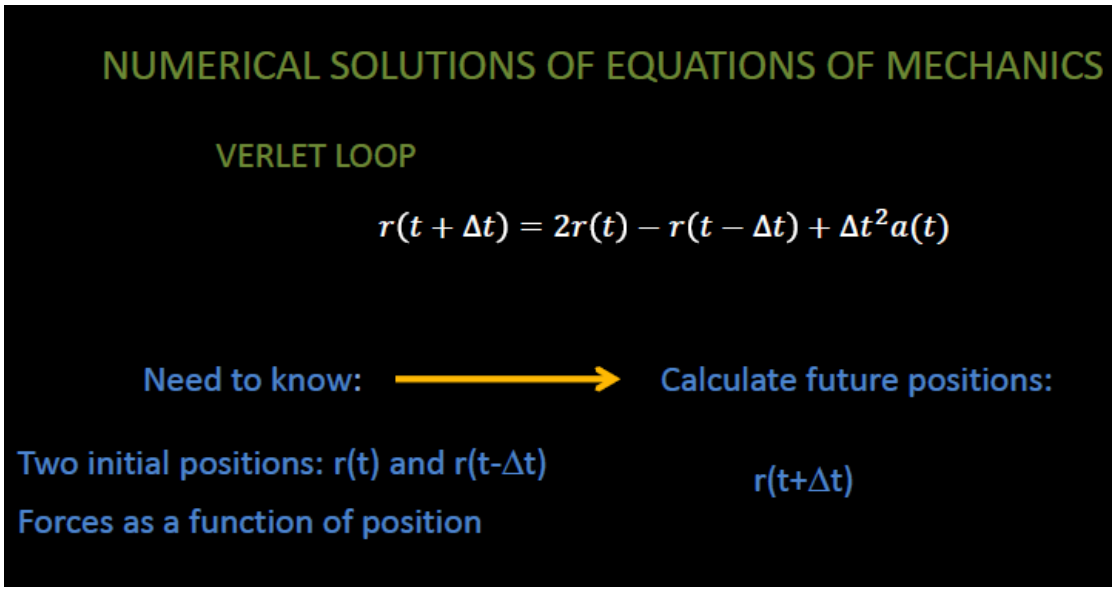

PARTICLE TRACING SIMULATIONS

NUMERICAL SOLUTIONS OF EQUATIONS OF MECHANICS

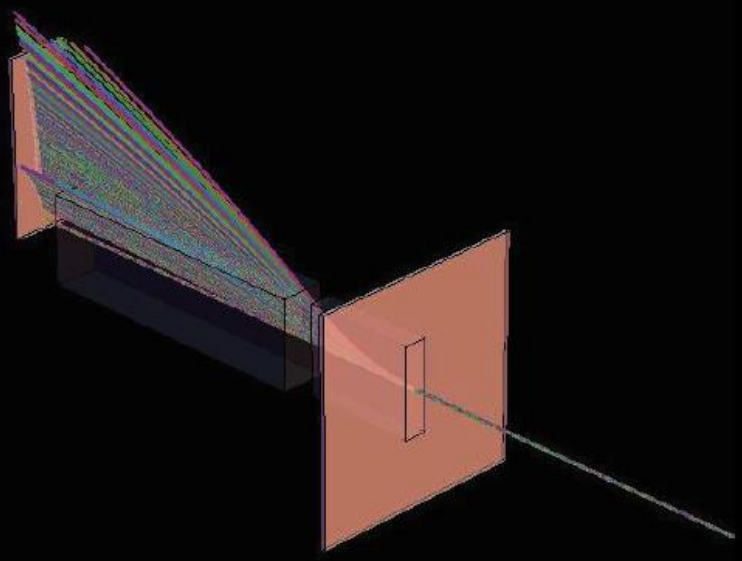

MAIN SOURCES OF ERROR :

FUNDAMENTAL DISPERSION RELATION ERROR

PUT LONGER PARABOLA AND BIGGER FIELDS

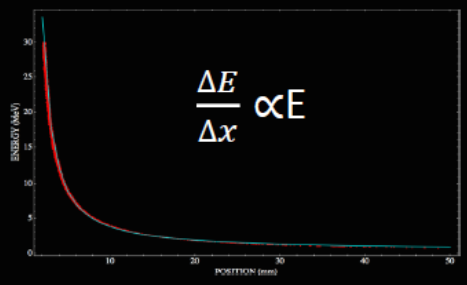

$$\frac{\Delta E}{\Delta x} \propto E$$

BEAM DIVERGENCE

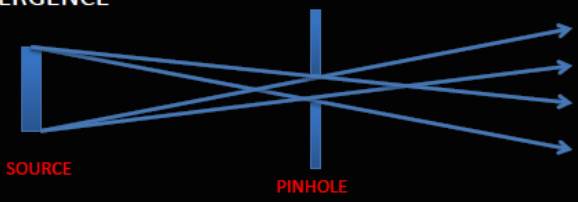

PUT SMALL PINHOLE AND FAR FROM TCC

TWO CASES OF DIVERGENCE:

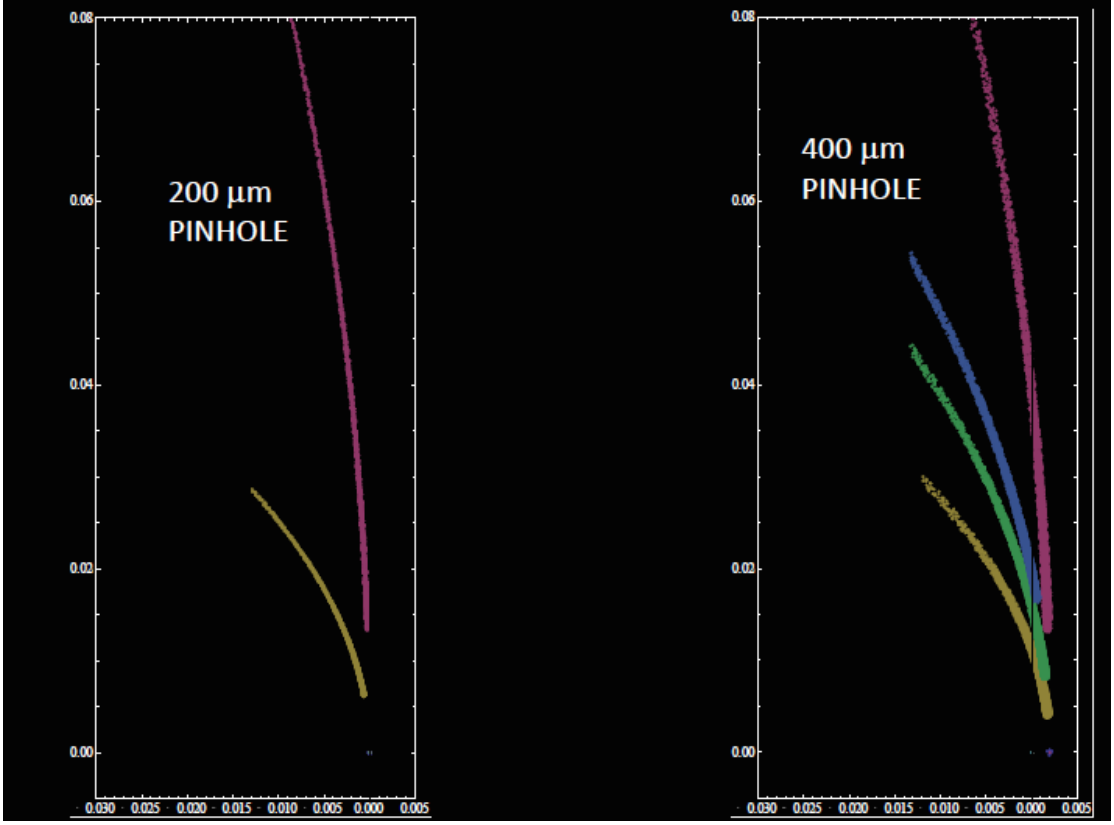

MAIN SOURCES OF ERROR :

MISALIGNMENT : PARTICLES ENTERING OUT OF AXIS

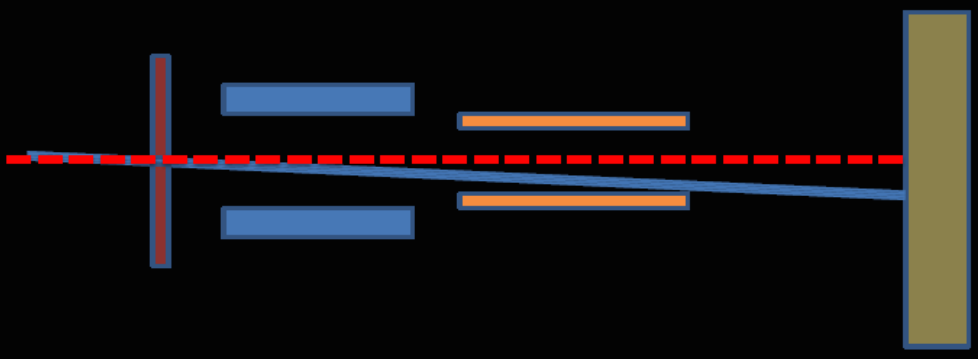

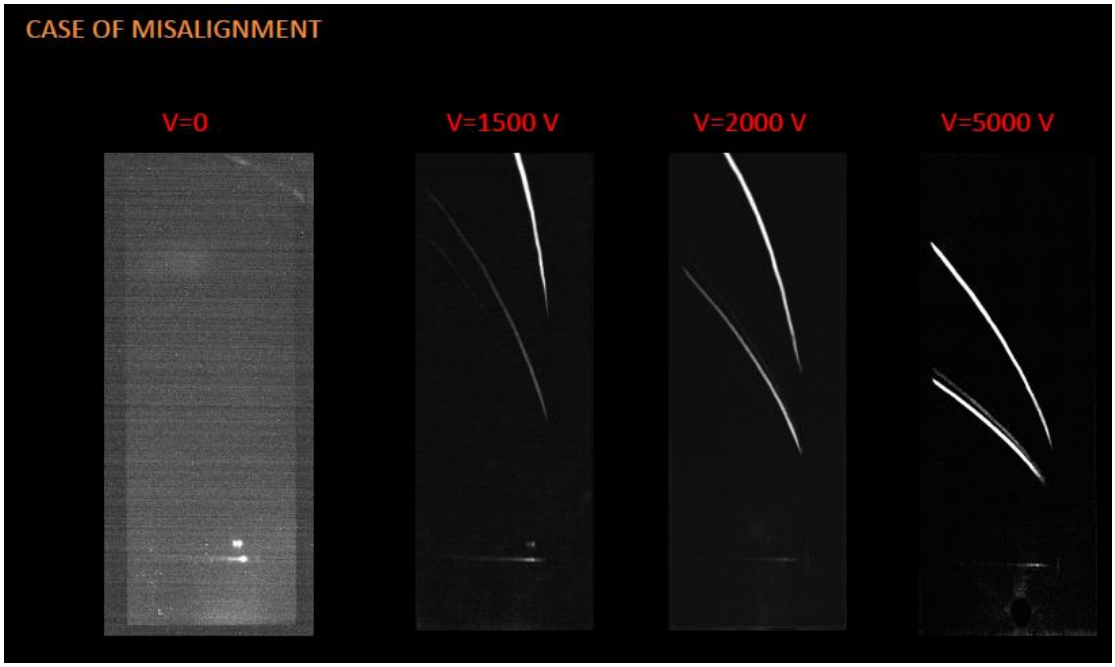
CASE OF MISALIGNMENT
V=0
V=1500 V
V=2000 V
V=5000 V

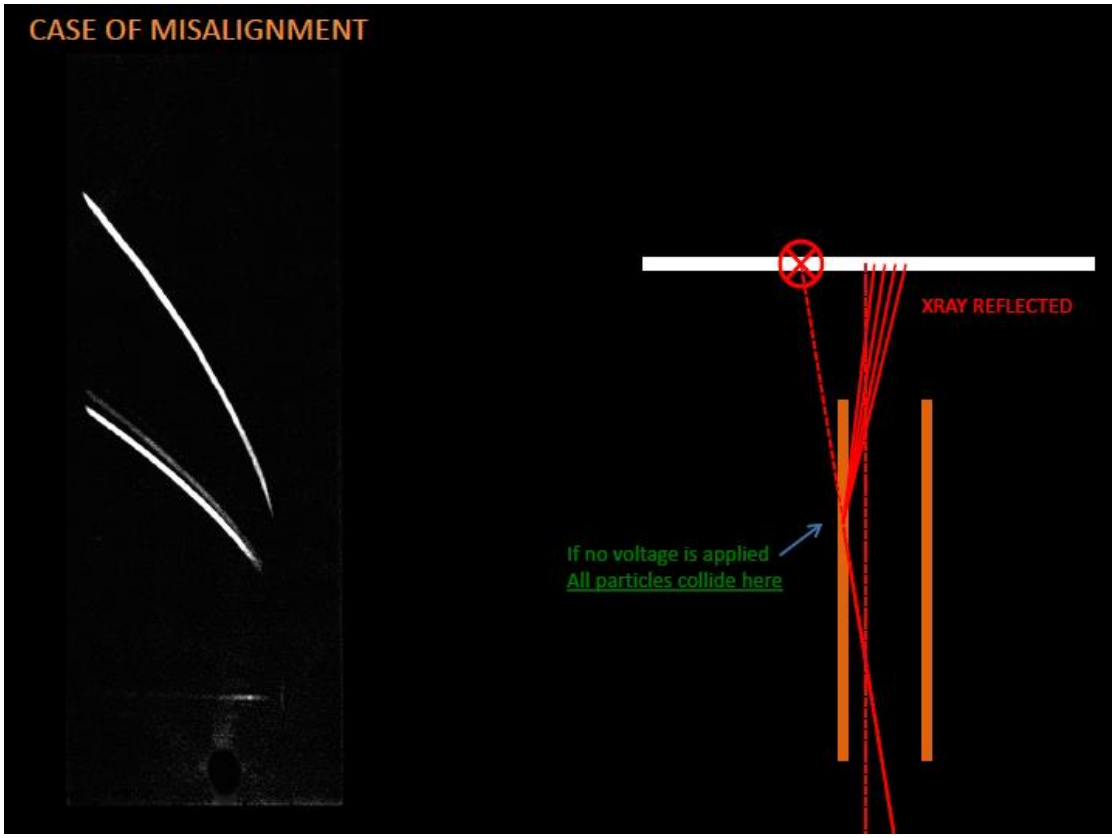
CASE OF MISALIGNMENT
XRAY REFLECTED
If no voltage is applied
All particles collide here

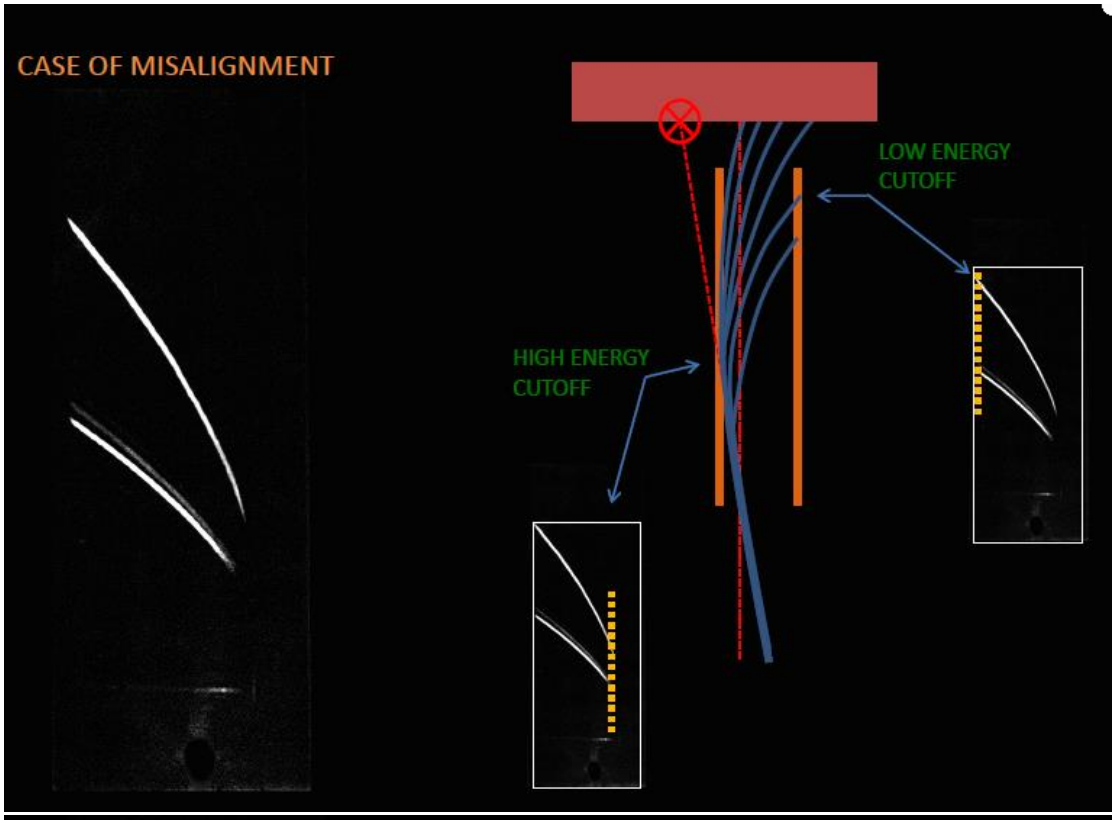
CASE OF MISALIGNMENT
LOW ENERGY CUTOFF
HIGH ENERGY CUTOFF

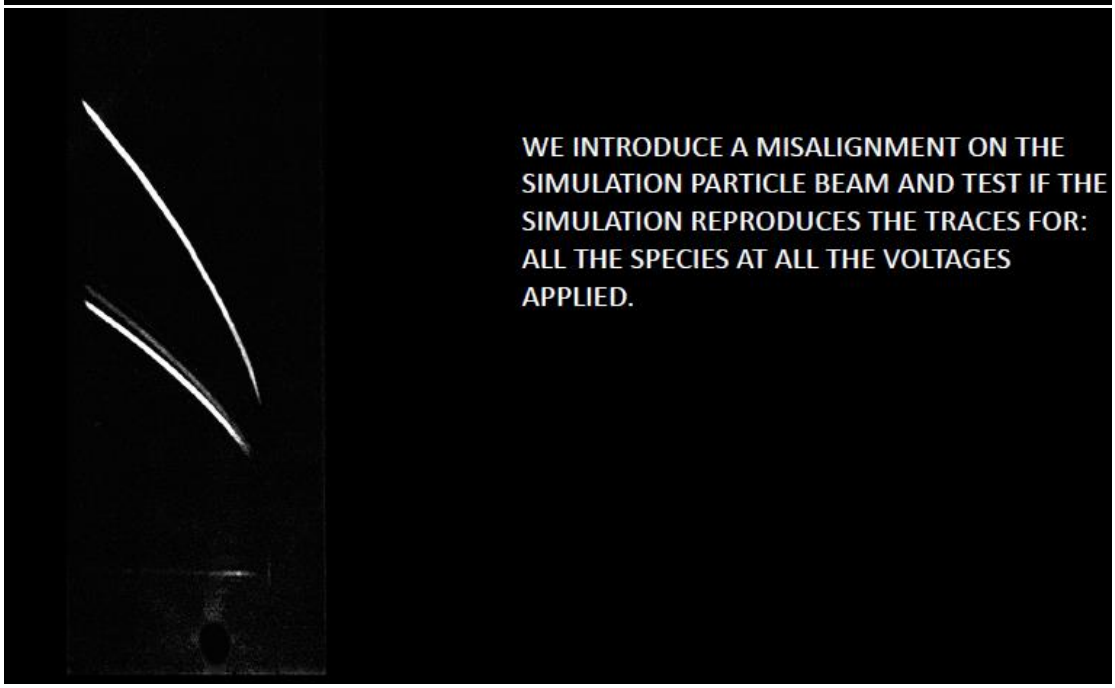
WE INTRODUCE A MISALIGNMENT ON THE SIMULATION PARTICLE BEAM AND TEST IF THE SIMULATION REPRODUCES THE TRACES FOR: ALL THE SPECIES AT ALL THE VOLTAGES APPLIED.

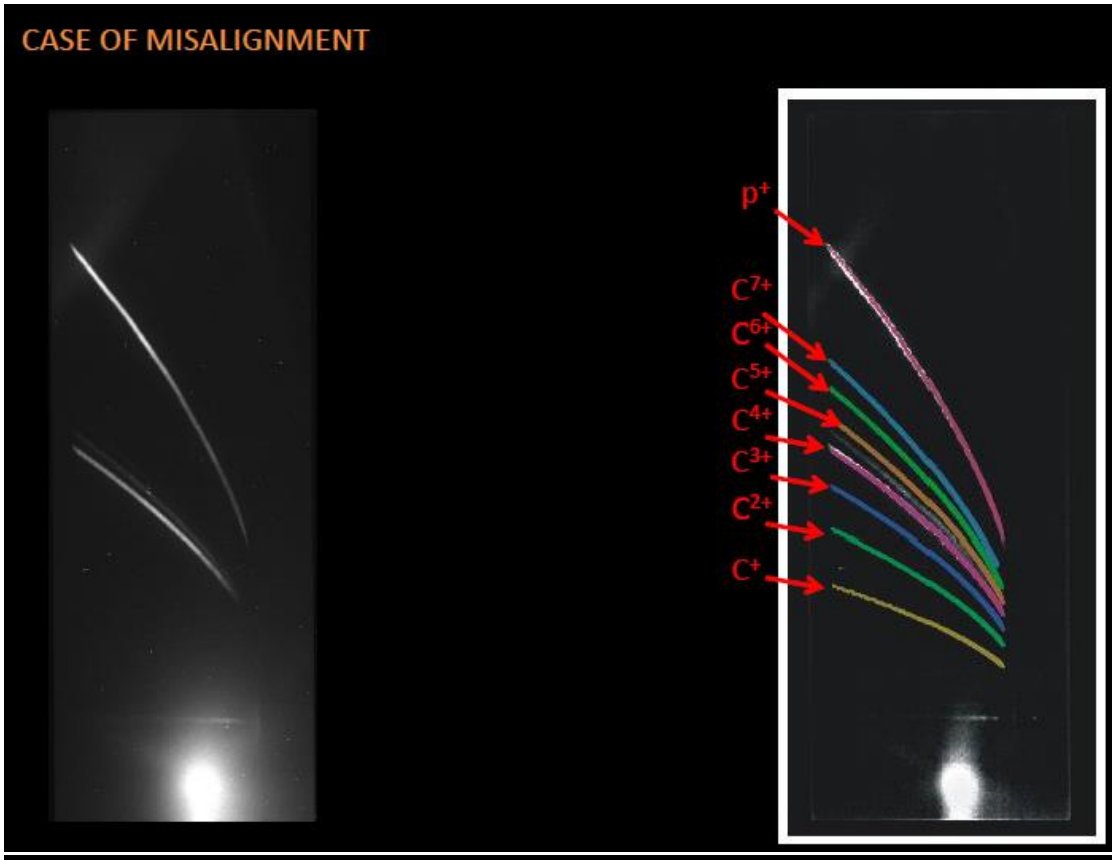
CASE OF MISALIGNMENT
p+
C7+
C6+
C5+
C4+
C3+
C2+
C+

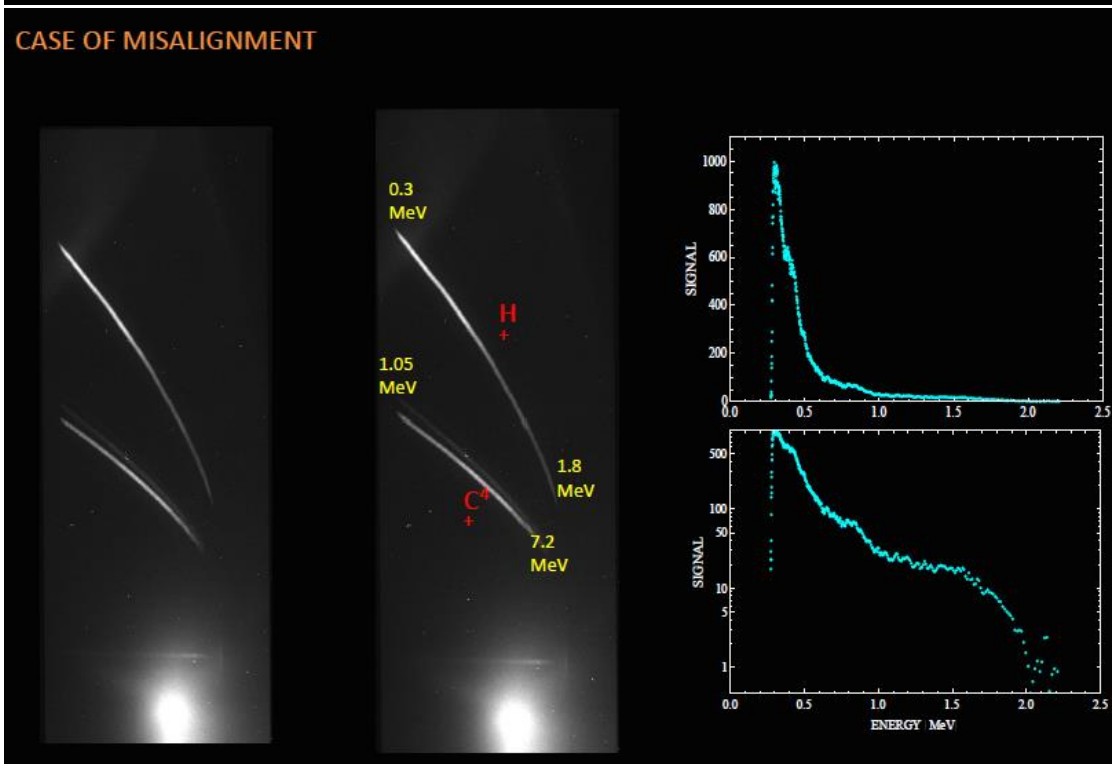
CASE OF MISALIGNMENT
0.3 MeV
H+
1.05 MeV
1.8 MeV
C4+
7.2 MeV
SIGNAL
ENERGY MeV

THINGS TO REMEMBER ABOUT THOMSON PARABOLA

THEY ARE DEFLECTION SPECTROMETERS WHICH COMBINE MAGNETIC AND ELECTRIC FIELDS.

THEY ARE SUITABLE FOR HIGH OR VERY HIGH ENERGIES, POSITIVE AND NEGATIVE SPECIES. BUT MUST BE GEOMETRICALLY OPTIMIZED FOR THE RANGE OF INTEREST

THEY ALWAYS PRESENT A LOW ENERGY CUTOFF IN DETECTION BECAUSE OF PARTICLE COLLISION WITH ELECTRIC PLATES. THIS CAN BE OPTIMIZED BUT NOT COMPLETELY AVIODED.

AS IN ALL TYPE OF SPECTROMETERS.... ENERGY RESOLUTION DECREASES WITH ENERGY, AND SIGNAL INTENSITY INCREASES. BOTH BECAUSE OF THE SAME REASON: THE BANDWIDTH PER PIXEL INCREASES WITH ENERGY.

$$\frac{\Delta E}{\Delta pixel} \propto E$$

MAIN PARAMETERS OF THOMSON PARABOLA

PARAMETER	YOU´D BETTER...
Fields intensity (3d map)	Increase them
Fields distance (3d map)	Increase them
Pinhole-detector distance	Increase it
Pinhole diameter	Decrease it
Source-pinhole distance	Increase it

PowerLaPs

Innovative Education & Training in High Power Laser Plasmas

Laser plasma diagnostics - Theory and Experiments

EXP 3: Laser Matter Interaction Diagnostics for the IPPL TW laser

I. Fitilis, S. Petrakis

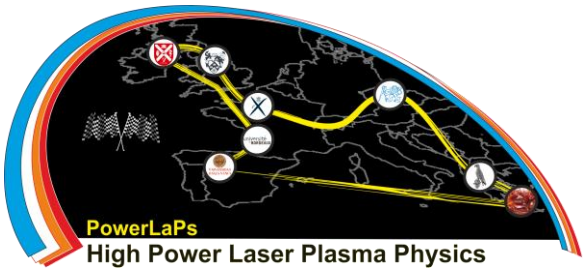

HELLENIC
MEDITERRANEAN
UNIVERSITY

PART A – DIAGNOSTICS FOR TW LASER SYSTEM

Description of the Zeus Laser System at IPPL

The Zeus laser system (Pulsar from Amplitude Technologies) at IPPL is a compact femtosecond laser source providing more than 1 J pulse energy at a 10 Hz repetition rate. The pulse length is about 25 fs and leads to a peak power higher than 40 TW.

Chirped pulse amplification (CPA)

The system is a Titanium-Sapphire laser based on the so-called "Chirped Pulse Amplification" (CPA) technique. The system amplifies pulses from a Ti:Sapphire Oscillator and consists of a booster, a stretcher, a regenerative amplifier, 10 Hz multi-pass amplifiers with respective pump lasers, vacuum and air compressors.The CPA technique consists of temporal stretching of the ultra short pulse delivered by an oscillator (by a factor of 1000 to 10000), in order to safely amplify the pulses in solid state materials. Stretching produces a "chirped" pulse. After amplification, the laser pulse is temporally compressed back to duration as close as possible to its initial value. After the compression stage, one should obtain in principle a high intensity ultra-short

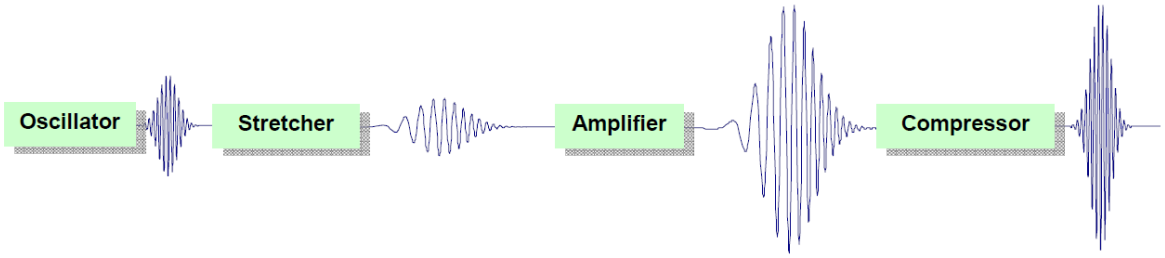

Figure 1.1: Chirped pulse amplification principle.

pulse free of chirp (see Figure 1.1).

Stretching and compression are usually achieved by means of dispersive systems such as gratings or prisms. The principle is to create different optical paths for each wavelength of the spectrum. Figure 1.2 shows a typical Stretcher design using two gratings and a telescope system. As shown in this Figure, the Blue path is longer than the Red one. Therefore, Blue wavelengths take more time to travel through the system than Red ones.

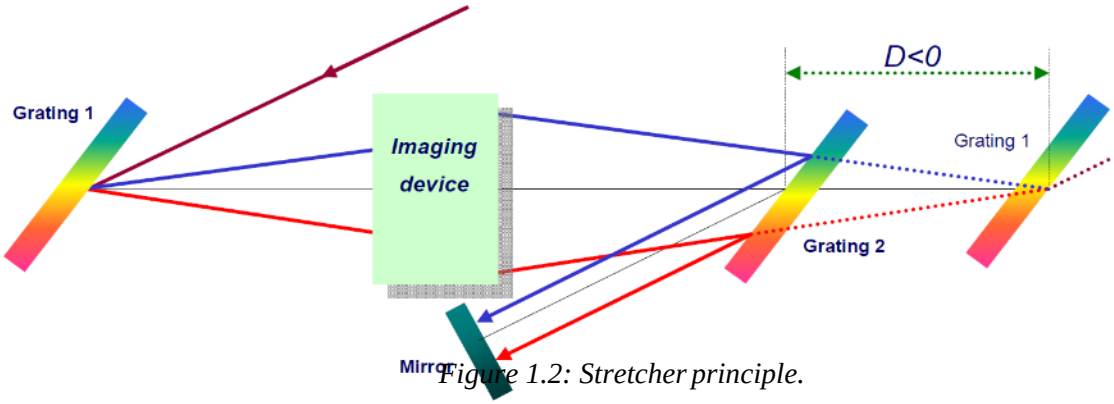

Figure 1.2: Stretcher principle.

Once stretched, the pulse can be amplified in several amplification stages, using regenerative and/or single-/multi-pass amplifiers. At the output of the amplifying system, the energy does not depend on the input pulse duration delivered by the oscillator. The limit comes from possible damage that could be caused to the amplifying material. The amplified pulse energy which can be reached without damage is higher if the stretched pulse is longer.

After amplification the pulse must be compressed. A Compressor device based on a wavelength dispersion system similar to the Stretcher (see Figure 1.3). This Compressor is theoretically able to compensate for any stretching introduced into the pulse, but the gratings need to be perfectly aligned. Particularly, the incident angle onto the compressor has to be finely adjusted in order to compensate for the stretcher

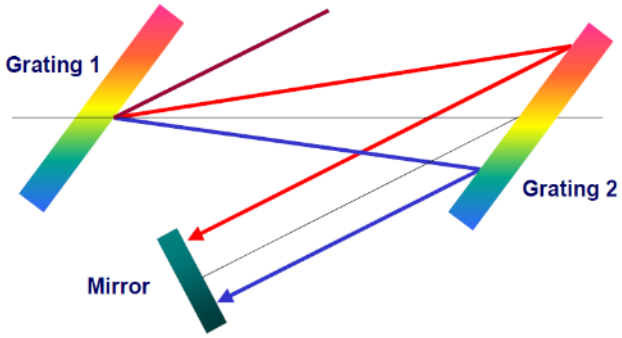

Figure 1.3: Pulse compressor principle.

and the dispersion effects through the amplifier.

Oscillator

The Oscillator Femtosecond seed pulses for the CPA amplifier are provided by a laser oscillator. The femtosecond laser oscillator has four major components: the gain material, the pump laser, the feedback mirrors that form an optical resonant cavity, and the dispersion compensation optics. Femtosecond pulses from the oscillator cavity are generated by a mechanism called mode locking. To generate 10 fs pulses, the phases of $N=10^6$ modes must be the same.

Contrast Ratio Booster

In order to improve contrast ratio, an optional module is available. This module consists of a compact multipass amplifier to amplify the oscillator output up to the microjoule level. The pulse is then cleaned by a saturable absorber that removes residual ASE (Amplified Spontaneous Emission) background of the oscillator pulses before seeding. This module also contains an electro-optical device, the pulse picker, which creates a 10 Hz pulse train from the 80 MHz oscillator pulse train.

Regenerative amplifier

The first amplification stage consists of a regenerative amplifier producing around 1mJ stretched pulses at 10Hz. It includes two Pockels cells: one is used to seed the stretched pulse into the regenerative cavity and the other dumps out the pulse at the maximum energy level. High power multipass amplifiers use only flat mirrors and do not affect the beam quality. An electronic module is installed to synchronize and switch the different Pockels cells involved in the system.

Multi-pass amplifiers

The high-power amplification delivered by the system is delivered by multi-pass amplifiers. The Nd:YAG CFR200 laser produces the gain in the first multi-pass amplifier (called Pre-amplifier). The second multi-pass amplifier is pumped by 1.2 J @ 532 nm delivered by one Propulse Nd:YAG laser The main amplifier is pumped by 5 J delivered by 2 Propulse+ Nd:YAG lasers. Due to the high average power of the pump beams a cryogenically cooled Ti:Sapphire mount is used in the main multi-pass amplifier.

Acousto-Optic Programmable Modulators

For short pulse (<30 fs) requirements, an optional Acousto-Optic Programmable Dispersive Filter (AOPDF) named Dazzler is added, right after the pulse stretcher. For standard laser systems, the *Dazzler* is used as a phase modulator to pre-compensate dispersion and phase distortions introduced throughout the laser system, but also as an amplitude modulator to optimize the laser output spectrum. In the Pulsar, the problems of phase compensation and amplitude modulation are totally de-correlated. The *Dazzler* would only be used for phase spectrum control, while another similar device, the Acousto-optic Programmable Gain Filter (AOPGF) *Mazzler*, would be used to optimize the amplitude spectrum. This allows decreasing the pulse duration to less than 25 fs.

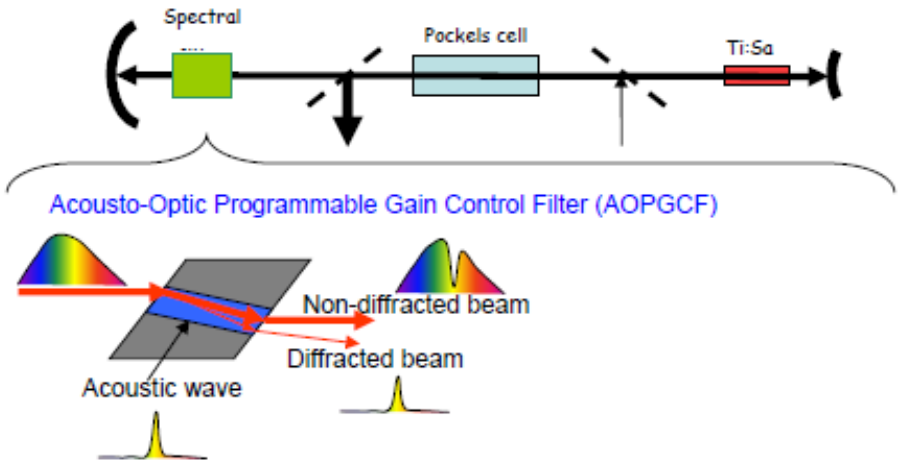

Figure 1.4: Principle of the Mazzler for a simple laser resonator

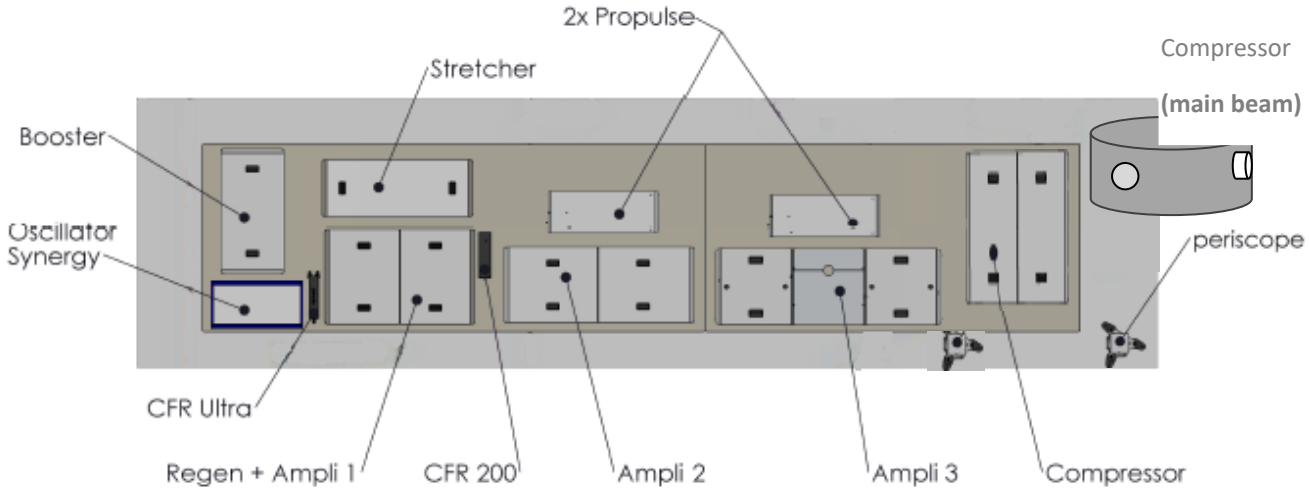

Figure 1.5: Schematic layout of the 40TW laser system arrangement

Operation of the Zeus Laser System at IPPL

Important precautions!

1) **Make sure you wear the laser safety goggles when the laser is on.**
2) **Remove any reflective items like watches, rings, etc.**
3) **Never look at the height level of the beam propagation.**
4) **Always follow the instructions that will be given to you by the lab staff.**

At the start of the session you will be asked to sign a declaration confirming that the above-mentioned instructions have been transmitted to you verbally by your tutor, and that you undertake to follow them to the letter.

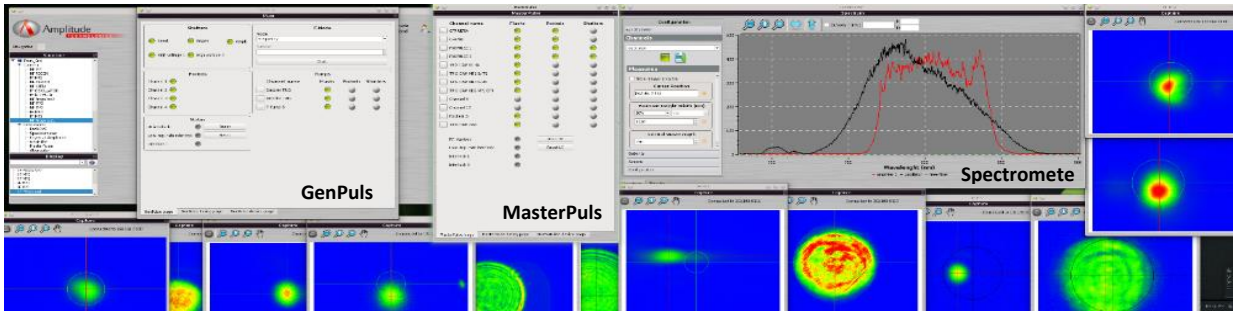

Figure 1.5. Screen capture of the main panels for controlling and monitoring the laser system.

The operation of the laser system is mainly realized from a terminal computer that controls and monitors several parts of the laser system (Figure 1.5). The spectrum and the beam quality are monitored at several stages of the laser system. The main controls are at two panels.

- **GenPulse** panel communicates with the Gepulse device that
  - controls the high voltage and the trigger of the 4 Pockels Cells (**Pockels**) at the **Booster** and Regenerative Amplifier (**Regen**)
  - controls the shutter for the seed beam and for the cavity of the Regen, as well as the shutter output of Amplifier-1 (**Ampli1**)
  - controls the trigger signals for the acousto-optic modulators, **Dazzler** and **Mazzler**
  - controls the single-shot/burst-mode/frequency-divider shutter
  - generates the 10Hz clock signal, from the division of the **Oscillator**'s pulse train (**RF**), that is used for all the synchronizations.
  - supply power to several photodiodes of the system
- **MasterPulse** panel communicates with the MasterPulse device that
  - controls the trigger signals of the flashlamps and the Pockels for all the pump laser, as well as their shutters.
  - generates self-clock from the RF signal and the 10Hz trigger from GenPulse to eliminate synchronization jitter
  - controls the trigger signals for all the cameras of the system.
  - receives external interlocks from the **Cryostat** system and the **Vacuum Compressor** and checks consistency of the RF signal, to disable channels in case of fault.

There are also other panels to control: the flashlamps voltage of the two **Propulse** pump laser, the Attenuator (**Atten**) of the last amplifier output (**Ampli3**), the vacuum and the motorized stages at the Vacuum Compressor chamber.

Laser Diagnostics of Zeus Laser System

For the operation of the ZEUS Laser System there are several checkpoints before the final exit of the beam to the experiment. More than ten cameras are used to record the position and the profile of the beam at several points of the beam path, as also of the pump beams.

- The first check is the output power of the oscillator. If the power is less than expected a cleaning of the Ti:Sa crystal usually improve it, or may needed the reposition of the crystal due to local burn spot or slight alignment of the cavity.
- A fast photodiode and oscilloscope are used to record the build-up of the laser pulses train in the Regenerative Amplifier (REGEN) during the pumping laser pulse. The buildup time difference with and without the seed-beam is checked to be as expected, a reduce of more than 50 ns on the build-up time when seeded (Fig. 1.6). This will affect the contrast ratio of the output laser and further checks and actions will be needed to improve it, as probably a realignment of the seeding beam. The recorded intracavity beam in the REGEN is also used to check the properly pulse extraction (pockel-cell PC3).

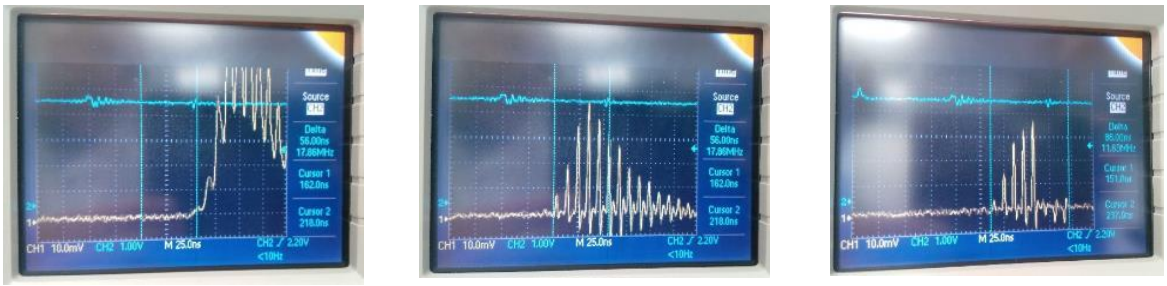

Figure 1.6: Photodiode signal (channel-1, yellow) of the intracavity beam in REGEN shows the pulses build-up time without (left figure) and with (middle figure) seed beam. The reduce time of more than 50 ns provide sufficient intensity contrast of the REGEN pulse output. At the right figure is the intracavity pulses after enabling the pockel-cell PC-3 that extract the proper pulse from the cavity. A followed pockel-cell (PC-4) cleans the beam from afterpulses.

- A spectrometer is used to record the spectrum of the output of the REGEN that is modified with the use of Mazzler to be wide (>60 nm) and flat as possible (Fig. 1.7). If it is not acceptable, a Mazzler feedback loop procedure is usually enough to improve it, else realignment maybe needed.
- The output energy measurement (value and stability) of the first amplification stage is a good indication of the proper operation of the former stages. The energy measurements are also made at the output of the following amplification stages, prior and after the use of the pumping lasers for consistency checking. Also, several irises at the beam path are used to check the beam position and assist the fine align

that may be needed, additionally to the cameras that record the beam profile and position.

- At the exit of the pulse compressor for the probe beam (Air Compressor) an intensity auto-correlator (Bonsai, from Amplitude Technologies) is used to measure the pulse duration and set it appropriate by changing the gratings distance in the Compressor. The Bonsai is a compact devise that features single shot, single beam operation making it very simple to align and to operate.

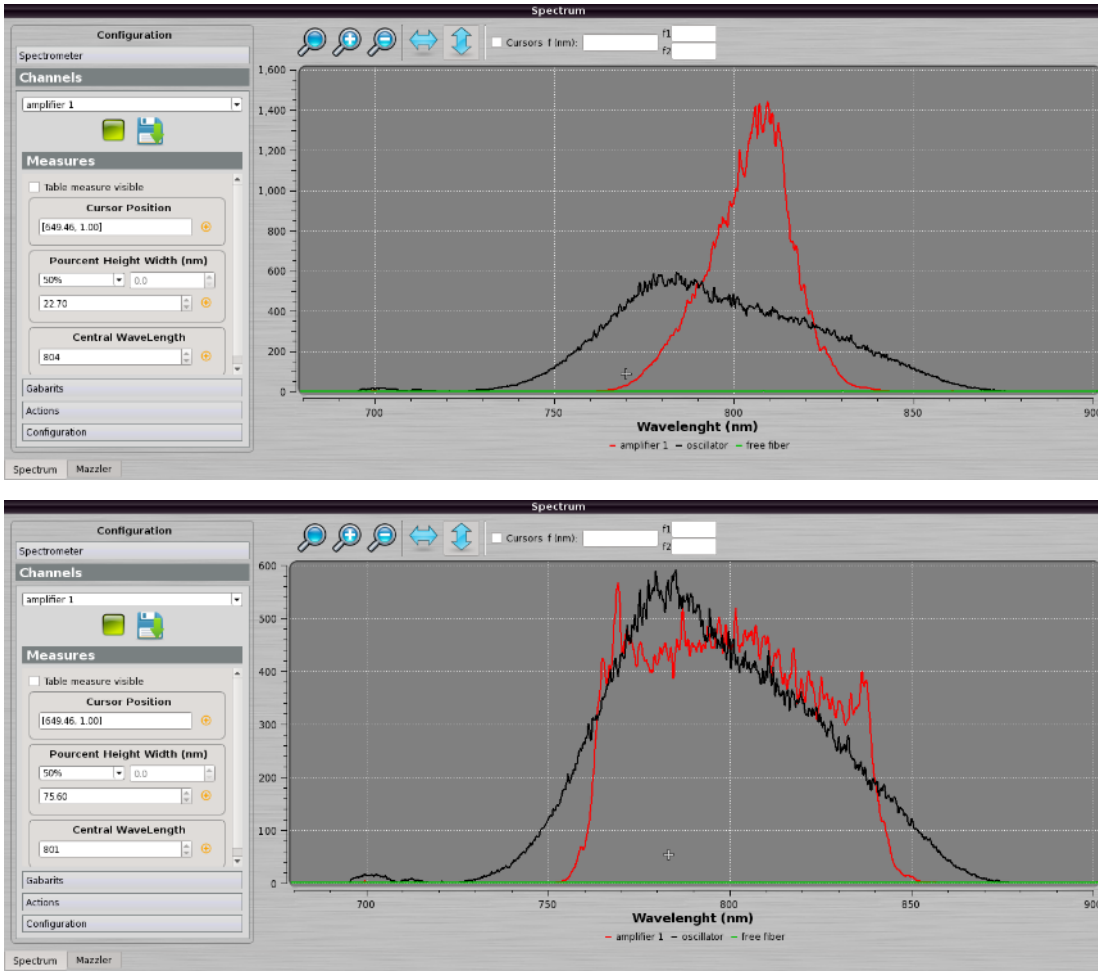

FIGURE 1.7: Spectrum of the regen output without (up) and with Mazzler (down). Starting from a spectrum FWHM of ~22 nm the Mazzler loop can lead to a FWHM of more than 70 nm by introducing a properly generated attenuation filter. This wide spectrum after amplification and proper compression is able to give pulse duration below 30 fs.

- At the exit of the pulse compressor for the main beam (Vacuum Compressor) a more sophisticated diagnostic system (Wizzler, from Fastlite) is used for properly measurement and fine adjustment of the pulse's characteristics. The Wizzler is based on the patented technique Self-Referenced Spectral Interferometry (SRSI) and delivers both spectral phase and amplitude measurements, i.e the complete temporal characterization of an ultrashort pulse. It provides also feedback to the Dazzler opto-acoustic modulator which applies phase correction to the beam at the output of the Stretcher in order to improve the measured pulses after the

Compressor. Wizzler/Dazzler feedback loops comprise a powerful compression optimization tool to achieve Fourier transform limited (FTL) pulses.

- A third order cross-correlator (SEQUOIA, from Amplitude Technologies) is used for the high dynamic range measurement of the temporal pulse shape of the beam. SEQUOIA offer an intensity contrast ratio of more than 9 orders, over a temporal measurement range of up to 500 ps, with a time resolution of down to 17 fs. It can provide information of the pulse pedestal, pre- or post-pulses and the Amplified Spontaneous Emission (ASE) which are very important parameters for the characterization of high energy laser pulses.

Pulse measurement/optimization with Wizzler/Dazzler

Introduction

The Wizzler is a pulse measurement system designed to measure accurately the spectral phase of amplified ultra-short, near Fourier-Transform Limited laser pulses. It is based on a pulse characterization technique invented and patented by FASTLITE: Self-Referenced Spectral Interferometry (SRSI). It is single-beam, single shot, and delivers both spectral phase and amplitude measurements, i.e the complete temporal characterization of an ultrashort pulse.

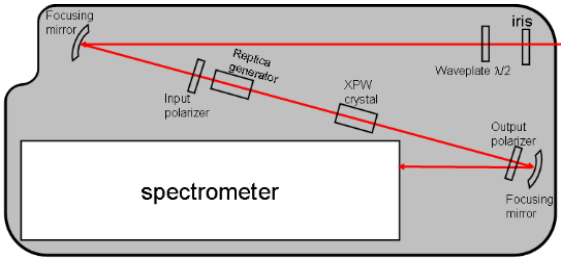

Figure 1.8: Wizzler optical setup

The Wizzler system is a standalone instrument with its hardware, implementing the optical setup that generates the SRSI signal and the spectrometer that records it, and its software, which extracts the pulse characterization from the SRSI interferogram. In case a DAZZLER pulse shaper is integrated in the laser chain, the software has also the capability to send the phase information back to this device to perform pulse optimization.

Fourier-Transform Spectral Interferometry

Fourier-Transform Spectral Interferometry (FTSI) [1][2], is the treatment of the frequency domain interference pattern between 2 pulses delayed in the time domain. Inverse Fourier transform of the spectral interferogram results in a 3 peaks structure in which the oscillating term in the spectral domain, centered at the delay τ between the 2 pulses in the temporal domain, is numerically filtered. A Fourier transform convoluted with this filter provides information about the difference of the spectral phases and the product of the spectral intensities. Additionally, a similar treatment of the continuous term in the spectral domain, centered at delay 0 in the temporal domain, provides information about the sum of the spectral intensities, which enables the reconstruction

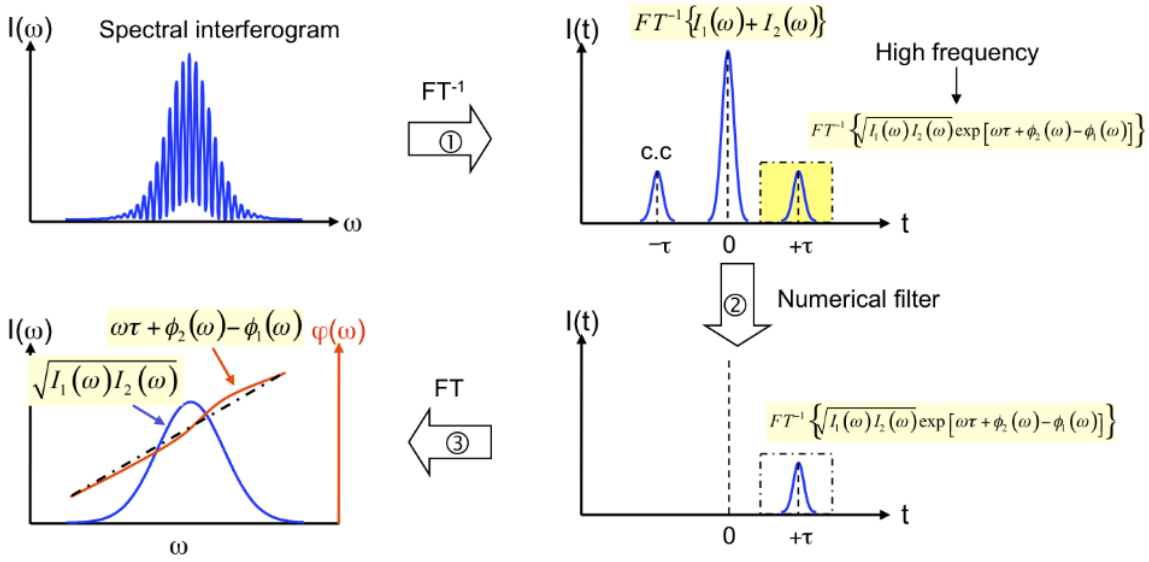

Figure 1.9: Fourier-Transform Spectral Interferometry (FTSI)

of the 2 spectral amplitudes provided that the 2 spectral intensities do not overlap.

The XPW effect

Cross-Polarized Wave Generation (XPW) [3][4] is a third-order nonlinear effect. As its name suggests, it is the generation of a linearly polarized wave, orthogonally to the polarization of a high-intensity linearly polarized input wave (see fig 1.10). Within the slowly-varying envelope, the undepleted regime and the thin crystal approximations [5].

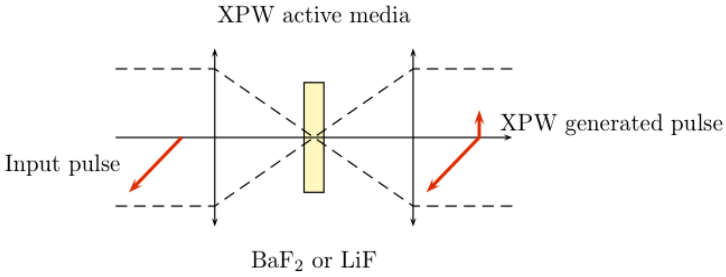

Figure 1.10: XPW generation

The XPW temporal amplitude is linked to the input temporal amplitude by the following:

$$E_{XPW}(t) \propto |E_{IN}(t)|^2 E_{IN}(t)$$

As can be seen, the XPW effect acts like a temporal filter: a XPW generated pulse is a replica of the initial pulse, filtered by its own temporal intensity. Thus, we expect it to be shorter in time ie to have a broader spectrum and a flatter spectral phase than the

input pulse. This is true, according to [6], when the pulse is close enough to the Fourier transform limit, ie when the spectral phase is flat enough for the pulse to be filtered by the XPW effect. It is worth noting that XPW generation is more sensitive to the chirp than to higher orders of the spectral phase, and that its efficiency vanished for pulses chirped to above 2 times their FTL pulse duration. [6]

Self-Referenced Spectral Interferometry

The Wizzler measurement technique name is "Self-Referenced Spectral Interferometry" (SRSI). The principle is pretty simple, and described on figure 1.11. From the pulse to be measured, a replica is created on a linear polarization different from the input one and delayed. The main pulse is used to generate a reference pulse with a broader spectrum and a flatter spectral phase, but with the same carrier frequency, via Cross-Polarized Wave Generation (XPW). This reference pulse is created on the perpendicular polarization, so that a polarizer can transmit the XPW pulse and the replica to a spectrometer which records an interference signal.

FTSI treatment is applied to this interferogram, and both spectral phase and spectral

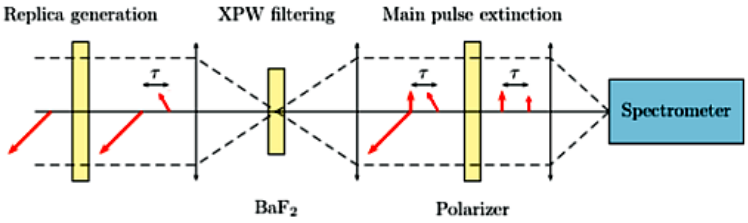

amplitude of the input pulse can be extracted assuming that the spectral phase of the reference pulse Φ1 is known. While Φ1 is not perfectly flat, it can be set to 0 as a first approximation, and the algorithm shown on figure 4.5 improves the accuracy of the reference pulse phase value. In the Wizzler, the algorithm used includes last data processing development and enhancement unpublished and done by FASTLITE. FASTLITE has published a number of articles describing SRSI technique as well as Wizzler experimental results. [7][8][9]

Measurerement and optimization of the pulse characteristics

Figure 4.5: Algorithm loop to improve accuracy of XPW phase value.

1) Set Wizzler to Specrtum mode and make fine alignment adjustment using the last mirror before the beam entrance in Wizzler to maximize the signal level and the fringes contrast.
2) Set Wizzler to SRSI mode and see the amplitude and phase spectra as well as the temporal pulse reconstruction. The Signal and Goodness indicators should be green.
3) Make remote desktop connection to Dazzler-PC and set Dazzler Phase to Polynomial only (apply by presing Load).
4) Make changes of the second order parameter by 200 fs^2 and observe the changes at the wizzler measurements. Find the parameter for the optimum results, smaller duration and smoother amplitude/phase spectrum.

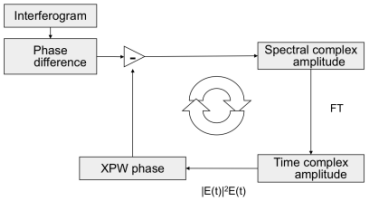

5) At Wizzler press to reset the previous feedback and press Feedback Now to sent feedback to Dazzler for otpimization. At Dazzler select Phase "both" and apply (Load).
6) Make feedback steps again to optimize the pulses characteristics (each time deselect and select "both" at Dazzler before apply). The feedbakck strength can be adjust if neededed at the Wizzler (normally 0.6 to 0.8).
7) Stop feedback loop when at Dazzler the real spectral tranfer function (Spectrum window) colored red has large difference from the programmed one colored black. The last feedback can be undo from the Wizzler.

Figure 1.12: Pulse improvement by feedback to Dazzler. Before feedback (left) the best measurements results by changing the grating distance of the compresor or the polynomial parameters of Dazzler are far away from the calculated Furier Tranform Limited (FTL) and the phase spectrum is not flat enough. After few feedback steps to Dazzler (right) the phase spectrum is optimized and the measured pulse characteristics is near the ideal FTL.

Pulse contrast ratio measurement with Sequoia

Introduction

The high dynamic measurement of the temporal contrast of the main pulse of the Zeus laser system is implement by a third order cross-correlator, the Sequoia from Amplitude Technologies. It uses the third harmonic generation to achieve the cross-corelation between a "delta" pulse - generated by the second harmonic - and the pulse itself. The optical layout is shown in Fig.1.13. The main pulse is separated in two lines, where one is frequency doubled (SHG) and delayed. The two beams are recombined into a crystal (C02) where the sum frequency process provides the third harmonic generation (THG) signal which is propotional to the temporal overlap between the two incident pulses. The wavelength of the cross-corelated signal is easily filtered from the incident pulses and is detected by a photomutiplier. The evolution of the signal with respect to the time delay gives the pulse temporal profile. The gain of the photomultiplier is dynamically controlled in order to adjust the measurement level between the noise and the saturation effect. The dynamic range of the measurement is also strongly increased by the use of calibrated neutral density (ND) filters at the Sequoia input which are dynamically exchanged during measurement. A computer software drives the instrument for the delay line setting, the gain control and data acquisition of the detector, the exchange of the ND filters, as shown in Fig. 1.14.

The high dynamic allows to detect temporal structures with power less than a factor 10^{-9} below the main pulse and combined with the large delay range (>500 ps) with precision steps (17 fs) Sequoia offers the ability to measure:

- Pules pedestal: precise measurement in the ±1 ps range gives important

information on this essential parameter

- Ghost pulses: the large temporal measurement range allows measurement of unwanted pre- and post-pulses, which can generated from dielectric coatings, birefringent optics,compression gratings etc.
- Amplified Spontaneous Emission: ASE level an important parameter for the characterization of high amplified pulses. The duration of the ASE is generally several orders of magnitude of the main pulse and can represent a significant fraction of the total pulse energy.

Measurement of the pulse contrast ratio with Sequoia

1) Set the laser pulse energy to have 0.3-0.5 mJ before the Sequoia and align the beam to the entrance.
2) Setup a telescope at the diagnostics table for reducing the beam size to be about 4 mm before the entrance to Squoia
3) Start the software of Sequoia and set the *Density* filter to zero.

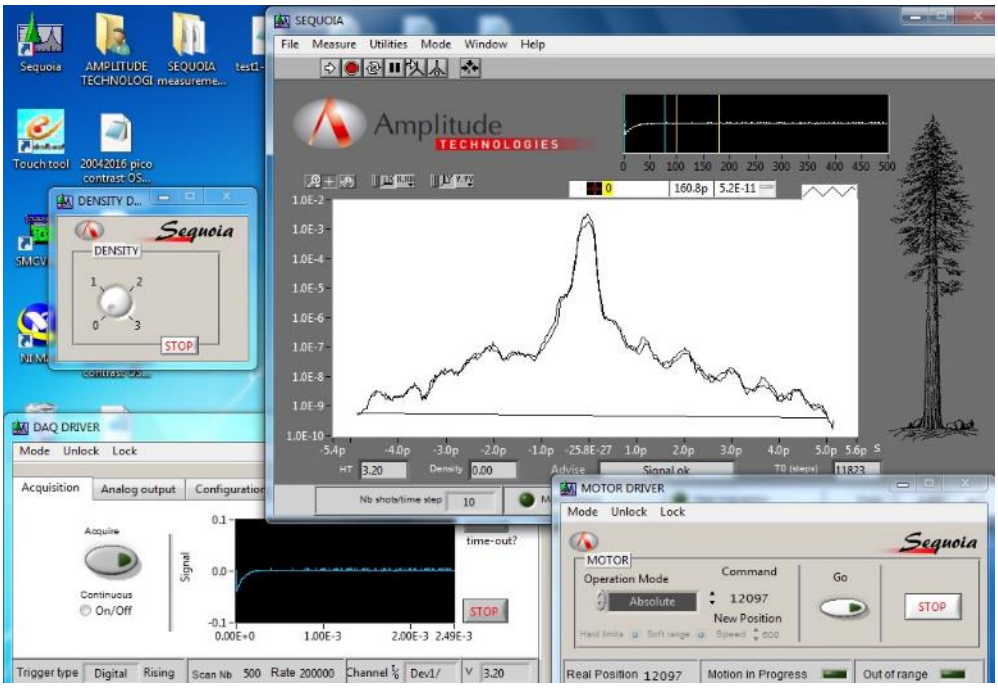

Figure 1.15: The software for the Sequoia

4) Open the cover of the Sequoia and align the beam to the SHG crystal.
5) Set at the *DAQ DRIVER* window at the software to have continuous acquisition of the photomultiplier signal and set the *analog output* voltage to 2.5V and press *Refresh*.
6) Fine align the beam to maximize the signal
7) At the main window of the Sequoia software select the *find max* button to make a delay scan for finding the maximum signal where the probe beam coincides with the main beam (zero point).
8) With the *Density* filter to zero make fine alignment or energy changes to have signal ~2.5
9) Set sequntely the Density filter to 1/2/3 and make fine alignment or energy

changes to have signal about 1.2/0.75/0.4

10) Setup the software for contrast ratio measurement. At the main window select Measure→Set-up and set the number of shot measurements per time-step (default is 10), the starting time T0 for the measurement in respect to the zero point and the time step (positive or negative).

11) At Measure-menu select "continue" to continue writing on the previous measurment data or "clean" to clean the previous data. With the first option is possible to stop at any time the measurment and continue with different time-step the measurement.

12) Pres the white arrow button to start the measurement. Press the red cycle button to stop the measurement.

13) After that you can save the measurement data and an otptions window allows you to normalize and sort the data, as also set zero-time at the maximum of the signal before save to file. Also you can save the graph as an image.

Bibliography & References

- User manual for the Pulsar laser system, Amplitude Technology S.A.
- User manual for Sequoia measurement system, Amplitude Technology S.A.
- User manual for Wizzler, Fastlite
- User manual for Dazzler, Fastlite
- User manual for Mazzler, Fastlite

[1] C.Dorrer, M.Joffre, Characterization of the spectral phase of ultrashort light pulses, C.R. Acad. Sci. Paris, t.2, Srie IV, p.1415-1426, 2001.

[2] L.Lepetit, G. Chriaux, M.Joffre, "Linear techniques of phase measurement by femtosecond spectral interferometry for applications in spectroscopy", JOSA B 12, 2467-2474(1995)

[3] N.Minkovski, G. I. Petrov, S.M. Saltiel, O. Albert, J. Etchepare, "Nonlinear polarization rotation and orthogonal polarization generation experienced in a single beam generation", JOSA B, 21, 9-1659 (2004)

[4] A. Jullien, O. Albert, G. Chriaux, J. Etchepare, S. Kourtev, N. Minkovski, S. M. Saltiel, "Nonlinear polarization rotation of elliptical light in cubic crystals, with application to cross-polarized wace generation" JOSA B 22, 12-2635 (2005)

[5] W.R.Boyd Nonlinear Optics 3rd edition, 2007.

[6] L. Canova, O. Albert, N. Forget, B. Mercier, S. Kourtev, N. Minkovski, S.M. Saltiel, R. Lopez Martens, "Influence of spectral phase on cross-polarized wave generation with short femtosecond pulses", App. Phys. B 93, 443-453 (2008)

[7] T.Oksenhendler, S.Coudreau, N.Forget, V.Crozatier, S.Grabielle, R.Herzog, O.Gobert, D.Kaplan,, Self-referenced spectral interferometry, Appl. Phys.B (2010).

[8] A.Moulet, S.Grabielle, C.Cornaggia, N.Forget, T.Oksenhendler, Single-shot, high dynamic-range measurement of sub-15fs pulses by self-referenced spectral interferometry, Opt.Lett. 35 (22), 3856-3858 (2010)

[9] S.Grabielle, A. Moulet, N.Forget,V.Crozatier, S.Coudreau, R. Herzog, T. Oksenhendler, C. Cornaggia, O. Gobert "Self-referenced spectral interferometry cross-checked with SPIC DER on sub-15 fs pulses.", Nuclear Instruments and Methods in Physics Research Section A: Accelerators, Spectrometers, Detectors and Associated Equipment DOI: 10.1016/j.nima.

PART B - LASER MATTER INTERACTION FOR HHG

Theoretical background

High-harmonic generation (HHG) provides a powerful source of ultrashort coherent radiation in the eXtreme UltraViolet (XUV) and soft-X-ray range and is the main research field in ultrafast science. Generally, when a non-linear medium is exposed to femtosecond laser radiation with intensities $\geq 10^{14}\,\mathrm{Wcm^{-2}}$ the atoms are ionized and the freed electrons are accelerated by the laser field in the presence of the core potential. A small number of these electrons may recombine with the parent ions emitting the gained energy.

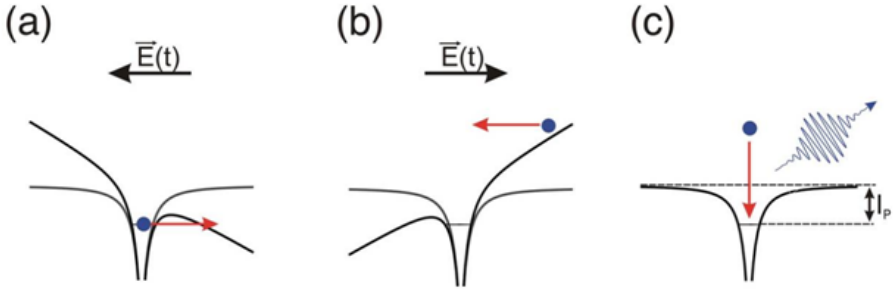

Figure 2.1 A typical HHG process from atomic gases

If the non linear media is centrosymmetric (e.g. atomic gases) the above process occurs twice per laser pulse period and thus resulting in a HHG spectrum which consists of the odd multiples of the fundamental photon frequency.

Changing scale from microscopic to macroscopic, the key issue for efficient HHG is the coherent addition of the generated pulses also known as phase-matching both in temporal and spatial domain. The main reasons for phase-mismatching are the dispersion, when the pulses propagate in the non-linear medium and the system geometry.

Experimental arrangements and considerations

The laser source used is the probe beam of 45 TW laser system. In the next figure the basic experimental setup is illustrated

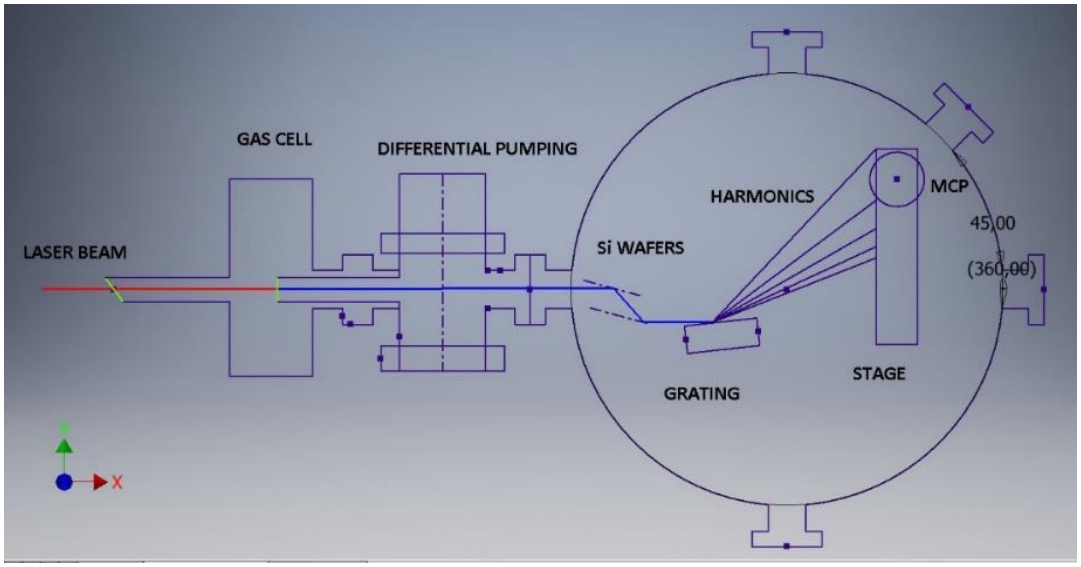

Figure 2.2 experimental setup

The laser beam is directed in the gas cell and is focused in a hole on a metal surface. This hole is created by the focused laser beam, so the diameter is similar with the spot size. This hole is also the outlet of the gas cell.

Figure 2.3 Gas cell. Is visible the plasma created by the focused beam on copper foil creating the outlet of gas cell.

The beam focus is in the gas sell near the metal foil. The produced harmonics and the laser beam are directed on a pair of silicon wafers in Brewster angle in order to filter the laser beam.

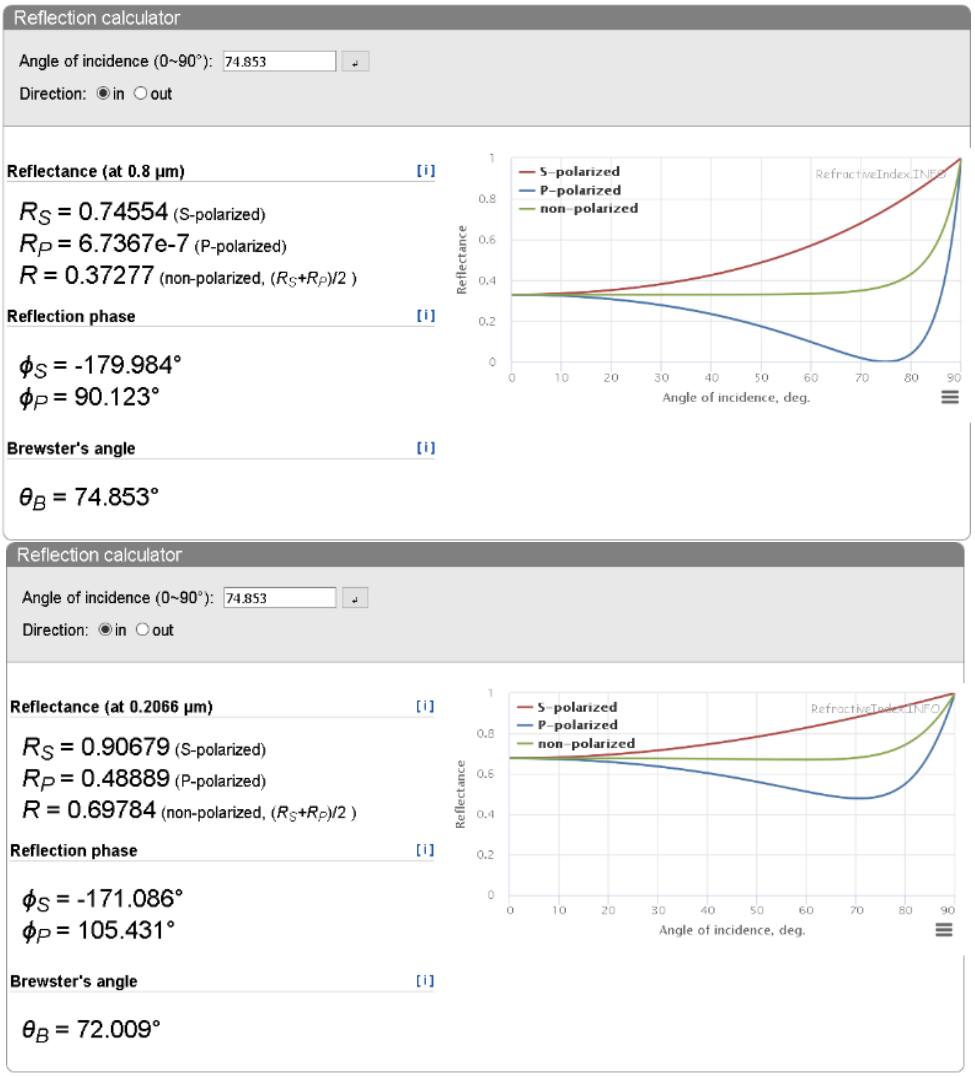

Figure 2.4 The reflectance for the 800 nm is of order e-7 while for 200 nm is almost 50%.

The XUV radiation is separated with a flat field grating and the harmonics are focused on a plane.

The detection made with microchannel plate (MCP) sensor moving on the plane of focused harmonics. An MCP is an array of 104-107miniature electron multipliers oriented parallel to one another.

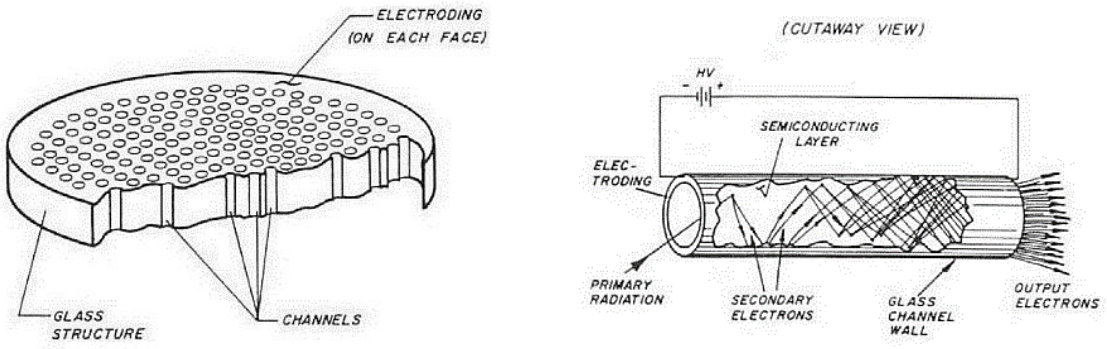

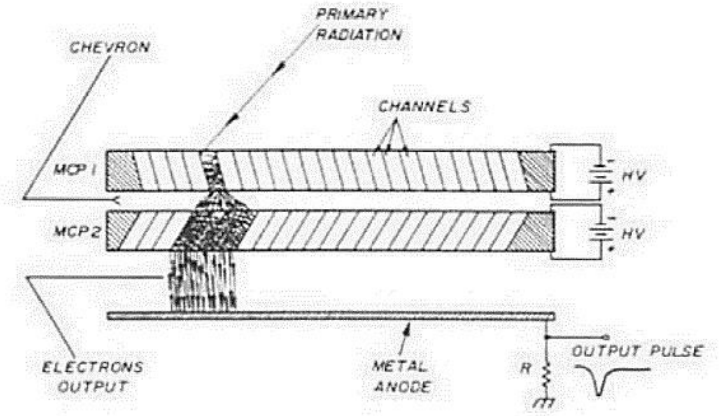

Figure 2.5 MCP main structure and operation

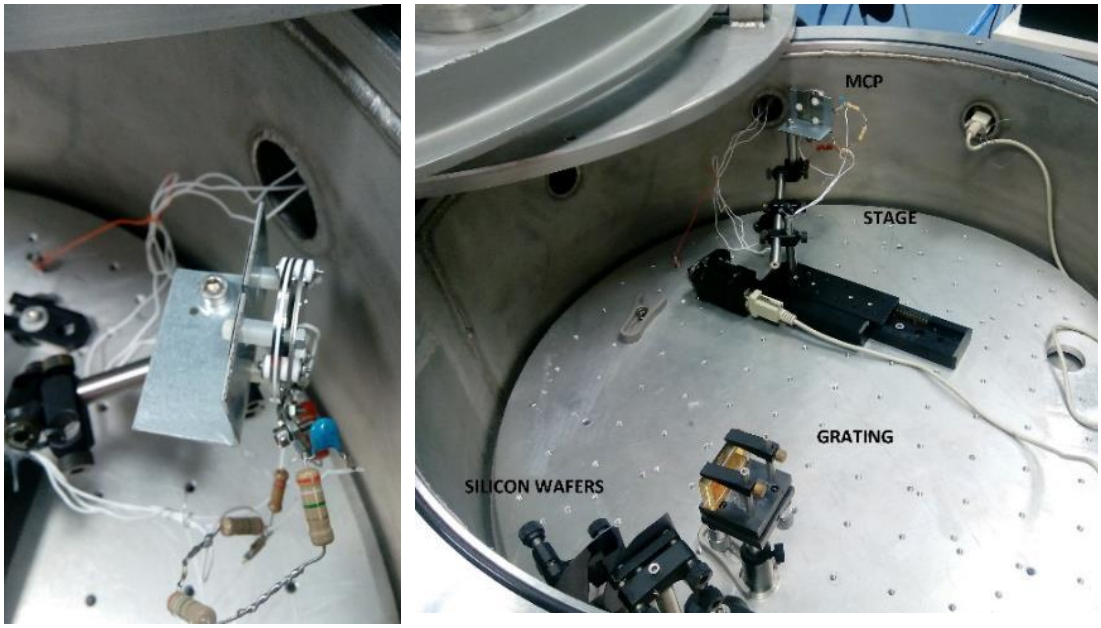

Figure 2.6 MCP on experimental setup inside the vacuum chamber.

A typical spectrum snapshot from the CCD camera is illustrated in Figure 2.7

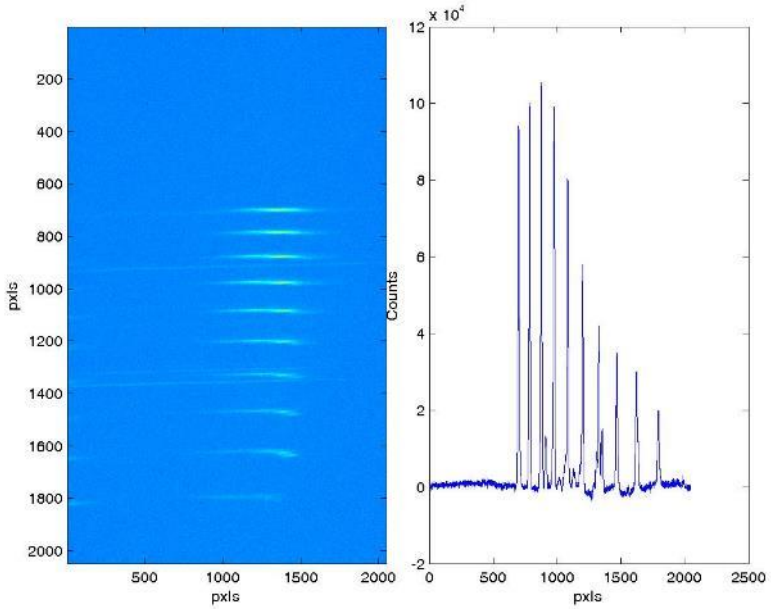

Figure 2.7 A typical spectrum snapshot from the CCD cameras. On the left are indicated the counts along the y-axes of the spectrum.

But in our case using the MCP we have this picture

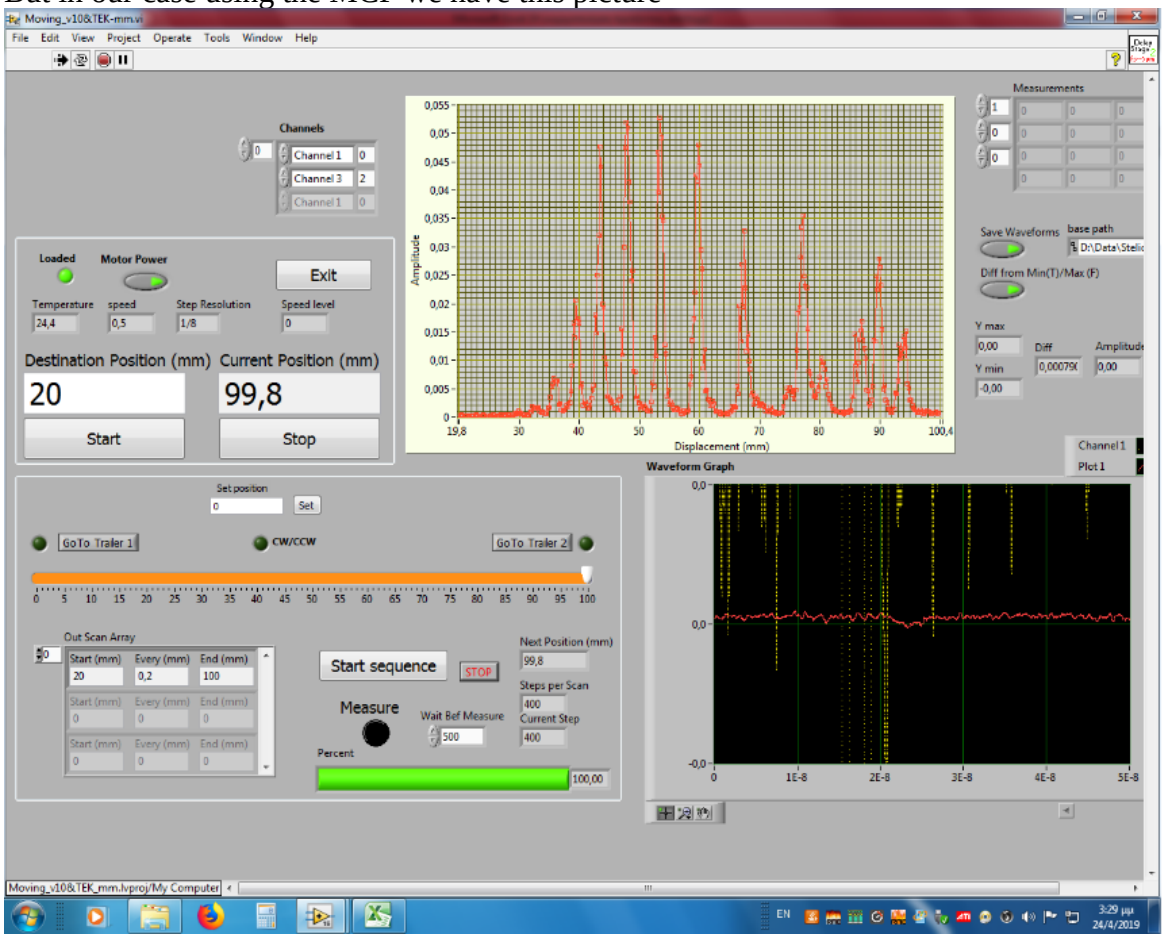

Figure 2.8 The main experimental setup components is connected to a computer and the procedure was automated using the LabView software.

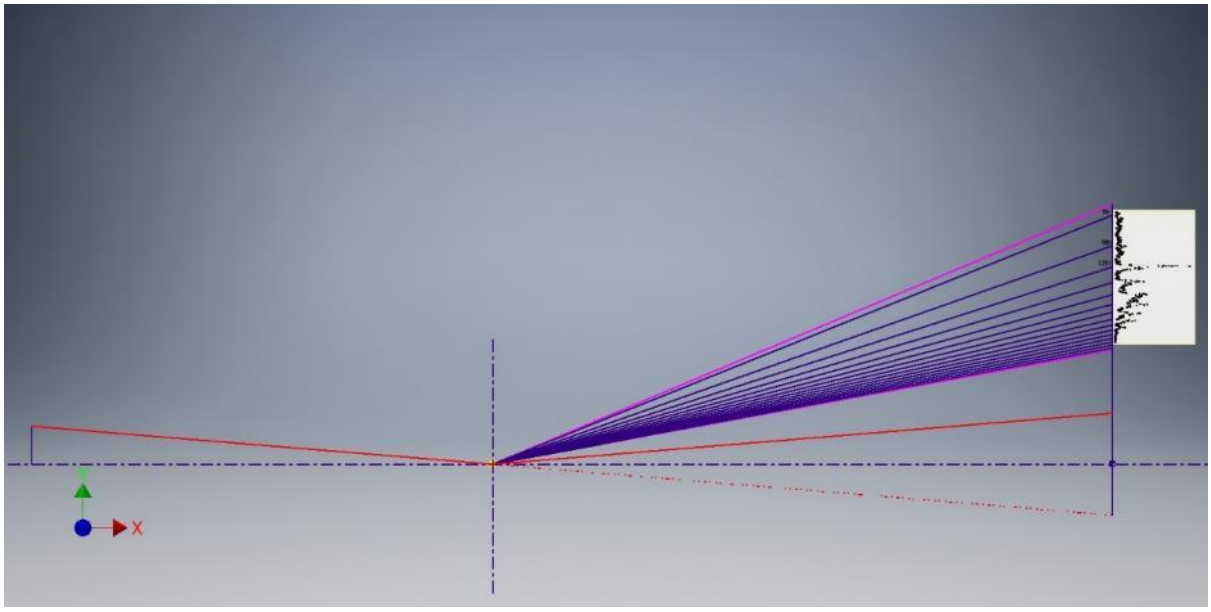

Figure 2.9 The order determination of the appeared harmonics can be uniquely identified by the distance between them taking in mind that $\lambda_q = \frac{\lambda_0}{q}$ *and that the used grating was flat field. Where* λ_q, λ_0 *and* q *are the qth harmonic wavelength, the fundamental frequency (800nm) and the harmonic order respectively.*

PowerLaPs

Innovative Education & Training in High Power Laser Plasmas

Laser plasma diagnostics - Theory and Experiments

EXP 4: Laser matter interaction diagnostics

Y. Orphanos, S. Petrakis

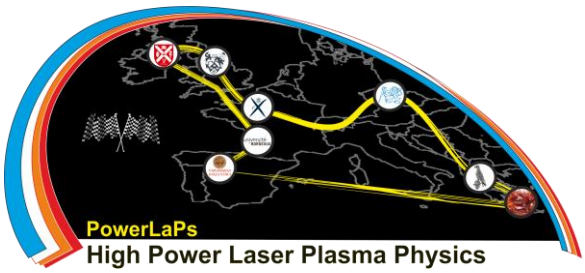

HELLENIC
MEDITERRANEAN
UNIVERSITY

1.1 Diagnostics of metallic film targets interacting with short laser pulses

The aim of this laboratory is to give you the opportunity to get practical experience on the diagnostics related with interaction of short laser pulses with metallic film targets.

Two are the diagnostics we are going to explore which are guided from the basic interferometry and more specific the Michelson Interferometer. The first one is a single interferometric image analysis that will show us the surface deformation due to ultrasound that travel across the surface. The second one is the White Light Interferometry setup which will show us the “damage” that the generation of the ultrasound may have produce in the metallic film surface.

1.2 Generation of ultrasounds and their analysis

Here is presented the generation of ultrasounds and the analysis of the surface deformation by using the interferometric images.

1.2.1 Generation of ultrasounds

When a solid material is irradiated with short laser pulses, the absorption of the irradiance causes the local temperature increase and its thermal expansion which leads to the generation of the ultrasounds in the material. The energy that is produced travels in all directions (Figure 10). The laser generated Surface Acoustic Waves (SAWs) depend on the metallic film properties as well as the substrate properties.

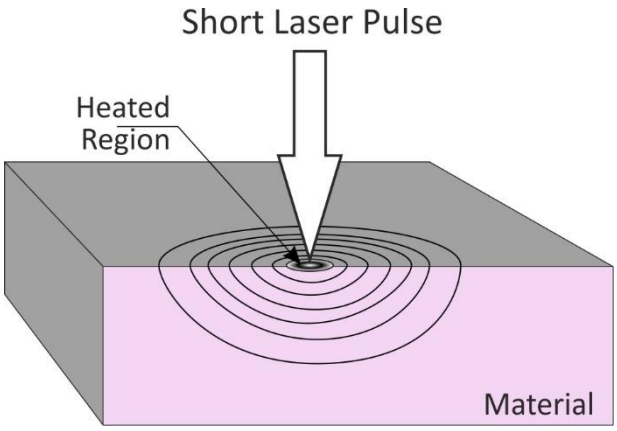

Figure 10 Interaction of short pulses with mater

For ns laser pulses, the electron cloud is always in thermal balance with the grid and their common temperature follows the classic heat treatment equation (1):

$$\dot{T} = \left(\frac{\kappa}{\rho c}\right)\nabla^2 T + \frac{Q}{\rho c} - \frac{T_0 \varepsilon}{\rho c}\nabla \dot{u} \qquad (1)$$

where T is the temperature transition function, $\dot{T}$ the temperature transition and T_0 the reference temperature, k, ρ, c the constants for thermal conductivity, density and specific heat respectively, ε the thermal acoustic coupling constant. Q the heat source defined as the energy absorbed per unit volume per second.

In the ns pulsed laser and mater interaction, three are the areas of interest (Figure 11), depending on the laser energy absorbed by the target and determine its behavior: a) the thermoelastic area, b) the melting range, and c) the area of ablation.

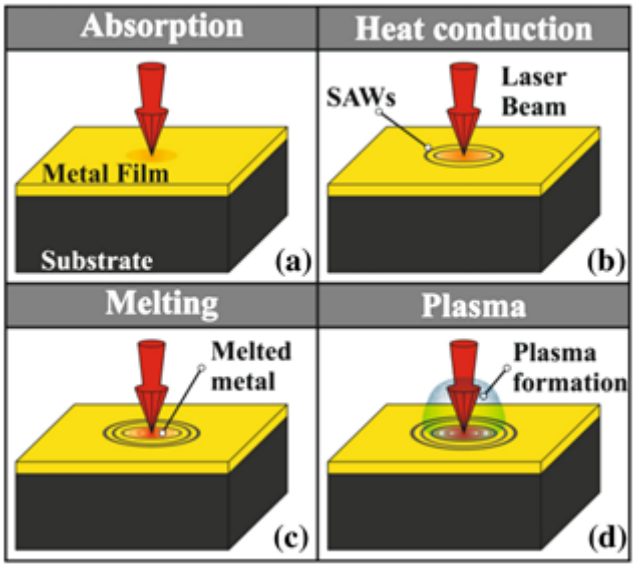

Figure 11 Matter states during irradiation with laser pulse

Using spherical lens, we can focus the laser pulse in the material's surface and produce the SAWs (Figure 12).

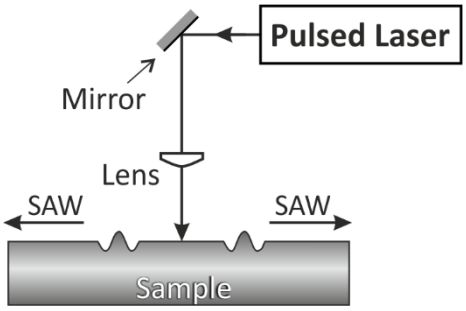

Figure 12 SAW production using point-focused pulsed laser

In order to produce the SAWs and analyze the deformation that they produce in the material, we constructed a setup (Figure 13) that splits (BS) the ns laser pulse in two parts: a) The "Pump Beam" is focused in the material's surface and produces the SAWs, b) The "Probe Beam" that travels in one of 4 different (by selection) optical path delays and ends in a Michelson Interferometer, where the one surface is the material's

surface and the other is a mirror. The output of the interferometer is captured from a CCD camera using an electronic delay trigger for further processing.

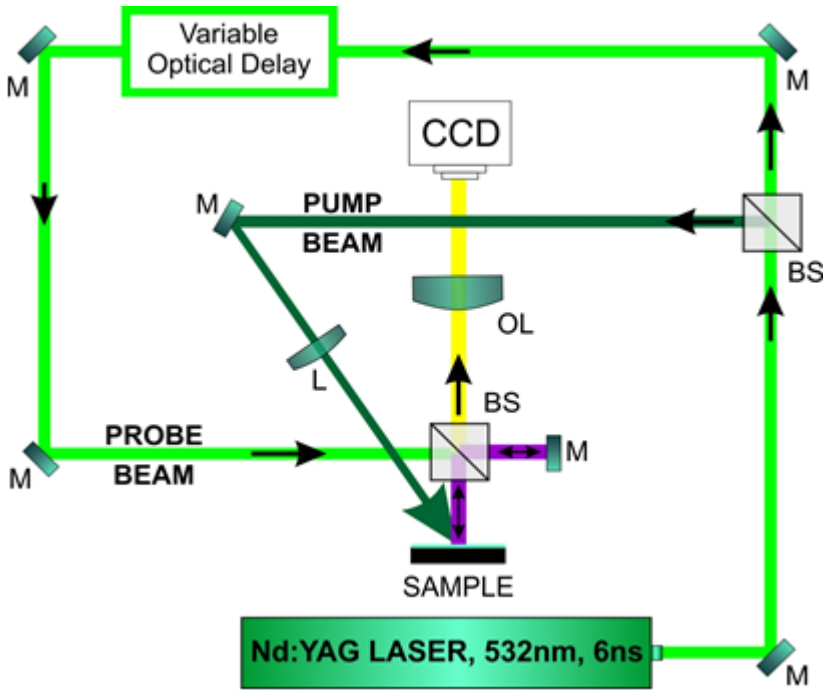

Figure 13 Simplified SAWs generation setup

1.2.2 Interferometric image analysis

The interferometric images are recorded using a customized recording software (Figure 14). The fringes density depends on the mirror tilt in the Michelson setup.

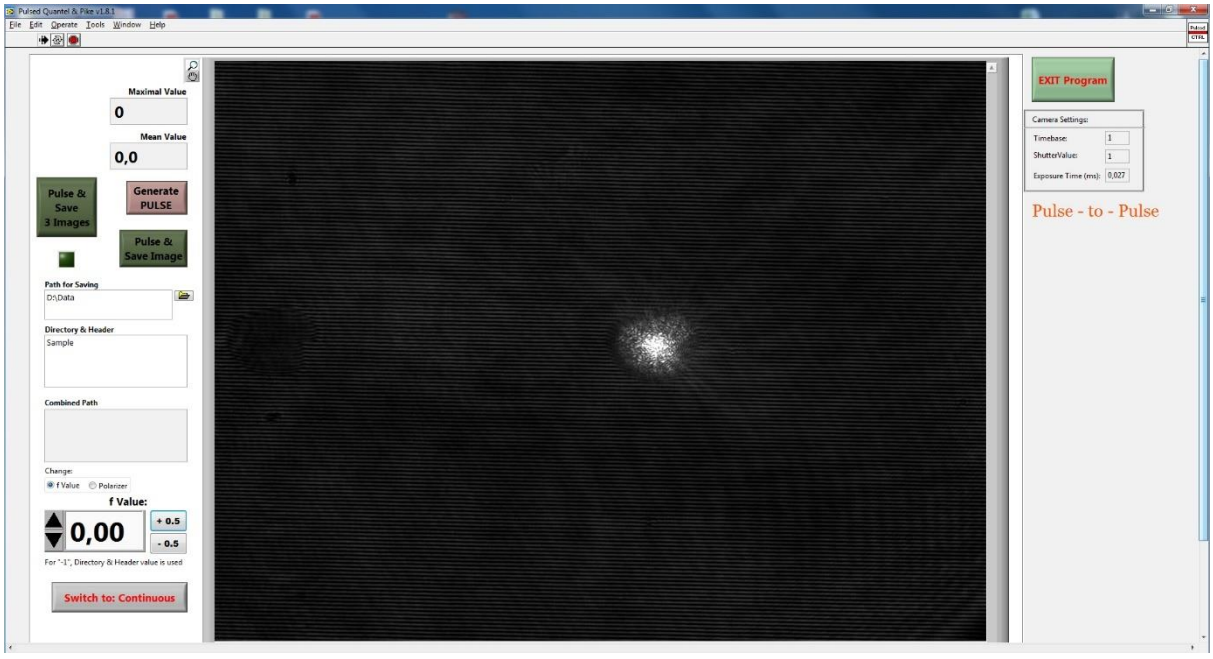

Figure 14 Interferometric Image recording

The recorded images are further processed using another customized software (Figure 15) that embodies 2D FFT algorithms as well as phase unwrapping techniques.

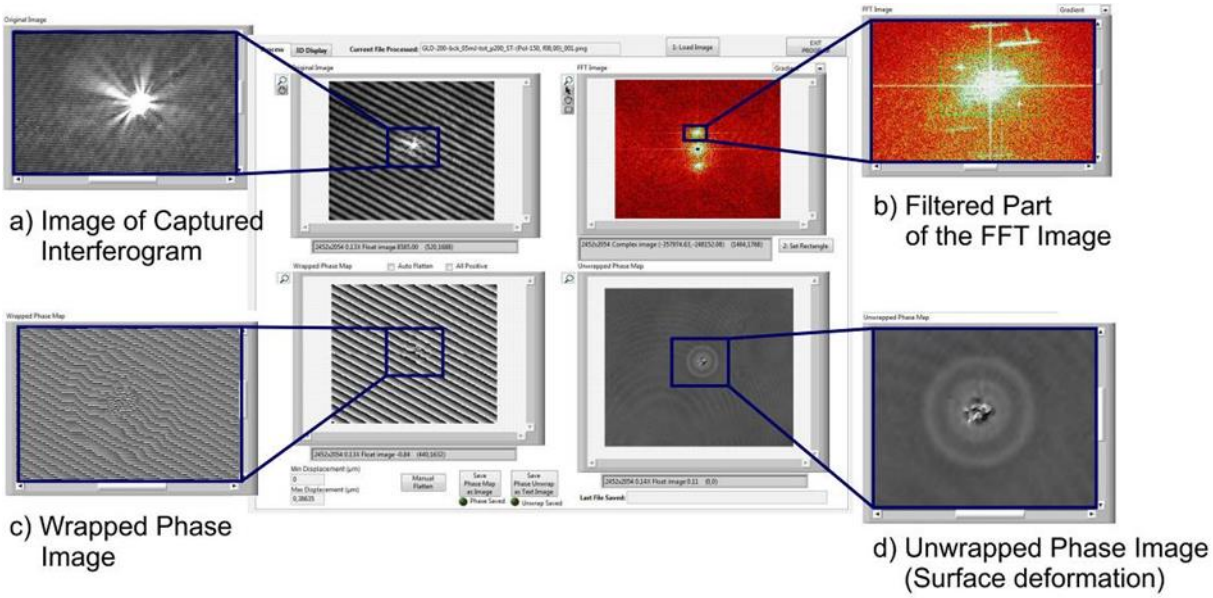

Figure 15 Software for the interferometric images processing

As a first step is to open an interferometric image (Figure 15-a). The image is automatically transformed in the Fourier space, where there are two lobes appear due to the parallel fringe formation. The next step is to select by using a rectangle tool the one of the two lobes (Figure 15-b) which filters the rest of the image to black and keeps only the selected lobe. The invert Fourier transformation gives us next the "wrapped" phase of the interferometric image (Figure 15-c). By using a special algorithm, the phase is unwrapped (Figure 15-d) and we can extract the deformation of the surface using the following equation:

$$d = \frac{\varphi \cdot \lambda}{4 \cdot \pi} \qquad (2)$$

where: λ, the wavelength of the laser source used to record the interferometric images

1.3 White Light Interferometry

In the White Light Interferometry, we get the advantage of the partial interference that appears when using broadband light sources (Figure 16).

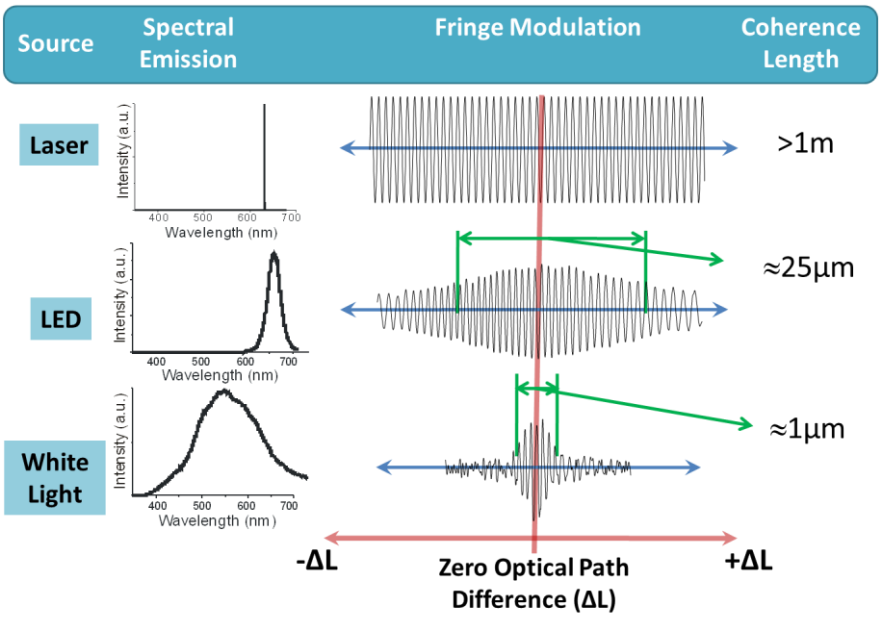

Figure 16 Light sources & Coherence

While in a coherent laser source, the total intensity is (3):

$$I_{tot} = I_1 + I_2 + 2\sqrt{I_1 I_2}\cos\left(\frac{2\pi}{\lambda}\Delta L\right) \quad (3)$$

where: λ, the wavelength and ΔL the optical path difference.
In partial interference, the total intensity is (4):

$$I_{tot} = I_1 + I_2 + 2\sqrt{I_1 I_2}\left|\gamma_{12}(\Delta L)\right|\cos\left(\frac{2\pi}{\lambda}\Delta L\right) \quad (4)$$

where: *the term* $|\gamma_{12}(\Delta L)|$ *is the complex degree of coherence* and gets values from 0 to 1.

The term $|\gamma_{12}(\Delta L)|$ *expresses the visibility of the interference fringes that appears in partially coherence (5):*

$$\left|\gamma_{12}(\Delta L)\right| = \frac{I_{max} - I_{min}}{I_{max} + I_{min}} = V \quad (5)$$

In order to locate the maximum value of the term $|\gamma_{12}(\Delta L)|$ *(zero optical path delay)*, we have to process the interferometric images and find the maximum of the envelop curve (Figure 17).

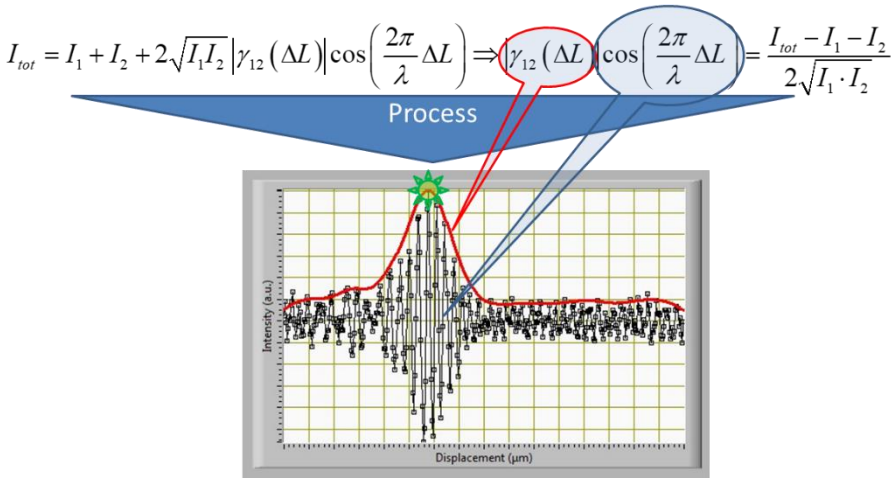

Figure 17 Location of the zero optical path delay

1.3.1 White Light Interferometry setup and image processing

In the White Light Interferometry setup (Figure 18), we use the same Michelson Interferometer we used to capture the interferometric images where instead of the mirror we use a Piezo-Transducer (PZT) to move the mirror in the Z-Axis.

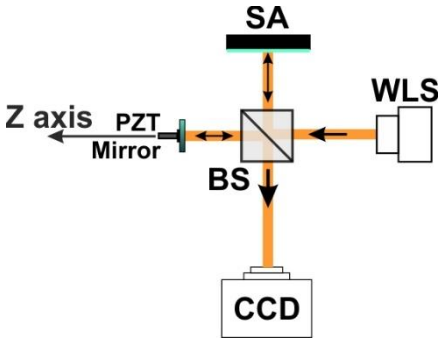

Figure 18 White Light Interferometry setup

The moving of the PTZ mirror produces a vertical stack of images that we collect using a CCD camera (Figure 19-a).

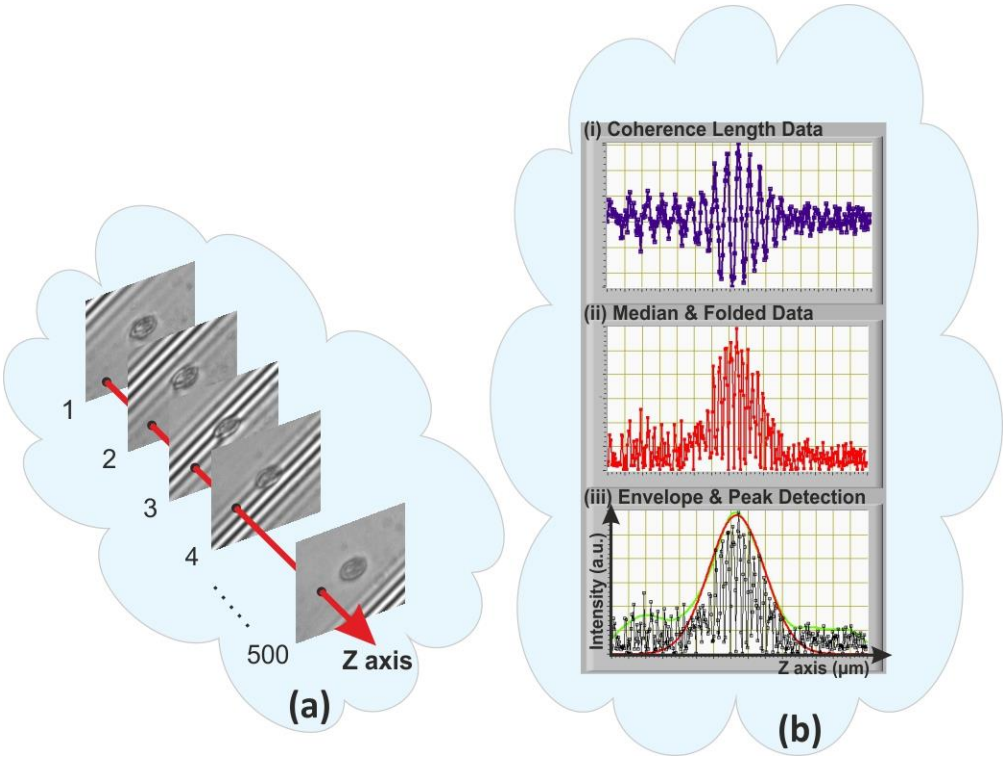

Figure 19 WLI image capture and processing

The stack of the images are further processed pixel-by-pixel in vertical axis (Z) using a custom software to extract the zero optical path delay (Figure 19-b) from each pixel.

The resulted image can be open using an image processing software like “ImageJ” and get the values for the 2D profile (Figure 20), or 3D prolife of the surface (Figure 21).

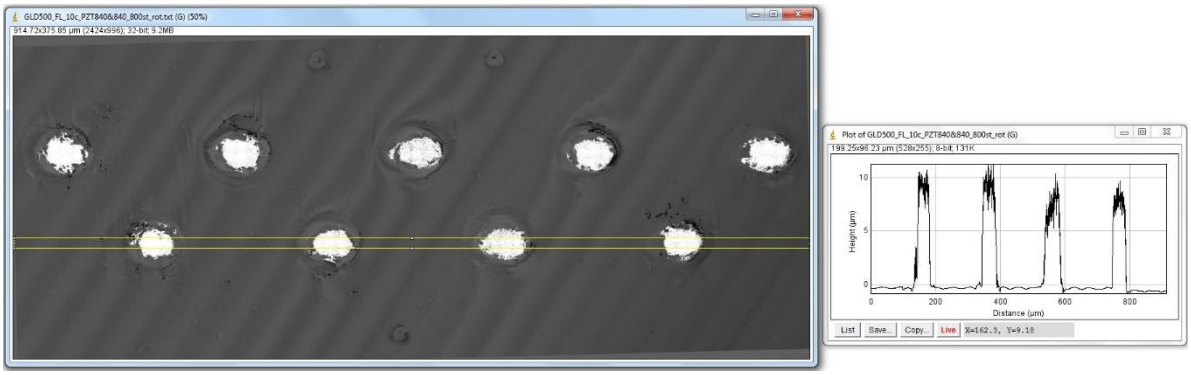

Figure 20 2D profile of a surface

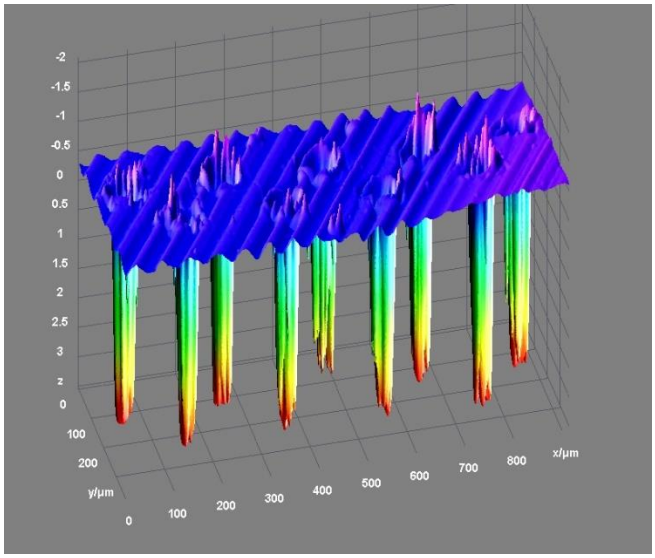

Figure 21 3D profile of a surface

BIBLIOGRAPHY & REFERENCES

- Y. Orphanos, V. Dimitriou, E. Kaselouris, E. Bakarezos, N. Vainos, M. Tatarakis and N.A. Papadogiannis "An integrated method for material properties characterization based on pulsed laser generated surface acoustic waves" Microelectronics Engineering 112, 249-254 (2013), doi:10.1016/j.mee.2013.03.146
- V. Dimitriou, E. Kaselouris, Y. Orphanos, E. Bakarezos, N. Vainos, M. Tatarakis, and N. A. Papadogiannis, "Three dimensional transient behavior of thin films surface under pulsed laser excitation", Applied Physics Letters 103, 114104 (2013); doi: 10.1063/1.4821274
- V. Dimitriou, E. Kaselouris, Y. Orphanos, M. Bakarezos, N. Vainos, I. K. Nikolos, M. Tatarakis and N. A. Papadogiannis "The thermo-mechanical behavior of thin metal films under nanosecond laser pulse excitation above the thermoelastic regime", Applied Physics A, (2014) doi: 10.1007/s00339-014-8792-6
- V. M. Papadakis, A. Stassinopoulos, D. Anglos, S. H. Anastasiadis, E. P. Giannelis and D. G. Papazoglou, *"Single shot temporal coherence measurements of random lasing media"*, J. Opt. Soc. Am. B 24, 31, 2007
- James C. Wyant and J. Schmit, *"Large Field of View, High Spatial Resolution, Surface Measurements"*, Int. J. Mach. Tools Manufact. Vol. 38. No 5-6, pp. 691-698, 1998

O4 – Annex